

Dijet Invariant Mass Studies in the Higgs boson $H \rightarrow b\bar{b}$ resonance search in association with a W/Z boson using the ATLAS detector



Manuel Daniel Proissl

A thesis submitted in fulfilment of the requirements
for the degree of Doctor of Philosophy to the
University of Edinburgh

November 2014

Abstract

The Standard Model of Particle Physics describes the fundamental building blocks of matter and phenomena up to the highest particle interaction energies. The theory demands the existence of a scalar particle: the Higgs boson. The Higgs boson was discovered by the ATLAS and CMS collaborations at CERN using bosonic final states and is measured to have a mass of around 125 GeV. This particle is predicted to decay predominantly into pairs of b -quarks at this mass, but suffers from overwhelming backgrounds from the multijet production expected from QCD interactions. Therefore, $H \rightarrow b\bar{b}$ production in association with a leptonically decaying W or Z boson is considered, with $Z \rightarrow \nu\bar{\nu}$, $W \rightarrow \ell\nu$ and $Z \rightarrow \ell\ell$, where ℓ denotes electrons and muons.

This thesis presents a search for the Higgs boson decaying into $b\bar{b}$ pairs in association with a W or Z boson using the ATLAS detector at the Large Hadron Collider (LHC) at CERN. The analysis uses the full dataset recorded during pp collisions at the LHC in Run-1, corresponding to 4.7 fb^{-1} at $\sqrt{s} = 7 \text{ TeV}$ and 20.3 fb^{-1} at $\sqrt{s} = 8 \text{ TeV}$. A multivariate technique and a kinematic cut-based approach have been used to maximize the signal over background ratio, where a particular emphasis on the latter approach is made in this thesis.

Final state radiation and reconstruction effects may decrease the $b\bar{b}$ resonance resolution significantly, while comparably decreasing the probability of observing the decay over the background. The b quark pairs from the Higgs boson are reconstructed as topological clusters formed to jets in the ATLAS calorimeter. Thus, the reconstruction and calibration of these jets are crucial for the final Higgs mass resolution and paramount for the search and for future precision measurements of VH , $H \rightarrow b\bar{b}$ production. This thesis presents the development and

evaluation of advanced techniques to improve the invariant dijet mass reconstruction of the $H \rightarrow b\bar{b}$ candidate. Sequential jet calibrations, semileptonic corrections and p_T corrections to account for the interplay between jet resolution/scale and the underlying signal p_T spectrum obtained from Monte Carlo simulations have been studied. A major focus has been made on the development and evaluation of an event-level kinematic likelihood fitting framework to exploit the full kinematic potential of VH topologies within the detector uncertainties of the reconstructed final state signatures in order to improve the measurement of the b -tagged jet kinematics.

The jet energy calibrations of the $H \rightarrow b\bar{b}$ signal candidates yield an overall improvement of the dijet invariant mass resolution of up to $\sim 30\%$, and of the expected statistical significance of $\sim 12\%$. The analysis procedure is validated using the resonant $VZ(b\bar{b})$ production in the same final states as for the Higgs boson search, and is observed, compatible with the Standard Model expectation, with a significance of 4.9 standard deviations and a signal strength of $\hat{\mu}_{VZ} = 0.74^{+0.17}_{-0.16}$. For a Higgs boson mass of 125.36 GeV, the observed (expected) deviation from the background-only hypothesis is found with a significance of 1.4 (2.6) standard deviations and a signal strength is determined to be $\hat{\mu}_{VH} = 0.52 \pm 0.32(\text{stat.}) \pm 0.24(\text{syst.})$.

Declaration

This dissertation is the result of my own work, except where explicit reference is made to the work of others, and has not been submitted for another qualification to this or any other university. This dissertation does not exceed the word limit for the respective Degree Committee.

A handwritten signature in black ink, appearing to read 'M. Proissl', with a large, stylized initial 'P'.

Manuel Proissl

Acknowledgements

I would like to express my gratitude to the Scottish Universities Physics Alliance (SUPA), the University of Edinburgh, the ATLAS collaboration and CERN for making my doctoral research in Particle Physics possible. Foremost, I would like to thank my supervisor, Dr. Victoria J. Martin, for supporting me throughout my Ph.D., for believing in me, and for giving me the opportunity to work at CERN for nearly two years. It has been a truly amazing experience to be part of the Edinburgh Particle Physics Experiment and ATLAS groups, and to work collaboratively with other ATLAS institutions worldwide. I also like to thank my second supervisor, Prof. Philip J. Clark, for his support while being at CERN. Thanks to many of my Ph.D. colleagues, particularly, Chiara Debenedetti, Francisca Garay, Karoline Selbach, and Ben Smart, for precious discussions and fun times. A special thanks goes Jane Patterson, for always taking time and being tremendously kind and helpful in all matters.

During my time at CERN, I have had the great pleasure to work on numerous interesting projects with many people from different ATLAS groups. Most notably, I would like to thank Gabriel Facini for guiding me, helping and advising me, and for being a friend. It has been a wonderful experience to be part of the HSG5 group and to work with many great people on the VH analysis. Particularly, I am very thankful to Heather Gray, Tim Scanlon, Giacinto Piacquadio, David Lopez and Andy Metha for their collaboration and constant support.

All my work would have been impossible without the incredible support of my family. First of all, I would like to thank my grandmother, Lore Proissl, for inducing the spark, when I was a young boy, that has led to my interest in physics and, ever since, dedication to research. I am extremely thankful to my parents and my sisters, for their loving support, their remarkable patience, and for always believing in me. Lastly, I would like to thank my amazing wife for always standing by my side, for encouraging and supporting me throughout this period, for being patient with me, and for believing in me. I am dedicating this thesis to my son, who makes me always smile.

TO MY FAMILY.

Preface

The work presented in this thesis is based on the work of thousands of people, who have contributed to the design, construction, operation and maintenance of the ATLAS detector, the Large Hadron Collider (LHC), the CERN computing infrastructure, and the international LHC computing grid. Furthermore, the ATLAS data analysis presented in this thesis relies on a number of different calibrations, particle reconstruction algorithms, and performance evaluations, which have been made by many others. The direct contributions by the author are summarized here, and for each chapter listed below. Generally, all figures and tables, which do not contain a reference in the caption, are the result of the author's own work.

The author has made direct contributions to the reconstruction and calibration of electrons, muons and (b -tagged) jets, foremost, in the analysis-specific context of the Higgs boson $H \rightarrow b\bar{b}$ resonance search in association with a W or Z boson, using the full LHC Run-1 dataset recorded by the ATLAS detector in 2011 and 2012. The detector-level reconstruction of these particles are described in Section 3.2, and the analysis-level reconstruction is the focus of Chapters 4, 5, and 6. Furthermore, the author has played a key role in the development of the Higgs boson analysis framework (e.g. implementing, validating, optimizing event selections; Table 5.2), which was used for the particle reconstruction studies mentioned above, and for optimizing the analysis, and for the final production of $WH \rightarrow \ell\nu b\bar{b}$ input distributions (see e.g. Figure 5.11b) for the profile likelihood fit (Section 5.7).

For muons, the author validated the ATLAS muon trigger wrapper algorithm (Trig-MuSuperEF) before it went into production, i.e. before it could be actively used in the ATLAS collaboration. This involved the development of validation software to compare track-based information with the standalone predecessors of this algorithm (Trig-MuonEF and TrigMuGirl). The author also designed, developed, implemented and managed two software packages for the ATLAS Virtual Point 1 (VP1) event display to access and process muon data from the online ATLAS trigger system, to filter and search

muon trigger data, and to associate this data to reconstructed muon tracks. This software helped in studying analysis-selected muons that have passed specified trigger criteria. The VP1 event displays in Figure 4.2 have been produced by the author. For isolated electrons and muons, the author measured track- and calorimeter isolation efficiencies and scale factors using a tag-and-probe method. This includes studies of the dependence of nearby jets. The measurement is presented in Section 4.2.3 and the resulting scale factors are used in Chapter 5 for the $WH \rightarrow \ell\nu b\bar{b}$ channel.

For jets, the author evaluated the impact of the global sequential calibration (Section 4.3.3) for b -tagged jets selected by the analysis (Section 5.3). The results of this evaluation are shown in Section 5.4.2. The author implemented and evaluated a semileptonic jet energy correction, the muon-in-jet correction, as shown in Section 5.4.3. The author derived, implemented and evaluated a jet energy resolution correction, as shown in Section 5.4.4. Furthermore, the author designed, developed, implemented and evaluated an event-level kinematic likelihood fit targeting the $ZH \rightarrow \ell\ell b\bar{b}$ process. Chapter 6 is dedicated to this fit and all presented material in this chapter are the result of the author's own work.

Additionally, the direct contributions by the author are briefly outlined for the relevant chapters below:

Chapter 3: The author, as mentioned above, validated muon trigger algorithms, as used by ATLAS (Section 3.2.7).

Chapter 4: The author produced for $H \rightarrow b\bar{b}$ candidates in ATLAS 8 TeV data the event displays for each analysis channel shown in Figure 4.2. The author derived and implemented tag-and-probe algorithms for the $WH \rightarrow \ell\nu b\bar{b}$ and $ZH \rightarrow \ell\ell b\bar{b}$ channels and measured the track- and calorimeter isolation efficiencies and corresponding scale factors presented in Section 4.2.3. The author extracted the average jet response as a function of p_T and η , and produced Figure 4.26b. The corresponding η correction factors are shown in Figure 4.27. The author studied the average number of tracks and the average track width associated to jets, and evaluated the relative impact of these quantities in the global sequential calibration in terms of the response to light-quark, b -quark, and gluon-induced jets (Figures 4.30 and 4.31). The author evaluated the efficiency of the overlap removal discussed in Section 4.5.

Chapter 5: The author contributed to the implementation and the optimization of the event selection discussed in Section 5.3, in order to improve the sensitivity of the $H \rightarrow b\bar{b}$ search. All jet energy calibrations presented in Sections 5.4.2 to

5.4.5 are the result of the author's own work. The author contributed to the data analysis framework producing the distributions of the 1-lepton channel shown in Figure 5.11b. The author's jet energy and isolation efficiency studies mentioned above also contributed to the systematic uncertainties discussed in Section 5.6.

Chapter 6: The author is the sole developer of the event-level kinematic likelihood fit presented in this chapter and therefore, all results shown in this chapter are based on the author's own work.

Chapter 7: The author has performed the statistical significance test discussed in Section 7.1 with results summarized in Table 7.1.

Contents

1. Introduction	2
2. The Standard Model and the Higgs boson	5
2.1. The Standard Model constituents	6
2.1.1. The QCD sector	9
2.1.2. The Electroweak sector	12
2.2. Electroweak Symmetry Breaking	15
2.3. Higgs boson searches at the LHC	18
2.3.1. Higgs boson production and decay modes	19
2.3.2. Discovery of the Higgs boson	22
2.3.3. ATLAS measurements of Higgs boson properties	23
2.4. Limitations of the Standard Model	27
2.5. Summary	29
3. The ATLAS Experiment at the LHC	31
3.1. The Large Hadron Collider	32
3.2. The ATLAS experiment	39
3.2.1. Coordinate system	41
3.2.2. Magnet system	42
3.2.3. Inner Detector	43
3.2.4. Calorimetry system	50
3.2.5. Muon Spectrometer	57
3.2.6. Forward Detectors	60
3.2.7. Trigger and Data Acquisition system	61
3.2.8. Physics Data Processing	63
3.3. Summary	63
4. Particle Reconstruction	64
4.1. Monte Carlo simulation	67

4.2. Electrons and Muons	69
4.2.1. Reconstruction, identification and classification	69
4.2.2. Energy/Momentum resolution and scale	75
4.2.3. Isolation efficiencies and scale factors	81
4.3. Jets	91
4.3.1. Topological energy clusters	91
4.3.2. Reconstruction algorithm	92
4.3.3. Jet energy calibrations	95
4.3.4. Identification of b -quark induced jets	102
4.4. Missing Transverse Momentum	106
4.4.1. Reconstruction principle	107
4.4.2. Resolution	108
4.5. Final object selection	109
4.6. Summary	110
5. The $(W/Z)H \rightarrow b\bar{b}$ Analysis Strategy	111
5.1. Analysis Overview	111
5.2. Data and MC samples	115
5.3. Physics object and event selection	117
5.4. Energy calibration of Higgs candidates	123
5.4.1. Mass resolution fit model	123
5.4.2. Evaluation of EM+JES and GS calibrations	124
5.4.3. Muon-in-jet correction	126
5.4.4. Jet momentum resolution correction	127
5.4.5. Energy calibration summary	129
5.5. Background composition	131
5.6. Systematic uncertainties	136
5.7. Statistical procedure	138
5.8. Summary	141
6. Event-level Kinematic Likelihood Fitting	142
6.1. Methodology	143
6.2. Likelihood model	144
6.2.1. Fit parameters and constraints	145
6.2.2. Event-level Likelihood Function	146
6.3. Fit resolutions	147
6.3.1. Electrons and muons	147

6.3.2. Jets	149
6.4. Kinematic fitting framework	155
6.5. Results	156
6.6. Summary	160
7. LHC Run-1 $VH(b\bar{b})$ Analysis Results	162
7.1. Significance of jet energy calibrations	162
7.2. Diboson observation	164
7.3. Final results	166
7.4. Summary	169
8. Conclusions	171
A. Supplemental VH analysis plots	174
B. Supplemental kinematic fit plots	185
Bibliography	190
List of Figures	207
List of Tables	214

Chapter 1.

Introduction

The fundamental building blocks of nature and their governing dynamics and interactions have been unified in a theoretical framework over the past 50 years: the Standard Model of Particle Physics. Until today, this model has proven to predict or to describe, with an extraordinary experimental agreement, all particle phenomenology observed at high energy particle accelerator experiments. At the centre of this model, there is a postulated particle, which is expected to give mass to other particles in the model: the Higgs boson. For many years, since it was proposed in 1964 [1–4], this particle has been only an unconfirmed prediction.

The unprecedented energy regime presented in proton-proton collisions at the Large Hadron Collider led to the announcement, by the ATLAS and CMS experiments in July 2012 [5, 6], of the observation of a new particle with a mass of ~ 125 GeV and with properties consistent with those predicted by the Standard Model. The measurements leading to this discovery have been mainly performed in the bosonic decay modes of the new particle. It is essential to also prove its coupling to fermions, as predicted by the theory. While the first evidence for the Higgs boson decay to a tau-lepton pair has been found [7], it remains of profound importance to confirm the Higgs boson’s predominant decay to a pair of bottom-quarks: $H \rightarrow b\bar{b}$.

An inclusive search for $H \rightarrow b\bar{b}$ signals is not feasible at hadron colliders, due to the overwhelming backgrounds produced via strong interactions. Alternatively, the associated Higgs boson production process, $VH \rightarrow \text{leptons} + b\bar{b}$, with additional electron, muon and neutrino final states from a leptonically decaying W or Z vector boson (V), can be used to efficiently trigger on a cleaner signature in the detector and to reduce the backgrounds

in the $H \rightarrow b\bar{b}$ signal search. This thesis presents a direct search for VH production¹ using the full LHC Run-1 dataset, collected by the ATLAS detector in proton-proton collisions at centre-of-mass energies of 7 and 8 TeV [8]. A special emphasis is made on reconstruction methods of VH final state signatures, in particular b -quark induced jets, with the aim to improve the discrimination from other Standard Model processes. The thesis is organized as follows:

IN CHAPTER 2, the Standard Model of Particle Physics is reviewed, from the assortment of fundamental particles and interactions to the theoretical underpinnings using the language of quantum field theory. In particular, the theory's mechanism of spontaneous symmetry breaking, predicting the existence of the Higgs boson, is described. Furthermore, an overview of the Higgs boson production and decay modes at the Large Hadron Collider is given, followed by a presentation of its discovery channels and recent measurements of its properties by the ATLAS experiment, which further motivate the search for the associated $H \rightarrow b\bar{b}$ production. Finally, some of the basic limitations of the Standard Model are summarized.

IN CHAPTER 3, an overview of the Large Hadron Collider with its performance capabilities, physics motivations and experiments is given, followed by a more detailed review of the ATLAS experiment. This includes a description of the experimental conditions during the data taking periods in 2011 and 2012, which have been used for the analysis presented in this thesis. As each ATLAS detector subsystem is presented, the corresponding methods to detect particles in the subdetector and to measure basic properties are introduced. Given the subject matter of this thesis, enhanced focus is made on Inner Detector and Calorimeter measurements. The discussion of particle reconstruction at the subdetector-level in this chapter serves as the basis for the higher physics object calibrations discussed in Chapter 4.

IN CHAPTER 4, the reconstruction and calibration of VH final states are described, namely electrons, muons, b -tagged jets and missing transverse energy. Data and simulated events, i.e. through Monte Carlo simulation, are compared to derive the (final) physics analysis objects of the $H \rightarrow b\bar{b}$ search, which are later used in Chapters 5 and 6. For electrons and muons, a *tag-and-probe* method is introduced to evaluate isolation criteria of these objects. For jets, b -tagging efficiencies are discussed and jet energy calibration methods are studied. For neutrinos, basic reconstruction techniques for missing transverse energy and their performance are reviewed.

¹The term " VH production" is commonly used in this thesis to denote the process: $VH \rightarrow \text{leptons} + b\bar{b}$.

IN CHAPTER 5, the analysis strategy to search for VH production in the LHC Run-1 dataset is presented, utilizing the different kinematics of the physics objects introduced in Chapter 4, and is summarized in terms of the following subjects: Monte Carlo datasets, kinematic selection of physics objects and events, background compositions obtained from Monte Carlo simulation and their modelling (i.e. comparisons with data), experimental and systematic uncertainties and the global fit model, merging decay channels and kinematic regions.

IN CHAPTER 6, the event-level kinematic likelihood fitting technique is introduced and the construction of a maximum-likelihood model targeting the $ZH \rightarrow \ell\ell b\bar{b}$ topology is presented, where ℓ denotes electrons or muons. The detector uncertainties of the decay channel's reconstructed final state signatures entering the fit are discussed and used to exploit the event topology's full kinematic potential. Furthermore, the corresponding software design and development of a kinematic likelihood fitting framework with its event-level implementation in the VH analysis are presented. Using this framework, the fit performance is evaluated using Monte Carlo events.

IN CHAPTER 7, the results of the VH analysis, using the full LHC Run-1 dataset and the Higgs boson search strategy and reconstruction methods described in Chapters 4 to 6, are presented. This includes the validation of the analysis procedure using the diboson production, $VZ \rightarrow \text{leptons} + b\bar{b}$, the extracted Higgs boson signal strength and limit, and the sensitivity improvements from jet calibrations and kinematic likelihood fitting.

IN CHAPTER 8, the content of this thesis is briefly summarized and an outlook with final remarks is given.

Chapter 2.

The Standard Model and the Higgs boson

The ancient idea, originating from natural philosophy, that a basic simplicity and regularity can govern the apparent complexity and diversity of the universe with matter of finite fragmentation has inspired modern particle physics to explore the crucial and pervasive role of symmetry in nature. It has led to a successful comprehensive formulation of a quantum field theory, classifying the fundamental building blocks of matter and describing their electroweak and strong interactions: The Standard Model of Particle Physics (SM). This model describes all particles discovered to date and represents one of the best experimentally validated theories in science achieving an impressive level of agreement.

In this chapter, the fundamental constituents and symmetries of the SM are reviewed in Section 2.1, followed by a discussion of the spontaneous symmetry breaking in the theory's electroweak sector and the Higgs boson in Section 2.2. Higgs boson production at the LHC and the latest experimental results from the ATLAS collaboration are briefly summarized in Section 2.3. Finally, some of the SM limitations are highlighted in Section 2.4. Throughout this chapter, natural units are adopted: $\hbar = c = 1$.

The review presented in this chapter highlights only the basic SM aspects, thus the interested reader is referred to the original literature or standard text books, such as [9–12].

2.1. The Standard Model constituents

The Standard Model defines two classes of elementary particles: *fermions* and *bosons*. The former are the matter constituents, composed of leptons and quarks, and the latter are the interaction quanta mediating the strong, electromagnetic and weak interactions and the mass-giving Higgs boson. Both classes and their phenomenological assortment of particles are briefly reviewed, followed by a more detailed discussion of the underlying gauge theory.

The fundamental fermions, also referred to as the matter fields, are spin- $1/2$ particles and are grouped into three generations of leptons and quarks, ordered by their increasing mass:

1. up-quark u , down-quark d , electron e , electron neutrino ν_e ,
2. charm-quark c , strange-quark s , muon μ , muon neutrino ν_μ ,
3. top-quark t , bottom-quark b , tau τ , tau neutrino ν_τ .

They can be represented by complex spinor fields $\psi(x)$ obeying the Dirac equation, $(i\cancel{\partial} - m_f)\psi(x) = 0$, where m_f is the fermion mass and the equation's negative energy solution is interpreted as the corresponding positive-energy antiparticle of opposite charge. Each fermion is decomposed into its left-handed (L) and right-handed (R) chirality components. The left-handed components form weak isodoublets, characterized by their same behaviour under weak interactions with the third component of the weak isospin $I^3 = \pm 1/2$ (total weak isospin: $I = 1/2$), whereas the right-handed components form weak isosinglets, which have $I^3 = 0$ and do not interact weakly. This is summarized in Table 2.1, including the different quantum numbers.

The three *lepton families* contain each a neutral neutrino and a corresponding charged massive lepton. While charged leptons interact both weakly and electromagnetically, the neutrinos only interact via the weak force. Despite the results from neutrino oscillation experiments, the Standard Model makes the approximation that neutrinos are massless and thus they appear only with their left-handed components in the model.

The three *quark families* contain each an up-type quark (u, c, t) and a down-type quark (d, s, b) carrying an electric charge of $+\frac{2}{3}$ and $-\frac{1}{3}$, respectively. Quarks distinguish themselves from leptons by also interacting strongly and carrying an additional colour quantum number - red, green, blue (RGB) - the charge of the strong interaction. Due to the confinement property of the strong force [13], quarks cannot be observed in isolation

Type	Generation			Quantum Numbers			
	I	II	III	I^3	Y	Q	C
Leptons	$\begin{pmatrix} \nu_e \\ e^- \end{pmatrix}_L$	$\begin{pmatrix} \nu_\mu \\ \mu^- \end{pmatrix}_L$	$\begin{pmatrix} \nu_\tau \\ \tau^- \end{pmatrix}_L$	$\begin{pmatrix} 1/2 \\ -1/2 \end{pmatrix}$	$\begin{pmatrix} -1 \\ -1 \end{pmatrix}$	$\begin{pmatrix} 0 \\ -1 \end{pmatrix}$	–
	e_R^-	μ_R^-	τ_R^-	0	–2	–1	
Quarks	$\begin{pmatrix} u \\ d \end{pmatrix}_L$	$\begin{pmatrix} c \\ s \end{pmatrix}_L$	$\begin{pmatrix} t \\ b \end{pmatrix}_L$	$\begin{pmatrix} 1/2 \\ -1/2 \end{pmatrix}$	$\begin{pmatrix} 1/3 \\ 1/3 \end{pmatrix}$	$\begin{pmatrix} 2/3 \\ -1/3 \end{pmatrix}$	$\begin{pmatrix} R, G, B \\ R, G, B \end{pmatrix}$
	u_R	c_R	t_R	0	4/3	2/3	R, G, B
	d_R	s_R	b_R	0	–2/3	–1/3	R, G, B

Table 2.1.: The fundamental fermions and their quantum numbers in the Standard Model, including the third component of the weak isospin I^3 , the hypercharge Y , the electric charge Q and the colour charge C . The corresponding anti-fermions have inverted quantum numbers.

but are bound in colour-singlet or “colour-neutral” composite particles, the *hadrons*. These appear in nature in the form of integer spin *mesons* ($q\bar{q}$ states) and odd half-integral spin *baryons* (qqq states).

The fundamental vector bosons, also referred to as the force carriers or gauge vector fields, are spin-1 particles that mediate the fundamental interactions:

- The massive charged W^\pm and neutral Z^0 , responsible for the weak interactions.
- The massless photon γ , the carrier of the electromagnetic force.
- The eight massless gluons g , the mediators of the strong interactions.

The fourth fundamental interaction, gravity, is not included in the SM, since a consistent formulation of quantum gravity does presently not exist. However, the strength of gravity is nearly 30 orders of magnitude weaker than the weak force. Thus gravitational effects are expected to become only relevant at energies near the Planck scale ($M_P \equiv 1.22 \times 10^{19}$ GeV) and are therefore negligible at the energy scales currently accessible by accelerator experiments with orders of a few TeV.

Symmetries and the application of group theory have played a profound role in modern physics, paving the way from special relativity, quantum mechanics to relativistic quantum field theories, and have guided the construction of a unified description of weak, electromagnetic and strong interactions between the elementary particles[14]. This theory must ensure the invariance under Poincaré transformations, i.e. space-time translations,

rotations and Lorentz boosts, for the compatibility with the laws of *special relativity*. From Noether's theorem [15] we know that the invariance of the theory's action (time integral of the Lagrangian) under some group of transformations (symmetry) implies the existence of conserved quantities, i.e. symmetries imply *conservation laws*. Moreover, demanding the theory's Lagrangian to be invariant under *local gauge transformations* leads to a dynamical description of interacting fields, i.e. symmetries imply dynamics. This also allows the *renormalizability* of the theory with a unitary behaviour at high energies, i.e. the independence of the dynamics at energy scale E_i from dynamical effects arising at $E_j \gg E_i$. These basic concepts in combination with phenomenological findings have governed the development of the Standard Model.

The electromagnetic and weak interactions between quarks and leptons are described by the Glashow-Weinberg-Salam Electroweak Theory (EW) [16–18], which is a Yang-Mills theory [19] based on the symmetry group $SU(2)_L \otimes U(1)_Y$ of left-handed weak isospin and hypercharge (Y). The strong interactions between quarks are described by the theory of Quantum Chromodynamics (QCD) [20–25] based on the colour-charge (C) symmetry group $SU(3)_C$. In the Standard Model, both QCD and EW theory are combined to build a unified framework to describe these three forces of nature. The associated Lagrangian density of the model,

$$\mathcal{L}_{\text{SM}} = \mathcal{L}_{\text{QCD}} + \mathcal{L}_{\text{EW}}, \quad (2.1)$$

is invariant under the gauge group

$$\underbrace{SU(3)_C}_{\text{QCD}} \otimes \underbrace{SU(2)_L \otimes U(1)_Y}_{\text{EW}}, \quad (2.2)$$

where the QCD sector, described in Section 2.1.1, can be treated separately from the EW sector, described in Section 2.1.2. Three independent coupling constants can be derived as a result of the independent product of the three symmetry groups and are discussed in the following sections. A cornerstone of the Standard Model is the introduction of a mechanism that spontaneously breaks the electroweak symmetry to allow particles to acquire mass and postulates the existence of a scalar boson: the Higgs boson. This mechanism was proposed by Higgs, Brout, Englert, Guralnik, Hagen and Kibble in 1964 [1–4] and will be summarized in the dedicated Section 2.2.

In summary, the Standard Model is a unified framework based on QCD and EW theory and comprises 3 charged leptons and 6 coloured quarks, described by 21 Dirac

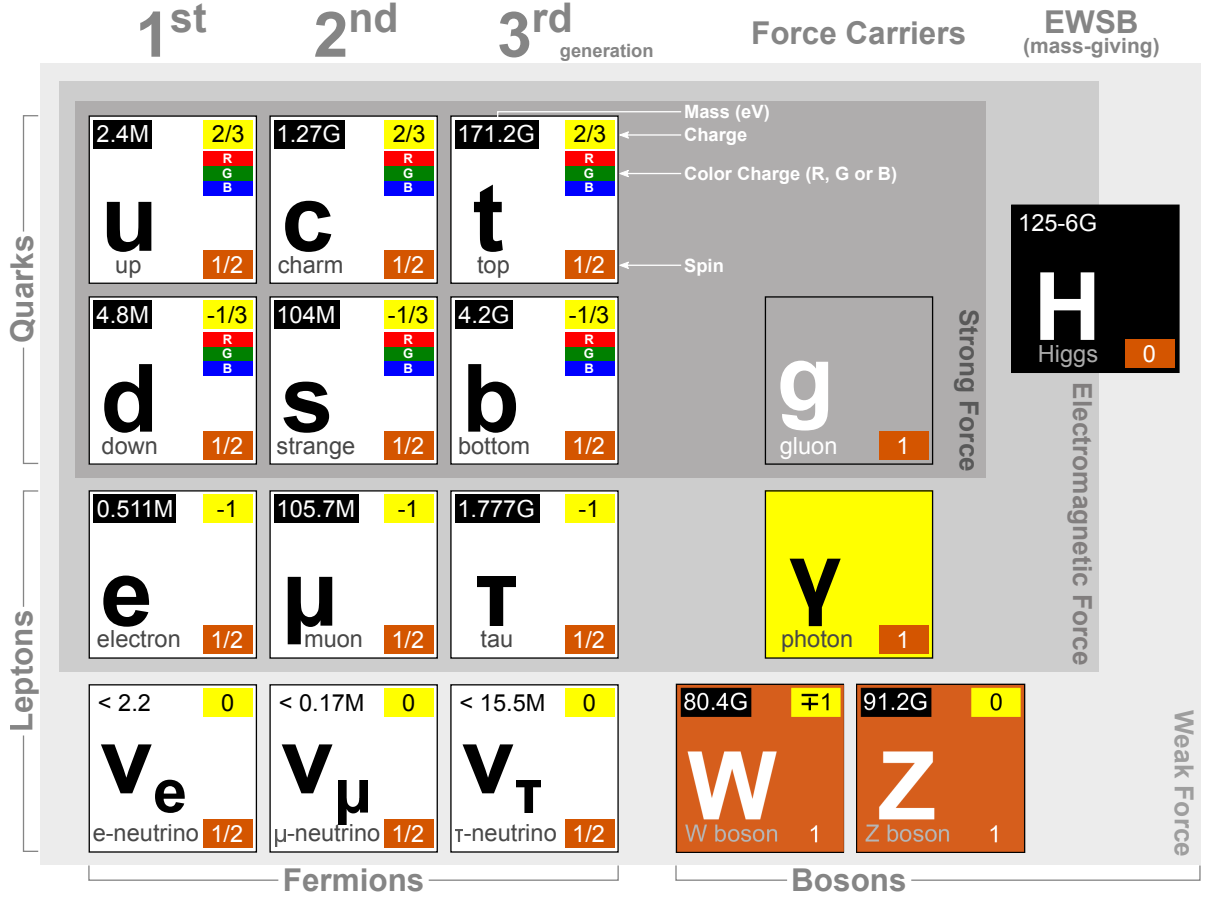


Figure 2.1.: The Standard Model of Particle Physics, showing the assortment of all fundamental fermions and bosons with their basic properties. $G/M \equiv \text{GeV/MeV}$.

spinors, 3 neutral leptons, described by 3 Weyl spinors [26], 5 electroweak and coloured strong force-mediating vector bosons, described by 12 gauge fields, and a mass-giving scalar boson field, described by a complex doublet. An overview of the Standard Model constituents and their basic properties is given in Figure 2.1.

2.1.1. The QCD sector

Quantum Chromodynamics is a non-abelian (non-commuting) gauge theory, invariant under local $SU(3)_C$ gauge transformations, and describes the strong interactions between coloured quarks in the Standard Model. The theory considers three colour-charge states (R , G , B or their corresponding anti-colours \bar{R} , \bar{G} , \bar{B}), replicated in six quark flavours (u , d , c , s , t , b), and eight types of gluons carrying and mediating colour-charge between the quarks, expressed by eight linearly independent colour/anti-colour combinations.

The quark fields q_r , with flavour index $r = 1, \dots, 6$, transform as $SU(3)_C$ triplets in colour space and the colour octet of gluon fields G_μ^a , $a = 1, \dots, 8$, corresponds to the eight generators of the $SU(3)_C$ group, $T^a = \lambda^a/2$, expressed by the Gell-Mann λ -matrices [27], and obey the commutation relations

$$[T^a, T^b] = if^{abc}T^c \quad \text{with} \quad \text{Tr}[T^a T^b] = \frac{1}{2}\delta_{ab}, \quad (2.3)$$

where the f^{abc} ($a, b, c = 1, \dots, 8$) are the $SU(3)_C$ structure constants, which are anti-symmetric in all indices. The *Lagrangian density of QCD* can be written as

$$\mathcal{L}_{\text{QCD}} = \sum_r \bar{q}_{r\alpha} i \not{D}_\beta^\alpha q_r^\beta - \frac{1}{4} F_{\mu\nu}^a F^{a\mu\nu}, \quad (2.4)$$

where quark fields couple minimally to gluon fields through the covariant derivative

$$D_{\mu\beta}^\alpha = (D_\mu)_{\alpha\beta} = \partial_\mu \delta_{\alpha\beta} + ig_s T_{\alpha\beta}^a G_\mu^a, \quad (2.5)$$

with $\alpha, \beta = 1, 2, 3$ referring to quark colour indices in the fundamental representation of $SU(3)_C$ and g_s referring to the QCD gauge coupling constant. The third non-abelian term of the strength tensor for the gluon fields,

$$F_{\mu\nu}^a = \partial_\mu G_\nu^a - \partial_\nu G_\mu^a - g_s f^{abc} G_\mu^b G_\nu^c, \quad (2.6)$$

gives rise to triple and quartic self-interactions of gluons. Although allowed by QCD alone, Equation 2.4 omits explicit mass terms for the quarks, which are forbidden by the chiral symmetry of the electroweak part of the Standard Model and instead will be generated later through spontaneous symmetry breaking (see Section 2.2).

The QCD Lagrangian is invariant under local gauge transformations, i.e. quark fields can be redefined independently at each space-time point x , without changing the physical content:

$$\begin{aligned} q(x) &\rightarrow q'(x) = e^{iT^a \alpha_a(x)} q(x) \equiv U(x) q(x) \\ D_\mu q(x) &\rightarrow D'_\mu q'(x) \equiv U(x) q(x) \end{aligned} \quad (2.7)$$

where $U(x) \in SU(3)_C$ and $\alpha(x)$ is an arbitrary function. In order to cancel unphysical polarization states of the gluons and allow the definition of inverse propagators, \mathcal{L}_{QCD} must be extended with so-called ghost and gauge-fixing terms [28], respectively.

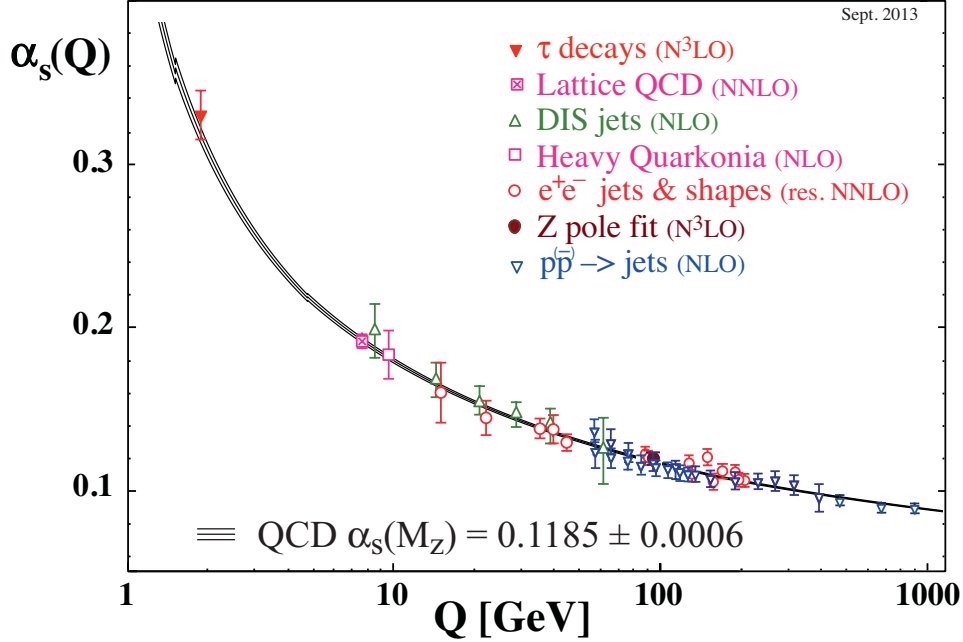


Figure 2.2.: Measurements of α_s as a function of the energy scale Q . The order of perturbative QCD calculations used in the extraction of α_s are denoted by NLO (next-to-leading order), NNLO (next-to-NLO), res. NNLO (NNLO with next-to-leading log resummation) and N³LO (next-to-NNLO) [12].

Two key features of QCD can be understood in terms of the variation of the strong coupling constant $\alpha_s \equiv g_s^2/4\pi$, the absolute size of which is not given by the theory, but is predicted through its energy scale dependence¹ and can be determined experimentally. The *running* coupling $\alpha_s(Q^2)$ [29] determines the effective strength of the strong force as a function of the momentum transfer Q^2 of the particle interaction process under study, governing the likelihood of a particular interaction, and can be expressed as

$$\alpha_s(Q^2) \propto \frac{1}{\beta_0 \ln\left(\frac{Q^2}{\Lambda_{\text{QCD}}^2}\right)} + \dots, \quad (2.8)$$

where the 1-loop β -function coefficient is defined as $\beta_0 = (33 - 2n_f)/(12\pi) > 0$ with n_f number of accessible quark flavours and Λ_{QCD} refers to the QCD scale. As shown in Figure 2.2, the running coupling decreases as the energy scale increases. As previously mentioned, coloured quarks and gluons are not observed as free particles (partons), but as hadrons, meaning as colour-singlet or colour-neutral combinations of quarks, anti-quarks and gluons. At low energies or large distances between colour-charges, α_s diverges and

¹The "beta function", $\beta(\alpha_s) = \mu^2(d\alpha_s/d\mu^2)$, encodes the energy scale (μ) dependence of the coupling α_s for a given QCD process (see renormalization group equation [12]).

exceeds unity below $Q^2 < 1 \text{ GeV}$, leading to the *confinement* of quarks and gluons. On the contrary, at high energies or short distances the coupling becomes weak and quarks may overcome the binding energy of the hadron (*asymptotic freedom*) [23, 24], which permits perturbative expansions in α_s . When these coloured partons are produced in high-energy collisions and the distance between colour-charges increases, it is energetically more favourable to fragment into colour-neutral hadrons (*hadronization*) and finally produce an entire hadron shower, which leaves a distinct signature in a particle detector, referred to as a *jet*. The reconstruction of jets and the identification of the their originating parton play a key role in this thesis and will be discussed in more detail in Chapters 3 and 4.

2.1.2. The Electroweak sector

The electroweak theory describes electromagnetic and weak interactions and is based on the symmetry group $SU(2)_L \otimes U(1)_Y$. As previously mentioned, fermion fields $\psi_{(L,R)_k}$, with the generation index $k = 1, 2, 3$, are described in terms of left-handed (L) doublets and right-handed (R) singlets, while the latter do not undergo weak interactions. They can be expressed through their corresponding chirality projection operators $P_{(L,R)}$:

$$\begin{aligned}\psi_{L_k} &\equiv P_L \psi_k = \frac{1}{2} (1 - \gamma^5) \psi_k \\ \psi_{R_k} &\equiv P_R \psi_k = \frac{1}{2} (1 + \gamma^5) \psi_k,\end{aligned}\tag{2.9}$$

with the “fifth gamma matrix” $\gamma^5 \equiv i\gamma^0\gamma^1\gamma^2\gamma^3$. The fermion current formed with ψ_k (i.e. $\bar{\psi}_k \gamma^\mu \psi_k$) transforms as a vector, while the fermion current formed with $\gamma^5 \psi_k$ (i.e. $\bar{\psi}_k \gamma^\mu \gamma^5 \psi_k$) is an axial vector, which exhibits the parity symmetry \mathcal{P} violating “ $V - A$ nature” of electroweak interactions. Thus, left- and right-handed fermionic multiplets can be defined for the lepton sector $\ell = e, \mu, \tau$ as

$$\psi_{L_k}^\ell = \begin{pmatrix} \nu_k \\ \ell_k \end{pmatrix}_L \quad \psi_{R_k}^\ell = \ell_{R_k},\tag{2.10}$$

and for the up-type $\mathfrak{U} = u, c, t$ and down-type $\mathfrak{D} = d, s, b$ quark sectors q as

$$\psi_{L_k}^q = \begin{pmatrix} \mathfrak{U}_k \\ \mathfrak{D}'_k \end{pmatrix}_L \quad \psi_{R_k}^{q(\mathfrak{U})} = \mathfrak{U}_{R_k} \quad \psi_{R_k}^{q(\mathfrak{D})} = \mathfrak{D}_{R_k},\tag{2.11}$$

where the quark colour charge index is omitted and $\mathfrak{D}'_k = \sum_m V_{km} \mathfrak{D}_k$ is a quark flavour rotated mixture using the Cabibbo-Kobayashi-Maskawa quark mixing matrix V_{km} [30, 31].

The unified electroweak force is carried by two charged and two neutral gauge bosons, where charged currents induce flavour transitions and neutral ones conserve flavour. The theory considers one gauge field B_μ that corresponds to the weak hypercharge generator Y of the $U(1)_Y$ group and three gauge fields W_μ^a ($a = 1, 2, 3$) that correspond to the weak isospin generators $I^a = \tau^a/2$ of the $SU(2)_L$ group, where τ^a are the non-commuting 2×2 Pauli matrices. These generators satisfy the commutation relations

$$[I^a, I^b] = i\epsilon_{abc}I^c \quad \text{and} \quad [Y, Y] = 0, \quad (2.12)$$

where ϵ_{abc} is the antisymmetric tensor. The weak hypercharge and the third component of the weak isospin are related to the electric charge Q (in units of e) via the relation²:

$$Q = I^3 + \frac{Y}{2}. \quad (2.13)$$

The corresponding quantum numbers (eigenvalues) for left- and right-handed fermions have been summarized in Table 2.1.

The local $SU(2)_L \otimes U(1)_Y$ gauge invariant *Lagrangian density of EW theory*³ can be written as

$$\mathcal{L}_{\text{EW}} = \underbrace{\sum_{\substack{\chi=L,R \\ k=1,2,3}} \bar{\psi}_{\chi k}^{(\ell,q)} i \not{D} \psi_{\chi k}^{(\ell,q)}}_{\mathcal{L}_{\text{fermion}}} - \underbrace{\frac{1}{4} W_{\mu\nu}^a W^{a\mu\nu} - \frac{1}{4} B_{\mu\nu} B^{\mu\nu}}_{\mathcal{L}_{\text{gauge}}} \quad (2.14)$$

The fermion term can be expanded in left- and right-handed fields:

$$\mathcal{L}_{\text{fermion}} = \sum_k \left(\bar{\psi}_{L_k}^\ell i \not{D} \psi_{L_k}^\ell + \bar{\psi}_{L_k}^q i \not{D} \psi_{L_k}^q + \bar{\psi}_{R_k}^\ell i \not{D} \psi_{R_k}^\ell + \bar{\psi}_{R_k}^{q(\mathfrak{L})} i \not{D} \psi_{R_k}^{q(\mathfrak{L})} + \bar{\psi}_{R_k}^{q(\mathfrak{D})} i \not{D} \psi_{R_k}^{q(\mathfrak{D})} \right),$$

with the gauge covariant derivative defined as

$$D_\mu = \partial_\mu + ig I^a W_\mu^a + ig' \frac{Y}{2} B_\mu, \quad (2.15)$$

²This relation is identical to the Gell-Mann-Nishijima relation obtained in the quark model of hadrons.

³Equation 2.14 does not contain any mass terms, which are introduced via electroweak symmetry breaking in Section 2.2.

where the coupling constants g and g' are associated with the gauge fields W_μ^a and B_μ , respectively. Their corresponding field strength tensors in $\mathcal{L}_{\text{gauge}}$ are

$$W_{\mu\nu}^a = \partial_\mu W_\nu^a - \partial_\nu W_\mu^a - g\epsilon_{abc}W_\mu^b W_\nu^c \quad (2.16a)$$

$$B_{\mu\nu} = \partial_\mu B_\nu - \partial_\nu B_\mu, \quad (2.16b)$$

and similar to Equation 2.6 in the QCD sector, the third term in Equation 2.16a gives rise to triple and quartic self-interactions of the W_μ^a fields. While these fields couple only to left-handed fermions, the B_μ field couples to both chiralities and has no self-interactions.

The physical fields of the gauge bosons, W^\pm , Z^0 and γ , can be obtained via a mixture of the gauge fields W_μ^a and B_μ ,

$$W_\mu^\pm = \frac{1}{\sqrt{2}} (W_\mu^1 \mp iW_\mu^2) \quad (2.17a)$$

$$Z_\mu^0 = \cos \theta_w W_\mu^3 - \sin \theta_w B_\mu \quad (2.17b)$$

$$A_\mu = \sin \theta_w W_\mu^3 + \cos \theta_w B_\mu, \quad (2.17c)$$

where the neutral Z_μ^0 boson and photon A_μ fields are formed by introducing the Weinberg (electroweak mixing) angle θ_w , which is related to the electric charge e and the coupling constants g and g' :

$$\theta_w \equiv \tan^{-1} \frac{g'}{g} \xrightarrow{\text{after EWSB}} \cos \theta_w = \frac{m_W}{m_Z} \quad (2.18a)$$

$$e = g \sin \theta_w = g' \cos \theta_w, \quad (2.18b)$$

where m_W and m_Z are the W^\pm and Z^0 boson masses, respectively. However, there are no mass terms in Equation 2.14, which means all particles are massless. Explicit mass terms cannot be introduced in \mathcal{L}_{EW} , as this would violate local $SU(2)_L \otimes U(1)_Y$ gauge invariance. For instance, a fermion mass term $m_\psi \bar{\psi} \psi = m_\psi \bar{\psi} (P_L + P_R) \psi = m_\psi (\bar{\psi}_R \psi_L + \bar{\psi}_L \psi_R)$ is manifestly non-invariant under $SU(2)_L$ transformations, since ψ_L (isodoublet) and ψ_R (isosinglet) have different gauge transformations. From experiments we also know that the W^\pm and Z^0 boson are massive. A mass term for the B_μ field of the form $\frac{1}{2} m_B^2 B_\mu B^\mu \neq \frac{1}{2} m_B^2 B'_\mu B'^\mu$ is clearly not invariant under local $U(1)_Y$ transformations, with $B_\mu \rightarrow B'_\mu = B_\mu + \partial_\mu \Lambda(x)$ and $\Lambda(x) \in U(1)_Y$. Similarly this can also be shown for the W_μ^a fields under $SU(2)_L$ transformations. In the following dedicated Section 2.2, we will discuss a solution to this famous problem through a mechanism based on spontaneous electroweak symmetry breaking (EWSB).

2.2. Electroweak Symmetry Breaking

The local gauge invariant and renormalizable theory we have introduced so far successfully describes strong and electroweak interactions between *massless* elementary particles. Particle masses can be generated in this theory through the Brout-Englert-Higgs (BEH) mechanism [1–4], which involves the symmetry of the electroweak sector to be broken spontaneously to the residual electromagnetic symmetry $U(1)_Q$:

$$SU(3)_C \otimes SU(2)_L \otimes U(1)_Y \xrightarrow{EWSB} SU(3)_C \otimes U(1)_Q. \quad (2.19)$$

The basic idea behind this concept is that the theory's vacuum state breaks the *internal* gauge symmetry and as particles are propagating through the vacuum, their effective masses can be induced. We shall see that this requires a scalar field, obeying rotational and translational invariance, with a non-vanishing and constant vacuum expectation value.

Let us begin by introducing an $SU(2)_L$ doublet of complex scalar fields with four degrees of freedom, the Higgs doublet:

$$\Phi(x) = \begin{pmatrix} \phi^+(x) \\ \phi^0(x) \end{pmatrix} = \frac{1}{\sqrt{2}} \begin{pmatrix} \phi_1(x) + i\phi_2(x) \\ \phi_3(x) + i\phi_4(x) \end{pmatrix}, \quad (2.20)$$

with a weak hypercharge of $Y = 1$ and weak isospin of $I^3 = \pm \frac{1}{2}$. A scalar contribution to the electroweak Lagrangian, defined in Equation 2.14, can be added in a minimal configuration, that respects the theory's $SU(2)_L \oplus U(1)_Y$ gauge invariance and renormalizability, of the form

$$\mathcal{L}_{\text{Higgs}} = (D^\mu \Phi)^\dagger D_\mu \Phi - V(\Phi), \quad (2.21)$$

with the covariant derivative declared in Equation 2.15, implying three and four-point interactions between gauge and scalar fields, and with the Higgs potential $V(\Phi)$ expressed in its most general form as

$$V(\Phi) = \mu^2 \Phi^\dagger \Phi + \lambda (\Phi^\dagger \Phi)^2 \quad \text{with} \quad \mu, \lambda \in \mathbb{R}, \quad (2.22)$$

where, despite the notation, the parameter μ^2 can be either positive or negative, while the λ parameter must be positive to ensure vacuum stability of the theory, i.e. the potential is bounded from below. The vacuum state $|0\rangle$ of Φ can be either unique or

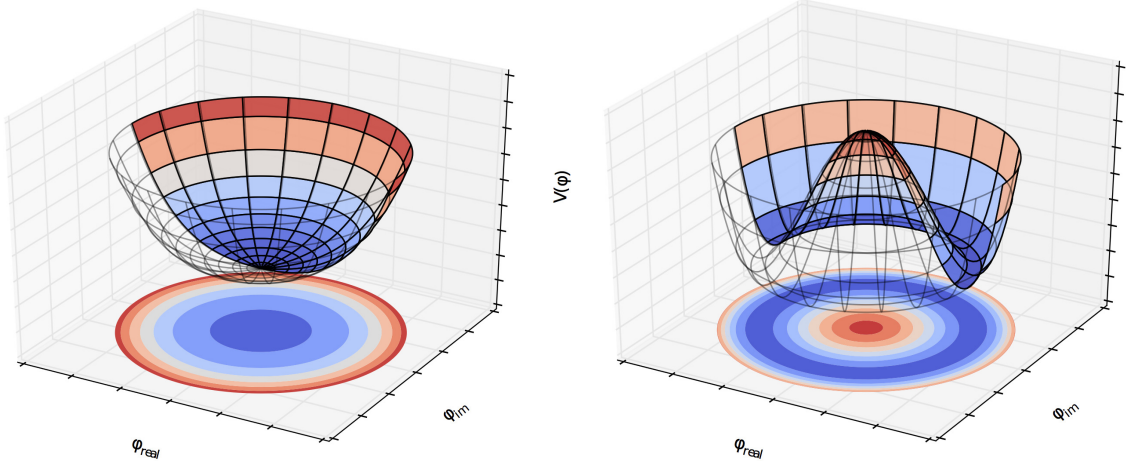


Figure 2.3.: Illustration of the Higgs potential $V(\Phi)$ with $\mu^2 > 0$ (left) and $\mu^2 < 0$ (right) [32].

degenerate. As shown in Figure 2.3, for the case that $\mu^2 > 0$, the potential has a unique global minimum at $\Phi = 0$, whereas for $\mu^2 < 0$, there is a local maximum at $\Phi = 0$ with an $SU(2)_L \otimes U(1)_Y$ invariant manifold of global minima lying on a non-zero circumference below $V(\Phi) = 0$. The minima of $V(\Phi)$ are specified by

$$\frac{dV}{d(\Phi^\dagger\Phi)} = \mu^2 + 2\lambda(\Phi^\dagger\Phi) = 0 \quad \Rightarrow \quad \Phi^\dagger\Phi|_{\min} = -\frac{\mu^2}{2\lambda} \equiv v^2/2 > 0. \quad (2.23)$$

By choosing a vacuum from these minima, one spontaneously breaks the symmetry in the ground state. In order for the photon to remain massless, a non-zero vacuum expectation value is assigned to the neutral field ϕ_3 , while the others are chosen to be zero:

$$\langle 0|\Phi|0\rangle = \begin{pmatrix} 0 \\ \frac{v}{\sqrt{2}} \end{pmatrix} \equiv \langle \Phi \rangle_0 > 0 \quad \text{with} \quad v = \left(-\frac{\mu^2}{\lambda} \right)^{1/2}. \quad (2.24)$$

Since the vacuum carries no electric charge, i.e. $Q\langle \Phi \rangle_0 = (I^3 + Y/2)\langle \Phi \rangle_0 = 0$, the $U(1)_Q$ group of electromagnetism remains unbroken, thus $SU(2)_L \otimes U(1)_Y \rightarrow U(1)_Q$.

At this point, we can expand Φ around the chosen ground state, rewrite it in terms of four real fields, $\theta_{1,2,3}(x)$ and $H(x)$ with $\phi_3 = v + H(x)$, and make a local gauge transformation to the unitary gauge [33]:

$$\Phi(x) \rightarrow e^{-\theta_a(x)\tau^a(x)}\Phi(x) = \frac{1}{\sqrt{2}} \begin{pmatrix} 0 \\ v + H(x) \end{pmatrix}, \quad (2.25)$$

in which the unphysical θ -fields, the so-called Goldstone bosons, disappear and the physical $H(x)$ field remains, the Higgs boson. Finally, one can expand $\mathcal{L}_{\text{Higgs}}$ in the

unitary gauge

$$\begin{aligned}
\mathcal{L}_{\text{Higgs}} &= (D^\mu \Phi)^\dagger D_\mu \Phi - \mu^2 \Phi^\dagger \Phi - \lambda (\Phi^\dagger \Phi)^2 \\
&= \frac{1}{2} \partial_\mu H \partial^\mu H + \frac{1}{8} (v + H)^2 [g^2 |W_\mu^1 + iW_\mu^2|^2 + |gW_\mu^3 - g'B_\mu|^2] \\
&\quad - \frac{\mu^2}{2} (v + H)^2 - \frac{\lambda}{4} (v + H)^4 \\
&= \frac{1}{2} \partial_\mu H \partial^\mu H + \frac{1}{4} (v + H)^2 \left[g^2 W_\mu^+ W^{-\mu} + \frac{g^2 + g'^2}{2} Z_\mu^0 Z^{0\mu} \right] \\
&\quad - \lambda v^2 H^2 - \lambda v H^3 - \frac{\lambda}{4} H^4,
\end{aligned} \tag{2.26}$$

where the inverse formulae of Equation 2.17 and the relation $(g \cos \theta_w + g' \sin \theta_w)^2 = g^2 + g'^2$ are used. The previously massless W^\pm and Z^0 boson fields have absorbed the three degrees of freedom of the Goldstone bosons to form their longitudinal polarizations and to acquire mass, while the photon remains massless:

$$m_W = \frac{1}{2} g v, \quad m_Z = \frac{1}{2} (g^2 + g'^2)^{1/2} v = \frac{m_W}{\cos \theta_w}, \quad m_\gamma = 0. \tag{2.27}$$

The above Lagrangian yields the Higgs boson mass m_H to be

$$m_H = \sqrt{2\lambda} v = \sqrt{-2\mu^2}. \tag{2.28}$$

The vacuum expectation value v of the Higgs field is fixed in terms of the Fermi coupling constant G_F :

$$v = \frac{1}{(\sqrt{2}G_F)^{1/2}} \simeq 246 \text{ GeV}, \tag{2.29}$$

but $\lambda(\mu)$ cannot be *directly* predicted or inferred by other Standard Model parameters. However, lower and upper bounds on the Higgs boson mass can be derived from theoretical considerations (i.e. stability, unitarity, triviality bounds). In the following Section 2.3, we will focus on the experimental search for the Higgs boson at the LHC.

Besides the generation of boson masses, the fermion masses can also be generated through the Higgs field by adding the $SU(2)_L \otimes U(1)_Y$ invariant Yukawa Lagrangian \mathcal{L}_{Yuk} to Equation 2.14:

$$\mathcal{L}_{\text{Yuk}} = - \sum_k \left(\lambda_\ell \bar{\psi}_{L_k}^\ell \Phi \psi_{R_k}^\ell + \lambda_{q(\mathfrak{D})} \bar{\psi}_{L_k}^{q(\mathfrak{D})} \Phi \psi_{R_k}^{q(\mathfrak{D})} + \bar{\psi}_{L_k}^{q(\mathfrak{U})} \tilde{\Phi} \psi_{R_k}^{q(\mathfrak{U})} \right) + \text{h.c.}, \tag{2.30}$$

where λ_ψ is a fermion Yukawa coupling to the Higgs field and $\tilde{\Phi} = i\tau_2\Phi^*$ is the isodoublet with hypercharge $Y = -1$. For instance, the electron Yukawa term can be written in the unitary gauge as

$$-\frac{\lambda_e}{\sqrt{2}} (\bar{\nu}_e, \bar{e}_L) \begin{pmatrix} 0 \\ v + H \end{pmatrix} e_R = -\frac{\lambda_e}{\sqrt{2}} (v + H) \bar{e}_L e_R, \quad (2.31)$$

and the electron mass can be identified as $m_e = \frac{\lambda_e v}{\sqrt{2}}$. Hence, the Yukawa couplings between the Higgs field and the fermions are proportional to the mass of the fermions.

2.3. Higgs boson searches at the LHC

The BEH mechanism, reviewed in the previous Section, allows the W^\pm and Z^0 vector bosons and charged fermions to acquire mass in the Standard Model, and predicts the existence of an observable massive particle, the Higgs boson, with $m_H = \sqrt{2\lambda}v$, where λ is an unknown parameter in the theory. Besides the small Higgs production cross-section and challenging experimental conditions, the *a priori* unknown mass leads to a very broad phase space region to develop search strategies for the Higgs boson. Furthermore, the collision energy to produce a Higgs boson was not achievable for sometime after its prediction. Thus, for decades it remained an unconfirmed prediction. Nevertheless, strong constraints on the Standard Model Higgs boson mass were made by theoretical arguments, direct searches at particle experiments, such as LEP (Large ElectronPositron Collider) at CERN and the Tevatron at Fermilab, and indirectly from fits to electroweak precision data.

Finally, on 4th July 2012, a Higgs-like boson with an invariant mass of ~ 125 GeV has been discovered at the Large Hadron Collider (LHC) at CERN. This has been a glorious milestone for Particle Physics and has opened the door to a rich precision physics programme. Given that all properties of the SM Higgs boson are determined once its mass is known, stringent experimental tests of these properties can be made to provide further constraints on the theory. These may include precision measurements of the SM Higgs mass, width, differential cross-sections, couplings and quantum numbers (charge, spin, CP). Moreover, these may also lead to hints beyond our Standard Model expectations.

After an overview of the different SM Higgs boson production and decay modes in proton-proton collisions at the Large Hadron Collider (LHC) at CERN in Section 2.3.1,

the Higgs discovery is reviewed in Section 2.3.2, followed by a brief summary of Higgs property measurements by the ATLAS experiment in Section 2.3.3.

2.3.1. Higgs boson production and decay modes

The main production modes of the Higgs boson at the LHC are gluon-gluon fusion (ggF), vector boson fusion (VBF), W/Z boson Higgs-strahlung (VH) and associated top-quark pair production ($t\bar{t}H$). Their corresponding Feynman diagrams are shown in Figure 2.4. The predicted cross-sections as a function of the Higgs mass m_H [34–36], based on *perturbative QCD calculations*, are shown for each process at a centre-of-mass energy of $\sqrt{s} = 8$ TeV as well as inclusively for $\sqrt{s} = 7, 8, 14$ TeV in Figure 2.5. The uncertainties on these cross-sections arise from e.g. the QCD scale, parton distribution functions and α_s [34] (see Sections 2.1.1 and 4.1). In order of decreasing production rates, the four processes are discussed below.

- **Gluon-gluon fusion**, i.e. $pp \rightarrow gg \rightarrow H$, is the dominant Higgs production mode at the LHC with a predicted cross-section of ~ 19 pb at $m_H = 125$ GeV. Since gluons do not couple directly to the Higgs boson, the production is mediated via a heavy-quark loop. As the Yukawa coupling strength is proportional to the fermion mass, the heaviest quark, the top-quark, is preferred in the loop.
- **Vector boson fusion (VBF)**, i.e. $pp \rightarrow qq \rightarrow qqV^*V^* \rightarrow qqH$ with $V = W, Z$, is the sub-leading production mode with a cross-section of ~ 1.6 pb at $m_H = 125$ GeV

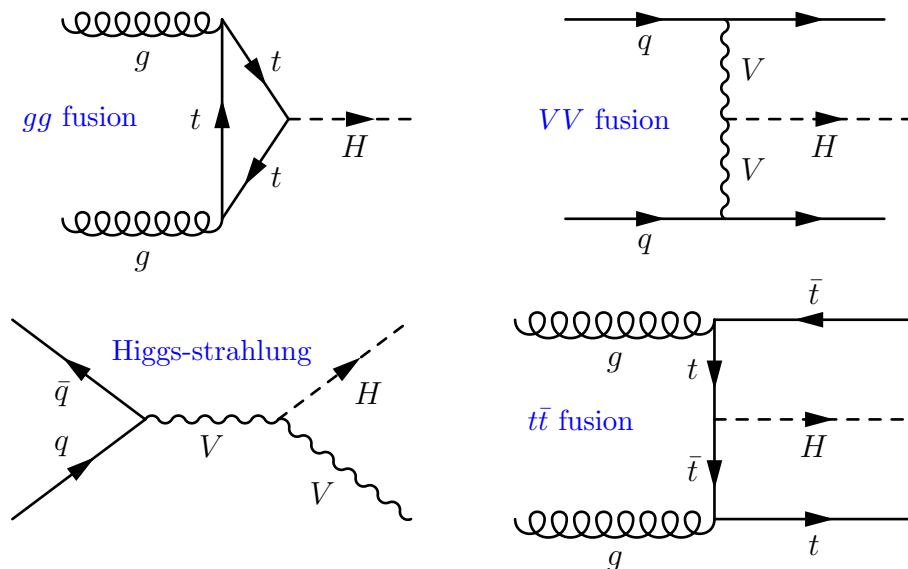


Figure 2.4.: Feynman diagrams of the main production modes of the Higgs boson at the LHC.

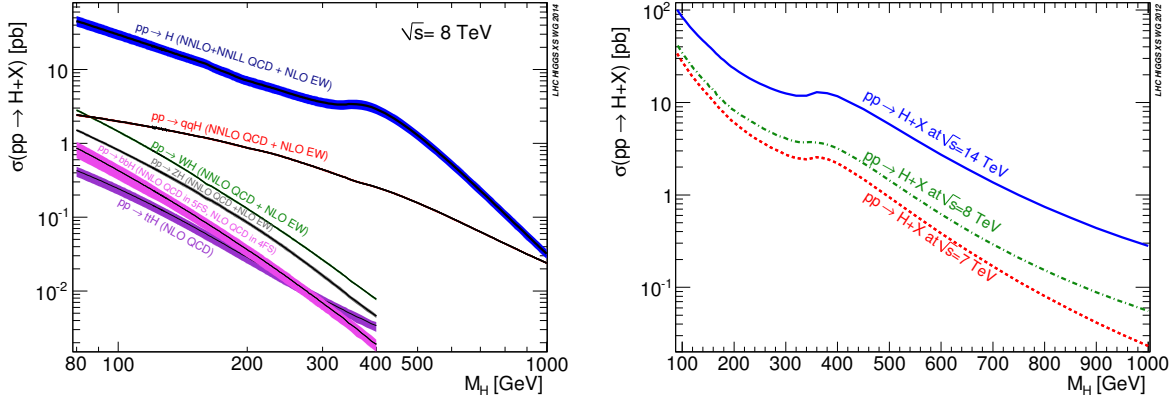


Figure 2.5.: Predicted production cross-sections of the Standard Model Higgs boson as a function of its mass for each production process exclusively (left) and inclusively (right) [34–36].

($\sim 8.2\%$ of ggF). This process leaves a distinct signature in a detector with two highly energetic jets in the very forward regions, nearly collinear to the proton beams.

- **Higgs-strahlung** from vector bosons, i.e. the *associated production with a W or Z boson*, $pp \rightarrow q\bar{q} \rightarrow V \rightarrow VH$, has a lower cross-section than VBF production with ~ 0.7 pb or ~ 0.4 pb at $m_H = 125$ GeV for the associated production with a W boson or Z boson ($\sim 3.7\%$ or 2.2% of ggF), respectively. The experimental signature of the vector boson decaying to leptons provides an improved trigger efficiency and reduces QCD background contributions.
- **Associated production with a top-quark pair**, i.e. $pp \rightarrow gg \rightarrow t\bar{t}t\bar{t} \rightarrow t\bar{t}H$, has a much lower cross-section than Higgs-strahlung with ~ 0.1 pb at $m_H = 125$ GeV ($\sim 0.7\%$ of ggF). While this process presents a challenging final state, with two W bosons, two b -quarks and a Higgs boson, it can probe the direct coupling of the Higgs boson to fermions.

The Higgs boson has different decay modes occurring at rates determined by the couplings, which are proportional to the fermion mass or to the square of the W/Z boson mass. Hence, the Higgs boson favours *decays to the heaviest kinematically accessible particles*, leading to variations of its decay fractions or branching ratios (BR) as a function of its mass, as shown in Figure 2.6a. In the following, the different decay modes for a Higgs mass of $m_H = 125$ GeV are briefly discussed.

At this mass, the Higgs boson predominantly decays into a pair of b -quarks with a branching ratio of 58% [37]. Therefore, the observation of this decay mode provides direct sensitivity to the Higgs boson coupling to fermions and is crucial to constrain the total Higgs boson decay width [38], and to enable a measurement of absolute Higgs boson couplings via a global combined fit to all accessible Higgs boson production and decay modes. However, the overwhelming QCD multijet background in the dominant gluon fusion production process $gg \rightarrow H \rightarrow b\bar{b}$ makes an inclusive search for $H \rightarrow b\bar{b}$ nearly impossible and experimentally extremely challenging. While the VBF and $t\bar{t}H$ productions suffer from large hadronic activity and complex final states with large QCD background contributions, the associated production of a Higgs boson with a weak vector boson, W or Z [39], offers a promising alternative, since the leptonically decaying vector bosons, $Z \rightarrow \nu\nu$, $W \rightarrow \ell\nu$, and $Z \rightarrow \ell\ell$ with $\ell = e, \mu$, can be efficiently used for triggering and background reductions [40, 41]. These Higgs boson decay channels are focus of this thesis.

Another important decay mode, sensitive to the coupling of the Higgs boson to fermions, is $H \rightarrow \tau^+\tau^-$ with a branching ratio of 6%. It can be exploited in all production modes, but is experimentally difficult due to neutrinos in the final state and the discrimination of hadronically decaying τ 's from light-quark (u, d) induced jets. Other fermionic decay modes, such as $H \rightarrow c\bar{c}$, probing the coupling to the second quark generation with the signal dominated by strong c -pair production, and $H \rightarrow \mu\mu$, probing

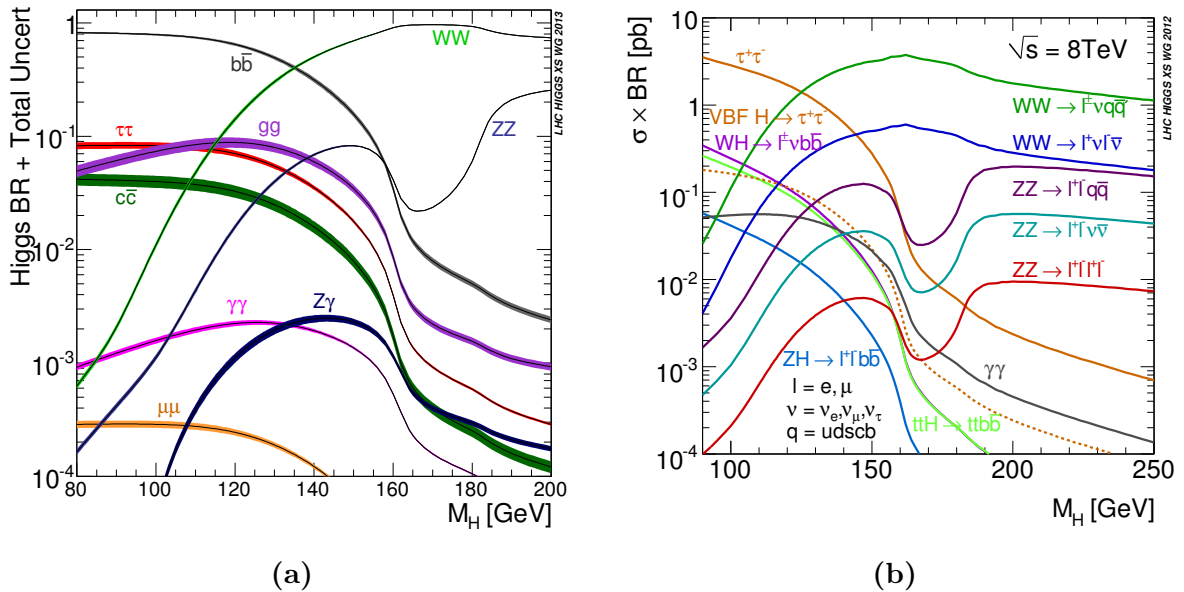


Figure 2.6.: Predicted branching ratios of the Standard Model Higgs boson decay as a function of its mass (left) and times the production cross-sections (right) [34–36].

the coupling to the second lepton generation with a very small signal, have a much lower rate with branching ratios of about 3% and 0.02%, respectively.

The dominant bosonic decay mode is $H \rightarrow WW^*$ with a branching ratio of 22%. The experimental challenges in this mode are: large hadronic activity in case of $W \rightarrow q\bar{q}$ decays and a large Higgs boson mass resolution in case of $W \rightarrow \ell\nu$ decays, due to the presence of neutrinos. $H \rightarrow gg$ is the second largest bosonic decay mode with a branching ratio of about 9%, however, it is indistinguishable from QCD backgrounds. Despite an even smaller branching ratio of about 3%, the $H \rightarrow ZZ^*$ decay mode provides a clean experimental environment with an excellent mass resolution, when considering charged leptonic Z boson decays. The $H \rightarrow ZZ \rightarrow 4\ell$ channel is also known as the “golden channel”. Similarly, the $H \rightarrow \gamma\gamma$ decay mode, mediated by a t -quark or W boson loop, has a very small branching ratio of 0.23%, but a distinctive signature with two isolated and energetic photons, identifiable against a smooth background of di-photon production.

In summary, the production cross sections times the corresponding branching ratios of accessible modes as a function of the Higgs boson mass are shown in Figure 2.6b.

2.3.2. Discovery of the Higgs boson

On 4th of July 2012, the ATLAS and CMS experiments at the LHC announced the discovery of a new boson with a mass of about $m_H = 125$ GeV and with properties consistent with those expected from the Higgs boson of the Standard Model [5, 6].

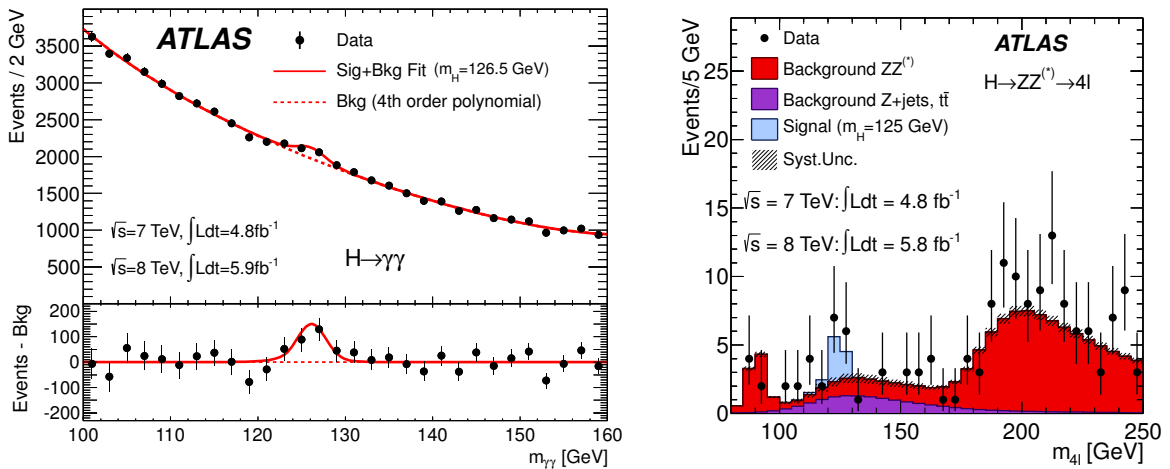


Figure 2.7.: Invariant mass distributions of the di-photon system in the $H \rightarrow \gamma\gamma$ search (left) and of the four-lepton system in the $H \rightarrow ZZ^* \rightarrow 4\ell$ search (right) [5].

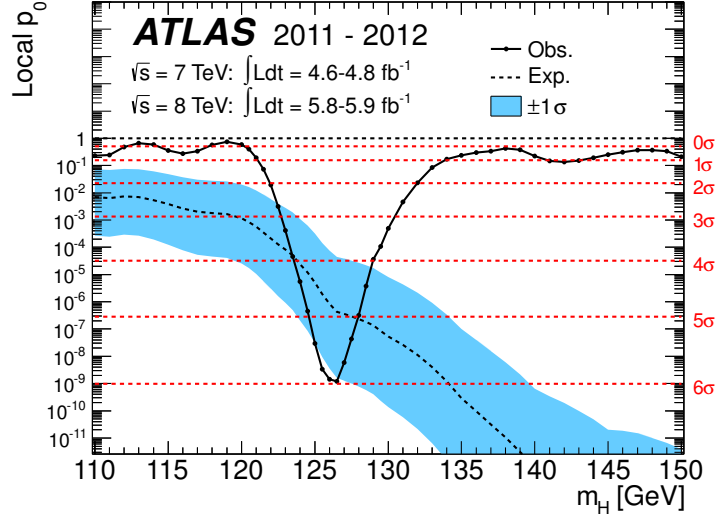


Figure 2.8.: The observed local significance (p_0) as a function of the Higgs boson mass. The dashed curve indicates the expectation for a SM Higgs boson signal hypothesis ($\mu = 1$) at the given mass and the horizontal lines show the corresponding significances in σ levels [5].

In the case of the ATLAS experiment, datasets corresponding to integrated luminosities of $4.6 - 4.8 \text{ fb}^{-1}$ collected at $\sqrt{s} = 7 \text{ TeV}$ in 2011 and $5.8 - 5.9 \text{ fb}^{-1}$ at $\sqrt{s} = 8 \text{ TeV}$ in 2012 have been used. An excess of events above the expected background yield was observed with a local significance of 5.9 standard deviations, corresponding to the probability of $p_0 = 1.7 \times 10^{-9}$, that the background can produce a fluctuation greater than or equal to the observed excess in data. The ratio of the measured signal yield to the Standard Model expectation was found to be $\mu = 1.4 \pm 0.3$ at the fitted Higgs boson mass. This observation was mainly driven by the combination of measurements in the bosonic decay modes: the $H \rightarrow \gamma\gamma$ and $H \rightarrow ZZ^* \rightarrow 4\ell$ channels with the highest mass resolution and the equally sensitive $H \rightarrow WW^* \rightarrow \ell\nu\ell\nu$ channel with a lower mass resolution. The invariant mass distributions of the high-resolution channels are shown in Figure 2.7 and the local significance as a function of the Higgs boson mass is shown in Figure 2.8.

2.3.3. ATLAS measurements of Higgs boson properties

Since the discovery of a Higgs-like boson, as described in the previous Section 2.3.2, its nature has been investigated more precisely in terms of property measurements, including mass, production strengths, couplings, and spin, to strengthen the hypothesis that this new particle is indeed the SM Higgs boson. Any deviations from the Standard Model

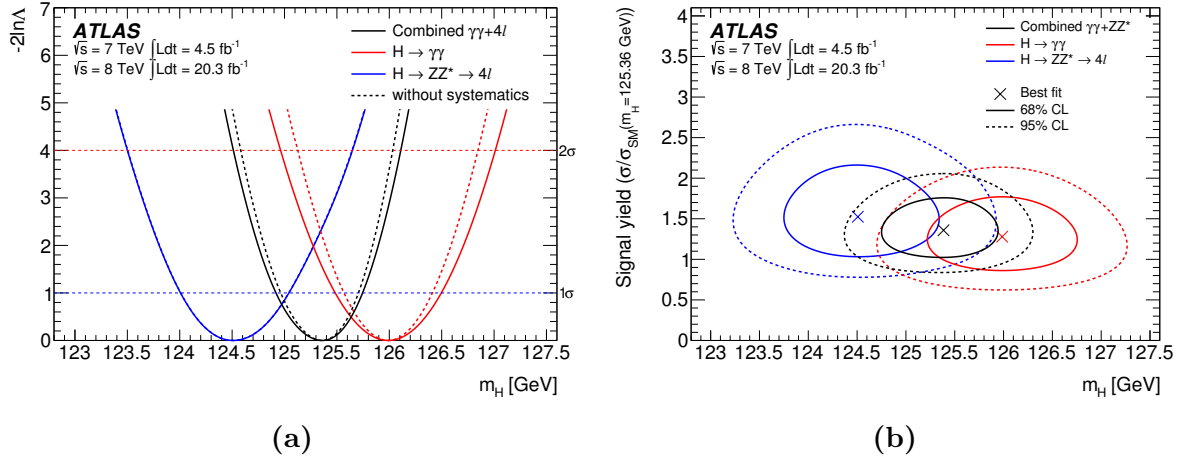


Figure 2.9.: The profile likelihood ratio $-2 \ln \Lambda(m_H)$ as a function of m_H (a) and the likelihood contour $-2 \ln \Lambda(S, m_H)$ as a function of the normalized signal yield $S = \sigma/\sigma_{\text{SM}}(m_H = 125.36 \text{ GeV})$ and m_H (b) for the $H \rightarrow \gamma\gamma$ and $H \rightarrow ZZ^* \rightarrow 4\ell$ decay channels and their combination [42].

expectations for these properties would be a sign for new physics. These measurements are made using the full LHC Run-1 dataset of proton-proton collisions recorded by the ATLAS experiment, consisting of integrated luminosities of $4.5 - 4.7 \text{ fb}^{-1}$ at $\sqrt{s} = 7 \text{ TeV}$ and $20.3 - 20.7 \text{ fb}^{-1}$ at $\sqrt{s} = 8 \text{ TeV}$.

An improved mass measurement is made using only the bosonic decay modes $H \rightarrow \gamma\gamma$ and $H \rightarrow ZZ^* \rightarrow 4\ell$, which have the best mass resolution [42]. Their reconstructed invariant mass spectra are combined in a profile likelihood ratio Λ as a function of the common Higgs mass m_H , which is profiled in the fit with the test statistics $-2 \ln \Lambda$. The measured combined mass is found to be:

$$m_H = 125.36 \pm 0.37(\text{stat}) \pm 0.18(\text{syst}) \text{ GeV}. \quad (2.32)$$

The individual and combined mass measurements are shown in Figure 2.9a. The two individual mass measurements are compatible within 2.0σ , corresponding to a probability of 4.8%. As the likelihood contours in Figure 2.9b show, the profile likelihood ratio as a function of the combined best-fit mass m_H and the normalized signal yield⁴, defined as $S = \sigma/\sigma_{\text{SM}}(m_H = 125.36 \text{ GeV})$, confirms that no significant correlation between S and m_H exists and thus exhibits the model independence of this mass measurement.

⁴The normalized signal yield S is very similar to the signal strength $\mu = \sigma/\sigma_{\text{SM}}(m_H)$, i.e. the m_H dependence of the SM cross-sections and BRs is removed and fixed to the combined best-fit mass.

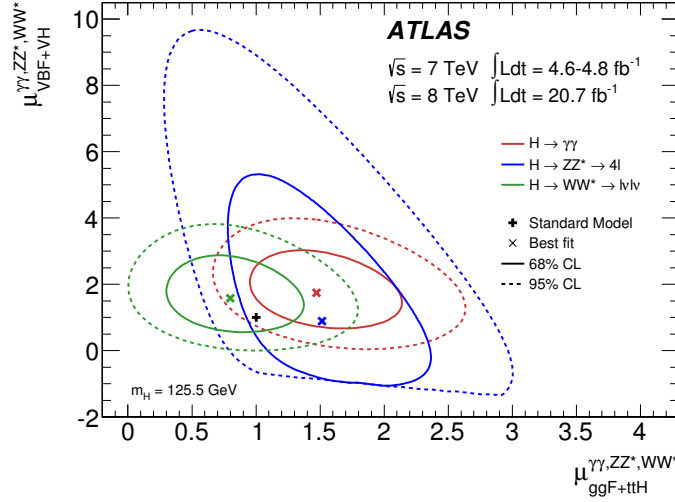


Figure 2.10.: Likelihood contours for diboson final states and a Higgs boson mass of $m_H = 125.5$ GeV in the $(\mu_{\text{ggF}+\text{t}\bar{\text{t}}\text{H}}, \mu_{\text{VBF}+\text{VH}})$ plane [43].

The relative contributions from different production modes can be evaluated with corresponding signal strengths contributing to the same final state. The gluon-induced and top-quark-mediated processes, ggF and $\text{t}\bar{\text{t}}\text{H}$, are assigned to $\mu_{\text{ggF}+\text{t}\bar{\text{t}}\text{H}}$, and the quark-induced and vector-boson-mediated processes, VBF and VH , are assigned to $\mu_{\text{VBF}+\text{VH}}$. The considered final states are from the $H \rightarrow \gamma\gamma$, $H \rightarrow \text{ZZ}^* \rightarrow 4\ell$ and $H \rightarrow \text{WW}^* \rightarrow \ell\nu\ell\nu$ decay channels. The resulting likelihood contours in Figure 2.10 show no significant deviation from the Standard Model coupling expectations. For the combination of all three diboson channels, similar to the method described above, the ratio $\mu_{\text{VBF}}/\mu_{\text{ggF}+\text{t}\bar{\text{t}}\text{H}} = 1.4^{+0.4}_{-0.3}(\text{stat})^{+0.6}_{-0.4}(\text{sys})$ provides a 3.3σ evidence that a fraction of the Higgs boson production proceeds through the VBF mode [43].

The coupling of the discovered Higgs particle to gauge bosons has been observed in different production and decay modes, and constraints have been made, directly and indirectly, at the $\pm 10\%$ level. Indirect evidence of the coupling to fermions, mainly through the top-quark loop in the ggF production mode, was found with a significance larger than 5σ [36, 43]. Recently, the first direct evidence of the coupling to fermions was found in the search for the $H \rightarrow \tau^+\tau^-$ decay channel [7]. Both, hadronic and leptonic τ decays have been considered and an excess of events above the expected background yield from other Standard Model processes was observed with a local significance of 4.5 standard deviations. As shown in Figure 2.11 for the individual channels and their combination, an overall signal strength of $\mu = 1.42^{+0.27}_{-0.26}(\text{stat.})^{+0.32}_{-0.24}(\text{syst.}) \pm 0.10(\text{theory syst.})$ for $m_H = 125.36$ GeV has been obtained. While $H \rightarrow \tau^+\tau^-$ confirms the direct coupling to the

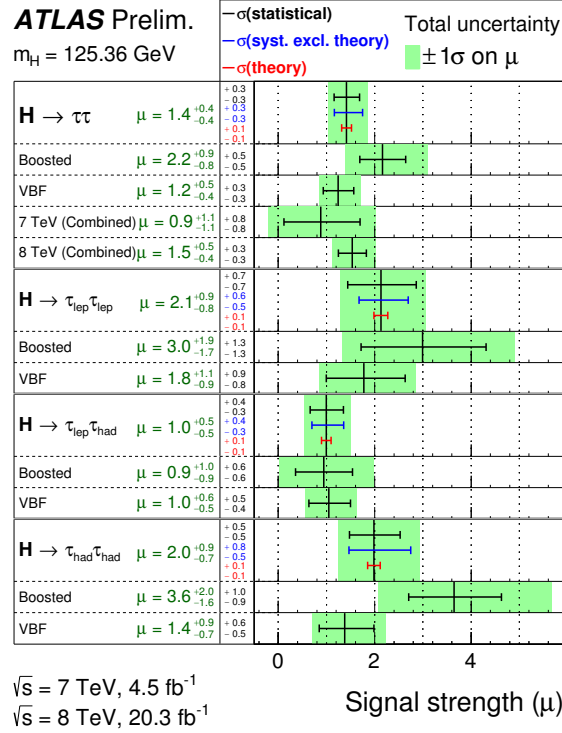


Figure 2.11.: The $H \rightarrow \tau^+ \tau^-$ best-fit value for the signal strength μ in the individual decay channels and their combination [7].

third generation leptons, the $H \rightarrow b\bar{b}$ decay mode remains to be observed and is crucial to confirm the direct coupling to the quark sector. Further details of the $H \rightarrow b\bar{b}$ search are discussed from Chapter 4 onwards, as it is the main topic of this thesis.

Besides the couplings, the Standard Model predicts the Higgs boson to be a spin-0 and CP-even particle: $J^P = 0^+$. This hypothesis is tested against the alternatives: 0^- , 1^\pm and 2^+ [44–46]. The tests are based on combinations of different kinematic observables of final states in the resonance rest frame [47]. The Higgs boson parity has been determined in the $H \rightarrow ZZ^* \rightarrow 4\ell$ channel, using the logarithm of a profile likelihood ratio to test $J^P = 0^+$ against $J^P = 0^-$, and is found to be "positive" with a confidence level of 97.8%. According to the Landau-Yang theorem, the direct decay of a spin-1 particle into a photon pair is forbidden [48, 49]. Since the $H \rightarrow \gamma\gamma$ process is observed, the 1^+ and 1^- hypotheses are strongly disfavoured and rejected at a confidence level of at least 99.7%, by combining measurements in the $H \rightarrow ZZ^* \rightarrow 4\ell$ and $H \rightarrow WW^* \rightarrow \ell\nu\ell\nu$ decay channels. Finally, the 2^+ hypothesis is tested in fractional variations of ggF and $q\bar{q}$ annihilation production processes, considering all three diboson channels, $H \rightarrow \gamma\gamma$, $H \rightarrow ZZ^* \rightarrow 4\ell$ and $H \rightarrow WW^* \rightarrow \ell\nu\ell\nu$, and is excluded at a confidence level of $> 99.9\%$. Thus, in

agreement with the Standard Model expectation, the discovered Higgs boson is indeed a spin-0 particle with even parity.

2.4. Limitations of the Standard Model

The Standard Model is a mathematically-consistent renormalizable quantum field theory and presently represents our best description of particle phenomenology with an impressive level of agreement. Over many decades the theory has been extensively tested by different particle experiments. A recent milestone has been the 2012-discovery of the 1964-predicted Higgs boson, and so far all of its property measurements, as described in Section 2.3.3, are in agreement with the Standard Model expectations. Assuming that all of the Higgs boson decay channels are observed and their properties are validated, one may think that the Standard Model is complete. However, the Standard Model⁵ cannot be considered to be even close to a complete theory of everything, as it fails to answer a number of critical questions and misses a number of ingredients to fully describe nature.

The Gauge Problem. There is no explanation in the SM for why only the electroweak part of the theory's gauge group⁶ $SU(3)_C \otimes SU(2)_L \otimes U(1)_Y$ is chiral. Furthermore, while charge quantization is incorporated in the model (multiplets of $e/3$), it can also not be explained by the theory.

The Fermion Problem. Since the construction of all matter under ordinary terrestrial conditions is possible with only the first fermion generation (ν_e, e^-, u, d), there is no obvious explanation in the theory for the existence of the first generation's heavier copies, which are known from the laboratory (but also seen in nature: atmospheric muons and muon-neutrinos from the sun). There is also no explanation or prediction for the observed hierarchical pattern of fermion masses, spanning over 5 orders of magnitude between the electron and the top-quark, and even more when considering non-zero neutrino masses. Aside from that, the Standard Model Lagrangian does not include right-handed neutrinos and thus they are considered massless, which is in contrast to neutrino oscillation phenomena observed in atmospheric, solar and accelerator-based experiments [50–52]. Before a formal incorporation of neutrino masses in the model, it still has to be determined if neutrinos are Dirac fermions, as all others in the Standard

⁵The SM contains 19 independent free parameters (or more when introducing massive neutrinos), which is considered excessive for a fundamental theory.

⁶The complexity of the gauge structure also suggests the existence of an underlying unification of the fundamental interactions.

Model, or if they are Majorana fermions (particle + anti-particle coincide) [26]. Another concern is, that there is neither the non-equilibrium condition nor sufficient CP violation built in the Standard Model to adequately explain the observed asymmetry between baryons and antibaryons in the universe.

The Gravity Problem. As discussed in Section 2.1, gravitational effects are not accounted for in the Standard Model, which are expected to have a non-negligible impact on particle phenomenology at the Planck scale (M_P). A quantum formulation of General Relativity [53–58] cannot be unified with the other fundamental interactions within the Standard Model framework, and moreover yields another problem related to the cosmological constant. The spontaneous $SU(2)_L \otimes U(1)_Y$ breaking, discussed in Section 2.2, generates an expectation value of $\langle 0|V(v)|0\rangle = -\mu^4/4\lambda$ for the minima of the Higgs potential $V(\Phi)$, which becomes crucial when the theory is coupled to gravity and hence, contributes to the cosmological constant

$$\Lambda_{\text{cosm}} = \underbrace{\Lambda_{\text{bare}}}_{8\pi G_N V(0)} + \underbrace{\Lambda_{\text{EWSB}}}_{8\pi G_N |\langle 0|V|0\rangle|} , \quad (2.33)$$

where G_N is the gravitational constant and the second term, induced via the BEH mechanism, is about 10^{56} times larger than the observed Λ_{obs} value. This can be solved through a fine-tuned cancellation, by adding a $+\mu^4/4\lambda$ term to the Higgs potential. This seems to be rather an unnatural feature of the Standard Model.

The Higgs/Hierarchy Problem. The Standard Model cannot explain why the electroweak scale is many orders of magnitude smaller than the Planck scale. As an effect of the large scale separation, the tree-level (bare) Higgs boson mass receives

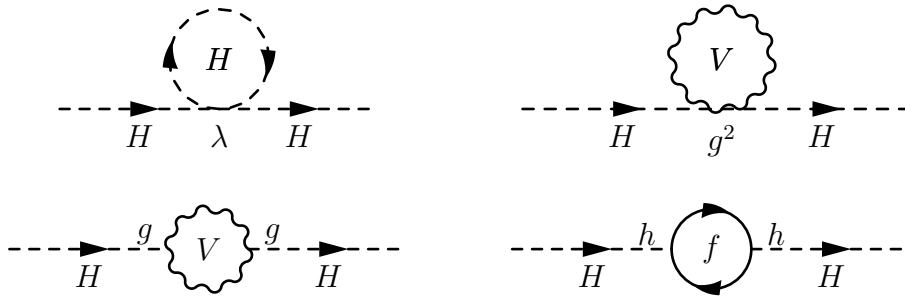


Figure 2.12.: Feynman diagrams for the one-loop corrections to the Higgs boson mass.

quadratically-divergent radiative corrections from the loop diagrams in Figure 2.12:

$$m_H^2 = (m_H^2)_{\text{bare}} + \mathcal{O}(\lambda, g^2, h^2)\Lambda^2, \quad (2.34)$$

where Λ is the next higher scale in the theory, i.e. if there is no new physics up to gravity, the next scale would be the Planck scale, $\Lambda = M_P$. Hence, the scale of m_H should be $\mathcal{O}(\Lambda)$ and thus very large, which is in contrast to direct/indirect experimental constraints, the discovery of a ~ 125 GeV Higgs boson and theoretical arguments suggesting $m_H < 1$ TeV (in order to unitarize the WW scattering amplitude). Therefore, a contrived non-natural fine-tuned cancellation between the bare Higgs mass and the radiative corrections is introduced, which clearly motivates the development of theories beyond the Standard Model, such as Supersymmetry.

The Strong CP Problem. Another fine-tuning problem is known as the strong CP problem. An additional term, with a small upper bound measured to be close to zero, can be added to the QCD Lagrangian in Equation 2.4, that would violate the CP symmetry in strong interactions, which however, has never been experimentally observed.

The Dark Matter/Energy Problem. Cosmological observations revealed that our universe is made of $\sim 68.3\%$ of dark energy (leading to the acceleration of the expansion of the universe [59]), $\sim 26.8\%$ of dark matter (emitting minimal to no light, but has gravitational effects), and $\sim 4.9\%$ of ordinary matter (mainly baryons), which is the only matter explained by the Standard Model [60]. For instance, a dark matter candidate is provided by supersymmetric models and this prediction is currently being tested at the LHC.

2.5. Summary

The Standard Model of Particle Physics represents a well-established quantum field theory, a unified framework of QCD and EW theory, describing the elementary particles and their strong, electromagnetic and weak interactions. Numerous experiments over nearly half a century have reassured the consistency of the model. The relic of the model's BEH mechanism, giving mass to the W^\pm and Z^0 vector bosons and chiral fermions, is the Higgs scalar boson, which remained undiscovered for decades.

A triumph of the Standard Model and certainly of theoretical physics in general has been the discovery of a new particle, consistent with the predicted Higgs boson, by

the LHC experiments, ATLAS and CMS. To date all measurements of its properties are compatible with the Standard Model expectations. While these measurements have been mainly performed in the bosonic decay modes of the new particle, it is essential to directly observe its coupling to fermions. Recently, a 4.5σ evidence was found in the $H \rightarrow \tau^+\tau^-$ search. The predominant Higgs decay mode, $H \rightarrow b\bar{b}$, is focus of this thesis.

Even though the Standard Model is currently the best description of observed particle phenomenology, there are a number of limitations. Therefore, even despite the discovery of the Higgs boson, and the measurements described in this thesis, the Standard Model cannot be a full description of nature at the quantum level and this motivates continued research into both theoretical and experimental particle physics.

Chapter 3.

The ATLAS Experiment at the LHC

The continuous desire of mankind to unravel the complex structure of our universe and to understand the underlying fundamental interactions and elementary particles, has led to the development of high-energy particle accelerator experiments to reproduce and study conditions close to the birth of our universe, while constantly stimulating and fostering engineering innovation and technological progress. Along with many physics discoveries and technological milestones, this desire and mission has been pursued since 1954 at CERN, the European Organization for Nuclear Research (acronym for *Conseil Européen pour la Recherche Nucléaire*) near Geneva, Switzerland. The latest addition to CERN's accelerator complex is today the world's largest and most powerful particle accelerator in history, the Large Hadron Collider (LHC) [61].

The LHC has opened a new era of Particle Physics with the unique opportunity to explore phenomena in nature at energies far above the electroweak scale. At the core of its physics programme stands the quest to understand the Higgs boson as predicted by the Standard Model of Particle Physics and any deviations of this grand theory to yield new physics beyond our current knowledge. This challenging task has been taken by two major LHC experiments, ATLAS (A Toroidal LHC ApparatuS) [62] and CMS (Compact Muon Solenoid) [63].

In this chapter, a general overview of the LHC and its experiments is given, followed by a more detailed presentation of the ATLAS detector.

3.1. The Large Hadron Collider

The LHC is a superconducting hadron accelerator and collider hosted by the 26.7 km circular tunnel¹ formerly used by the Large Electron-Positron collider (LEP) [64] and brings two counter-rotating beams to collision at four interaction points. Each interaction point is the home of a large particle detector. It is designed to collide proton beams with a centre-of-mass energy, corresponding to twice the beam energy, up to $\sqrt{s} = 14$ TeV and an instantaneous luminosity, representing the collision rate per unit area, up to $\mathcal{L} = 10^{34} \text{ cm}^{-2}\text{s}^{-1}$ as well as heavy ion (Pb) beams with an energy of 2.76 TeV per nucleon and a peak luminosity of $\mathcal{L} = 10^{27} \text{ cm}^{-2}\text{s}^{-1}$.

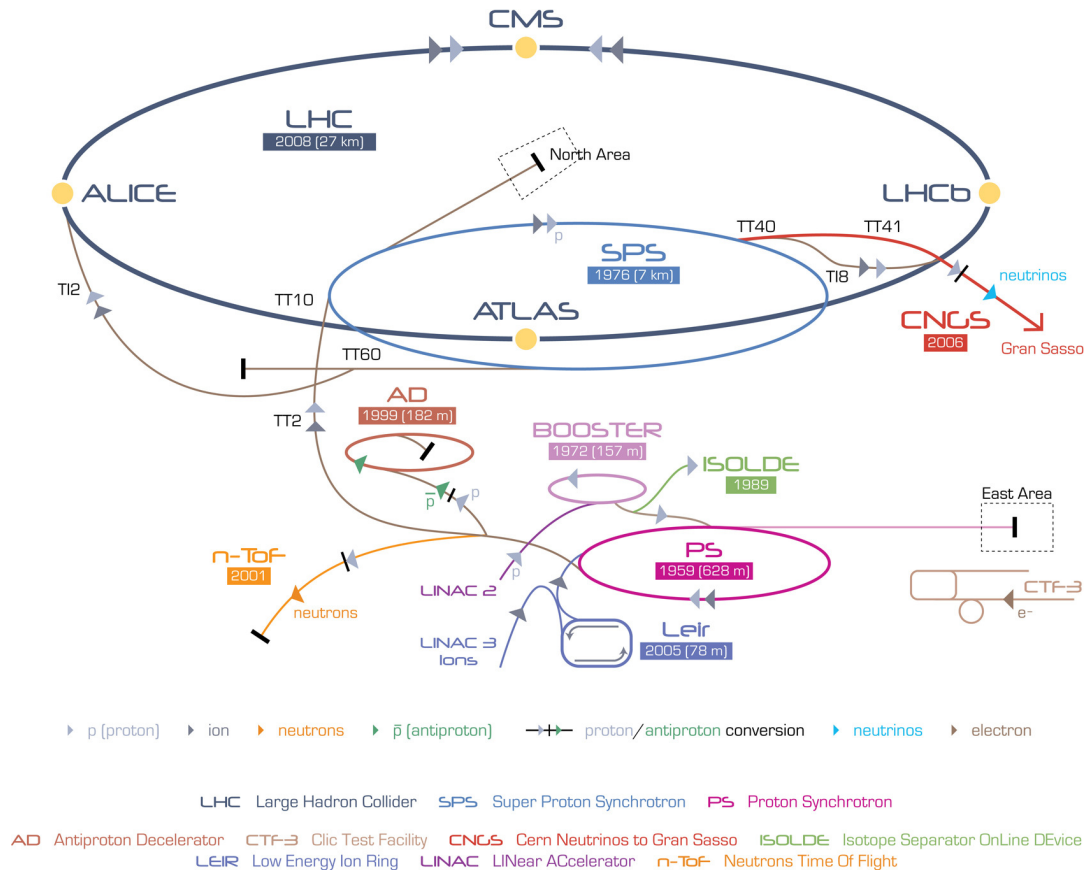


Figure 3.1.: Schematic overview of the CERN accelerator complex [65]: from initial particle sources, LINear ACcelerators (LINACs) and synchrotrons to the LHC.

In order to achieve such high collision energies, the LHC depends on an entire accelerator chain prior to its beam injections, as shown in Figure 3.1. For proton

¹The LHC tunnel lies between 45 m and 170 m below the surface on a 1.4% inclined plane with a slope towards the *Léman* lake of Geneva.

beams the journey begins with protons stripped from hydrogen atoms from a bottle of hydrogen gas entering a linear accelerator (LINAC2) to increase their energy up to 50 MeV before injecting them into the Proton Synchrotron Booster (PSB), reaching 1.4 GeV. Subsequently, protons are fed into the Proton Synchrotron (PS) to accelerate them up to 25 GeV and are passed to the Super Proton Synchrotron (SPS) to finally inject proton bunches into the LHC machine with an energy of 450 GeV.

For nominal LHC operation, 2808 bunches per proton beam are injected at a bunch spacing of 24.95 ns (~ 7.5 m) with each bunch containing $\sim 1.15 \times 10^{11}$ protons. These bunch trains are then accelerated by a 400.8 MHz superconducting Radio Frequency (RF) cavity system, increasing the beam energy by 485 keV at each turn, and governed by superconducting magnets with a 8.33 T field and an operating temperature below 1.9 K. Given the spatial limitations in the tunnel, the magnet system adopted a two-in-one design with counter-circulating magnetic fluxes passing through the two beam channels within the same cold mass (iron yoke) and cryostat using superfluid helium. Figure 3.2 shows a schematic cross-section of a LHC dipole magnet and supporting structures.

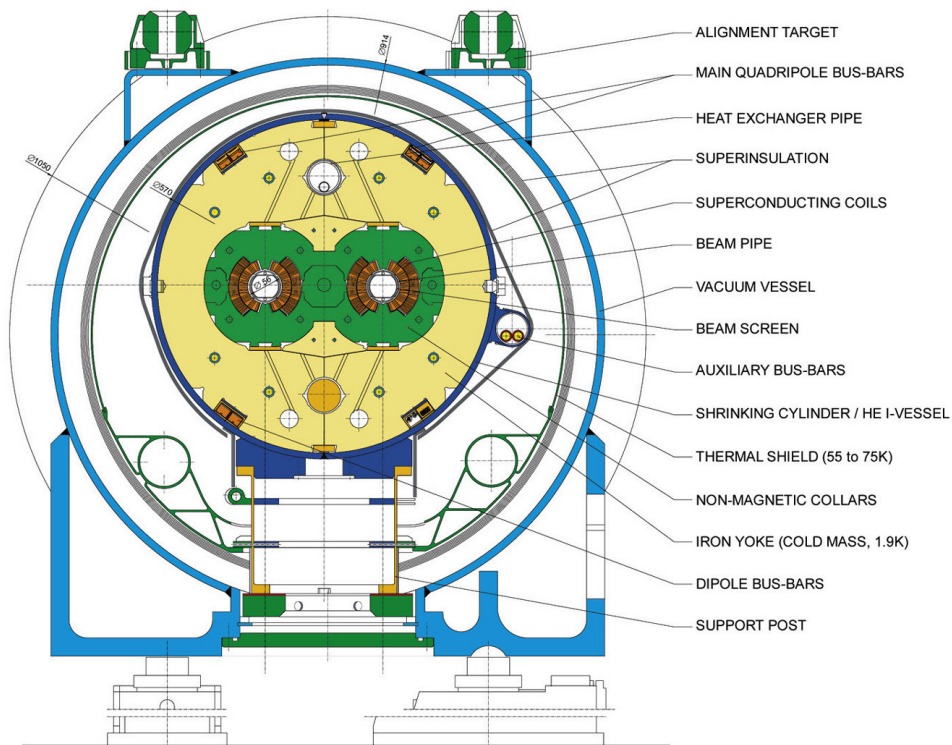


Figure 3.2.: Schematic cross-section of a superconducting LHC dipole magnet system and supporting structures [61].

Rare decay processes such as for the Higgs boson or processes involving new physics beyond the Standard Model are generally characterized by orders of magnitude smaller production cross-sections σ_{process} at the LHC, as shown in Figure 3.3. The rate of a particular process of interest dN_{process}/dt should be maximized, where N_{process} is linearly

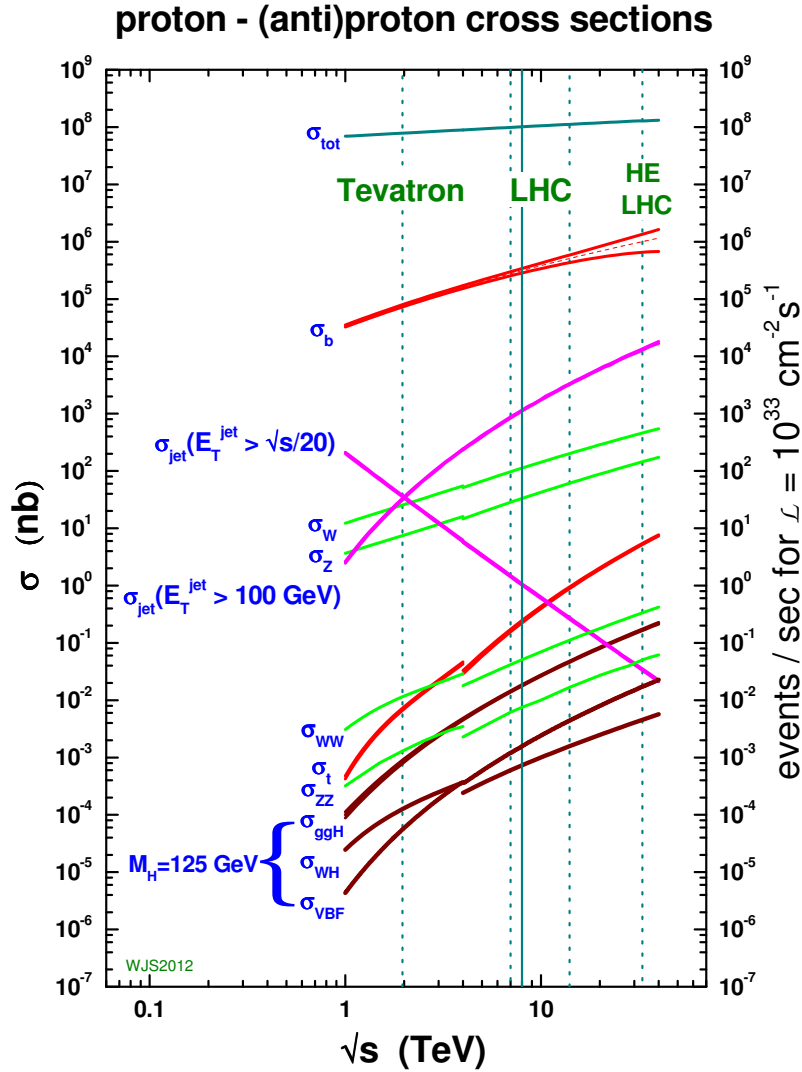


Figure 3.3.: Standard Model cross-sections σ for interesting physics processes as a function of the centre-of-mass energy \sqrt{s} . The discontinuity at ~ 4 TeV is due to the transition from proton-antiproton collisions at the Tevatron to proton-proton collisions at the LHC. The vertical lines indicate the Tevatron energy (1.96 TeV), the past LHC energies in 2011 (7 TeV) and 2012 (8 TeV), the LHC design energy (14 TeV) and the future High-Energy LHC (33 TeV) [66].

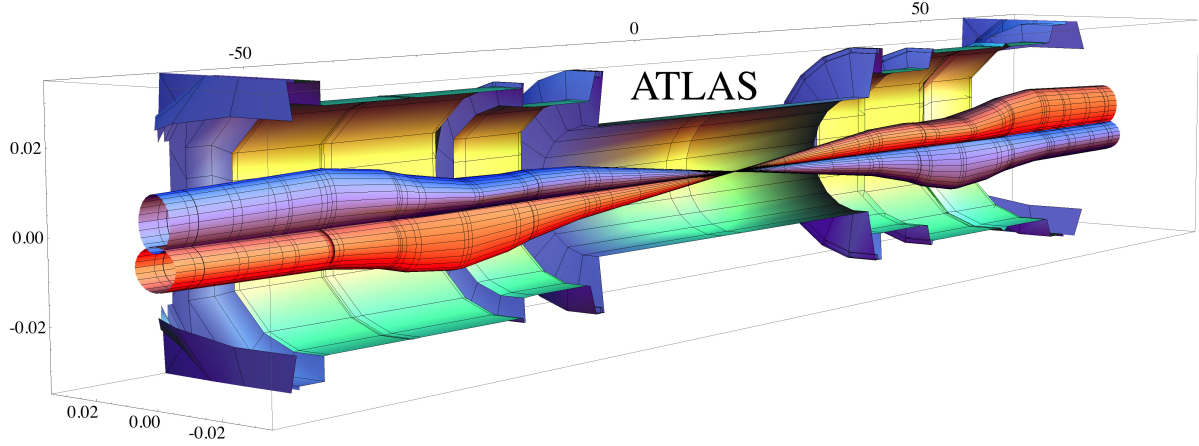


Figure 3.4.: Simulation of beam envelopes in the ATLAS interaction region, showing how the LHC clockwise (blue) and anti-clockwise (red) beams are squeezed at the interaction point (units in m). [67].

related to the *instantaneous luminosity* \mathcal{L} ,

$$N_{\text{process}} = \sigma_{\text{process}} \times \int \mathcal{L} dt, \quad (3.1)$$

where the *integrated luminosity*² $L = \int \mathcal{L} dt$ is independent of the physics process, assuming a Gaussian beam distribution with two identical circular beam structures, it can be expressed by only characteristic LHC beam parameters:

$$L = \frac{N_b^2 n_b f_{\text{rev}} \gamma_r}{4\pi \epsilon_n \beta^*} \times \underbrace{\frac{1}{\sqrt{1 + \left(\frac{\theta_c \sigma_z}{2\sigma^*}\right)^2}}}_{F(\theta_c)}, \quad (3.2)$$

where N_b denotes the number of protons in each bunch, n_b the total number of circulating bunches in each proton beam, f_{rev} the frequency of revolution in the ring, γ_r the relativistic gamma factor for a given beam energy, ϵ_n the normalized transverse beam emittance, β^* the beta function at the point of collision, and the geometric term $F(\theta_c)$ to account for the luminosity reduction as a result of the beam crossing angle θ_c at the interaction point, where σ_z and σ^* are the RMS of the bunch length and transverse beam size respectively. Therefore, intense beams (\Uparrow : N_b, n_b) of small emittances (\Downarrow : ϵ_n) with strongly focussed profiles (\Downarrow : β^*) at the interaction point are needed in order to increase the luminosity and the statistically limited discovery reach for processes with small cross-sections. As

²The integrated luminosity $L = N/\sigma$ is usually expressed in inverse cross-section units, i.e. fb^{-1} , and is a measure of the collected data size.

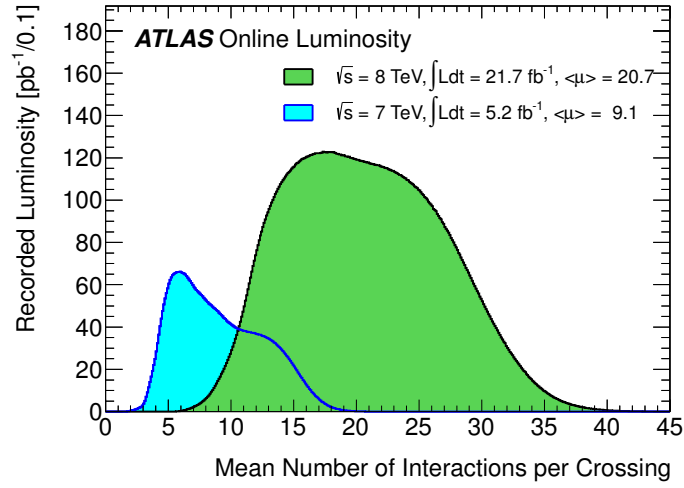
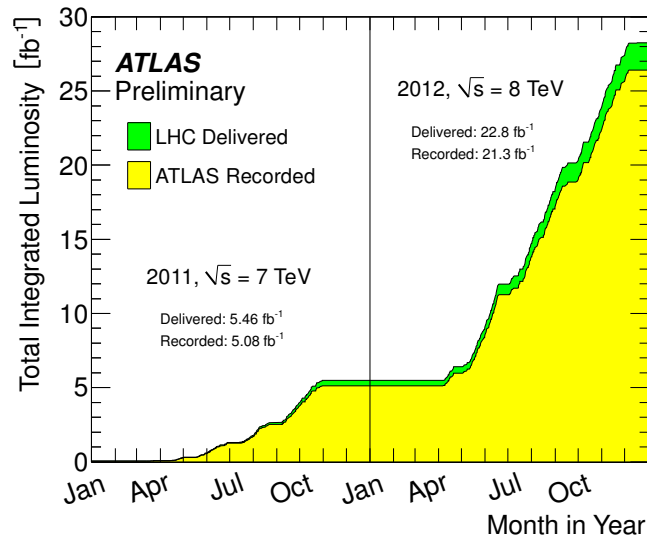
illustrated in Figure 3.4, proton beams are squeezed in the transverse plane by magnetic quadrupoles to achieve a confined target area of $\mathcal{O}(\mu\text{m} \times \mu\text{m})$.

LHC Parameter	2010	2011	2012	Design
Beam energy [TeV]	3.5	3.5	4	7
β^* for ATLAS & CMS [m]	2.0/3.5	1.5/1.0	0.6	0.55
Bunch spacing [ns]	150	75/50	50	25
Number of bunches	368	1380	1380	2808
Number of p /bunch	1.2×10^{11}	1.45×10^{11}	1.7×10^{11}	1.15×10^{11}
Peak luminosity [$\text{cm}^{-2}\text{s}^{-1}$]	2.1×10^{32}	3.7×10^{33}	7.7×10^{33}	1×10^{34}
Stored beam energy [MJ]	~ 28	~ 110	~ 140	~ 362
Max. $\langle\mu\rangle$	4	17	37	19

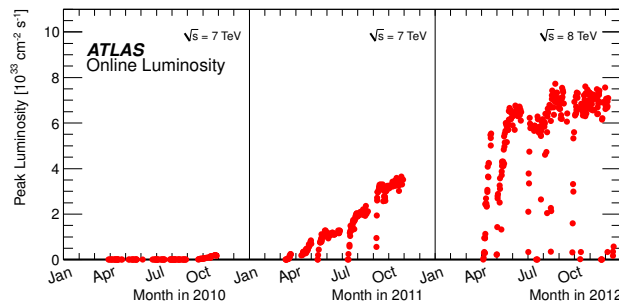
Table 3.1.: LHC beam parameters and performance overview for runs in 2010, 2011 and 2012 in comparison with the design values [68].

After the very first LHC p - p collisions at a centre-of-mass energy of 900 GeV in November 2009, the collider reached $\sqrt{s} = 7$ TeV in 2010, which was mostly dedicated to the commissioning of the machine. To increase the luminosity in 2011 and 2012, the number of bunches and p /bunch was significantly increased, while the bunch spacing was reduced. As a consequence, the presence of so-called *pile-up* events increased, which come from multiple multiple pp interactions from the same bunch crossing as the hard collision of interest ("in-time pile-up") or from a previous bunch crossing with electronic signals still present in the detector due to the integration time of the readout systems ("out-of-time pile-up"). Pile-up can be expressed with the integrated luminosity as a function of the mean of the Poisson distribution on the number of interactions per bunch crossing calculated for each bunch $\langle\mu\rangle$ for centre-of-mass energies of 7 and 8 TeV separately. Some of the key design parameters of the LHC are summarised and compared to previous collider runs in Table 3.1 and Figure 3.5.

The LHC delivered to ATLAS a total integrated luminosity of 5.46 fb^{-1} and 22.8 fb^{-1} at $\sqrt{s} = 7$ TeV in 2011 and $\sqrt{s} = 8$ TeV in 2012 respectively. Between these two years the peak instantaneous luminosity was raised from 3.7×10^{33} to 7.7×10^{33} , while the maximal $\langle\mu\rangle$ increased from 17 to 37. This data taking period is referred to as Run-1 in this thesis. The LHC is expected to restart for Run-2 in 2015 with a 25 ns bunch spacing and a $\sqrt{s} = 13$ TeV.

(a) Luminosity-weighted $\langle \mu \rangle$ 

(b) Integrated luminosity



(c) Peak luminosity

Figure 3.5.: The mean number of interactions per bunch crossing (a) and the total integrated (b) and peak instantaneous (c) luminosity delivered by the LHC to, and recorded by ATLAS during stable beams at $\sqrt{s} = 7 \text{ TeV}$ and $\sqrt{s} = 8 \text{ TeV}$ [69].

The LHC hosts seven experiments to probe nature in the high-energy domain: the general-purpose detectors ATLAS and CMS are focussed on the search for new particles and physics phenomena beyond our current knowledge, ALICE (A Large Ion Collider Experiment) [70] is dedicated to understand the quark-gluon plasma created in Pb ion and p -Pb collisions, LHCb (Large Hadron Collider beauty) [71] is devoted to heavy flavour physics and precise \mathcal{CP} violation measurements in B meson decays, TOTEM (TOTAl Elastic and diffractive cross section Measurement) [72] at the CMS interaction point and LHCf (Large Hadron Collider forward) [73] at the ATLAS interaction point study forward particles travelling close to the beams and simulate reaction chains induced by cosmic rays in the atmosphere, and MoEDAL (Monopole and Exotics Detector at the LHC) [74] at the LHCb interaction point searches for the magnetic monopole and highly-ionising Stable Massive Particles (SMPs), which are predicted by theories beyond the Standard Model of Particle Physics.

In the remainder of this chapter, the ATLAS detector and its recent performance are presented.

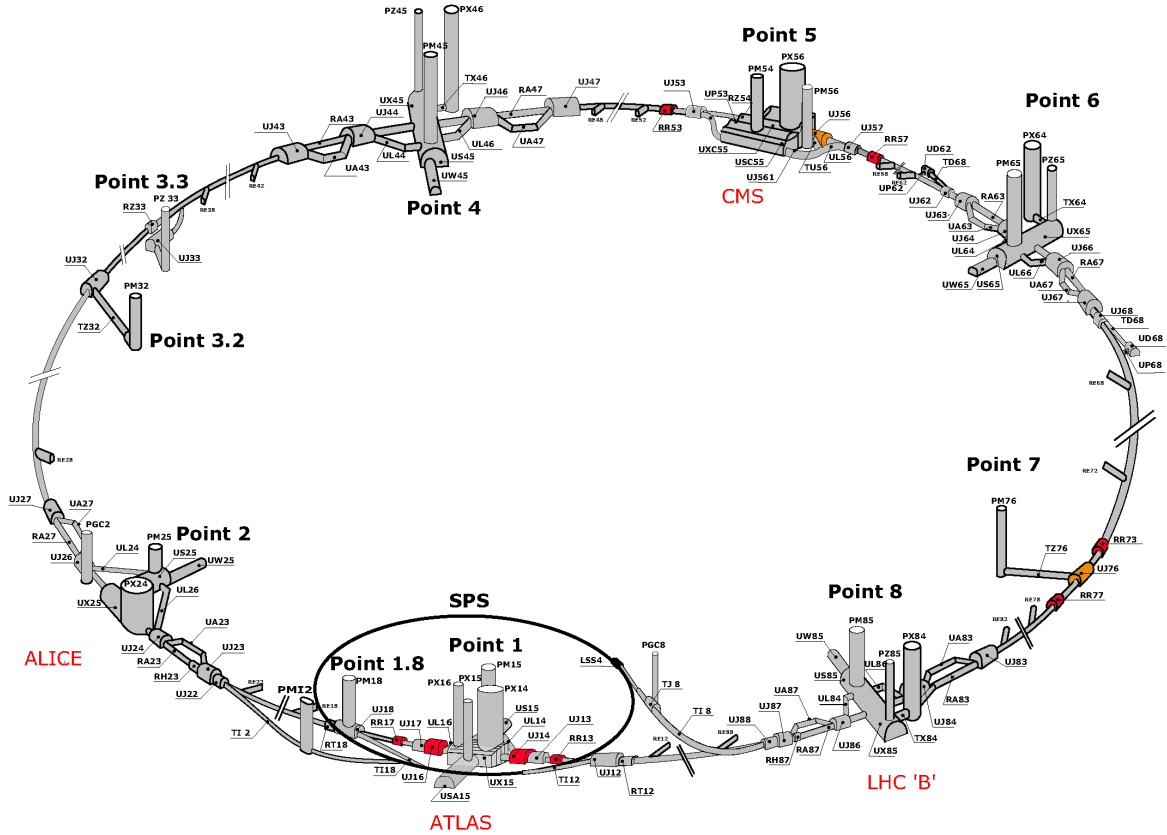


Figure 3.6.: The underground LHC layout, feeding 4 major experiments to probe nature: ATLAS (Point 1), CMS (Point 5), LHCb (Point 8) and ALICE (Point 2) [75].

3.2. The ATLAS experiment

The ATLAS experiment is driven by an international collaborative effort of over 3000 physicists from 38 countries to probe nature at the unprecedented high-energy frontier presented by the LHC. The ATLAS detector represents one of the largest and most complex scientific machines ever constructed and has been designed and optimized for the high-luminosity LHC environment. It is 44 m long, has a diameter of 25 m, weighs approximately 7000 t and is located ~ 92 m below the ground at the LHC Point 1, as illustrated in Figure 3.6.

The detector is based on a cylindrical layout with the interaction point at its centre and nominally obeys a forward-backward symmetry and an almost hermetic coverage with respect to this point. It consists of subdetector systems, utilizing different state-of-the-art technologies, high granularities and radiation resistances, to perform dedicated high-precision measurements, which in combination allow the reconstruction and characterization of particles and event topologies. As shown in Figure 3.7, the subdetectors in ATLAS are arranged coaxial ("barrel region") or perpendicular to the beam ("end-cap region") and are composed of tracking, electromagnetic/hadronic calorimetry and muon

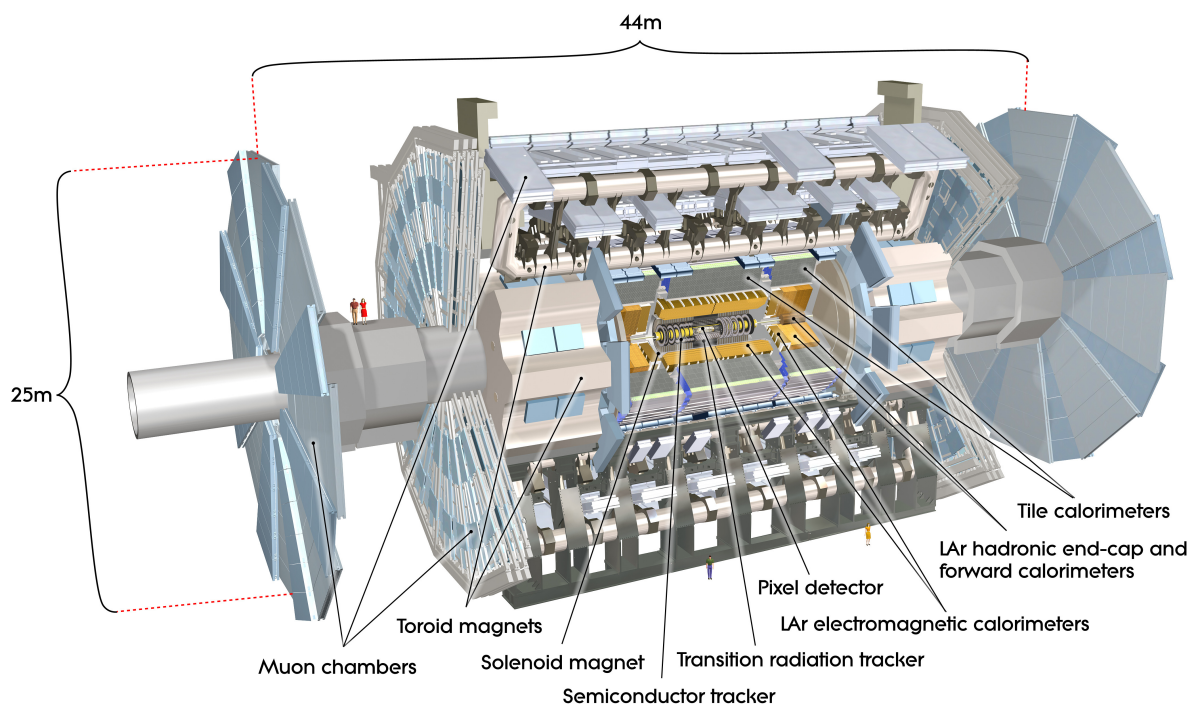


Figure 3.7.: Schematic cut-away view of the ATLAS detector [62].

spectrometry components. As particles transverse these different subdetector volumes, they interact with different materials and transfer their energy in a characteristic recognizable way. This basic particle identification principle is illustrated in Figure 3.8 and described below.

The *innermost* precision tracking detector system is operated in a solenoidal magnetic field to bend the trajectories of electrically charged particles (e.g. electrons, muons, hadrons) using a Lorentz force and to measure their momenta from the curvature of the reconstructed ionization tracks. Furthermore, the identified trajectories are used to reconstruct interaction vertices. The *intermediate layer* comprises the calorimetry system to absorb both incident neutral and charged particles and to measure their energy deposits. Electromagnetic (EM) calorimeters use scintillating material to reconstruct dense/short showers (e.g. from initial photons, electrons) with a cascade of photon production via bremsstrahlung and e^\pm pair production from energetic photons. Hadronic calorimeters use heavy material to reconstruct broad/long hadron showers produced by a cascade of strong force interactions. The *outermost* muon spectrometer is operated in a toroidal magnetic field to bend the muon trajectories, to extrapolate the tracks in the muon chambers to the matching tracks in the inner tracking detector and to measure

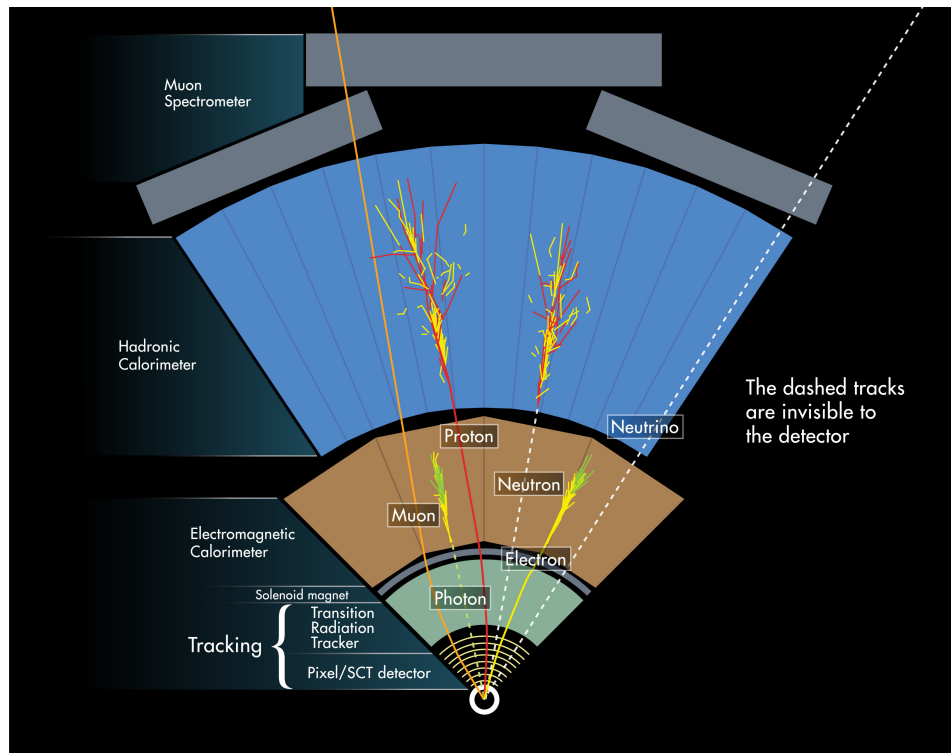


Figure 3.8.: Illustration of different particles interacting with ATLAS detector volumes.

the muon momenta from the track curvatures. Weakly interacting particles, such as neutrinos, do not interact with the detector material and can be reconstructed using the transverse energy imbalance of the event. A more detailed discussion of the particle reconstruction relevant to this thesis and for final states from the W/Z associated $H \rightarrow b\bar{b}$ production is presented in Chapter 4.

In order to cope with the challenging LHC conditions while maximizing the physics reach, ATLAS requires subdetectors with ultra-fast, radiation-hard front-end electronics and sensors, high granularity and excellent particle reconstruction efficiencies over a large acceptance range. Furthermore, an highly efficient trigger system is needed to identify events of interest. The basic performance goals for each detector component are summarized in Table 3.2. The following sections describe each subdetector in more detail.

Detector component	Required Resolution	Pseudorapidity Coverage	
		Measurement	Trigger
Tracking	$\sigma_{p_T}/p_T = 0.05\%p_T \oplus 1\%$	± 2.5	
EM calorimetry	$\sigma_E/E = 10\%/\sqrt{E} \oplus 0.7\%$	± 3.2	± 2.5
Hadronic calorimetry			
\Rightarrow barrel & end-cap	$\sigma_E/E = 50\%/\sqrt{E} \oplus 3\%$	± 3.2	± 3.2
\Rightarrow forward	$\sigma_E/E = 100\%/\sqrt{E} \oplus 10\%$	$3.1 < \eta < 4.9$	$3.1 < \eta < 4.9$
Muon spectrometer	$\sigma_{p_T}/p_T = 10\%$ at $p_T = 1$ TeV	± 2.7	± 2.4

Table 3.2.: Basic ATLAS performance goals for each detector component [62].

3.2.1. Coordinate system

A consistent description of ATLAS detector regions and interacting particles demands the definition of a coordinate system and common nomenclature, which are introduced here and used throughout this thesis. The nominal interaction point (IP), where collisions are expected to occur, marks the centre of the coordinate system with the z -axis along the beam line and the $x - y$ plane transverse to the beam line. A positive z is defined in the anti-clockwise LHC direction (called side-A) and a negative z is defined vice versa (called side-C), using the view as in Figure 3.6. A positive x is defined horizontally towards the centre of the LHC ring and a positive y is defined vertically facing upwards from the IP. This is also known as a right-handed coordinate system.

Transverse quantities used in this thesis are commonly labelled with a $_T$ -index, such as e.g. the transverse momentum p_T , and are measured in the $x - y$ plane. The azimuthal angle ϕ and radius ρ are measured around the beam line in the $x - y$ plane relative to the positive x -axis and the polar angle θ is measured from the beam line relative to the positive z -axis. The polar angle can be conveniently expressed through the pseudorapidity:

$$\eta \equiv -\ln \left[\tan \left(\frac{\theta}{2} \right) \right]. \quad (3.3)$$

It is a widely used quantity for relativistic particles and derives from the limit case for massless particles of the rapidity,

$$y \equiv \frac{1}{2} \ln \left(\frac{E + p_z}{E - p_z} \right) \quad (3.4)$$

$$\stackrel{m_0 \rightarrow 0}{\approx} \frac{1}{2} \ln \left(\frac{|p| + p_z}{|p| - p_z} \right) = \frac{1}{2} \ln \left(\frac{1 + \cos \theta}{1 - \cos \theta} \right) = -\ln \left[\tan \left(\frac{\theta}{2} \right) \right] = \eta,$$

where $E = \sqrt{p^2 + m_0^2}$ is the particle's energy and p_z is the momentum components along the z -axis. The rapidity is typically used for massive objects such as jets. Differences in rapidity are Lorentz-invariant³; this is only approximately the case for the pseudorapidity.

Another important Lorentz-invariant quantity is the distance between two particles in the $\eta - \phi$ plane:

$$\Delta R \equiv \sqrt{(\Delta \eta)^2 + (\Delta \phi)^2}. \quad (3.5)$$

3.2.2. Magnet system

The ATLAS magnet system comprises four large superconducting magnets: one central solenoid providing a 2 T axial magnetic field along the beam axis for the inner tracking detector and three external toroids providing a 0.5 T and 1 T toroidal magnetic field (B -field) for the muon chambers in the barrel and end-cap regions, respectively. Together a B -field over a volume of approximately 12,000 m³ is provided.

In order to retain an excellent calorimeter performance, the solenoid was optimized to achieve a nominal contribution of ~ 0.66 radiation lengths to incident particles, which

³In a $p - p$ collision, partons carry *a priori* an unknown proton momentum fraction, meaning the overall boost of the collision is unknown. Thus Lorentz-invariant quantities are preferred.

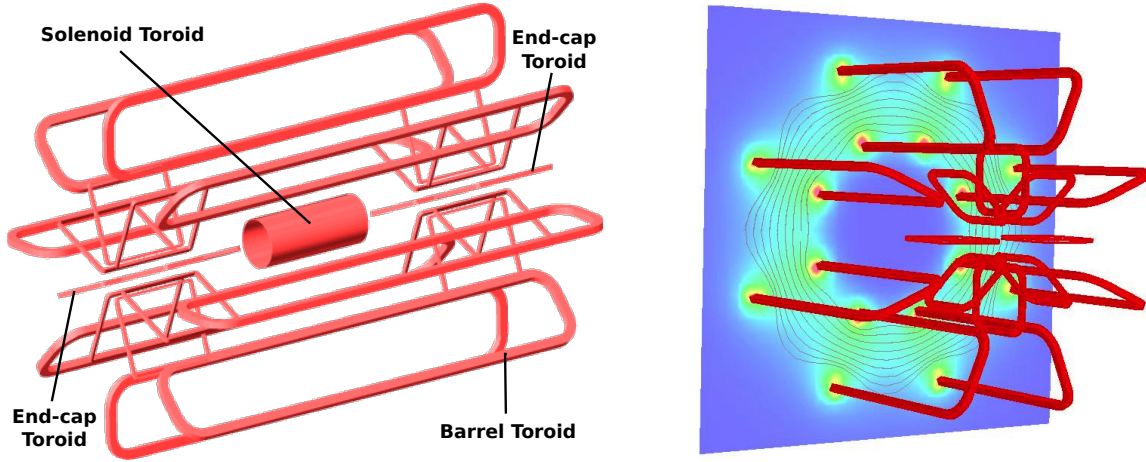


Figure 3.9.: Geometry of the ATLAS magnet system (left) and a simulation of the magnetic field map (right).

also required the solenoid windings to share a common vacuum with the LAr calorimeter. The solenoid is 5.8 m long and has an inner/outer diameter of 2.46/2.56 m.

The toroid systems are each composed of 8 coils, aligned radially and distributed symmetrically. The coils are cooled down to ~ 4.5 K using individual cryostats in the barrel region and a common cryostat in the end-cap regions. The barrel toroid is 25.3 m long and has an inner/outer diameter of 9.4/20.1 m. The bending power in the interfacing regions of the barrel and end-cap toroids is optimized by rotating the coils of the end-cap toroids by 22.5° with respect to the coils of the barrel toroid. The end-cap toroids are each 5.0 m long and have an inner/outer diameter of 1.65/10.7 m. The geometry of the entire magnet system and a simulation of the magnetic field map are shown in Figure 3.9.

3.2.3. Inner Detector

The ATLAS Inner Detector (ID) is a high-precision tracking system surrounding the interaction point and is designed to reconstruct the trajectories of charged particles above a transverse momentum of $p_T > 0.1$ GeV⁴ and within a pseudorapidity range of $|\eta| < 2.5$. As discussed in Section 3.2.2, the ID operates within a solenoidal (homogeneous) B -field to perform transverse momentum measurements and to determine both primary and secondary vertices, whereas the latter is crucial for the identification of long-lived heavy flavour particles such as b -quark initiated jets. Furthermore, electrons can be detected

⁴The *nominal* p_T threshold for charged track reconstruction in the ID is at 500 MeV.

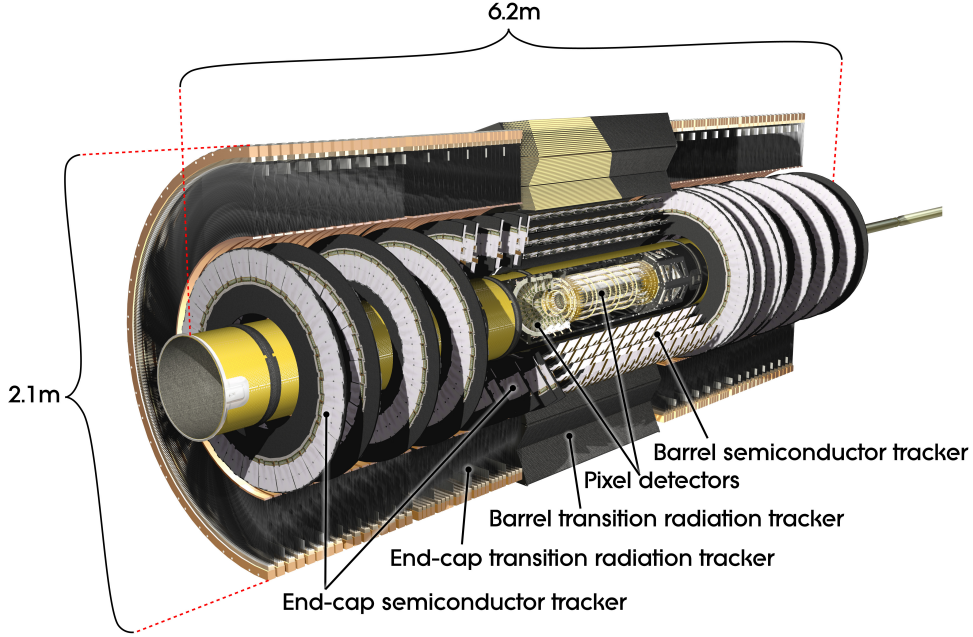


Figure 3.10.: Layout of the ATLAS Inner Detector with the Pixel, SCT and TRT subdetectors in the barrel and end-cap regions [76].

over a transverse energy range of $0.5 < E_T < 150$ GeV and within a pseudorapidity range of $|\eta| < 2.0$. The system's superior pattern recognition and sustainability is the result of fine detector granularity, radiation-tolerant components and the combination of independent "- but complementary -" subdetectors, while the high particle flux environment presented by the LHC pushes the limit of currently existing technology. This challenging environment has driven the design of the ID, as laid out in Figure 3.10. Charged tracks traversing the different layers from the interaction point in the barrel and end-cap regions is illustrated in Figures 3.11 and 3.12 respectively.

From inner to outer radii, the ID comprises in a cylindrical envelope a Pixel detector followed by a Semiconductor Tracker (SCT) and a Transition Radiation Tracker (TRT). In order to minimize the material or occupancy in front of the calorimeter and to reduce a bias of measurements, the tracking and calorimeter performance must be balanced. Therefore, a *tracking strategy*⁵ has been adopted, where a few high-precision measurements at inner radii using fewer layers close to the interaction point are combined with many lower precision measurements at outer radii using more layers apart from the interaction point.

⁵Since the particle flux decreases with $1/r^2$ from the interaction point, the tracking detector with the highest granularity is placed closest to the interaction point.

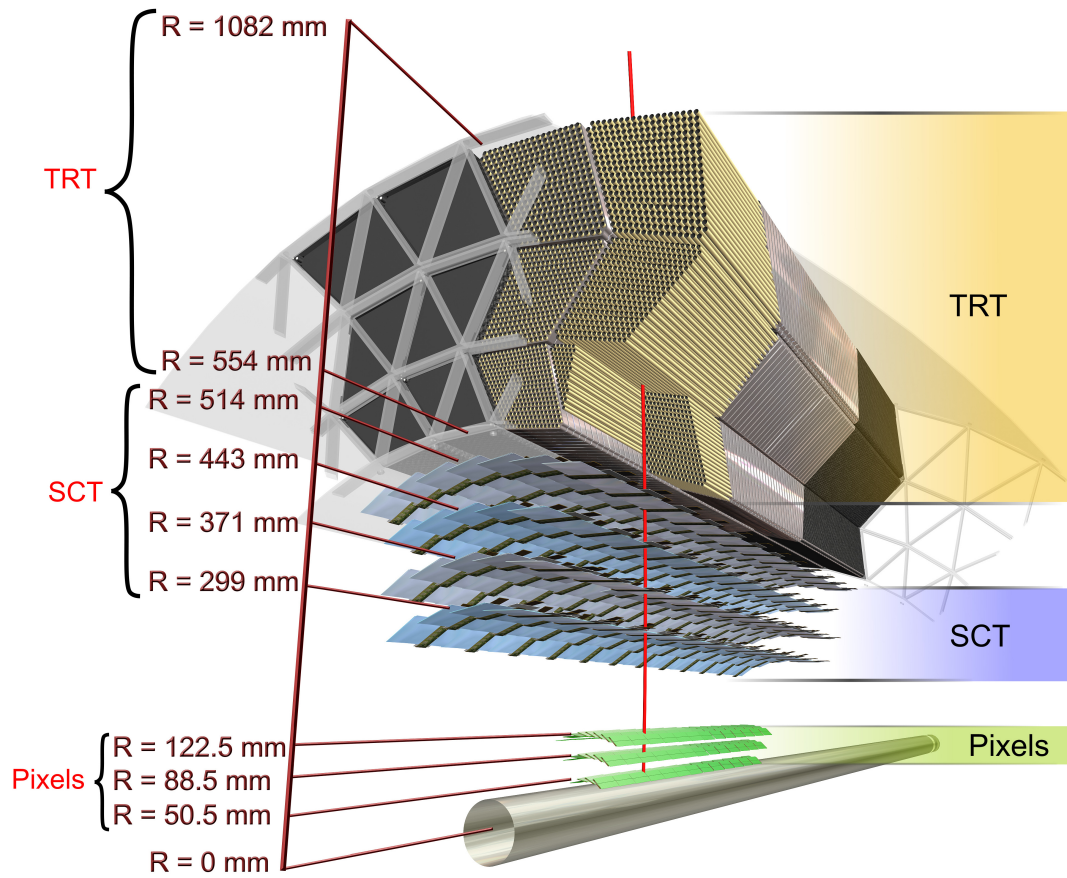


Figure 3.11.: Illustration of a charged track traversing the different barrel layers of the ATLAS Inner Detector from the interaction point [76].

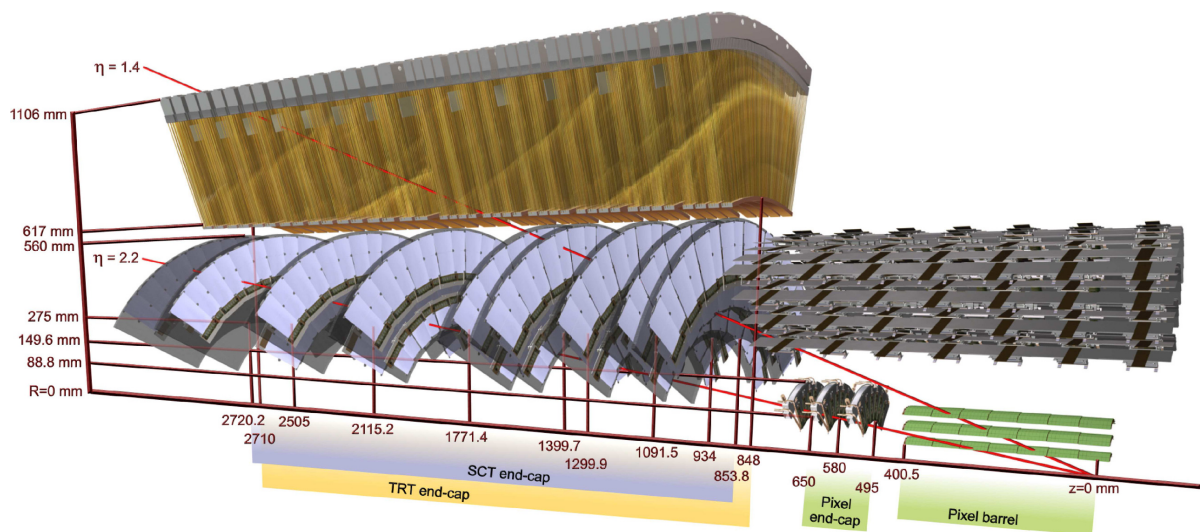


Figure 3.12.: Illustration of charged tracks traversing the different end-cap layers of the ATLAS Inner Detector from the interaction point [76].

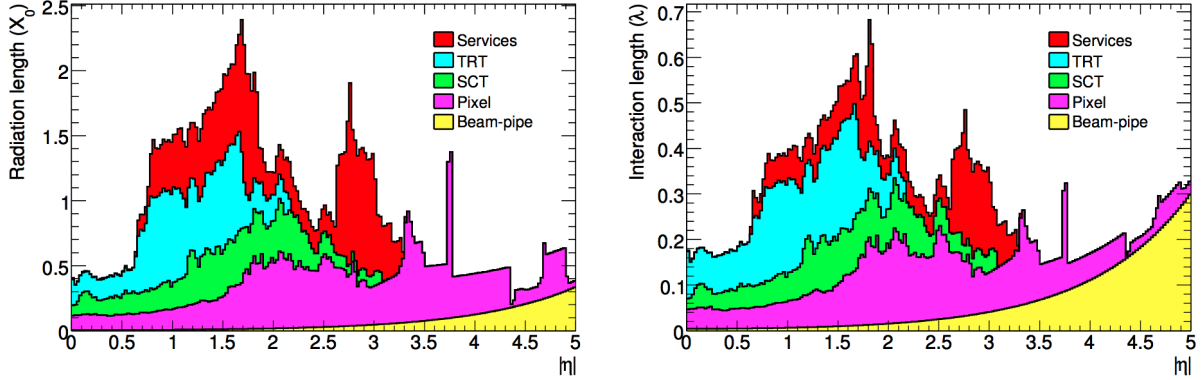


Figure 3.13.: The ID material distribution in terms of radiation length X_0 (left) and interaction length λ (right) as a function of $|\eta|$ and averaged over ϕ [77].

Together with the required mechanical support structures, readout electronics and cooling services, the total material of the ID is measured in radiation and interaction lengths as shown in Figure 3.13 and mainly affects the efficiency of reconstructing low momentum tracks.

As previously stated, one of the key measurements of the ID is to determine the *momentum of charged particles*. As the simplified illustration in Figure 3.14 shows, the trajectory⁶ of a charged particle leaving the interaction point in the $x - y$ plane (perpendicular to the beam pipe) is bent in ϕ by a uniform B field along the z -axis (parallel to the beam pipe). At least three close-by detector layers register discrete space points of the traversing particle to reconstruct its track. The direction of the track curvature is a sign for a positive or negative charge of the particle. With the Lorentz force and centripetal force acting on the particle, the radius R of the track curvature is directly proportional to the momentum of the particle: $p[\text{GeV}] = 0.3B[\text{T}]R[\text{m}]$. The radius can be measured as a function of the sagitta s ,

$$R = \frac{s}{1 - \cos \alpha} = \frac{s^2 + (L/2)^2}{2s} \approx \frac{L^2}{8s} \quad \text{for } R \gg L, \quad (3.6)$$

where the arc's angle is defined as 2α (see Figure 3.14), L is the tracking detector's lever arm and length of the tracking coverage in the $x - y$ plane. The momentum can then be defined as:

$$p = \frac{0.3BL^2}{8s}. \quad (3.7)$$

⁶The charged particle trajectory in an homogeneous B -field is given by an helix and its projection on the $x - y$ plane by a circle.

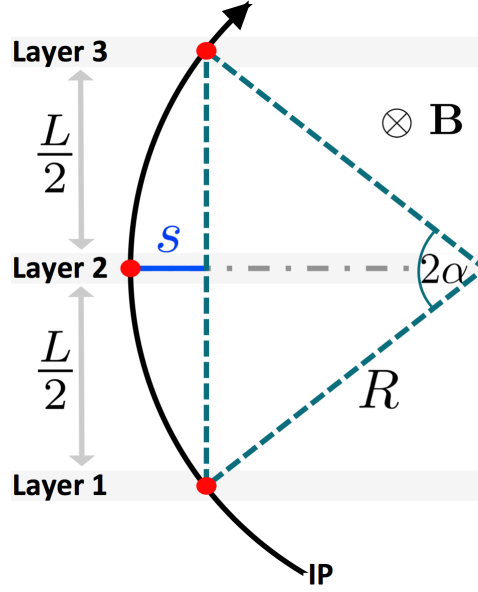


Figure 3.14.: Illustration of a charged particle traversing three detector layers perpendicular to a uniform B field, where R is the radius of curvature, s the sagitta of the arc with angle 2α and $L/2$ the separation of the detector layers.

The momentum resolution thus depends on the accuracy in measuring $s = L^2/8R$ and can be derived as

$$\frac{\sigma_p}{p} = \frac{\sigma_R}{R} = \frac{L^2}{8Rs} \cdot \frac{\sigma_s}{s} = \frac{L^2}{8R} \cdot \frac{\sigma_s}{L^4/64R^2} = \frac{\sigma_s}{L^2} \cdot 8R = p\sigma_s \cdot \frac{8}{0.3BL^2} \sim p \cdot \frac{\sigma_s}{0.3BL^2}, \quad (3.8)$$

where the sagitta uncertainty σ_s depends on the number N and the spacing of track point measurements. At the limit $N \rightarrow \infty$ assuming uniform spacing, σ_s is found to be [78, 79]

$$\sigma_s = \frac{\sigma_{\rho\phi}}{8} \underbrace{\sqrt{\frac{720}{N+5}}}_{\text{limit case } N \rightarrow \infty}, \quad (3.9)$$

with $\sigma_{\rho\phi}$ for the resolution of measuring a track point in the $\rho - \phi$ plane. Therefore, a good momentum resolution requires a large path length L , a strong magnetic field B and an accurate measurement of s . These requirements have been challenging constraints in the design of the ID. For example, the reconstruction of a high p_T track with small s requires detector layers with high granularity to be well-separated, while conversely the reconstruction of a low p_T track with larger s requires detector layers to be closer

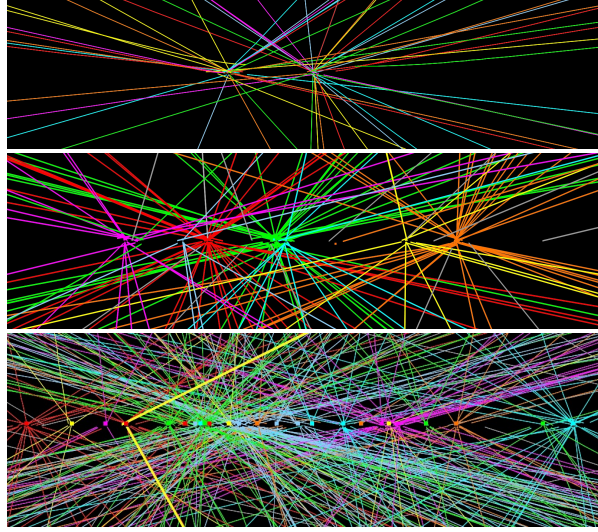


Figure 3.15.: Vertex displays of collision events in ATLAS with 2 (top), 7 (middle) and 25 (bottom) reconstructed vertices [80].

together. As summarized in Table 3.2, the overall p_T resolution of the ID is

$$\frac{\sigma_{p_T}}{p_T} = 0.05\% \cdot p_T \oplus 1\%, \quad (3.10)$$

where \oplus denotes the addition in quadrature.

Once the trajectories of charged particles have been reconstructed, it is crucial to extrapolate them back to inside the beam pipe and to associate them with a p - p collision – a *common primary vertex*. An important measure to classify tracks is the impact parameter, which is the distance of the track’s closest approach to its primary vertex on the z -axis. Good quality tracks of stable particles are expected to have a small impact parameter, while conversely a large impact parameter is expected for long-lived unstable particles such as B -hadrons, which decay at a *displaced secondary vertex*. The ID is responsible to distinguish between primary and secondary vertices and thus plays a key role in the identification of long-lived particles. In order to cope with additional vertices from pile-up, as introduced in Section 3.1 and demonstrated in Figure 3.15, the ID requires also an excellent position resolution along the z -axis.

The following paragraphs describe each subdetector in more detail.

Pixel detector. The Pixel detector is the innermost component of the ID and comprises three concentric silicon pixel cylinders centred around the beam pipe at radii 50.5, 88.5 and 122.5 mm in the barrel region and three silicon pixel disks perpendicular

to the beam pipe at $|z| = 495, 580$ and 650 mm in each end-cap region. There are 1744 pixel sensors with each containing 47232 silicon pixels of nominal size $50 \times 400 \mu\text{m}^2$ and covering an active area of $\sim 1.7 \text{ m}^2$. As a charged particle passes through a pixel, which is a reverse-bias diode [81], electron-hole pairs are produced in the silicon and if the resulting pulse of current exceeds a signal-to-noise threshold, a hit is registered and the corresponding pixel position is stored. The detector measures in average three points on a charged track within $|\eta| < 2.5$ and achieves an intrinsic position resolution of $10 \mu\text{m}$ in the $\rho - \phi$ plane⁷ and $115 \mu\text{m}$ along the z or ρ -direction in the barrel or end-cap regions respectively. The total number of readout channels is ~ 80.4 M. The impact parameter resolution in the transverse plane is better than $15 \mu\text{m}$. The barrel pixel layer closest to the interaction point is also referred to as the *B*-layer, since it identifies secondary vertices and plays a key role in the identification of *b*-quark induced jets in conjunction with calorimeter information. To improve the vertex resolution and to enhance the reconstruction of *b*-jets, an additional pixel layer, the Insertable *B*-layer (IBL) [82], has been installed even closer to the interaction point at radius ~ 31 mm for the upcoming LHC Run-2 in 2015.

Semiconductor Tracker. The Semiconductor Tracker (SCT) is a silicon strip detector covering an active area of 63 m^2 with four cylindrical layers around the beam pipe at radii $299 - 514$ mm in the barrel region and nine disk layers perpendicular to the beam pipe at $853.8 < |z| < 2720.2$ mm in each end-cap region. Based on similar sensor technology used in the Pixel detector, SCT micro-strip sensors [83] are paired back-to-back at a stereo rotation angle of 40 mrad to measure space points in both $\rho - \phi$ and z or ρ coordinates. The SCT measures on average four points on a charged track within $|\eta| < 2.5$ and with a mean strip pitch of $80 \mu\text{m}$ achieves an intrinsic position resolution of $17 \mu\text{m}$ in the $\rho - \phi$ plane and $580 \mu\text{m}$ along the z or ρ -direction in the barrel or end-cap regions respectively. The total number of readout channels is ~ 6.3 M.

Transition Radiation Tracker. The Transition Radiation Tracker (TRT) is a proportional drift tube tracker consisting of carbon-fibre reinforced Kapton straw tubes⁸ with a diameter of 4 mm and gold-plated tungsten wires with a diameter of $31 \mu\text{m}$ in the centre of each tube. The tubes are filled with a gas mixture of 70% Xe, 27% CO₂ and 3% O₂ at $5 - 10 \text{ mbar}$ over-pressure and are operated as proportional counters, with the

⁷Using equation 3.9 and for $N = 3$ replacing the limit case with the derived factor $\sqrt{81}$ from [78], we find a sagitta resolution of $\sigma_s \sim 11.25 \mu\text{m}$ in the barrel region.

⁸Each TRT tube wall is coated on one side with a $0.2 \mu\text{m}$ Al cathode layer, which is protected by a $5 - 6 \mu\text{m}$ graphite-kapton layer, and coated on the other side with a heat-sealing $45 \mu\text{m}$ polyurethane layer.

anode wire at ground potential and the cathode tube wall at a voltage of -1530V for an expected gain of 2.5×10^4 . The barrel region at radii 560 - 1080 mm and $|z| < 720$ mm contains in 76 layers a total of 52 544 tubes of 144 cm in length and are aligned parallel to the beam pipe. The two symmetric end-cap regions at radii 617 - 1106 mm and $827 < |z| < 2744$ mm contain each in 160 straw planes a total of 122 880 tubes of 37 cm in length and are arranged perpendicular to the beam pipe [84]. As a traversing charged particle ionizes the gas in the tubes, the resulting free electrons drift towards the wire, where they cascade in the strong electric field close to the wire and produce a detectable signal, which is amplified, shaped and discriminated against a low 300 eV threshold and a high 6 – 7 keV threshold. The thresholds are used for measuring tracking information, i.e. the drift time and thus distance of the charged track from the wire, and for particle identification, i.e. larger energy deposits from transition radiation. The tubes are interleaved with polypropylene fibres (barrel) and foils (end-caps) to create transition radiation photons, which are emitted by relativistic charged particles as they cross a boundary between two media of different dielectric constants. The emission of transition radiation depends on the Lorentz factor $\gamma = E/mc^2$ and is more likely to occur for relativistic electrons than for heavier hadrons. These X-ray photons radiated by electrons are absorbed in the Xe gas and yield much larger readout signals [85]. Each signal hit can be measured with an intrinsic resolution of $130 \mu\text{m}$ in the $\rho - \phi$ plane. Charged tracks with a $p_{\text{T}} > 0.5 \text{ GeV}$ and $|\eta| < 2.0$ cross, on average, 36 tubes, except in the transition between barrel and end-cap regions, $0.8 < |\eta| < 2.0$, where this number is reduced to 22. Due to the large number of track measurements and the high lever arm, the TRT complements and significantly improves the precision of the momentum measurements by the SCT and Pixel detectors.

3.2.4. Calorimetry system

Calorimetry finds its origin in thermodynamics and is based on a destructive measurement process through which incident particles are fully absorbed in a block of matter and through electromagnetic or strong interactions produce a shower of secondary particles with progressively degraded energy. The deposited energy of charged shower particles can then be detected in the form of charge or light and serves as a measurement of the incident particle's energy, which however must be calibrated as discussed in Chapter 4.

The ATLAS calorimetry system, as shown in Fig. 3.16, consists of sampling calorimeters, using alternating layers of an absorber for energy degradation and an active medium

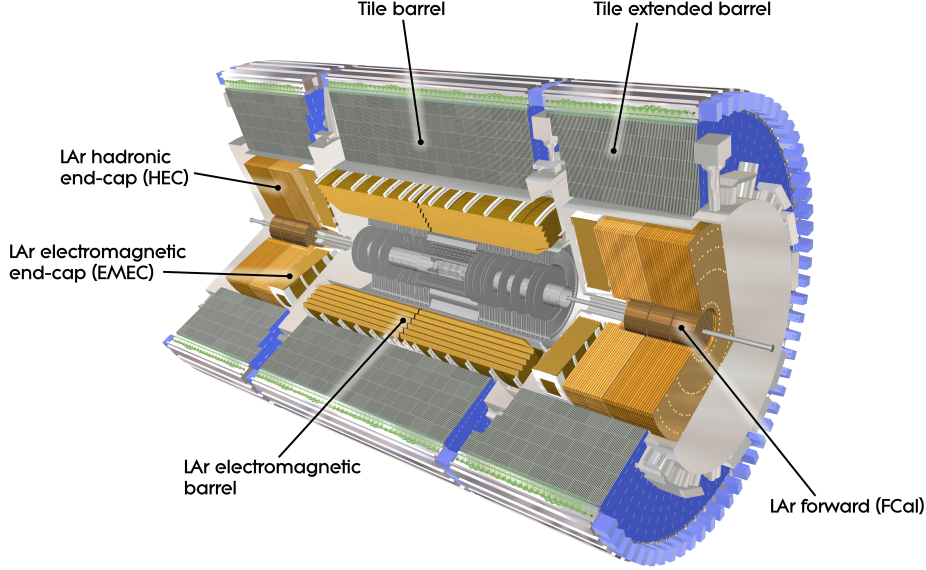


Figure 3.16.: The detector layout of the ATLAS calorimetry system [62].

for the energy measurement. This method can provide information about the longitudinal shower development and stands in contrast to homogeneous calorimeters, which use a common material for both energy degradation and signal generation, resulting in a better energy resolution.

The inner layer of the calorimetry system uses electromagnetic calorimeters to mainly measure electrons and photons through their electromagnetic interactions (e.g. bremsstrahlung, pair-production) and are followed by the outer layer using hadronic calorimeters to mainly measure hadrons through their strong interactions. The calorimeters cover a large pseudorapidity range of $|\eta| < 4.9$, which is in particular important to reconstruct neutrinos by determining from the missing energy in the event.

The resolution of the energy measurement can be generally approximated by the following expression:

$$\frac{\sigma_E}{E} = \underbrace{\frac{a}{\sqrt{E}}}_{\text{stochastic}} \oplus \underbrace{\frac{b}{E}}_{\text{noise}} \oplus \underbrace{c}_{\text{const.}}. \quad (3.11)$$

The stochastic term is mainly due to sampling or statistical fluctuations related to the physical shower development and originate from variations of the number of produced charged particles crossing the active layers and the energy loss in the interleaved absorbing

layers. Generally the resolution improves with the energy of the incident particle as $1/\sqrt{E}$. The noise term comes from the electronic noise of the readout chain and is pileup sensitive. This term can be decreased by increasing the sampling fraction of the calorimeter to raise the signal from the active medium and to achieve a higher signal-to-noise ratio. The constant term includes contributions which are not directly related to the particle energy, but to instrumental effects, such as energy calibration instabilities (e.g. from temperature gradients, radiation damage), non-uniform signal response (e.g. from imperfections in detector geometry and readout system), longitudinal/lateral leakage effects and energy losses in detector mechanical structures.

Electromagnetic Calorimeter

A system of electromagnetic (EM) sampling calorimeters surrounding the Inner Detector captures electromagnetic cascades or showers produced mainly by incident electrons, positrons and photons. Governed by the laws of Quantum Electrodynamics, the cascade for incident particle energies⁹ $E_0 \gtrsim 1$ GeV is built by two alternating processes: (i) an e^\pm radiates photons via bremsstrahlung as a result of the Coulomb interaction with electric fields generated by atomic nuclei and over a radiation length X_0 reduces to $1/e$ of its initial energy; (ii) a photon with the energy twice the electron rest mass (2×511 keV) converts into a e^+e^- pair and over $\frac{9}{7}X_0$ reduces to $1/e$ of its initial intensity [86]. The cascade stops after reaching a critical energy¹⁰ E_c with an approximated total depth of $X = X_0 \ln(E_0/E_c)/\ln 2$ and has a mean longitudinal shower profile described by a gamma distribution with $dE/dt \propto t^\alpha e^{-\beta t}$, where $t \equiv x/X_0$ with the shower position $x \leq X$ and incident particle and detector media dependent parameters α and β [87]. In order to fully absorb electromagnetic showers with incident particle energies < 5 TeV before reaching the hadronic calorimeter systems, the total thickness of the EM calorimeter is chosen to be $> 22X_0$ in the barrel and $> 24X_0$ in the end-cap regions.

The ATLAS EM calorimeter system comprises a barrel covering $|\eta| < 1.475$ and two end-cap wheels covering $1.375 < |\eta| < 3.2$. In an accordion geometry, lead as the passive absorbing material ($X_0 = 0.56$ cm) is interleaved with liquid argon (LAr) as the active material ($X_0 = 14.0$ cm). A calorimeter module, as shown in Figure 3.17, consists of three high-granular layers and different characteristics from inner to outer radii:

⁹At lower energies, i.e. $E_0 \ll 1$ GeV, electrons lose mainly their energy through ionization and photons through Compton scattering and the photoelectric effect.

¹⁰The critical energy is $E_c \sim 610(710)$ MeV/ $(Z + 1.24(0.92))$ for solid (gaseous) absorbers with the atomic number Z .

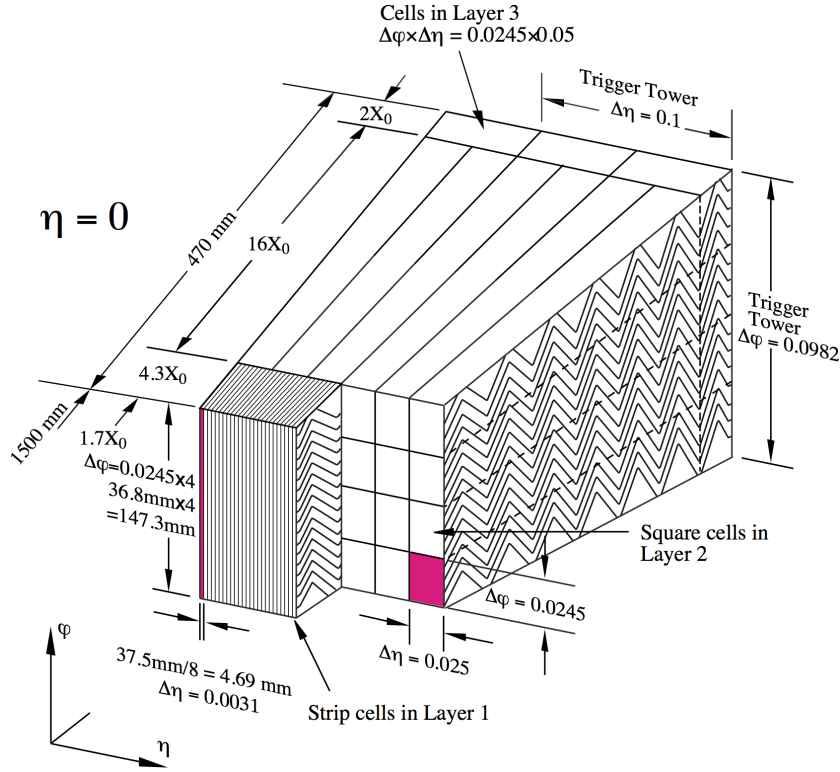


Figure 3.17.: An illustration of the different layers of a barrel module of the ATLAS electromagnetic calorimeter [62].

1. Highly η -segmented strips of e.g. $\Delta\eta \times \Delta\phi = 0.025/8 \times 0.1$ at $|\eta| < 1.8$ and a layer thickness of $\sim 4.3X_0$ allow to resolve photon pairs from π^0 decays.
2. Squared towers of e.g. $\Delta\eta \times \Delta\phi = 0.025 \times 0.025$ at $|\eta| < 2.5$ with a layer of $\sim 16X_0$ capture the main part of the EM shower.
3. Towers of $\Delta\eta \times \Delta\phi = 0.050 \times 0.025$ with a layer depth of $\sim 2X_0$ are used for the containment of larger showers in η with $E_T > 50$ GeV.

The overall required energy resolution, as summarized in Table 3.2, is

$$\frac{\sigma_E}{E} = \frac{10\%}{\sqrt{E}} \oplus 0.7\%, \quad (3.12)$$

whereas (see Equation 3.11) test beam measurements have determined the stochastic term a to be 10 – 12%, the constant term c to be 0.2 – 0.35% and the noise per cluster to be ~ 250 MeV [88].

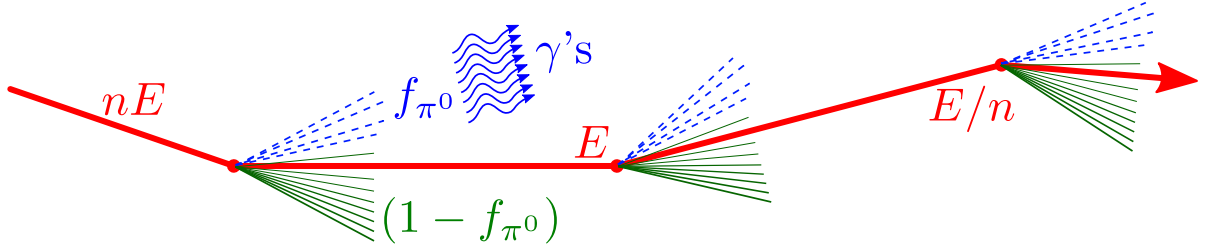


Figure 3.18.: Simplified schematic illustration of an hadron-induced cascade with a mean energy fraction f_{π^0} (blue) leaving the hadronic sector (green) via π^0 production and the average energy (red) decreases by a factor n after each generation.

Hadronic Calorimeter

A system of hadronic sampling calorimeters enclosing the EM calorimeters captures cascades or showers with both hadronic and electromagnetic components produced mainly by incident hadrons. The cascade is built by two classes of phenomena: (i) the production of energetic secondary hadrons with a nuclear interaction length¹¹ of $\lambda \sim 35A^{1/3} \text{ g cm}^{-2}$ between interactions with nuclei¹²; (ii) the production of sequential decays from nuclear processes such as (de-)excitation, spallation, nucleon evaporation, fission etc. [86, 87].

In these showers, as Figure 3.18 illustrates, a substantial fraction of the incoming hadron energy E is transferred from the hadronic to electromagnetic sectors¹³ via mainly π^0 production with decays to photons, $\pi^0 \rightarrow \gamma\gamma$. The relation between the average electromagnetic (π^0) energy fraction F_{π^0} and the average hadronic energy fraction F_h can be described via a power law [89]:

$$F_h \equiv (1 - F_{\pi^0}) = \left(\frac{E}{E_0} \right)^{k-1} = \langle m \rangle^{n(k-1)}, \quad (3.13)$$

where E_0 is a scale energy corresponding to the average energy needed for the production of one pion, $\langle m \rangle$ is the average multiplicity per nuclear interaction with n cascade generations and $k = 1 + \ln(1 - f_{\pi^0})/\ln \langle m \rangle$ defines the energy dependence of the EM shower fraction with f_{π^0} for the mean fraction of π^0 production per nuclear interaction.

Nuclear effects such as those mentioned in (ii) produce a form of undetectable or "invisible" energy, mainly caused by nuclear binding energy losses, soft neutrons, neutrinos, muons and photons emitted with a considerable time delay ($\lesssim 1\mu\text{s}$). The fractions of

¹¹The atomic weight of the absorbing detector material is denoted by A .

¹²The *punch-through* probability for hadrons traversing the detector material over a distance z without nuclear interaction is $P \approx \exp(-z/\lambda)$.

¹³On average one third of produced pions after each generation are π^0 's ($f_{\pi^0} \approx 1/3$).

the EM (e) and hadronic (h) shower components resulting in visible signals represent an important intrinsic characteristic of the hadronic calorimeter. For an incident pion with energy E , the energy ratio of visible signals, which is commonly denoted by the e/π ratio, can be derived based on the logic flow shown in Figure 3.19 as follows,

$$\begin{aligned}
 E_{\pi}^{\text{vis}} &= eF_{\pi^0}E + hF_hE \\
 &= \underbrace{eE}_{E_e^{\text{vis}}} \left(F_{\pi^0} + \frac{h}{e}F_h \right) \\
 \frac{E_{\pi}^{\text{vis}}}{E_e^{\text{vis}}} &= 1 - F_h + \frac{h}{e}F_h \\
 &= 1 - \left(1 - \frac{h}{e} \right) F_h \\
 &= 1 - \left(1 - \frac{h}{e} \right) \left(\frac{E}{E_0} \right)^{k-1} \\
 &\equiv \left(\frac{e}{\pi} \right)^{-1}
 \end{aligned} \tag{3.14}$$

and serves as an indicator for the performance of the hadronic calorimeter. Usually $e \neq h$ and $e/\pi > 1$ with a non-linear mean calorimeter response as a function of the energy due to a decreasing F_h fraction as the incident hadron energy increases. Any deviation of the e/h ratio from 1 typically leads to an increase in the uncertainty of the energy measurement and gives rise to a constant term for the energy dependence of the uncertainty. While the e/h ratio cannot be measured directly, it can be derived from e/π signal ratios obtained from fits to experimental data.

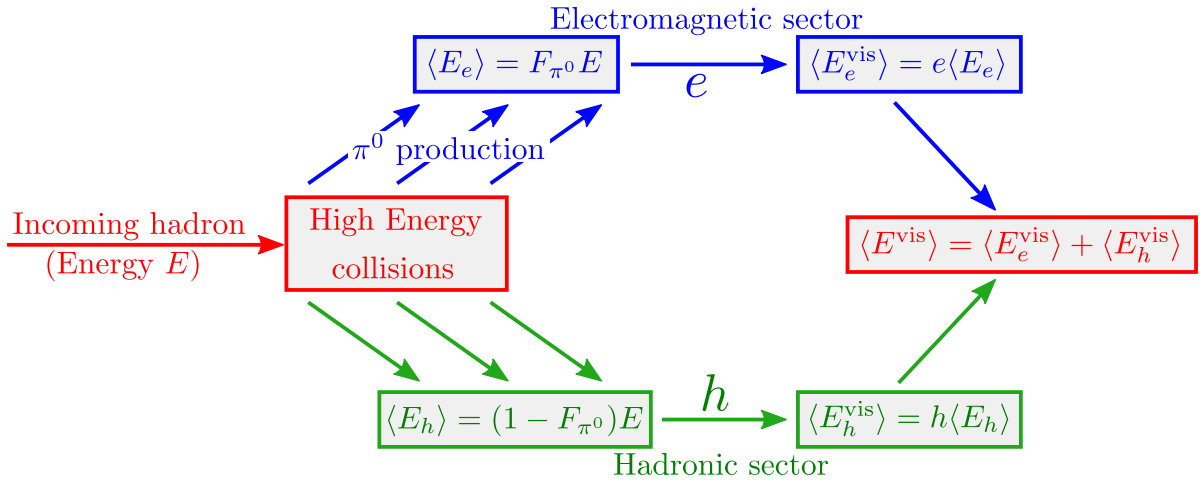


Figure 3.19.: Logic energy flow diagram of an hadronic shower.

Several compensating techniques have been developed to *tune* the e/π calorimeter response in order to achieve $e/\pi \approx 1$ for optimized performance. Offline hadronic calibrations, as further discussed in Chapter 4, must then account for event-to-event fluctuations in the invisible/escaped energy fraction. With this in mind, the choice of passive absorbing and active readout materials, sampling fractions and detector geometry has been carefully tuned for the ATLAS calorimetry system to achieve an optimal intrinsic e/π response. The system comprises the Tile Calorimeter (TileCal), the Hadronic End-cap Calorimeter (HEC) and the Forward Calorimeter (FCal).

The **TileCal** consists of a long central barrel with an extending barrel on each side covering the region $|\eta| < 1.7$ and uses 14 mm low-carbon steel (iron) plates as absorbers interleaved with 3 mm plastic scintillating tiles as active medium. As traversing shower particles ionize the scintillator, the recombination of ion-electron pairs produces UV light flashes, which are collected by wavelength shifting fibres and carried to photomultiplier tubes for readout. There are three layers with a segmentation of $\Delta\eta \times \Delta\phi = 0.1 \times 0.1$ in the first two layers and 0.2×0.1 in the last layer [90].

The **HEC** consists of two wheels in each end-cap region covering the range of $1.5 < |\eta| < 3.2$ and uses 25-50 mm copper plates as absorbers interleaved with 8.5 mm liquid argon (LAr) as active medium. The ionization charge from shower particles in the LAr is collected via an applied high voltage between electrodes, producing a pulse of current for readout. There are four layers with a segmentation of $\Delta\eta \times \Delta\phi = 0.1 \times 2\pi/64$ at $|\eta| < 2.5$ and $0.2 \times 2\pi/32$ at larger $|\eta|$ [91].

The **FCal** consists of three cylindrical modules in each end-cap region covering the region $3.1 < |\eta| < 4.9$ and uses a coaxial hole matrix filled with an electrode structure made of concentric rods and tubes, which are made of copper or tungsten as absorbers. The 0.25 – 0.50 mm gaps between the rod and the tube are filled with LAr as the active medium [92].

The overall required energy resolution, as summarized in Table 3.2, is

$$\frac{\sigma_E}{E} = \underbrace{\frac{50\%}{\sqrt{E}} \oplus 3\%}_{\text{TileCal \& HEC}} \quad \text{and} \quad \frac{\sigma_E}{E} = \underbrace{\frac{100\%}{\sqrt{E}} \oplus 10\%}_{\text{FCal}} \quad (3.15)$$

whereas (see Equation 3.11) test beam measurements have determined the stochastic and constant terms $a(c)$ to be 56%(5.5%) for the TileCal, 71%(5.8%) for the HEC and

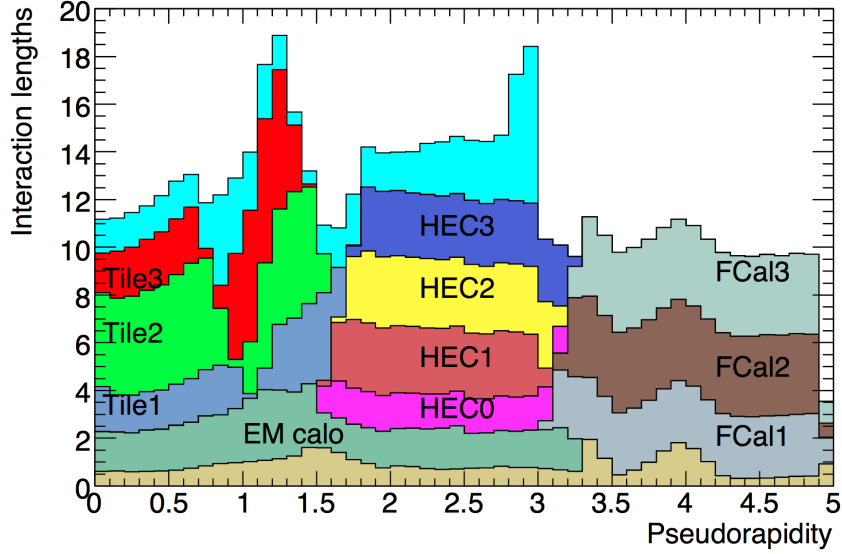


Figure 3.20.: The calorimeter material distribution in terms of interaction length λ as a function of $|\eta|$. This includes all material from the interaction point outwards. For completeness, the material up to the entrance of the first muon spectrometer layer is shown [62].

70%(3.0%) for the FCal [62]. The contribution from noise was less than ~ 3 GeV and the e/h ratio was determined to be between $1.36 - 1.49$ [88].

The thickness of the ATLAS detector is $> 9.5\lambda$, which is sufficient for the full containment of hadronic showers. The material distribution of the calorimeters over the full pseudorapidity range is shown in Figure 3.20 and can be compared to Figure 3.13.

3.2.5. Muon Spectrometer

Muons do not interact strongly and with a long lifetime ($\sim 2.2\mu\text{s}$, $c\tau \sim 0.7$ km) are the only charged particles expected to penetrate all subdetectors in ATLAS. The fact that muons pass through the calorimeters already serves as a basic identification of muons. Therefore, the ATLAS muon spectrometer system (MS) forms the most outer layer of ATLAS and encloses the calorimeters. As described in Section 3.2.2, the MS uses a complex toroidal magnetic field to bend muons in the $\rho - z$ plane, which is orthogonal to the solenoidal field in the ID. The \mathbf{B} -field map is reconstructed using 1800 *Hall sensors* by determining the non-uniform bending power along muon trajectories and also the relative position of each detector component is monitored using 12000 precision optical sensors, which is crucial for a precise modelling of the spectrometer resolution.

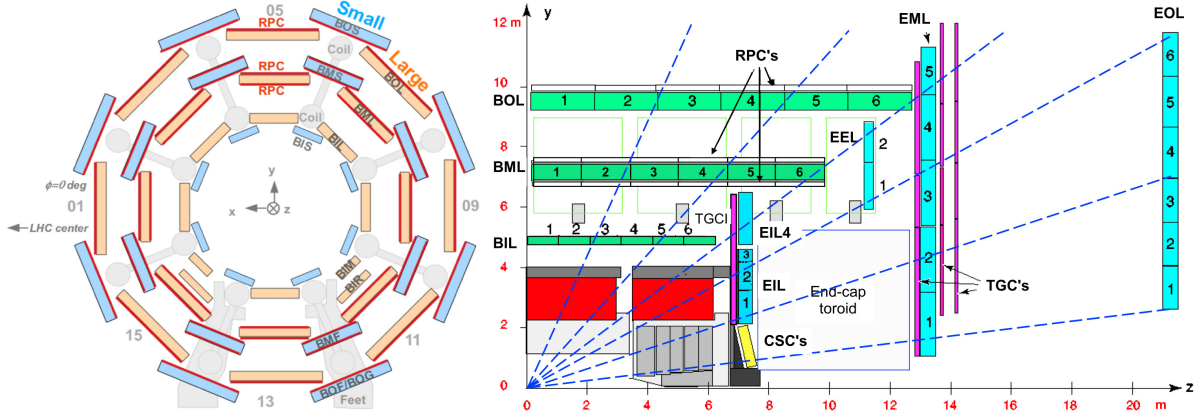


Figure 3.21.: Cross-sectional views of the ATLAS Muon Spectrometer: (left) the non-bending plane in the barrel region with small/large MDT chambers in blue/orange and RPC chambers in red [93]; (right) the bending plane with the barrel MDT chambers in green, the end-cap MDT chambers in blue and the barrel/end-cap RPC/TGC chambers in black/purple [62].

As shown in Figure 3.21, the MS comprises different chambers in the barrel and end-cap regions. These subdetectors can be classified in two types: (i) high precision tracking chambers to reconstruct the momentum of muons and (ii) fast-response chambers for online triggering on muons and the identification of their originating bunch crossing. The detectors belonging to type (i) are the Monitored Drift Tube (MDT) and the Cathode Strip Chamber (CSC) and belonging to type (ii) are the Resistive Plate Chamber (RPC) and the Thin Gap Chamber (TGC). These are all gaseous detectors using high voltage across electrodes to collect the ionization charge deposited from traversing muons.

The **MDT** consists of Al cathode tubes with a diameter of 30 mm, central tungsten-rhenium anode wires with a diameter of 50 μm at 3080 V and contain a gas mixture of 93% Ar and 7% CO_2 at 3 bar. The maximal drift time from the tube wall to the wire is ~ 700 ns and the average spatial resolution per tube is ~ 80 μm . The tubes are arranged along ϕ , combined in layers and grouped in chambers. These cover a range of up to $|\eta| < 2.7$, except in the innermost end-cap layer reaching up to $|\eta| < 2.0$, as they are replaced by CSC's in this region.

The **CSC** consists of two end-cap wheels made of eight alternating small and large chambers, covering the region $2.0 < |\eta| < 2.7$. Each chamber contains anode multi-wire layers with a wire diameter of 30 μm and interleaving layers of cathode readout strips oriented perpendicular to the wires for measurements in the bending plane (ρ) and oriented parallel to the wires for measurements in the transverse plane (ϕ). The wire-strip spacing is equal to the wire pitch of 2.5 mm and the strip pitch is 0.25 mm with

strip widths of 1.519 mm and 1.602 mm in the large and small chambers respectively. Using a gas mixture of 80% Ar and 20% CO₂ and an operating wire voltage of 1900 V, the avalanche formed on the anode induces a charge on the cathode strips, which are used for readout. The electron drift time is ≤ 40 ns leading to a time resolution of ~ 7 ns per plane. Charge interpolation between neighbouring strips can be used to improve the spatial resolution, which reaches $\sim 60 \mu\text{m}$ in the ρ coordinate per plane and ~ 5 mm in the ϕ coordinate.

The **RPC** consists of three concentric cylindrical trigger stations attached to MDT chambers in the barrel region with a coverage of $|\eta| < 1.05$. Each station uses two parallel resistive plates with a 2 mm spacing containing a gas mixture of 94.7% C₂H₂F₄, 5% Iso-C₄H₁₀ and 0.3% SF₆ and an applied field of 4.9 kV/mm. Metallic strips with a width of 25 – 35 mm are connected to the outer faces of both plates to read out the signal via capacitive coupling. These pick-up strips are arranged on one plate parallel to the MDT wires for the bending view of the trigger and on the other plate orthogonal to the MDT wires for a ϕ measurement.

The **TGC** consists of multi-wire proportional chambers and is very similar to the CSC, except that the wire-strip spacing of 1.4 mm is smaller than the wire pitch of 1.8 mm and thus allows for faster charge collection. The anode wire with a diameter of $30 \mu\text{m}$ is operated at nominally 2.9 kV within a highly quenching gas mixture of 55% CO₂ and 45% n-C₅H₁₂. The chambers are arranged in concentric wheels covering a range of $1.05 < |\eta| < 2.4$ and complement the MDT with a measurement of the ϕ coordinate.

The main parameters of each subdetector of the muon spectrometer are summarized in Table 3.3. The spectrometer is able to determine the sagitta of high-momentum muon tracks ($p_T \sim 1$ TeV) with a precision of about 10%. While stand-alone measurements of lower momentum tracks down to ~ 3 GeV can be made, energy losses in the calorimeters

Detector	Chamber resolution			Measurements/track		Number of	
	z/R	ϕ	time	barrel	endcap	chambers	channels
MDT	$35 \mu\text{m} (z)$	—	—	20	20	1088	339k
CSC	$40 \mu\text{m} (\rho)$	5 mm	7 ns	—	4	32	30.7k
RPC	10 mm (z)	10 mm	1.5 ns	6	—	544	359k
TGC	2-6 mm (ρ)	3-7 mm	4 ns	—	9	3588	318k

Table 3.3.: Summary of main parameters of the ATLAS muon spectrometer subdetectors [62].

and multiple scattering effects start to dominantly limit the sagitta resolution and therefore the measurement is complemented with the tracking information from the ID to achieve a resolution of $2 - 3\%$ in the low- p_T region.

3.2.6. Forward Detectors

The ATLAS detector is extended in the very forward region on each side by three detectors: LUCID (Luminosity measurement using Čerenkov Integrating Detector), ZDC (Zero-Degree Calorimeter) and ALFA (Absolute Luminosity For ATLAS). Their locations along the beam pipe are shown in Figure 3.22.

LUCID consists of Čerenkov counters placed at $z \pm 17$ m and ~ 10 cm from the beam pipe ($|\eta| \approx 5.8$) to detect inelastic p - p scattering for measurements of the integrated luminosity and for online monitoring of beam conditions and the instantaneous luminosity.

ZDC consists of EM and hadronic calorimeter modules placed between the two beam pipes after the split at $z \pm 140$ m to detect forward neutrons with $|\eta| > 8.3$ in heavy-ion collisions. Besides determining the centrality of these collisions and reducing beam-gas/halo effects via a tight coincidence requirement between ZDC arms, the interaction point in ATLAS can be located with a 3 cm resolution in z .

ALFA consists of scintillating-fibre trackers inside Roman pots at $z \pm 240$ m and ~ 1 mm from the beam pipe to detect elastic scattering at small angles, where the amplitude is directly connected to the total cross-section via the optical theorem.

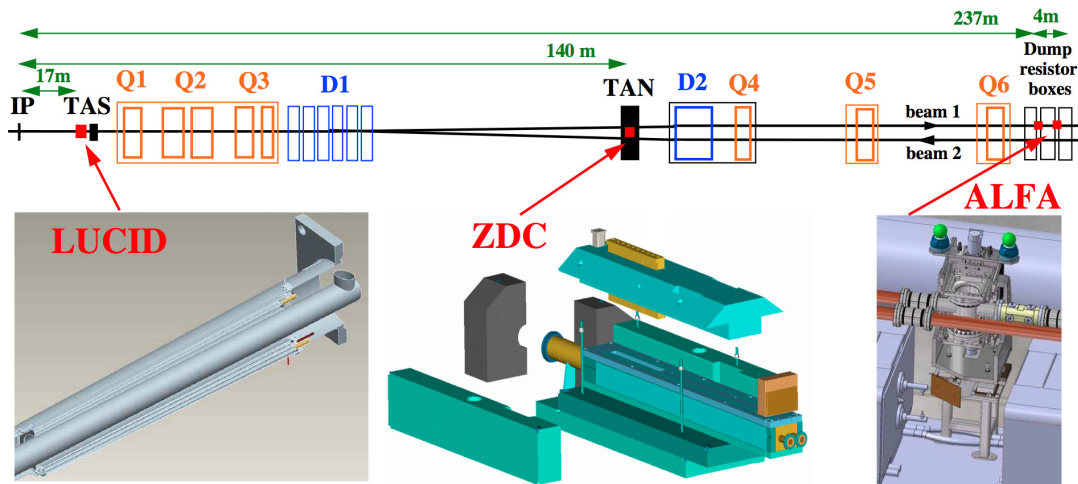


Figure 3.22.: Location of forward detectors along the beam pipe with respect to the ATLAS interaction point (IP) [62].

3.2.7. Trigger and Data Acquisition system

At the nominal LHC luminosity of $\mathcal{L} = 10^{34} \text{ cm}^{-2}\text{s}^{-1}$, as discussed in Section 3.1, the total p - p cross-section with an interaction rate of about 10^9 evt/s (10^8 evt/s for $\mathcal{L} = 10^{33} \text{ cm}^{-2}\text{s}^{-1}$, see Figure 3.3) is many orders of magnitude higher than the rare physics processes of interest, such as Higgs boson production. ATLAS captures event data using millions of read out channels, but technological constraints limit the amount of data that can be recorded for offline physics analyses and thus a strict online selection of interesting events must be deployed. This challenging task is taken by the ATLAS Trigger and Data Acquisition system (TDAQ) with the aim to reduce the final data storage rate from the incoming bunch-crossing rate of 40 MHz (20 MHz at 8 TeV with a 50 ns bunch spacing) to 200 Hz (600 Hz in 2012) [62, 94–96]. In other words, with a typical event data size of 1.5 MB (1.6 MB in 2012), the TDAQ system must reduce the storage rate from 60 TB/s (32 TB/s in 2012) to 300 MB/s (960 MB/s in 2012).

As illustrated in Figure 3.23, the TDAQ system is based on a three-level sequential data filtering architecture: the custom hardware-based Level 1 (L1) utilizing coarse calorimeter and muon spectrometer information and the software-based High Level Trigger (HLT) composed of the Level 2 (L2) and the Event Filter (EF) utilizing online and offline reconstruction algorithms running on a high-performance computing farm. Each level has distinct duties:

- **Level 1.** Dedicated hardware components receive reduced-granularity information from the RPCs and TGCs of the Muon Spectrometer - to identify high- p_T muons - and from the calorimeters to search for signatures such as large electromagnetic energy deposits, jets, τ leptons, large transverse and missing energy. Identified features are then collected and sent to the *Central Trigger Processor* to compare with a menu of trigger conditions, before a *L1 Accept* event status is issued, which initiates further feature extractions on event fragments by Read-Out Drivers (ROD) with subsequent data transfers to the Read-Out System (ROS) for buffering. Meanwhile, small *Regions-of-Interest* (RoIs) data packages are compiled, containing the $\eta - \phi$ location and energies of triggered objects. RoIs hold only a few percent of the data for each event and are sent to Level 2 to seed further processing. The entire procedure introduces a latency of $< 2.5 \mu\text{s}$, compared to a bunch-crossing interval of 25 ns (50 ns in 2012) and muon times-of-flight and broad calorimeter signal widths exceeding this interval. Therefore, the event data from all detector channels is moved into pipeline memories of dedicated buffering front-end electronics.

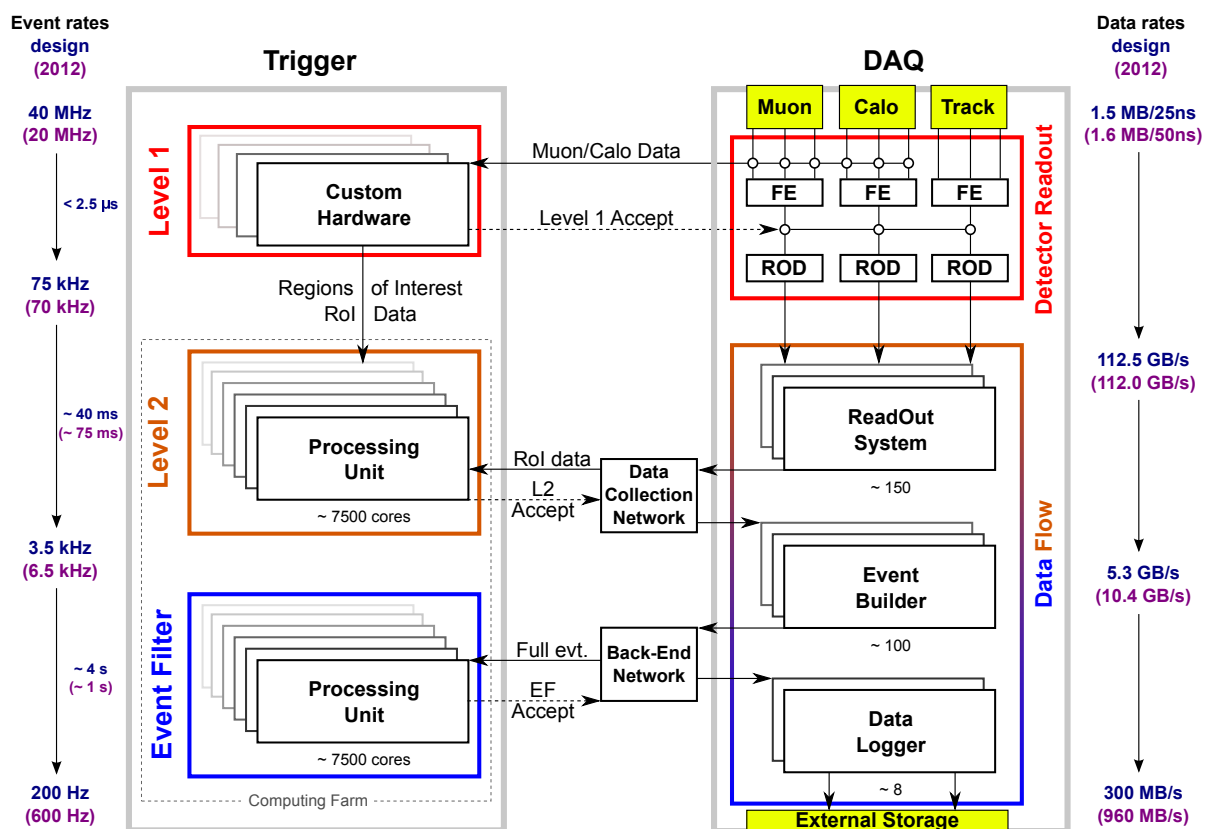


Figure 3.23.: Schematic overview of the ATLAS Trigger and Data Acquisition system with both design [62] and 2012 (Run-1) configurations [94–96].

- **Level 2.** Event fragments for the L1 RoIs are requested from the ROS with access to the full detector granularity in these regions, which now includes the tracking information from the Inner Detector. Reconstruction and signature algorithms analyse features within the RoIs (e.g. track, calorimeter cluster) and determine whether a particular feature meets certain criteria (e.g. p_T threshold, shower shape, track-cluster match). In case the event fulfils a list of trigger selection criteria, a *L2 Accept* event status is issued, which initiates the event to be fully built, prior to the Event Filter processing.
- **Event Filter.** The L2 accepted events are completely reconstructed using the full event information including object calibrations (e.g. calorimeter energy deposits) and are analysed to make a final decision whether the event is of interest to any offline physics analysis. The event is tagged and classified under ATLAS-defined physics streams, such as electrons, muons, jets, photons, missing transverse energy and τ leptons, and B -physics. Finally a *EF Accept* event status is issued, which initiates the event data transfer to external permanent mass storage.

3.2.8. Physics Data Processing

The collected Event Filter RAW data files are transferred to the Tier-0 CERN computing centre, where physics object reconstruction is applied to generate a data structure with all the variables needed for offline physics analyses and a size of about 500 KB per event: the Event Summary Data (ESD) files. Other file formats contain ESD subsets with only reconstructed final physics objects, such as AOD (Analysis Object Data) files with an event size of about 100 KB and even further reduced DPD (Derived Physics Data) files [97]. The latter file format has been chosen to produce customized slimmed ROOT-based n-tuple versions (D3PD) for the analysis presented in this thesis.

For an efficient international collaborative data analysis effort, the processed Tier-0 data is distributed and replicated on the LHC Computing Grid (LCG) with a Tier 1-3 chain structure [98]. The analysis presented in this thesis has been performed using the LCG as well as CERN-local computing clusters.

3.3. Summary

At the LHC, currently the world's most powerful particle collider, the ATLAS experiment explores phenomena in nature at unprecedented energies and at the boundary of current technological limits, the ATLAS detector reconstructs particles leaving the interaction point using superconducting solenoidal and toroidal magnets, precision inner tracking detectors, hermetic electromagnetic and hadronic calorimeters, stand-alone muon chambers and forward detectors. The ATLAS high-performance TDAQ system has collected and distributed collision data during the LHC Run-1, from which 4.7 and 20.3 fb⁻¹ of p - p collision data at $\sqrt{s} = 7$ TeV in 2011 and $\sqrt{s} = 8$ TeV in 2012 respectively are used for the analysis presented in this thesis.

Chapter 4.

Particle Reconstruction

The high-energy proton-proton collisions at the LHC produce many different particles, interacting with the different subdetector systems of ATLAS and resulting in a wealth of complex final state signatures. The corresponding electronic signals are passed through a particle reconstruction, identification and calibration chain to finally form “physics objects”. These objects represent either individual particles and particle jets, i.e. through the interaction with ATLAS, or missing transverse energy inferring to non-interacting particles. Each object contains a selection of different kinematic properties and information about its path through the detector. The reconstruction algorithms to build these objects in data are also used in simulations to test Standard Model predictions and to evaluate the performance of the reconstruction.

The basic reconstruction of particles at the individual detector-level has been already discussed in Section 3.2. The focus of this chapter is the high-level reconstruction and calibration of physics objects, i.e. the final state particles, of the quark-initiated W/Z vector boson associated $H \rightarrow b\bar{b}$ production, as shown in Figure 4.1. The topology of these physics objects are then used to derive the Higgs boson search strategy presented in Chapter 5. As mentioned in Section 2.3.1, the analysis presented in this thesis considers

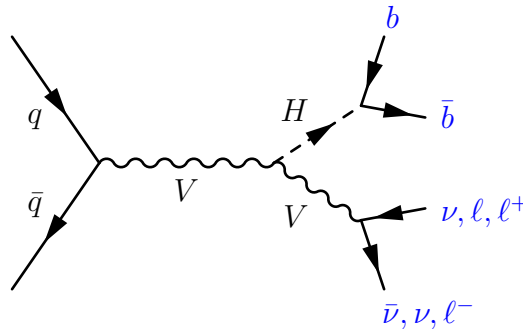


Figure 4.1.: Leading-order Feynman diagram for quark-initiated VH production.

the following decay channels: $ZH \rightarrow \nu\bar{\nu}b\bar{b}$, $WH \rightarrow \ell\nu b\bar{b}$ and $ZH \rightarrow \ell^+\ell^-b\bar{b}$ with $\ell = e, \mu$. Respectively, these channels are classified by their number of charged leptons in the final state and referred to the “0-lepton”, “1-lepton” and “2-lepton” channels. The physics objects are *electrons*, *muons*, *jets* and neutrinos, whereas the presence of neutrinos refers to an overall *transverse momentum imbalance*, E_T^{miss} , after considering all reconstructed interacting particles. The event displays in Figure 4.2 show VH production candidates in each decay channel with their corresponding physics objects reconstructed in the ATLAS detector.

Charged tracks from particles traversing the detector must pass a minimum p_T threshold of 400 MeV to be considered in the object reconstruction. These tracks are then extrapolated and associated to a collision vertex. If a vertex has more than three associated tracks and the corresponding $\sum p_T^2$ of the tracks is the largest in the event, it is labelled as the *primary collision vertex*.

In Section 4.1, an overview of Monte Carlo simulations is given, followed by Sections 4.2 to 4.4 with a detailed discussion of the reconstruction of each physics object used in the VH analysis, presented in Chapter 5. Unless otherwise noted, all *studies* presented in this chapter are based on the $\sqrt{s} = 8$ TeV data recorded by ATLAS, corresponding to an integrated luminosity of 20.3 fb^{-1} .

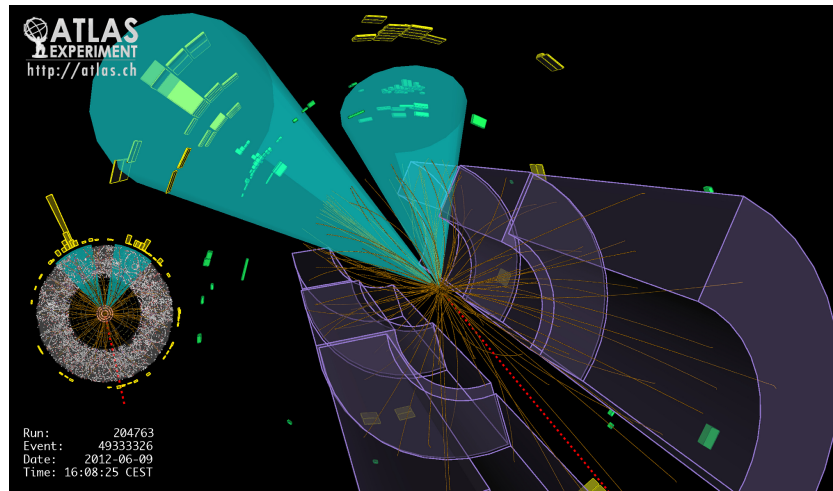
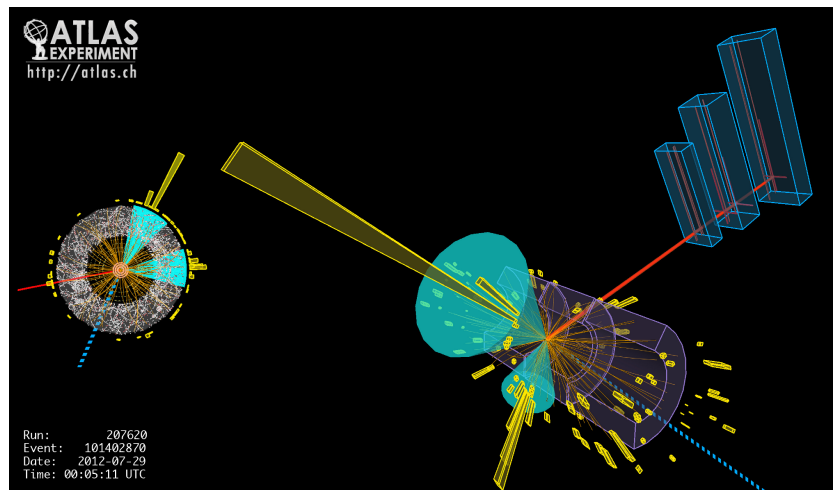
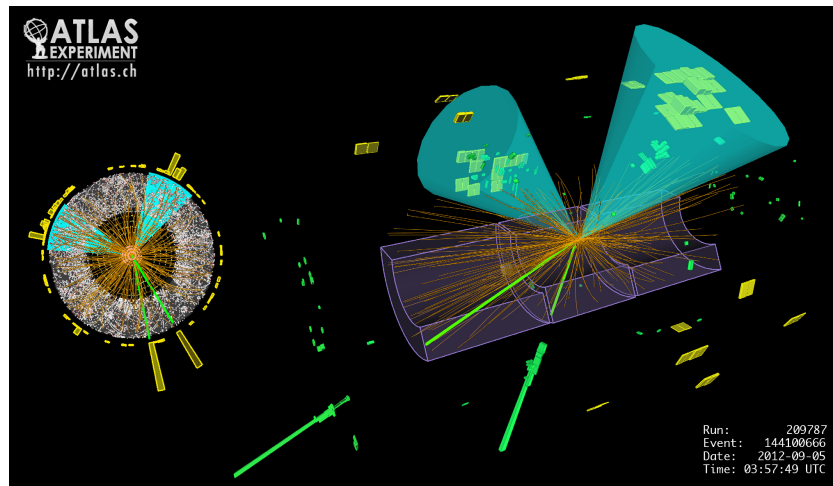
(a) $ZH \rightarrow \nu\bar{\nu}b\bar{b}$ candidate(b) $WH \rightarrow \mu\nu b\bar{b}$ candidate(c) $ZH \rightarrow e^+e^-b\bar{b}$ candidate

Figure 4.2.: ATLAS event displays of Higgs boson $H \rightarrow b\bar{b}$ candidates in (a) the 0-lepton channel, (b) the 1-lepton channel and (c) the 2-lepton channel in $\sqrt{s} = 8$ TeV proton-proton collision data [99]. The topological calorimeter clusters associated to b -quark induced jets from the Higgs boson candidate are shown in cones. For the vector boson, the E_T^{miss} is shown as a dotted line, the muon as a solid red line, and the electron as a solid green line.

4.1. Monte Carlo simulation

Monte Carlo (MC) simulated samples are generated at the same centre-of-mass energy as the corresponding data samples and are crucial to test or to extrapolate the particle reconstruction performance for different collision run conditions, to derive calibrating scale factors (SF) to match with data, to estimate signal and background events in physics analyses and to compare measured data to Standard Model expectations or to new physics models.

The production of MC samples generally follows a two-step procedure:

1. **Event generation.** The generation of an high-energy proton-proton collision event can be factorised into different stages, spanning over the perturbative ($\alpha_s \ll 1$ and high Q^2) to the non-perturbative ($\alpha_s \simeq 1$ and low Q^2) regime of QCD (see Section 2.1.1). These stages are illustrated in Figure 4.3 and include:

- a *hard scattering process*, involving coloured parton (quark/gluon) creation, based on matrix element computations, using fixed-order perturbation theory;
- a *parton showering process* with multiple QCD bremsstrahlung in the initial and final state, evolving down to low momentum scales, until perturbation theory breaks down (at the hadronization scale, of the order of a few Λ_{QCD});
- a *hadronization process*, occurring at the hadronization scale of the order of a few Λ_{QCD} , confines a system of QCD partons into colourless primary hadrons by utilizing phenomenological fragmentation models;
- a *hadron decay process* accounts for unstable primary hadrons decaying into stable particles, which are expected to propagate through a part of the detector;
- an *underlying event process* with secondary interactions between proton remnants is based on phenomenological models with free parameters to be determined by experimental data, and typically produces soft hadrons throughout the event.

The distribution of partons within the incoming protons governs the probability of a particular interaction to take place. These distributions, can be modelled by fitting parameterised functions, parton distribution functions (PDFs), to experimental data and serve as external inputs to event generator tools. The main generators used for the simulation of the signal and background processes in the VH analysis

presented in this thesis are PYTHIA [101, 102], SHERPA [103] and HERWIG [104] (see Section 5.2). The modelling of some particular processes can be improved by combining different generators, e.g. the hard process generation with POWHEG [105–107] or ACERMC [108] interfaced with PYTHIA for the remaining processes. Additionally, different tunes can be employed to adjust various modelling assumptions in different event stages, i.e. effects which are not directly constrained by the theory.

2. **ATLAS simulation.** The particles produced by the event generator in step (1) are propagated through a full model of the ATLAS detector based on the GEANT4 toolkit (GEometry ANd Tracking) [109]. This allows to simulate the passage of particles through matter and their interactions with the active and passive detector materials. In order to reduce the burden on computing resources and to increase

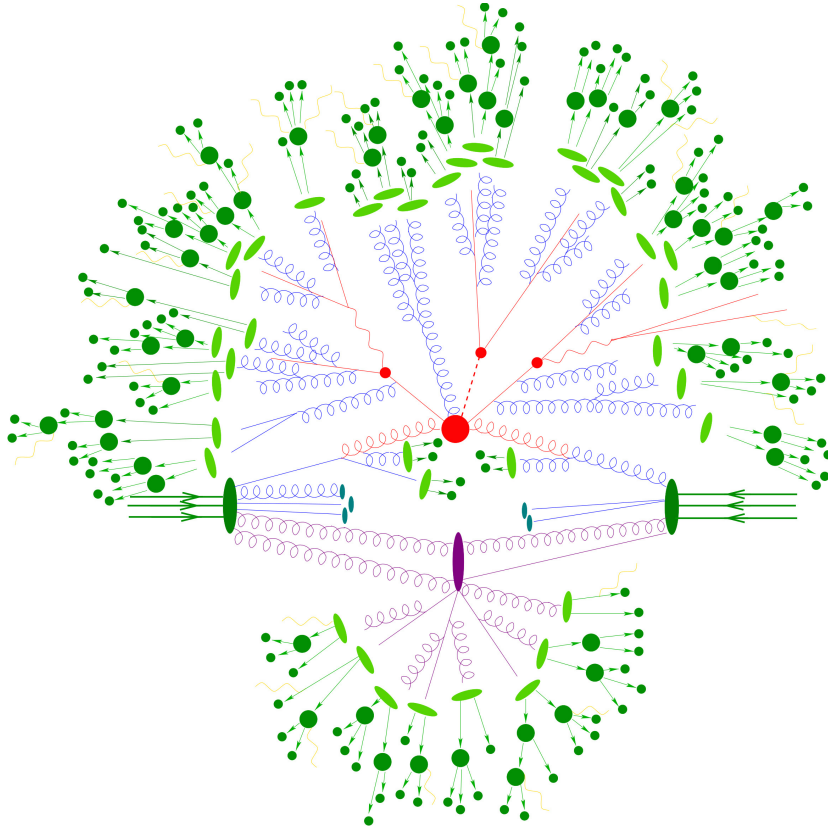


Figure 4.3.: Illustration of a $t\bar{t}H$ event in a proton-proton collision produced by an event generator. The hard scatter (big red blob) with subsequent decay of top quarks and the Higgs boson (small red blobs) is accompanied with additional QCD radiation (blue) in the parton showering process, before the hadronization sets in (light green blobs) and hadrons decay (dark green blobs). The underlying event (purple), beam remnants (small turquoise blobs) and photon radiation (yellow) are also shown [100].

the MC event statistics, the ATLFast-II simulation [110] can be used to reduce the simulation time by more than one order of magnitude. It parametrises the longitudinal and lateral energy profiles of electromagnetic and hadronic showers for the response of the calorimeters, but still uses a full simulation for the Inner Detector and Muon spectrometer. Finally, the deposited particle energies in sensitive detector components run through a virtual digitization simulation [111], i.e. electronic signals are produced according to the ATLAS detector readout system. These virtual electronic detector signals are then treated in the same way as real experimental data and passed through the same trigger and particle reconstruction chain.

4.2. Electrons and Muons

In this section, electron and muon physics objects, which are most relevant to the analysis of the $WH \rightarrow \ell\nu b\bar{b}$ and $ZH \rightarrow \ell\ell b\bar{b}$ channels, are introduced. This includes specific reconstruction quality criteria, in order to achieve a high selection efficiency or fake rate reduction.

4.2.1. Reconstruction, identification and classification

The reconstruction and identification of *electrons* [113] is subject to large backgrounds from misidentified hadron jets, secondary electrons from photon conversions, and non-isolated electrons from heavy-flavour hadron decays. The following procedure has been employed to provide good discrimination against these backgrounds. For the highest precision, only electron candidates in the central region (with coverage by the Inner Detector) with $|\eta| < 2.47$ are reconstructed. In this region, a *sliding-window* algorithm [114] scans EM calorimeter cells with a window size of $N_\eta \times N_\phi = 3 \times 5$ in $\eta - \phi$ space and identifies energy deposits with a total $E_T > 2.5$ GeV as a seed cluster. If this energy cluster can be associated to a reconstructed track in the Inner Detector (ID), an electron candidate is found. At this stage, the electron-candidate reconstruction optimizes the overall cluster energy using enlarged sliding window sizes and accounts for bremsstrahlung effects [115]. The total reconstructed electron-candidate energy is calibrated, considering different sources of energy loss, such as the material in front of the calorimeter, dead material inside the calorimeter, lateral energy leakage outside of the reconstructed cluster and longitudinal energy leakage beyond the calorimeter. Reference processes, such as

$Z \rightarrow ee$, are used to determine the absolute energy scale and to inter-calibrate the different regions of the EM calorimeter, aiming for measured electron-candidate energies to reproduce those obtained from Monte Carlo simulations [116]. The selected electron candidates are then distinguished from backgrounds using a multivariate analysis (MVA) technique: a likelihood-based electron identification method [112, 117]. This method combines EM shower-shape information, ID track reconstruction quality, track-cluster matching quality (direction, momentum/energy), TRT information (high-threshold hits) and photon conversion identification. The combination utilizes data-driven signal (S) and background (B) probability density functions ($P_{S/B,i}(x_i)$) of electron discriminating variables (\mathbf{x} with x_1, \dots, x_n) and merges these in a likelihood discriminant ($d_{\mathcal{L}}$), defined as:

$$d_{\mathcal{L}} = \frac{\mathcal{L}_S}{\mathcal{L}_S + \mathcal{L}_B}, \quad \mathcal{L}_{S/B}(\mathbf{x}) = \prod_{i=1}^n P_{S/B,i}(x_i). \quad (4.1)$$

Different operating points or menus are derived by choosing \mathbf{x} (different sets of variables) and cutting loosely or tightly on $d_{\mathcal{L}}$ to achieve different signal electron efficiencies and background rejections. These operating points, in increasing order of purity (from

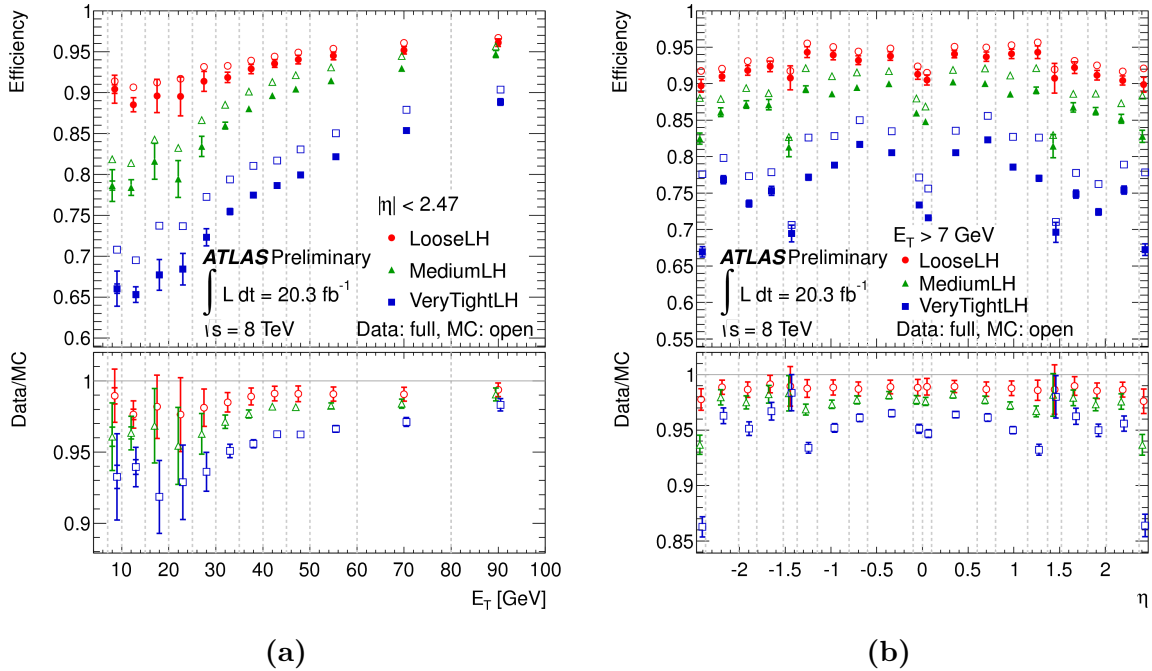


Figure 4.4.: Electron identification efficiency measured in data for different likelihood operating points as a function of (a) E_T and (b) η , compared to the MC prediction for electrons from $Z \rightarrow ee$ decays [112].

Menu	Data eff.	Data eff.	MC eff.	Bkg. composition (%)		
	$Z \rightarrow ee$	bkg	bkg	non-iso e	bkg e	hadron
VeryLooseLH	97.8 ± 0.1	3.0 ± 0.02	2.9 ± 0.03	15.7	67.1	13.9
LooseLH	92.8 ± 0.2	1.0 ± 0.01	1.0 ± 0.02	36.6	38.3	16.3
MediumLH	87.8 ± 0.3	0.5 ± 0.01	0.6 ± 0.01	41.8	34.8	9.1
TightLH	84.2 ± 0.3	0.4 ± 0.01	0.5 ± 0.01	49.1	24.1	9.2
VeryTightLH	77.0 ± 0.3	0.3 ± 0.01	0.3 ± 0.01	50.1	22.7	5.8

Table 4.1.: Electron likelihood identification menus and their signal and background efficiencies, averaged over η and with $20 < E_T < 50$ GeV, in 8 TeV data and MC simulation, containing all relevant $2 \rightarrow 2$ QCD processes. Based on MC information, different background contributions after using each menu are shown: non-isolated electrons from heavy-flavour hadron decays, background electrons from photon conversions and Dalitz decays, and hadrons [112, 117].

VeryLooseLH to VeryTightLH), and their corresponding data and background efficiencies are summarized in Table 4.1. The electron identification efficiency is shown as a function of E_T and η in Figure 4.4. The final electron physics objects considered in the VH analysis must have $E_T > 7$ GeV and satisfy the “very-loose likelihood” (VeryLooseLH) identification criteria [117]. This operating point has a signal data efficiency of about 98% and offers a good rejection against light-flavour hadron jets.

The identification and reconstruction of *muons* [118] relies mainly on the Muon Spectrometer (MS) and the Inner Detector measurements, while the energy deposit (on average $\sim 2 - 3$ GeV) in the calorimeters can also be used. Depending on the available information from the different subdetectors, the muon identification considers independent track reconstructions in the MS and ID, and is performed according to different reconstruction criteria. This leads to the following classification (types) of muons.

- **Stand-alone (SA) muon:** The trajectory of the muon is reconstructed using only the MS information with coverage up to $|\eta| < 2.7$. The muon’s direction of flight and impact parameter at the interaction point are determined by extrapolating the reconstructed MS track back to the beam line, for which the estimated energy loss in the calorimeters is taken into account.
- **Combined (CB) muon:** A combined track is formed from the combination of an independently reconstructed MS track and ID track. This combination provides

a good rejection against muons from secondary interactions and from pion/kaon decays-in-flight. Due to the limiting ID acceptance, only muons in the range of $|\eta| < 2.5$ are reconstructed.

- **Segment-tagged (ST) muon:** If a track reconstructed in the ID can be extrapolated to at least one track segment in the MDT or CSC muon chambers, it is identified as a muon. All track parameters are obtained from the ID measurements with coverage up to $|\eta| < 2.5$.
- **Calorimeter-tagged (CaloTag) muon:** If a track reconstructed in the ID can be associated to a characteristic charge deposit expected from minimum ionizing particles in the calorimeters, it is identified as a muon. All track parameters are obtained from the ID measurements with coverage up to $|\eta| < 2.5$.

CB muon candidates provide the best muon purity and represent the main type of muons used as physics objects. While CB, ST and CaloTag muons depend on the reach of ID measurements, SA muons can be used to extend the acceptance beyond the coverage of the ID: $2.5 < |\eta| < 2.7$. In the MS region $1.1 < \eta < 1.3$, muons traverse only one muon chamber and thus, SA muons cannot be reconstructed. In cases in which muons only cross one layer of MS chambers, ST muons can be used to increase the acceptance. The reconstruction of CaloTag muons is optimized in the region $|\eta| < 0.1$ with muon momenta between $25 \lesssim p_T \lesssim 100$ GeV. While they still have the lowest purity of all the muon types, they can recover the acceptance in the non-instrumented (service) region of the MS at $\eta \approx 0$. The actual reconstruction of SA, CB and ST muons in ATLAS can be performed by three independent algorithms or chains¹ in ATLAS [77]. One of these, the MuID algorithm [119], also named "Chain 2", performs a global fit to all muon hits in the ID and MS, and is used to reconstruct all muons in the VH analysis. Additionally, ID tracks, associated to CB, ST or CaloTag muons, must comply with the following *ID track quality* (hit) requirements:

- ≥ 1 Pixel hit²
- ≥ 5 SCT hits²
- ≤ 2 Pixel or SCT holes³

¹The **Staco** algorithm, also named "Chain 1", performs a statistical combination of SA and ID tracks using covariance matrices. The **Muons** algorithm, also named "Chain 3", unifies both Chain 1 and 2 approaches.

²If a track traverses an identified dead sensor, this number is reduced by one.

³A sensor is traversed by a track, but without hits.

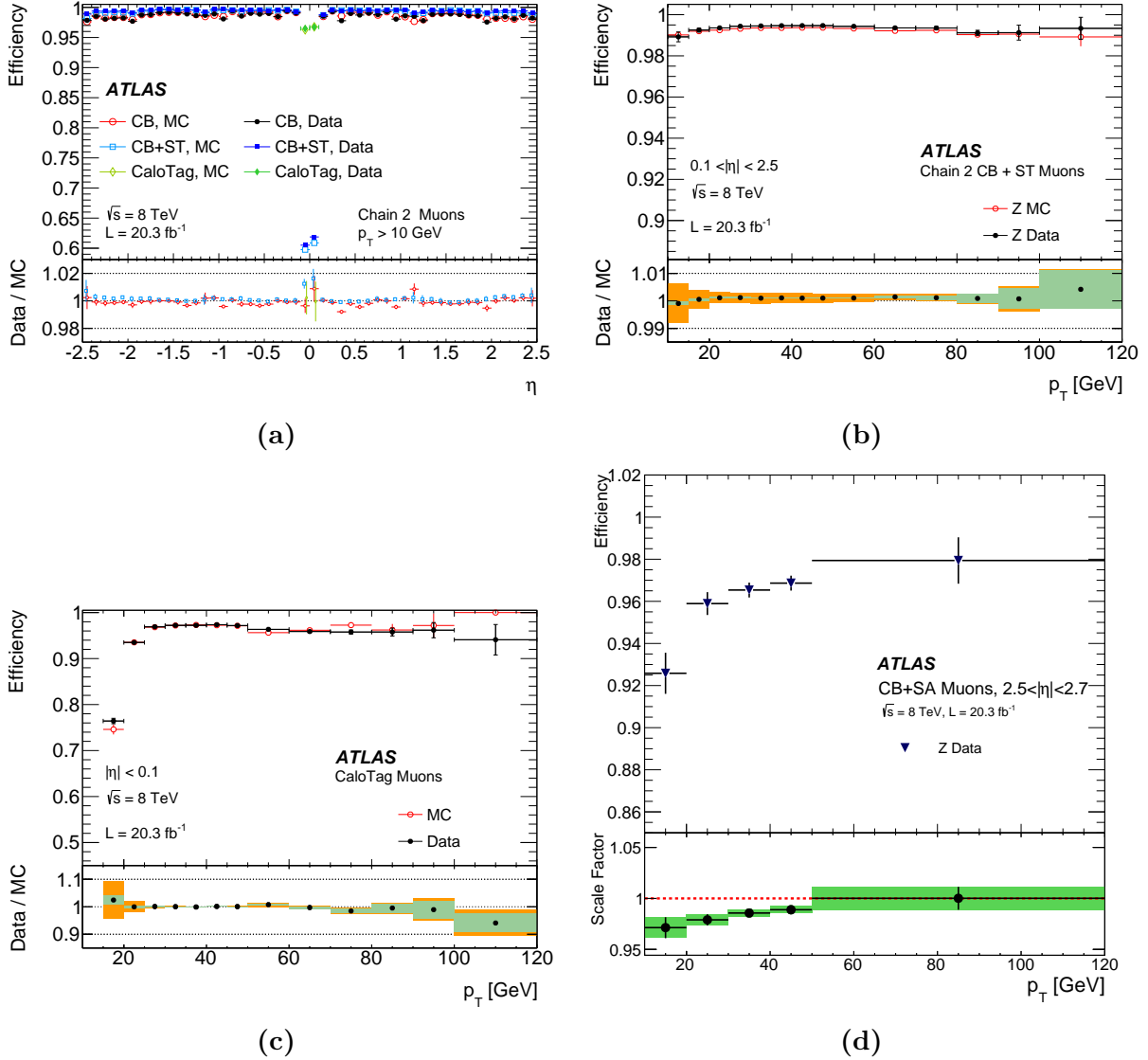


Figure 4.5.: Muon reconstruction efficiency measured in $Z \rightarrow \mu\mu$ events for different muon reconstruction types as a function of (a) η with $p_T > 10$ GeV, and as a function of p_T for (b) CB and ST muons with $0.1 < |\eta| < 2.5$, (c) CaloTag muons with $|\eta| < 0.1$ and (d) SA muons with $2.5 < |\eta| < 2.7$ [118].

- ≥ 9 TRT hits within $0.1 < |\eta| < 1.9$.

The muon reconstruction efficiency for different muon types is shown in Figure 4.5. When all muon types combined, the efficiency is about 99%. An overall good agreement between data and MC simulation is found. In order to maximize the acceptance, the final muon physics objects considered in the VH analysis may be any of the reconstructed muon types discussed above, but they must satisfy even further requirements: all muons have $p_T > 7$ GeV, CaloTag muons have $p_T > 20$ GeV and ID tracks with $|\eta| < 0.1$, SA muons

have MS tracks with $2.5 < |\eta| < 2.7$, and except for SA muons, the reconstructed muon track impact parameter with respect to the primary vertex must be less than 0.1 mm in the $x - y$ plane (d_0) and less than 10 mm along the z -axis (z_0).

In this analysis, electrons and muons are further categorized in *loose*, *medium* and *tight leptons*⁴, referring to an increasing level of purity.

- **Loose leptons** are all those that pass the reconstruction criteria mentioned above, and in addition, are *isolated* from other particles (tracks, energy deposits). The *track isolation* is defined as

$$iso_{\text{trk}}(\ell) = \frac{1}{p_{\text{T}}^{\ell}} \sum_{\text{trk}} p_{\text{T}}^{\text{trk}} \quad \text{for} \quad \Delta R(\ell, \text{trk}) < 0.2, \quad (4.2)$$

and is required to be less than 10% of the selected lepton candidate's p_{T} (i.e. $iso_{\text{trk}}(\ell) < 0.1$). In order to avoid double-counting, CaloTag muon candidates within $\Delta R < 0.1$ of a CB, ST or SA muon candidate are rejected.

- **Medium leptons** are loose leptons, with transverse energies/momenta larger than 25 GeV, however, only CB and ST muons with $|\eta| < 2.5$ are considered⁵.
- **Tight leptons** are medium leptons, but with more stringent isolation criteria: besides tightening the track isolation limit to 4%, i.e. $iso_{\text{trk}}(\ell) < 0.04$, the nearby calorimeter energy deposit is also limited. The *calorimeter isolation*, defined as

$$iso_{\text{calo}}(\ell) = \frac{1}{p_{\text{T}}^{\ell}} \sum_{\text{TC}} E_{\text{T}}^{\text{TC}} \quad \text{for} \quad \Delta R(\ell, \text{TC}) < 0.3, \quad (4.3)$$

is required to be also less than 4% of the selected lepton candidate's energy. It is reconstructed using noise-suppressed three-dimensional clusters of energy in the calorimeters, based on a *topological clustering* (TC) algorithm [114]. The basic idea of this algorithm is to build clusters by grouping neighbouring calorimeter cells, which have significant energy deposits above the expected noise, and by following the shower development (see Section 4.3.1). For electron candidates, $iso_{\text{calo}}(e)$ is corrected for small out-of-cluster leakage in the isolation cone [120], and the estimated ambient energy density contributions from the underlying event and from

⁴Electrons and muons are commonly referred to as *leptons* in this analysis.

⁵Studies have shown, SA and CaloTag muons increase the multijet background in the VH analysis, if they are used to identify the vector boson decay products.

Flavour	Electrons	Muons		
Type	Calo/Track-based	CB/ST	CaloTag	SA
Loose				
Quality	VeryLooseLH	MuID & <i>ID track quality</i>		
$ \eta $	< 2.47	< 2.7	< 0.1	$2.5 - 2.7$
E_T (GeV)	> 7	> 7	> 20	> 7
$ d_0 $ (mm)	–	< 0.1	< 0.1	–
$ z_0 $ (mm)	–	< 10	< 10	–
iso_{trk}	< 0.1	< 0.1	< 0.1	–
Medium				
E_T (GeV)	> 25	> 25	–	–
$ \eta $	–	< 2.5		
Tight				
Quality	VeryTightLH	–		
iso_{trk}	< 0.04	< 0.04		
iso_{calo}	< 0.04	< 0.04	–	–

Table 4.2.: Inclusive *loose*, *medium* and *tight* lepton object definitions in the VH analysis. The medium definition is built upon the loose definition, and the tight definition is built upon the medium definition.

pileup are subtracted on an event-by-event basis, using the jet-area based technique discussed in Section 4.3.3.

A summary of these lepton definitions is shown in Table 4.2.

4.2.2. Energy/Momentum resolution and scale

The miscalibration of the reconstructed electron cluster energy, i.e. the difference between the measured response in data and MC simulation, can be expressed as $E^{\text{data}} = E^{\text{MC}}(1+\alpha)$. Electron energy scale corrections (α) as a function of η can then be derived in $Z \rightarrow ee$ events, where the miscalibration induces a shift of the dielectron invariant mass peak. Assuming that the distribution of the energy resolution (intrinsically known to 10%, see

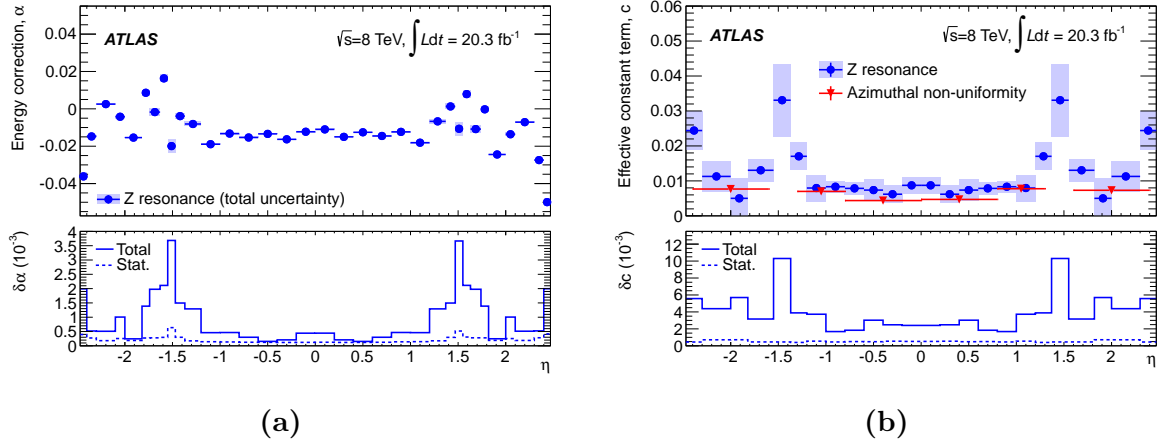


Figure 4.6.: Electron energy scale α (a) and effective constant term c (b) corrections derived from $Z \rightarrow ee$ events, as a function of η [116].

Table 3.2) is well described by the MC, up to a Gaussian constant term (c),

$$\left(\frac{\sigma_E}{E}\right)^{\text{data}} = \left(\frac{\sigma_E}{E}\right)^{\text{MC}} \oplus c, \quad (4.4)$$

a MC-driven template method [116] can be used to derive these resolution corrections from $Z \rightarrow ee$ events. The resulting scale factors, α and c , are shown in Figure 4.6.

The Z boson resonance width measured in 8 TeV data provides a direct constraint on the total energy resolution at a particular η and for the average E_T of electrons from Z boson decays, with $\langle E_T^{e(Z \rightarrow ee)} \rangle \sim 40$ GeV. Taking these constraints into account, the derived electron energy resolution, as shown in Figure 4.7a, is affected by different

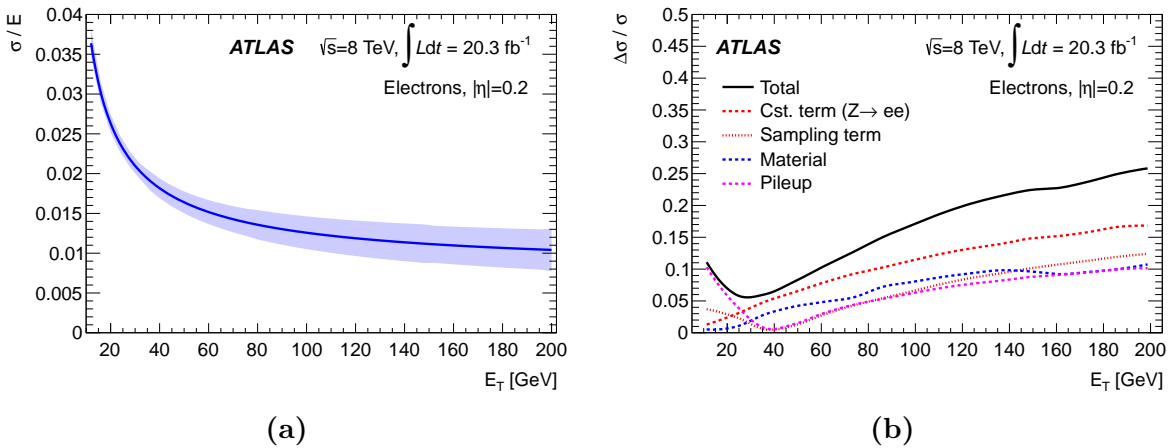


Figure 4.7.: Fractional electron energy resolution distribution (a) and different contributing uncertainties (b) as a function of E_T at $|\eta| = 0.2$ [116].

contributing uncertainties, as shown individually in Figure 4.7b. These include the intrinsic resolution (sampling term), the impact of the detector material uncertainty, pileup effects, and the constant term c . Contributions from pileup dominate at low E_T , while c dominates at high E_T . At $E_T = 40$ GeV, the relative uncertainty is minimal, where c contributes with an uncertainty of about 5%.

Similarly, the momentum scale and resolution of muons is studied. The simulated muon p_T , reconstructed in the ID and MS subdetectors, can be smeared to agree with data. This requires a good understanding of the muon transverse momentum resolution, which can be parametrized as

$$\frac{\sigma(p_T)}{p_T} = \frac{r_0}{p_T} \oplus r_1 \oplus r_2 \times p_T, \quad (4.5)$$

where r_0 (proportional to $1/p_T$) accounts for energy loss fluctuations in the traversed material, r_1 (constant in p_T) exhibits the mis-modelling of local B -field inhomogeneities, multiple scattering and local radial detector displacements, and r_2 (proportional to p_T) represents the intrinsic detector resolution (see Table 3.2). Furthermore, the scale difference, induced by the imperfect description of the radial detector dimensions and the magnetic field integral, as well as the p_T -dependence of the scale, induced by energy losses between the interaction point and the MS, must be derived in detail.

The relative dimuon mass resolution, $\sigma_{m_{\mu\mu}}/m_{\mu\mu}$, for two muons with similar momentum resolution, assuming $\sigma(p_1) \approx \sigma(p_2)$, is proportional to the relative momentum resolution:

$$\frac{\sigma_{m_{\mu\mu}}}{m_{\mu\mu}} = \frac{1}{2} \frac{\sigma(p_1)}{p_1} \oplus \frac{1}{2} \frac{\sigma(p_2)}{p_2} \approx \frac{1}{\sqrt{2}} \frac{\sigma(p)}{p}. \quad (4.6)$$

Thus, the momentum dependence of the muon momentum resolution can be better understood in terms of $\sigma_{m_{\mu\mu}}/m_{\mu\mu}$, by looking at the ID and MS measurements separately. Generally, the ID measurements have a better momentum resolution than the MS. The linear rise of the ID resolution in Figure 4.8a demonstrates a non-zero r_2 term in Equation 4.5. A non-zero r_0 term corresponds to an increase of the MS resolution at low momentum in Figure 4.8b. Given Equation 4.6, a relative momentum resolution can be extracted, ranging from around 1.7% at central η and low momentum to about 4% at forward η and higher momentum.

The different correction factors for both ID and MS measurements can be obtained via a MC-driven template maximum likelihood fit [118] to compare $Z \rightarrow \mu\mu$ events in

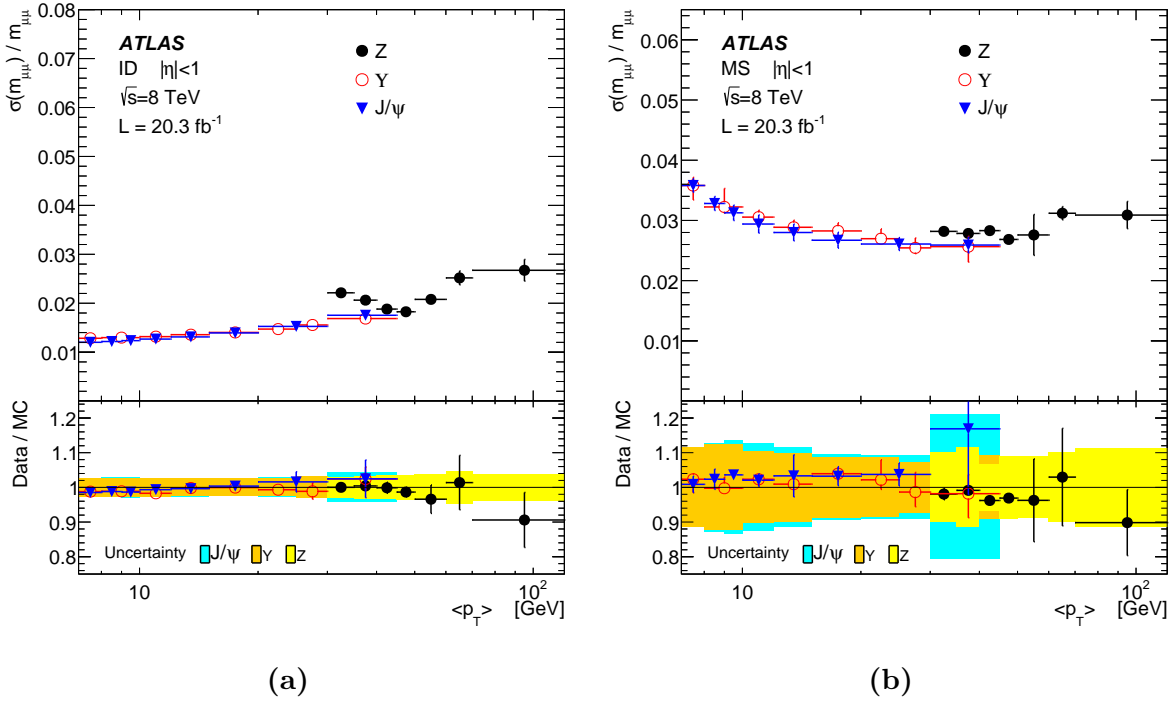


Figure 4.8.: Relative dimuon mass resolution as a function of the average transverse momentum, $\langle p_T \rangle$, for muons, from $Z \rightarrow \mu\mu$, $\Upsilon \rightarrow \mu\mu$ and $J/\psi \rightarrow \mu\mu$ events, reconstructed with only (a) the ID and (b) the MS [118].

simulation and data. A different methodology, using the muon track fit uncertainty on a muon-by-muon basis, is described in the following.

Muon momentum uncertainty corrections

Since muon momenta are determined through track fits, their corresponding uncertainty can be estimated from the shape of the χ^2 function in the vicinity of its minimum. Due to the approximate treatment of the detector alignment uncertainties in the χ^2 function, the momentum uncertainties from the track fit must be scaled to obtain the correct momentum resolution.

The curvature of the muon trajectory, measured by the tracking system, is expected to be proportional to the Gaussian pull distribution of the inverse muon momentum:

$$\frac{1}{p_{\text{reco}}} - \frac{1}{p_{\text{gen}}}, \quad (4.7)$$

$\sigma_{q/p}$

where $1/p_{\text{reco}}$ and $1/p_{\text{gen}}$ are respectively the inverse reconstructed and generator-level (after final state radiation) momenta, and $\sigma_{q/p}$ is the muon track fit uncertainty (charge over momentum ratio error). Simulation studies have shown [121, 122], the track fit underestimates $\sigma_{q/p}$ with non-Gaussian tails, originating from the Landau tails of the muon energy loss distribution in the calorimeters. One can show that $1/p_{\text{reco}}$ is to a good approximation Gaussian-distributed around the true value, $1/p_{\text{gen}}$, and a pull of width 1 can be achieved with a corrected $\sigma_{q/p}$ as the standard deviation. Hence, a *momentum scale factor* $\alpha(\eta)$ and a *resolution scale factor* $\beta(\eta)$ can be introduced to correct for p_{reco} systematic shifts with respect to p_{gen} , and any $\sigma_{q/p}$ underestimation. This yields the following response (resolution) function for muon momenta:

$$T(p_{\text{reco}}^{-1}, p_{\text{gen}}^{-1}) \equiv \frac{1}{\sqrt{2\pi}\beta(\eta)\sigma_{q/p}} \exp \left[-\frac{\left(\frac{1}{p_{\text{reco}}} - \frac{1}{\alpha(\eta)p_{\text{gen}}} \right)^2}{2(\beta(\eta)\sigma_{q/p})^2} \right]. \quad (4.8)$$

The parameters α and β can be determined from the measured dimuon spectrum in $Z \rightarrow \mu\mu$ events. As a result of an excellent momentum resolution, the invariant dimuon mass $m_{\mu\mu}$ at reconstruction level is also to a good approximation Gaussian-distributed around the dimuon mass m_{gen} at generator level. Since the mass resolution, $\sigma_{m_{\mu\mu}}$, varies according to its muons in (η, ϕ, p_T) -space, it follows a superposition of Gaussian distributions with different variances, $\sigma_{m_{\mu\mu}}^2$. If one requires that both muons fall into the same η interval, with $\sigma_{m_{\mu\mu}}$ not correlated with $m_{\mu\mu}$, a mass response function can be

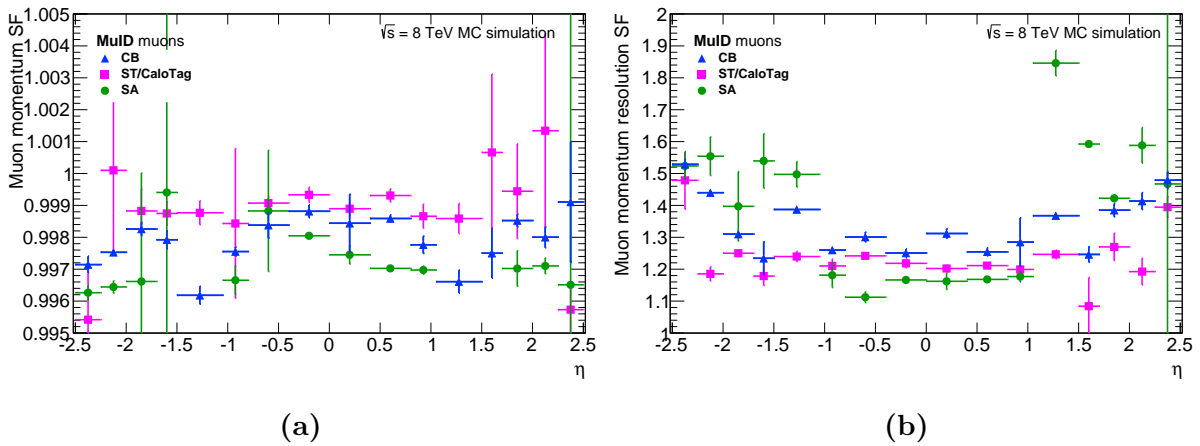


Figure 4.9.: Muon momentum scale factor α (a) and momentum resolution scale factor β (b) as a function of η .

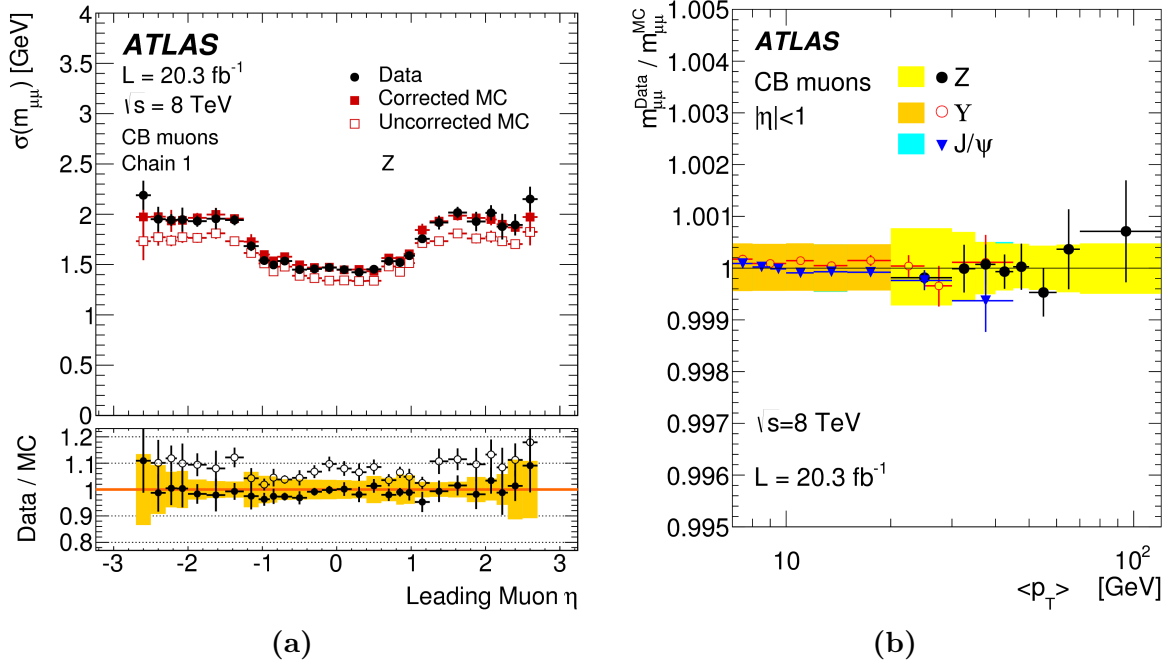


Figure 4.10.: Dimuon invariant mass resolution as a function of the leading muon η for CB muons from $Z \rightarrow \mu\mu$ events (a), and dimuon mass ratio for data and corrected MC for CB muons from $Z \rightarrow \mu\mu$, $\Upsilon \rightarrow \mu\mu$ and $J/\psi \rightarrow \mu\mu$ events (b) [118].

defined as:

$$T(m_{\mu\mu}, m_{\text{gen}}) \equiv \int_0^\infty f(\sigma_{m_{\mu\mu}}^2) \times \frac{1}{\sqrt{2\pi}\beta(\eta)\sigma_{m_{\mu\mu}}} \exp\left[-\frac{(m_{\mu\mu} - \alpha(\eta)m_{\text{gen}})^2}{2(\beta(\eta)\sigma_{m_{\mu\mu}})^2}\right] d\sigma_{m_{\mu\mu}}^2, \quad (4.9)$$

where $f(\sigma_{m_{\mu\mu}}^2)$ is the probability function of the mass variances. The momentum and resolution scale factors can be extracted through a χ^2 fit of this function to the dimuon mass spectrum at reconstruction level, measured in $Z \rightarrow \mu\mu$ events. The obtained scale factors are shown as a function of η in Figure 4.9, and are used as part of an event-level kinematic likelihood fit, discussed in Chapter 6.

The derived corrections improve the modelling⁶ of the dimuon mass resolution, as shown in Figure 4.10a, and also the ratio of the fitted dimuon mean mass for data and corrected MC shows an overall good agreement in Figure 4.10b.

⁶There are several sources of the observed data/MC discrepancy, as discussed above (see also Sections 4.1 and 3.2). For instance, uncertainties related to the detector material simulation and alignment.

4.2.3. Isolation efficiencies and scale factors

As discussed in Section 4.2.1, stringent requirements on the track- and calorimeter isolation of electrons and muons are made, as defined in Equations 4.2 and 4.3, respectively. Loose and medium leptons must have $iso_{\text{trk}} < 0.1$, while tight leptons must have both iso_{trk} and iso_{calo} less than 0.04. The efficiency of these cuts can be measured in both data and MC simulation using a *tag-and-probe* technique. Any differences in the modelling of the isolation efficiency can then be corrected by deriving corresponding scale factors. In the following, a measurement of isolation efficiencies and scale factors for tight electrons and muons is presented, using $Z \rightarrow e^+e^-$ and $Z \rightarrow \mu^+\mu^-$ resonances in 2012 LHC data and $Z + \text{jets}$ events generated with SHERPA and simulated with ATLFast-II.

Tag-and-probe algorithms

The basic idea of the tag-and-probe algorithm is to select the decay products of a well known resonance using a discriminating variable (e.g. the dilepton invariant mass), and to identify one associated *tag-lepton* of high quality to tag an interesting event and one corresponding *probe-lepton* to probe or measure the efficiency of a particular cut.

There are two algorithms: one to probe track- and calorimeter isolation for electrons in $Z \rightarrow e^+e^-$ events, and one for muons in $Z \rightarrow \mu^+\mu^-$ events. Both algorithms follow the same procedure. Firstly, any given event must have fired a single-lepton trigger with an energy/momentum threshold of at least 24 GeV (at Event Filter level; see Section 5.2) and must contain at least two loose leptons, but without requiring any criterion on isolation variables (see Table 4.2). In order for leptons to qualify as a tag or probe candidate, the following minimal criteria must be satisfied:

- reconstructed as a **VeryTightLH** electron or tight MuID muon,
- an electron $E_T > 20$ GeV or a muon $p_T > 15$ GeV,
- within $|\eta| < 2.47$ (electron) or $|\eta| < 2.5$ (muon).

In addition, the tag selection excludes any leptons in the *transition region*⁷, $1.37 < |\eta| < 1.52$, and asks for an energy/momentum larger than 25 GeV. Since previous studies indicated a bias of efficiency measurements resulting from the event trigger

⁷The transition region, $1.37 < |\eta| < 1.52$, between the barrel and end-cap sections of the EM calorimeter contains significantly material in front of the first active calorimeter layer ($5 - 10X_0$), and is not suitable for precision measurements.

pre-selection [123], the selected candidates must be matched in $\eta - \phi$ space to the fired trigger object. Furthermore, the following four systematic quality variations, based on the isolation of the tag candidate, are used:

1. no isolation requirement,
2. pass track isolation ($iso_{\text{trk}} < 0.04$) only,
3. pass calorimeter isolation ($iso_{\text{calo}} < 0.04$) only,
4. pass both track- and calorimeter isolation ($iso_{\text{trk}} < 0.04, iso_{\text{calo}} < 0.04$).

Once a tag-lepton candidate is found, a probe-lepton is matched: it must be of opposite charge and form together an invariant dilepton mass close to the Z boson pole mass, $m_Z = 91.1876 \pm 0.0021$ GeV [12], using three quality variations:

1. loose mass window of $|m_Z - m_{\ell\ell}| < 30$ GeV,
2. medium mass window of $|m_Z - m_{\ell\ell}| < 20$ GeV,
3. tight mass window of $|m_Z - m_{\ell\ell}| < 10$ GeV.

All possible permutations of tag-and-probe pairs in any given event are used for each of the $N_v \equiv 4 \times 3$ systematic quality variations (v) and finally contribute to the efficiency measurement, which is defined as

$$\varepsilon = \frac{N_{\text{probe} + \text{iso}}}{N_{\text{probe}}} \quad \text{per variation and event}, \quad (4.10)$$

where N_{probe} is the number of probe-leptons passing the basic selection criteria described above and $N_{\text{probe} + \text{iso}}$ is the number of probe-leptons that pass additionally the track- and calorimeter isolation criteria: $iso_{\text{trk}} < 0.04$ and $iso_{\text{calo}} < 0.04$. This procedure is performed for both data and MC events in order to derive scale factors, i.e.

$$\text{SF}_v = \frac{\varepsilon_{\text{data}}}{\varepsilon_{\text{MC}}}, \quad (4.11)$$

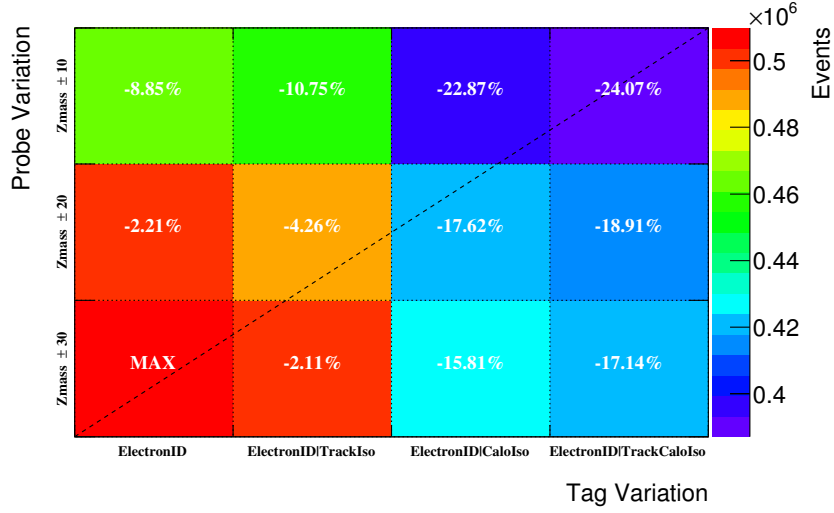


Figure 4.11.: Statistics in tag-and-probe quality variation bins for VeryTightLH electrons in data. The relative difference to the loosest selection (max) is shown.

for each variation v . These scale factors are then combined using the standard error propagation⁸:

$$\text{SF}_{\text{comb}} = N_v^{-1} \sum \text{SF}_v, \quad (4.12)$$

$$\sigma_{\text{comb}}^{\text{stat}} = N_v^{-1} \sum \sigma_{\text{SF}_v}^{\text{stat}}, \quad (4.13)$$

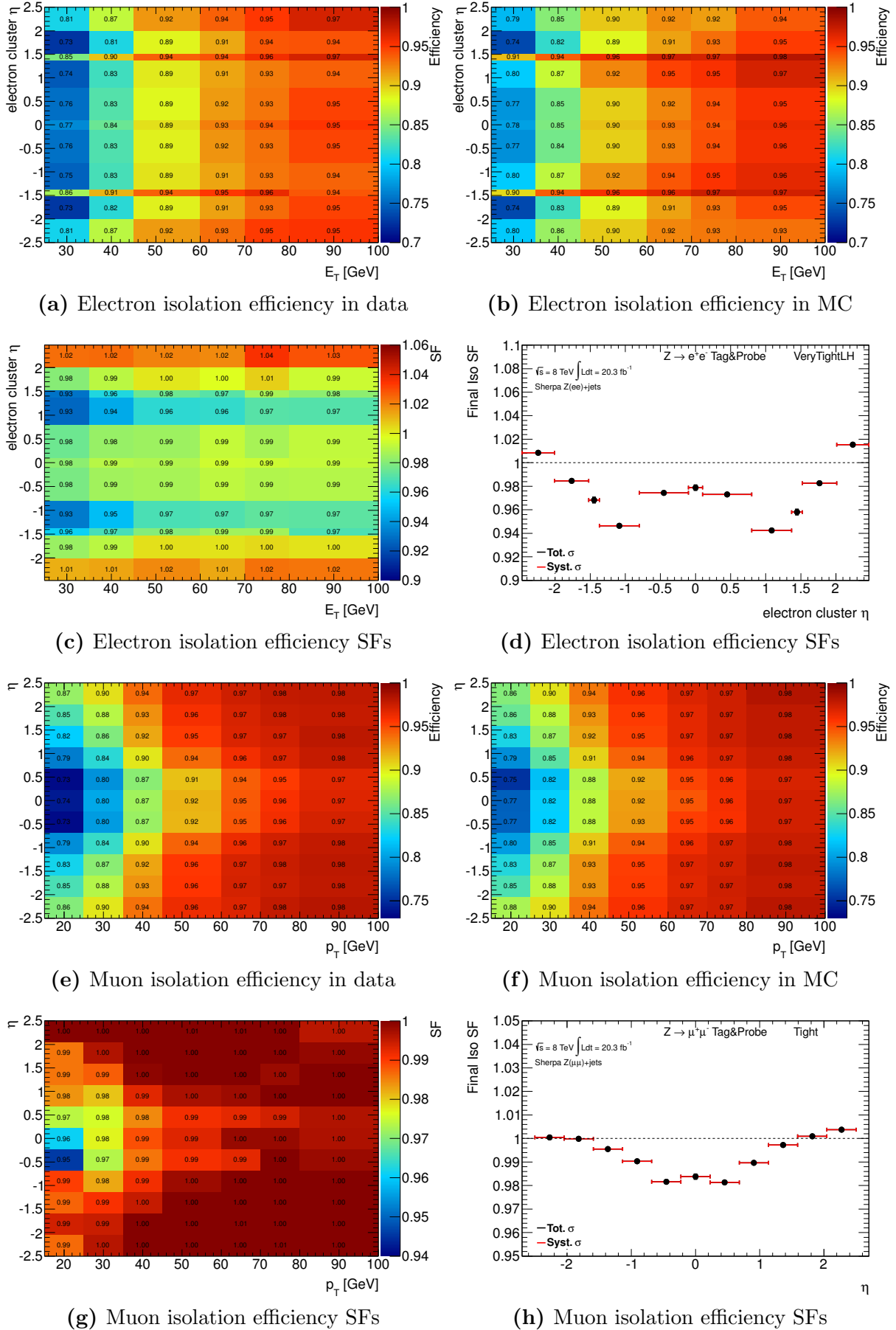
$$\sigma_{\text{comb}}^{\text{syst}} = \sqrt{N_v^{-1} \sum (\text{SF}_v - \text{SF}_{\text{comb}})^2}, \quad (4.14)$$

where SF_{comb} is the combined isolation efficiency scale factor, $\sigma_{\text{comb}}^{\text{stat}}$ is the combined statistical uncertainty and $\sigma_{\text{comb}}^{\text{syst}}$ is the estimated systematic uncertainty, as a result of the event-level tag-and-probe quality variations. The impact of the selection criteria on the resulting scale factors are expected to be dominant at low E_T (see Sections 4.1 and 3.2).

Nominal results

The nominal isolation efficiency and corresponding scale factors are measured as a function of η and E_T or p_T in 8 TeV data and Z +jets MC events using the tag-and-probe method described above. Figure 4.11 illustrates the statistics in the different variation bins, showing as expected most events in the bin with the loosest criteria (no tag isolation,

⁸This combination has been evaluated in [123, 124] and is used for tag-and-probe measurements in ATLAS.

Figure 4.12.: Lepton isolation efficiencies/SFs in 8 TeV data and Z +jets MC.

loose mass window) and least events in the bin with the tightest criteria (track- and calorimeter tag isolation, tight mass window).

The combined isolation efficiency measured in data and Z +jets MC is shown for electrons in Figures 4.12a and 4.12b, and for muons in Figures 4.12e and 4.12f. The data efficiency for both electron and muons drops down to $\sim 73\%$ at low transverse energy/momentum and central η , and rises above 90% over the entire η range for $E_T > 60$ GeV for electrons or $p_T > 45$ GeV for muons. The resulting 2D scale factor map is shown in Figure 4.12c for electrons and in Figure 4.12g for muons. The scale factors range between 0.93 – 1.03 for electrons and 0.95 – 1.00 for muons. Figures 4.12d and 4.12h show them also inclusively in energy/momentum. The 2D scale factor maps are used in the final analysis of the $WH \rightarrow \ell\nu b\bar{b}$ channel and have shown to improve the background modelling with respect to previous isolation efficiency calibrations. As discussed in Section 5.6, these scale factors contribute to the experimental systematic uncertainties.

A similar measurement has been made for VeryLooseLH electrons, probing only the efficiency of track isolation, in the $ZH \rightarrow \ell\ell b\bar{b}$ analysis. As explained in Chapter 5, this channel uses only loose and medium leptons. Since the values of the resulting scale factors are close to one, no correction needs to be applied in this channel.

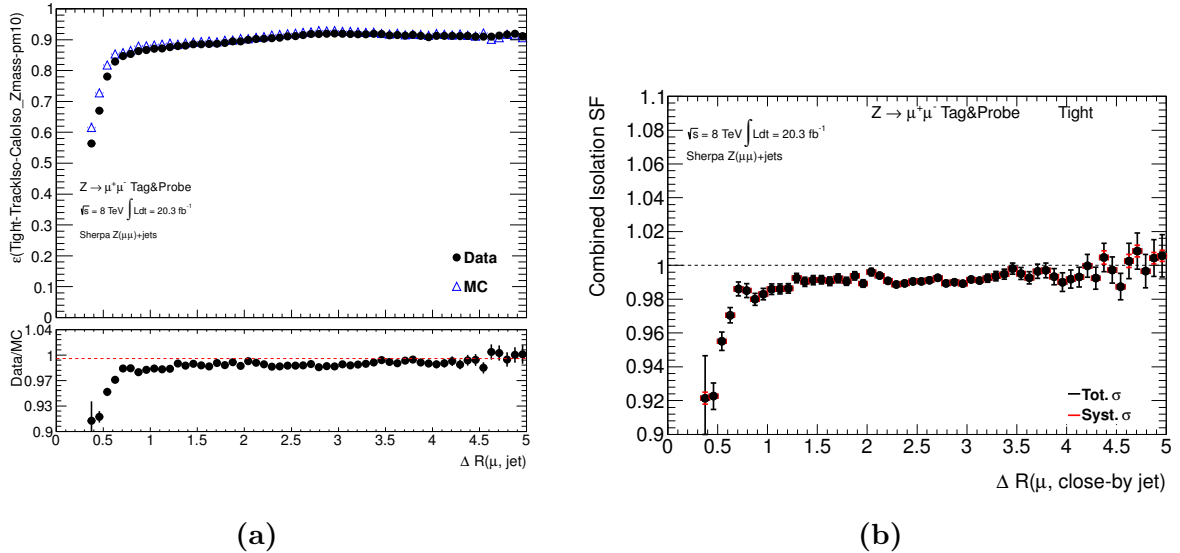


Figure 4.13.: Muon isolation efficiency in the tightest tag-and-probe variation bin (a) and combined scale factors (b) as a function of $\Delta R(\mu, \text{close-by jet})$.

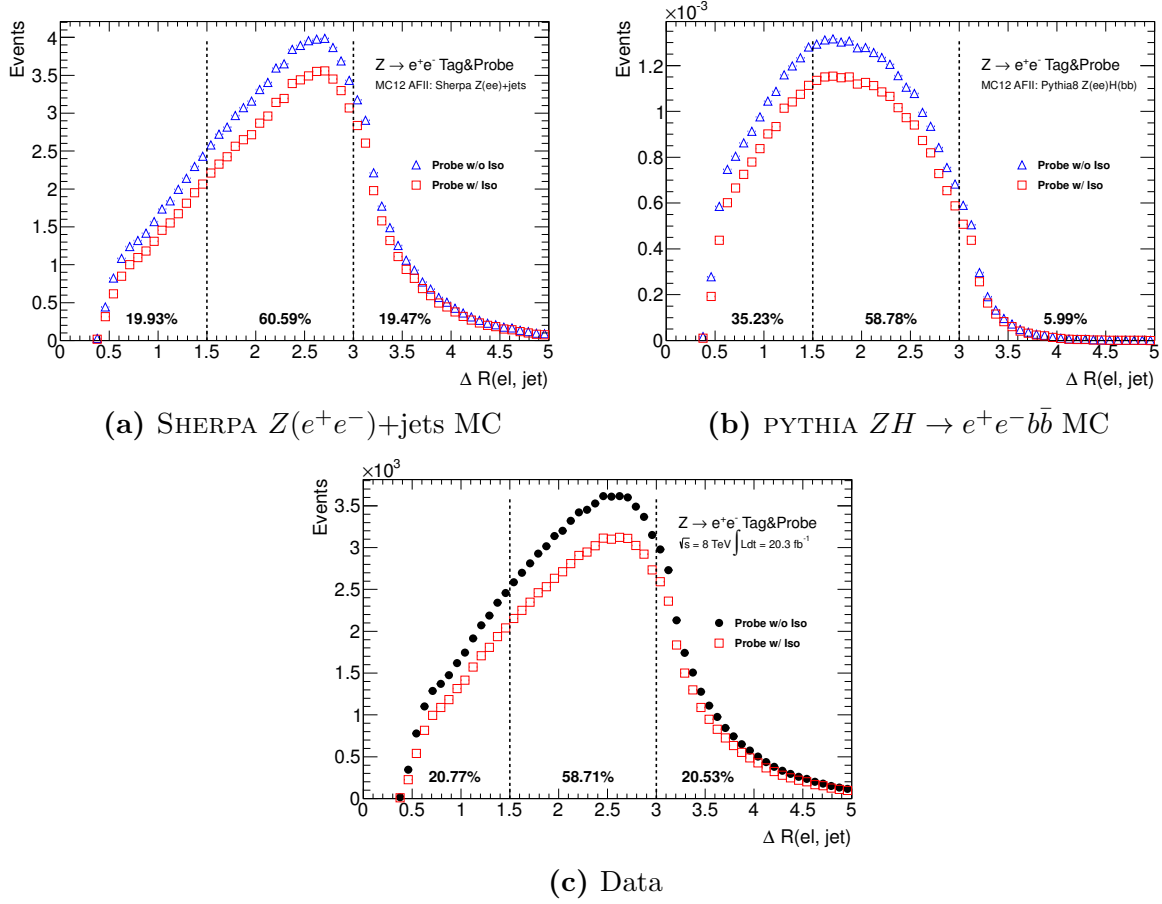


Figure 4.14.: Distribution of the ΔR between a probe-electron, with/without track- and calorimeter isolation criteria, and its nearest jet, measured in two different MC (a/b) and data (c). The relative statistics (%) in three ΔR bins is shown.

Isolation dependence on close-by jets

The dependence of the isolation efficiency can be further tested by probing leptons in the vicinity of jets. In fact, the efficiency reduces significantly with the nearby presence of jets. Figure 4.13 shows the muon isolation efficiency as a function of the ΔR between the probe-muon and its nearest jet. The efficiency decreases by about 30% when jets are closer to the probing muon. In terms of the modelling, the resulting scale factors drop by about 8%. Very similar results are found for electrons.

One finds a distinctive distribution of the ΔR between a probe-electron and its nearest jet, as shown in Figure 4.14 (a nearly identical distribution is found for probe-muons). The distribution is very similar between data and the MC simulation of the $Z(e^+e^-)+\text{jets}$ process, but is for instance quite different when compared to the MC simulation of

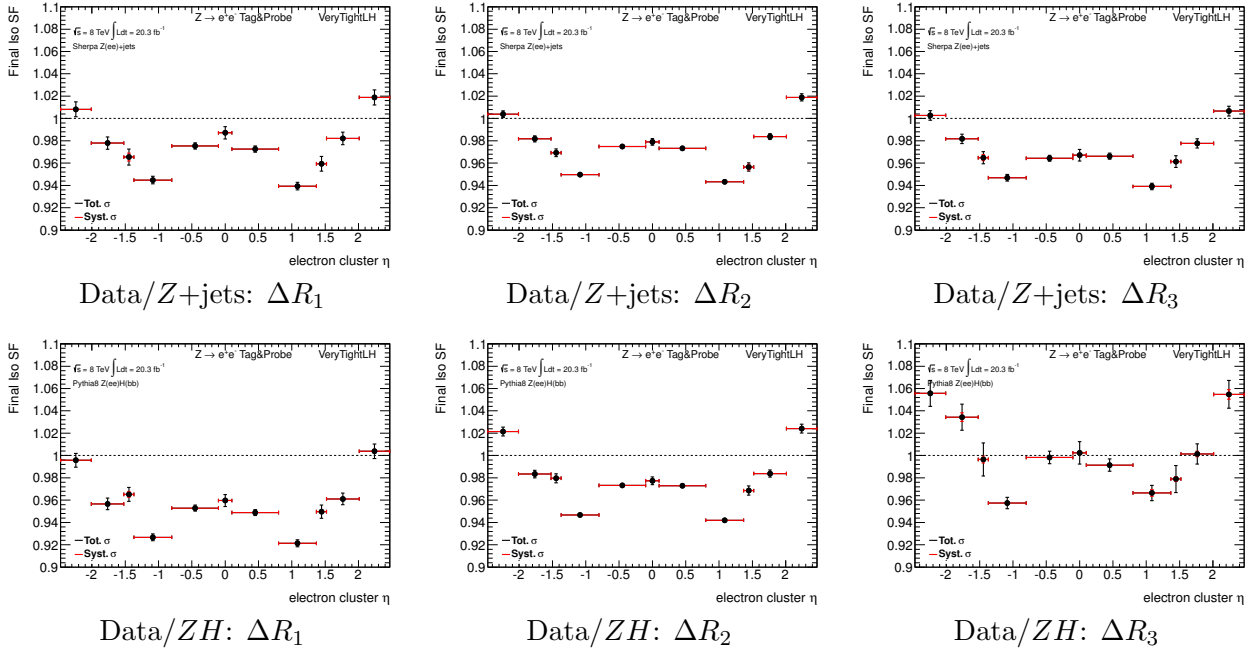


Figure 4.15.: Electron isolation scale factors as a function of η in three $\Delta R(e, \text{close-by jet})$ bins, using $Z+\text{jets}$ MC in the top row and ZH MC in the bottom row.

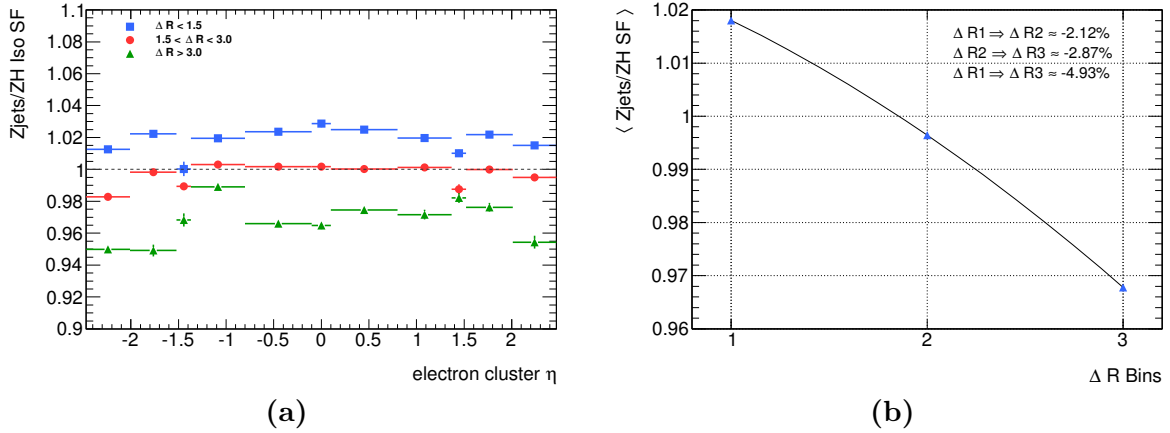


Figure 4.16.: Ratio of electron isolation efficiency scale factors using $Z+\text{jets}$ MC and ZH MC for three different $\Delta R(e, \text{close-by jet})$ regions as a function of η (a) and their total average (b).

the $ZH \rightarrow e^+e^-b\bar{b}$ process. This is expected, given the very different event kinematics between the two simulated processes. The $\Delta R(e, \text{jet})$ distribution can be divided in a close-by region ($\Delta R_1 = [0, 1.5)$), a central region ($\Delta R_2 = [1.5, 3.0)$) and a forward region ($\Delta R_3 = [3.0, \infty)$). The statistics is very similar between data and $Z+\text{jets}$ MC. Comparing the ZH simulation to data, the jet multiplicity is about 15% higher in ΔR_1 and similar in ΔR_2 , but shifted to the lower edge of this bin.

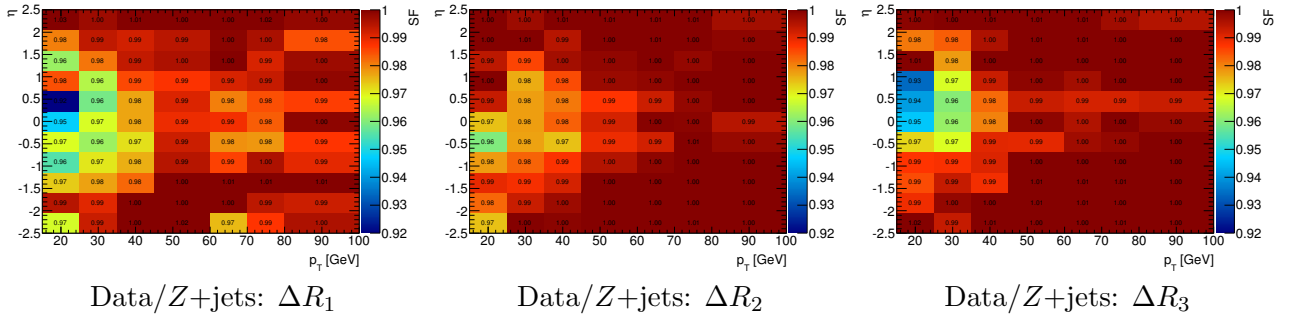


Figure 4.17.: Muon isolation scale factors as a function of η and p_T in three $\Delta R(\mu, \text{close-by jet})$ bins, using Z +jets MC.

The isolation scale factors can be derived in each ΔR bin and compared between the two simulations. These are shown, inclusively in E_T , as a function of η in Figure 4.15. When using the Z +jets MC, the scale factor distributions are similar across all ΔR bins. This is not the case when using the ZH MC, where the distribution shifts up towards higher ΔR bins.

The differences between the two simulations and their relative impact on the nominal isolation efficiency scale factors, which use Z +jets MC, can be roughly estimated with an envelope of the three ΔR variations. The ratio of the scale factors obtained with Z +jets and ZH MC is shown in Figure 4.16a as a function of η in the three ΔR regions. The

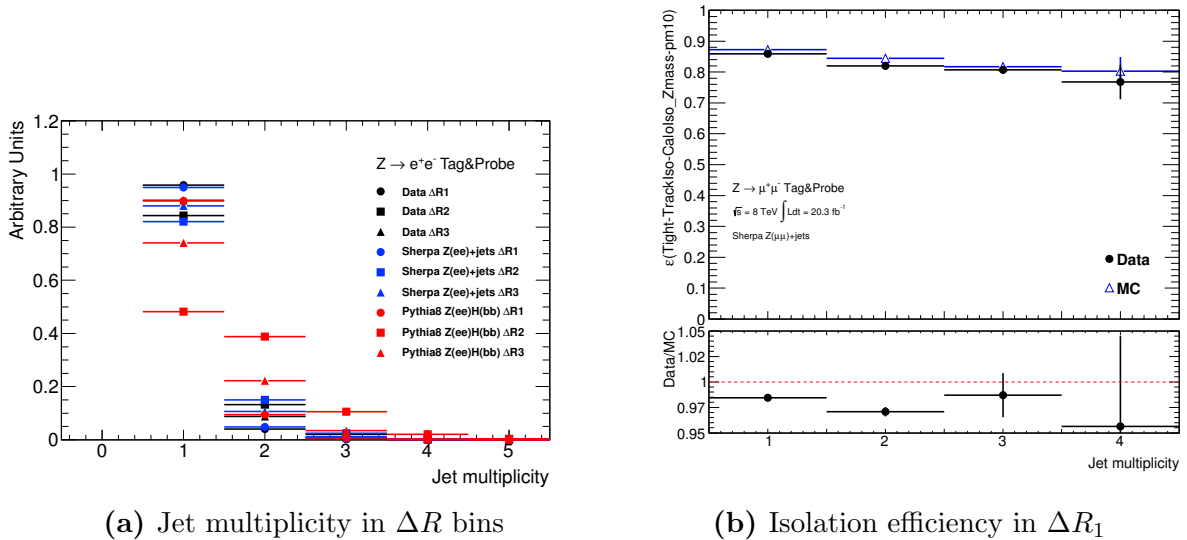


Figure 4.18.: The normalized jet multiplicity in the ΔR_1 , ΔR_2 and ΔR_3 of probe-electrons in data, $Z(e^+e^-)$ +jets and $ZH \rightarrow e^+e^-b\bar{b}$ MC (a); the isolation efficiency of probe-muons for the tightest tag-and-probe variation as a function of the jet multiplicity in the ΔR_1 bin (b).

best agreement is found at central η in the high-statistics ΔR_2 bin. The corresponding average, i.e. inclusive in η and E_T , is shown in Figure 4.16b. This reveals a total on-average scale factor variation of $\sim 4.9\%$.

Based on the top row of Figure 4.15, one may misconceive that the nominal isolation efficiency scale factors, shown in Figure 4.12, are almost insensitive to ΔR variations. However, the energy/momentum dependence has been neglected in this context. The scale factors as a function of η and p_T do indeed change under ΔR variations, as shown in Figure 4.17 for muons (similar results are found for electrons). The largest mis-modelling is seen in ΔR_1 .

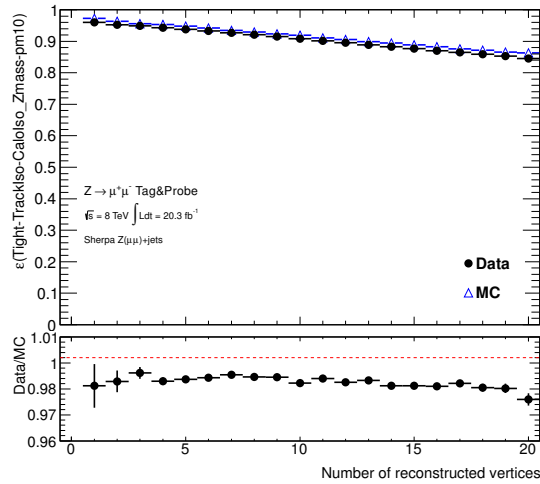
Besides the presence of *one* jet, one can probe the isolation efficiency dependence on the jet multiplicity in the different $\Delta R(\ell, \text{jet})$ regions. The jet multiplicity, normalized to unity for comparison, in each ΔR bin of a probe-electron is compared between data and simulations of $Z(e^+e^-)+\text{jets}$ and $ZH \rightarrow e^+e^-b\bar{b}$ in Figure 4.18a. The relative contributions in each bin are very similar between data and $Z+\text{jets}$ MC, while a generally higher jet multiplicity is seen in case of the ZH MC. This is equivalent to the observations shown in Figure 4.14. The isolation efficiency decreases as the number of close-by jets increases. This is shown in Figure 4.18b for probe-muons and the jet multiplicity in its close-by region, ΔR_1 , where the efficiency drops by about 8%.

Isolation dependence on the number of vertices

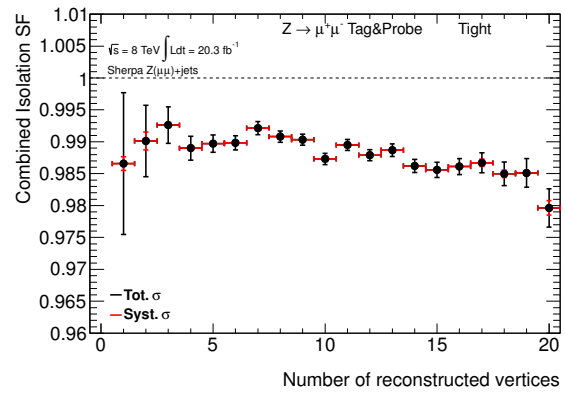
The dependence of the isolation efficiency can also be studied in terms of the number of reconstructed vertices. Figure 4.19a shows a linearly decreasing isolation efficiency as the number of vertices increases. From one to twenty vertices, the efficiency drops by about 11%, and, as Figure 4.19b shows, the combined scale factors decrease as well, i.e. the modelling degrades.

This pileup dependence can be understood by separating the track- and calorimeter criteria for the probing leptons. Figure 4.20 reveals that only the calorimeter isolation efficiency is very sensitive to pileup, while track isolation benefits from the required small impact parameter with respect to the primary vertex and thus has an efficiency nearly insensitive to pileup.

In conclusion, the isolation effects discussed in this section contribute to the systematic uncertainties, which affect the VH analysis (see Section 5.6).

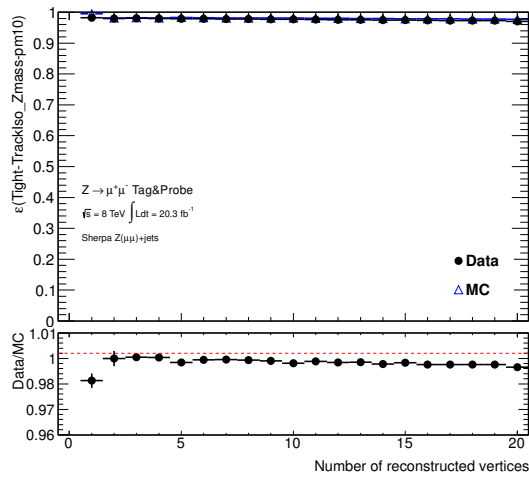


(a) Track & Calorimeter Iso. Eff.

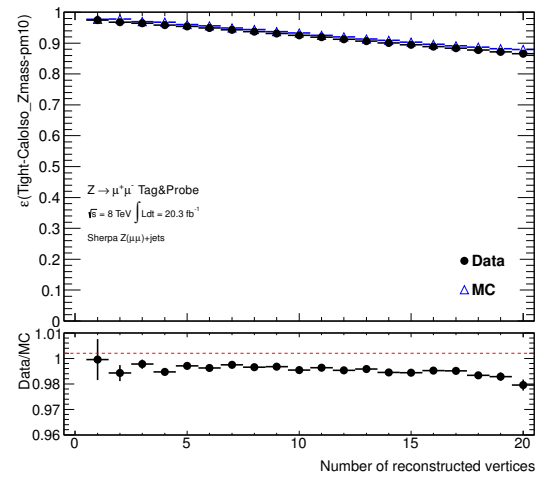


(b) Track & Calorimeter Iso. SF

Figure 4.19.: Muon isolation efficiency in the tightest tag-and-probe variation bin (a) and combined scale factors (b) as a function of the number of reconstructed vertices.



(a) Track Iso. Eff.



(b) Calorimeter Iso. Eff.

Figure 4.20.: Muon track (a) and calorimeter (b) isolation efficiency as a function of the number of reconstructed vertices.

4.3. Jets

As a result of the strong interaction (see Section 2.1.1), a quark or a gluon, produced in high-energy proton-proton collisions, almost instantly fragments and hadronises, and subsequently leads to a collimated spray of hadrons and other secondary decay products: a so-called *jet*. The definition of a jet is unavoidably ambiguous, as it requires the definition of an algorithm with a prescription for identifying and grouping its constituents. In that sense, *a jet is an algorithm*, containing a particular choice of clustering rules. This choice often depends on the particular topology of interest and the kinematic range. The ultimate goal is to map the observed final state hadrons onto their originating energetic partons. The ATLAS calorimeters are well suited for the reconstruction of jets and to extract their kinematic properties (e.g. momenta).

Topological energy clusters in the calorimeters (Section 4.3.1) serve as inputs to the jet finding algorithm (Section 4.3.2) and the resulting jet energy must be calibrated (Section 4.3.3). Furthermore, jets induced by b -quarks must be identified with a high efficiency (Section 4.3.4). In the following, an overview of these jet reconstruction steps is presented, and defines the final jet physics objects used in the VH analysis.

4.3.1. Topological energy clusters

The energy contributions of individual particles can only be approximately disentangled as a result of the finite granularity of calorimeters and interleaved dead material as well as different sources of signal noise. The calorimeter system in ATLAS has a fine segmentation with about 200 000 individual cells of various sizes. As particles traverse the calorimeters, energy is deposited in cells, both in the lateral and longitudinal directions. These energy deposits must then be grouped into clusters, i.e. referring to a single-particle-induced shower. There are mainly two types of clustering algorithms: one based on energy deposits in fixed-size calorimeter towers of 0.1×0.1 in $\Delta\eta \times \Delta\phi$ (see Section 4.2.1), and one based on the dynamic three-dimensional combination of topologically connected cells, called *topoclusters* [114]. The latter approach is chosen as the input to the jet finding algorithm, discussed in the following section, and therefore is briefly discussed here.

A topocluster is built from an energetic seeding cell and the combination of neighbouring cells in $\eta - \phi$ space, which are selected, if their energy is significantly above the expected noise from the readout electronics and pileup. The algorithm is illus-

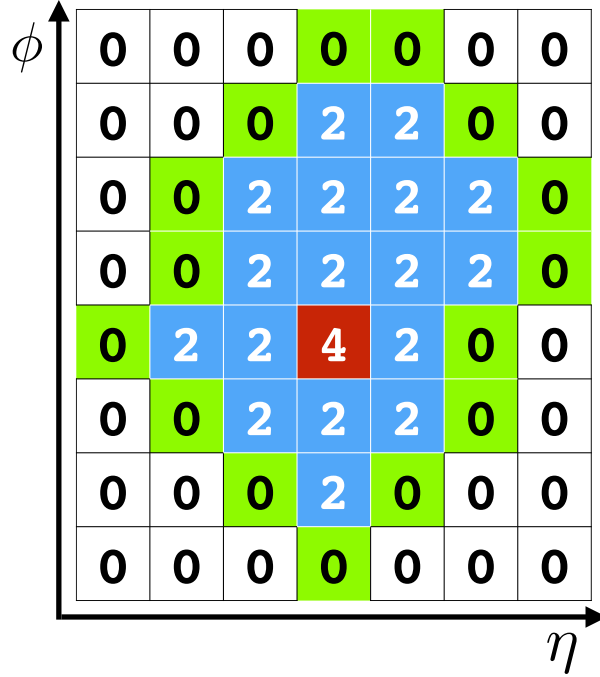


Figure 4.21.: Illustration of topological energy cluster building; the signal-to-noise ratio labels each cell. All non-white space belongs to one topocluster.

trated in Figure 4.21 and begins with identifying a seed cell with a signal-to-noise ratio, $|E_{\text{cell}}|/\sigma_{\text{cell}}|_{\text{noise}}$, above 4. The direct neighbours of the seed cell, in all three dimensions, are then added to the cluster, if their signal-to-noise ratio is above a threshold of 2. Finally, the cluster growth terminates, if a guarding ring of cells with a signal-to-noise ratio above 0 is added to the cluster. A subsequent algorithm then searches for local maxima in the 3D cluster, with energies larger than 500 MeV and larger than directly neighbouring cells. In case more than one local maximum is found, the cluster is split.

4.3.2. Reconstruction algorithm

All topoclusters found in a given event serve as input objects to a *jet finding algorithm*. There are many different jet algorithms, and the interested reader is referred to [125] for an excellent review. Generally, a jet algorithm should be:

1. defined at any order of perturbation theory,
2. insensitive to the details of the hadronization process,
3. behaving equally at the parton, hadron and detector levels.

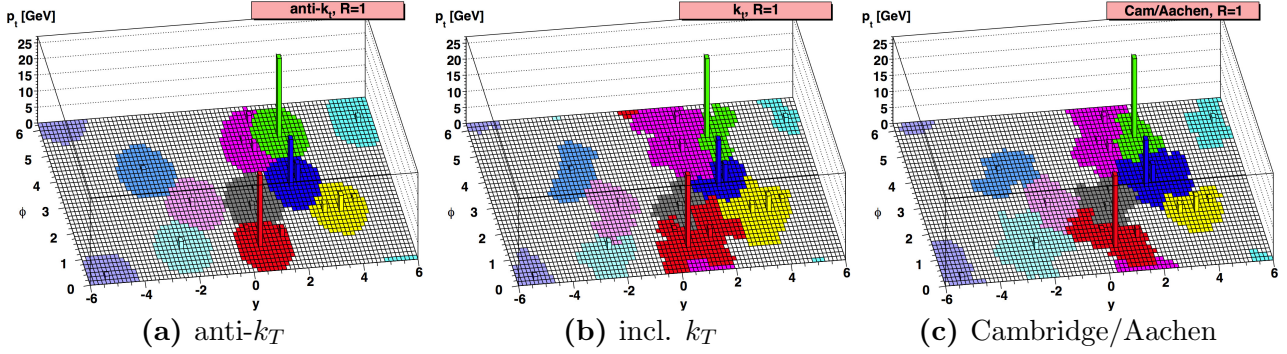


Figure 4.22.: Simulation of a parton-level event, generated with HERWIG, showing the particle clustering of different jet algorithms [125].

The second point refers to a property called infrared and collinear safety⁹. The former implies that the algorithm must be insensitive to soft radiation, and the latter implies an independence of having a fraction of p_T carried by one particle or by two collinear particles.

There are mainly two classes of algorithms: those based on geometrical (fixed) cones in $\eta - \phi$ space [126, 127], and those based on the *sequential recombination of nearby particles with respect to a certain distance measure* [128–132]. The latter approach is used for the jets defined in this thesis and is briefly discussed in the following.

All pairs (i, j) of noise-suppressed input objects, i.e. topoclusters, are evaluated in terms of their relative distance measures, d_{ij} (particle-particle) and with respect to the beam d_{iB} (particle-beam), which are defined as follows:

$$d_{ij} = \min(p_{T,i}^{2\rho}, p_{T,j}^{2\rho}) \frac{\Delta R_{ij}^2}{R^2} \quad \text{with} \quad \Delta R_{ij} = \sqrt{\Delta\eta_{ij}^2 + \Delta\phi_{ij}^2}, \quad (4.15a)$$

$$d_{iB} = p_{T,i}^{2\rho}, \quad (4.15b)$$

where R is a cone-radius parameter [133], determining the extension of the jet, and ρ is an integer number (distance scale). The particle-beam measure accounts for divergences in the QCD branching probability between initial state and final state partons. The algorithm begins by determining the minimum d_{\min} of all d_{ij} and d_{iB} in the event. If d_{\min} is among one of the d_{ij} , the objects i and j are combined into a single new object k using four-momentum¹⁰ recombination, and both i and j are removed from the input object list, while k is added to it. If d_{\min} is one of the d_{iB} , the object i is considered

⁹If one changes a given event by introducing a collinear splitting or by adding a soft-gluon emission, the collection of hard jets, determined before the event modification, should remain unchanged.

¹⁰The contravariant four-momentum, also denoted by the *four-vector*, is defined as $p^\mu = (E, p_x, p_y, p_z)$.

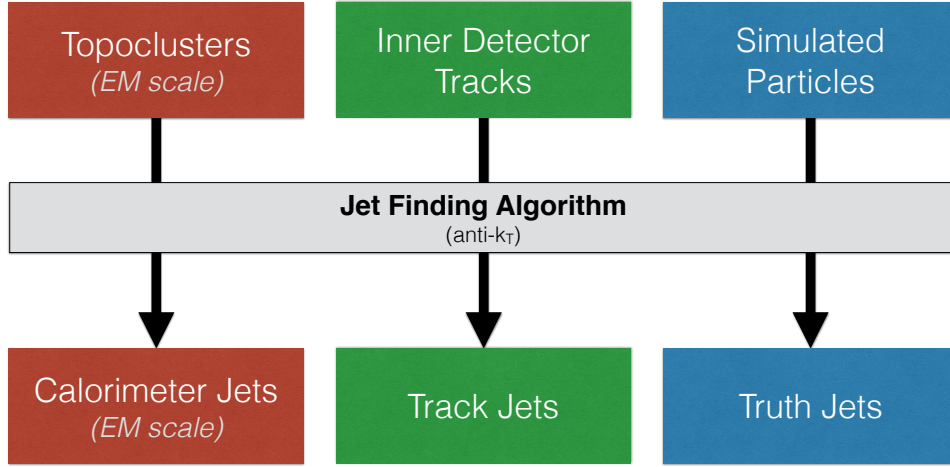


Figure 4.23.: Overview of the jet reconstruction channels used in the VH analysis

to be a jet by itself and is thus removed from the list. This procedure is carried out iteratively until all objects are removed from the list. By construction, this algorithm is infrared and collinear safe.

The parameter ρ can be chosen to obtain different algorithms with different properties, as illustrated in Figure 4.22. For $\rho = 0$, one obtains the inclusive Cambridge/Aachen algorithm [134–136], which performs the energy-independent recombination of objects close in ΔR , i.e. leading to irregularly shaped jets, and reflects the angular ordering of QCD radiation. For $\rho = 1$, one obtains the inclusive k_T algorithm [137], which starts by clustering soft (low- p_T) particles and results in irregularly shaped jets. For $\rho = -1$, one obtains the anti- k_T algorithm [138], which begins by clustering hard (high- p_T) particles and results in regularly (circular) shaped jets. The anti- k_T algorithm is currently the default jet reconstruction algorithm in ATLAS and is also used for defining jets in the VH analysis. ATLAS uses two different radius parameters, namely $R = 0.4$ and $R = 0.6$. Unless otherwise noted, all jets are based on $R = 0.4$ in this thesis.

Different jet collections can be defined based on the input to the jet finding algorithm:

- **Calorimeter jets** use topoclusters (as described above);
- **Track jets** use charged particle tracks reconstructed in the Inner Detector ($|\eta_{\text{track-jet}}| < 2.5 - R = 2.1$) and associated to the hardest primary collision vertex (PV)¹¹ [139]. As a result, their p_T is resistant to pileup effects and serves as a stable kinematic reference to match to calorimeter jets.

¹¹PVs must maximize $\sum(p_T^{\text{trk}} > 500 \text{ MeV})^2$ and have ≥ 1 Pixel hit, ≥ 6 SCT hits, $|d_0| < 1.5 \text{ mm}$ and $|z_0 \sin \theta| < 1.5 \text{ mm}$.

- **Truth jets** use stable particles (i.e. lifetime τ with $c\tau > 10$ mm [12]) generated in MC simulations. Unless otherwise noted, these jets exclude final-state muons and neutrinos. They may be used to calibrate simulated calorimeter jets.

All of these jet collections, summarized in Figure 4.23, are used in the VH analysis.

4.3.3. Jet energy calibrations

The energy of calorimeter jets is measured from associated topoclusters at the electromagnetic scale (EM), i.e. the baseline scale for the energy deposited by electromagnetic showers in the calorimeters. Due to the non-compensating nature of the ATLAS calorimeters (e/π response ratio; see Section 3.2.4), the jet energy for hadrons is typically 15-55% lower than the true energy. Besides fluctuations in the hadronic shower development and its electromagnetic content (non-uniform response), there are pileup contributions and energy losses in the dead material or cracks and out-of-cone effects. Therefore, the jet energy has to be calibrated, before jets can be used in a physics analysis.

A 5-step calibration scheme for calorimeter jets at the EM scale is implemented and aims to restore the *jet energy scale* (JES) to that of truth jets and to utilize internal jet properties to improve the jet energy resolution without changing the average calibration (GSC: global sequential calibration). This scheme, denoted by the *EM+JES+GSC calibration* and summarized in Figure 4.24, is used for jets in the VH analysis and is reviewed in the following.

Pileup suppression

The challenging pileup conditions at the LHC (see Figure 3.5a) significantly degrade the jet energy resolution. The contribution of pileup interactions is corrected using a *jet-area based technique* [140] as well as a residual correction derived from MC simulations [141, 142]. Both in-time pileup, i.e. additional proton-proton collisions in a recorded event, and



Figure 4.24.: Overview of the basic jet calibration chain used in the VH analysis

out-of-time pileup, i.e. past/future collisions influencing energy deposits in the current bunch-crossing, affect the jet energy scale. The in-time pileup activity can be characterized by the number of reconstructed primary vertices N_{PV} , and the out-of-time pileup activity can be estimated by the expected average number of interactions $\langle\mu\rangle$. The correction, p_T^{corr} , of the reconstructed jet p_T^{EM} , accounting for both in-time and out-of-time pileup signal contributions, can be defined as follows:

$$\begin{aligned} p_T^{\text{corr}} &= p_T^{\text{EM}} - \rho \cdot A_T - \frac{\partial p_T^{\text{EM}}}{\partial N_{PV}}(N_{PV} - 1) - \frac{\partial p_T^{\text{EM}}}{\partial \langle\mu\rangle} \langle\mu\rangle \\ &= p_T^{\text{EM}} - \underbrace{\rho \cdot A_T}_{\text{jet-area corr.}} - \underbrace{\alpha(N_{PV} - 1) - \beta\langle\mu\rangle}_{\text{residual corr.}}. \end{aligned} \quad (4.16)$$

The jet-area correction estimates the pileup p_T density (ρ) in the event and corrects the jet p_T^{EM} according to its area A_T [140]. It reduces the effect of global pileup fluctuations and improves the jet energy resolution. The residual correction accounts for signal threshold effects, in particular in the forward region, and out-of-time pileup effects. The η -dependent correction factors α and β are obtained by comparison to truth jets in simulated dijet events. As Figure 4.25 shows, the jet-area correction has a residual

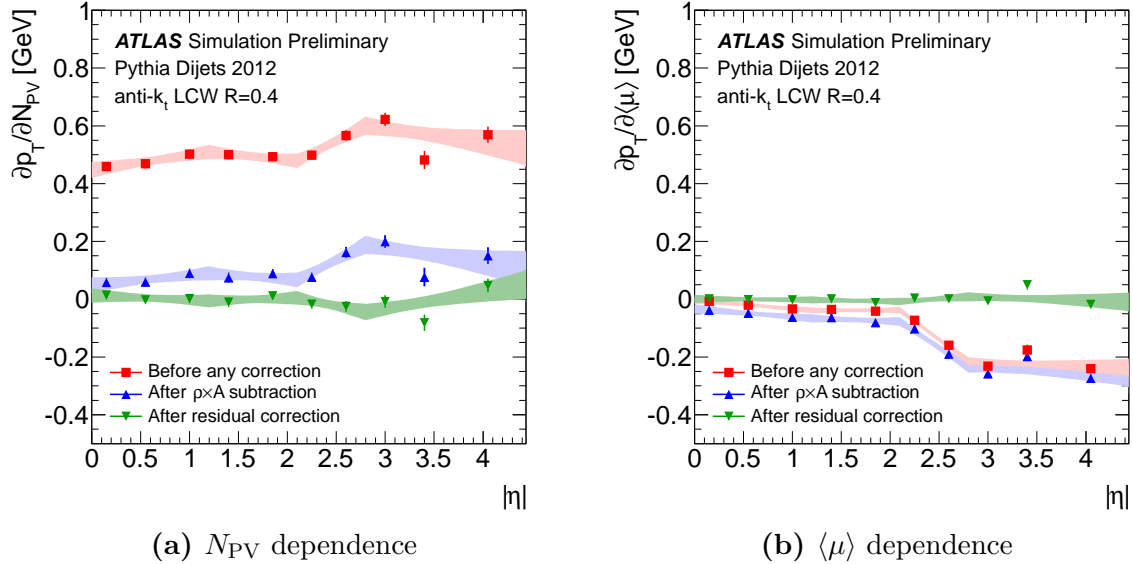


Figure 4.25.: Performance of pileup suppression techniques in terms of their effect on the sensitivity to in-time pileup, i.e. the jet p_T^{EM} dependence on N_{PV} average over all $\langle\mu\rangle$ (a), and to out-of-time pileup, i.e. the jet p_T^{EM} dependence on $\langle\mu\rangle$ averaged over all N_{PV} (b) [141].

dependence on N_{PV} at high η and has nearly no effect on the $\langle\mu\rangle$ dependence. The residual correction then removes these dependences over the entire η range.

Origin correction

The calorimeter jet direction is corrected to point back to the primary event vertex instead of the nominal centre of the ATLAS detector. This correction does not affect the jet energy.

Jet Energy Scale and Eta Calibration

The jet energy scale calibration is a MC simulation-based correction, which relates the reconstructed jet energy to the corresponding one of the matched truth jet. In other words, the average energy response,

$$\mathfrak{R}^{\text{EM}} = \frac{E_{\text{jet}}^{\text{EM}}}{E_{\text{jet}}^{\text{truth}}}, \quad (4.17)$$

is restored to unity by applying the multiplicative jet energy scale calibration, which is $1/\mathfrak{R}^{\text{EM}}$ as a function of detector η . The response is shown in Figure 4.26.

After the above energy calibration, a bias found in the η distribution with respect to the truth jets, is calibrated using an additive correction to the reconstructed η . This correction is shown in Figure 4.27.

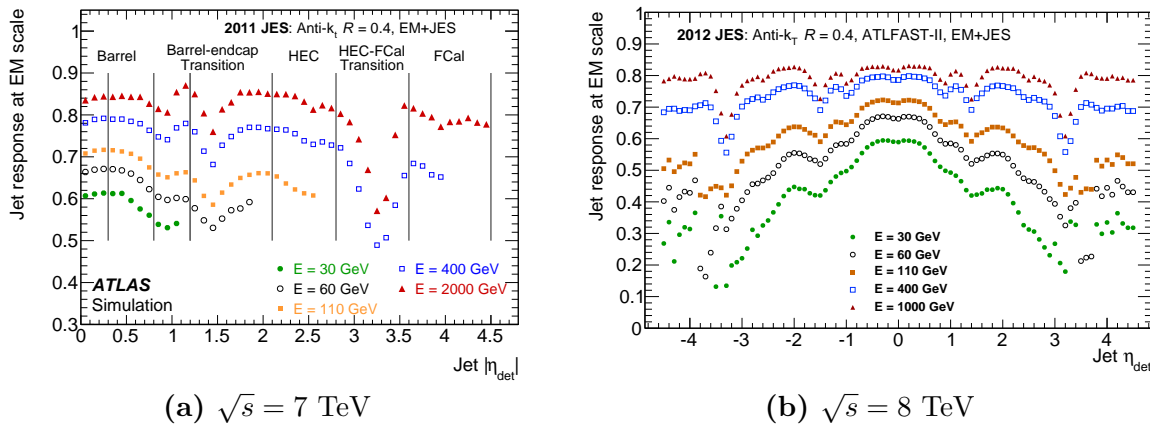


Figure 4.26.: Average jet response at the EM scale as a function of jet η for 7 TeV [143] (a) and 8 TeV (b), using each simulated dijet events.

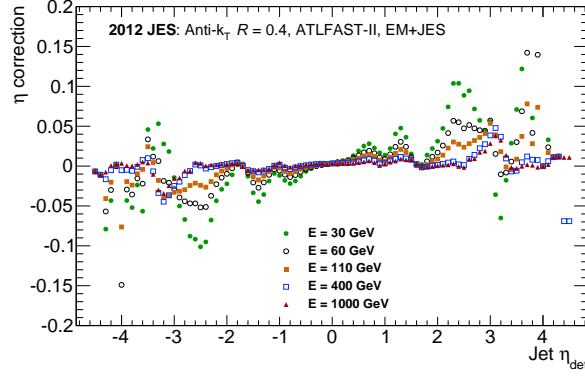


Figure 4.27.: Eta correction factors to be added to the reconstructed jet η .

Global Sequential Calibration

While the EM+JES calibration discussed above achieves an average jet response near unity, the response remains dependent on the non-trivial details of the fragmentation and showering properties of the jet and translates into a correlation to the particular flavour of the parton inducing the jet [144]. This correlation leads to a degraded jet energy resolution and contributes to the jet energy scale uncertainty in an analysis, which employs a different event selection than the one used to derive the JES correction. The effect is most pronounced when comparing the response to jets induced by light quarks (u - and d -quarks) and by gluons [145, 146]. This arises from their different characteristics: Gluon-induced jets tend to contain more particles, which generally have a lower p_T than those originating from light quarks. Moreover, their angular energy profile is wider before interacting with the ATLAS detector, and thus, the core of gluon jets has typically a lower energy density when compared to light-quark jets. This effect is particularly exacerbated by the magnetic field of the Inner Detector, which bends low- p_T charged particles more than those with a higher p_T . Since the higher- p_T particles in light-quark jets are more likely to penetrate further into the calorimeter system, more of those will be reaching the hadronic calorimeter layers. When considering the calorimeter response to soft particles and topological clustering and noise threshold effects, one can expect a lower response to gluon jets than to light-quark jets. The difference in calorimeter response between EM+JES calibrated light-quark (q) and gluon (g) jets, $\mathfrak{R}_q - \mathfrak{R}_g$, is shown in Figure 4.28a. The response difference reaches up to 8% at low p_T and reduces down to about 2% at high p_T . This has a direct impact on analyses, where the exact flavour composition in a particular sample is not well known. For instance, a JES uncertainty can be extracted from Figure 4.28a, assuming the flavour composition in a given sample is known within

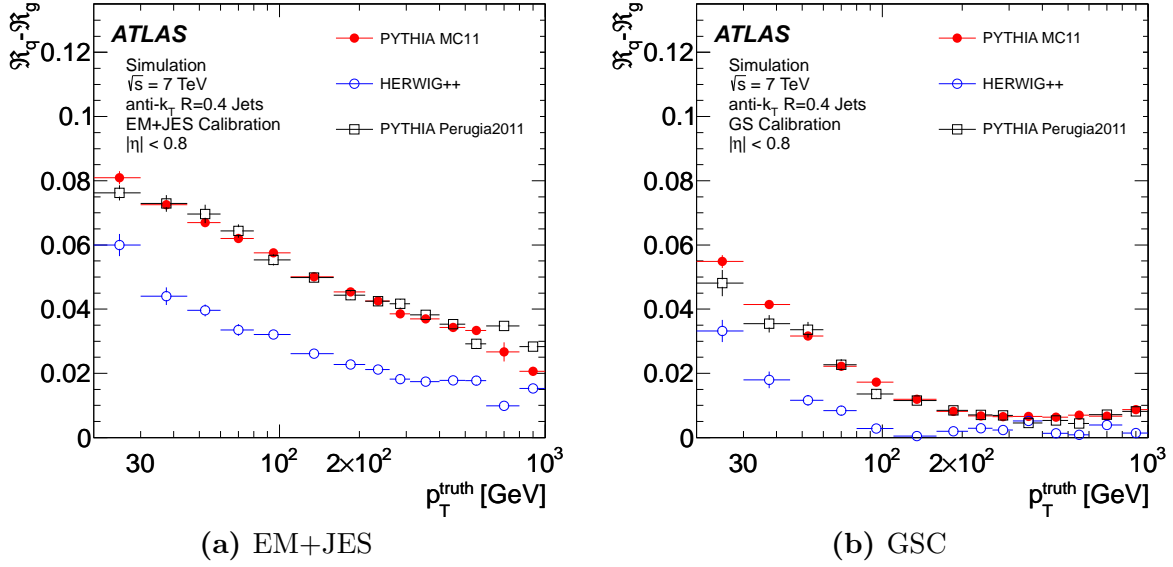


Figure 4.28.: Jet response difference of light-quark and gluon-induced jets as a function of the truth jet p_T for two different calibration schemes: the EM+JES calibration (a) and the GSC (b) [143].

25% and the MC modelling of the data is established. One finds this uncertainty to be about 2% at low p_T and about 0.5% at high p_T . However, a more sophisticated calibration scheme can be derived by utilizing different internal jet properties, such as the *Global Sequential Calibration* (GSC), which, as Figure 4.28b shows, significantly reduces the response differences.

The GSC is applied on top of the EM+JES calibration and aims to not only reduce the sensitivity to jet flavours, but also to improve the jet energy resolution without changing the average jet energy scale. The calibration exploits the longitudinal and transverse structure of the calorimeter shower associated to a jet, in order to compensate sequentially for fluctuations in the jet energy measurement. The technique is illustrated in Figure 4.29. The average jet response is parameterised as a function of the reconstructed jet p_T^{reco} and an observable χ (see definitions further below), which characterizes a particular property of a jet: $\mathcal{R}(p_T^{\text{reco}}, \chi)$. The response dependence on χ is determined from MC simulations in different regions of η and is then used to correct p_T^{reco} based a jet's particular value of χ : $p_T^{\text{corr}} = p_T^{\text{reco}} \times \mathcal{R}^{-1}(p_T^{\text{reco}}, \chi)$. This correction is applied sequentially for different jet properties of each jet in the event. While, before the correction, different jets with different values of χ also have different average responses, after the correction, the average response dependence on χ is removed and the average response is one. This results in

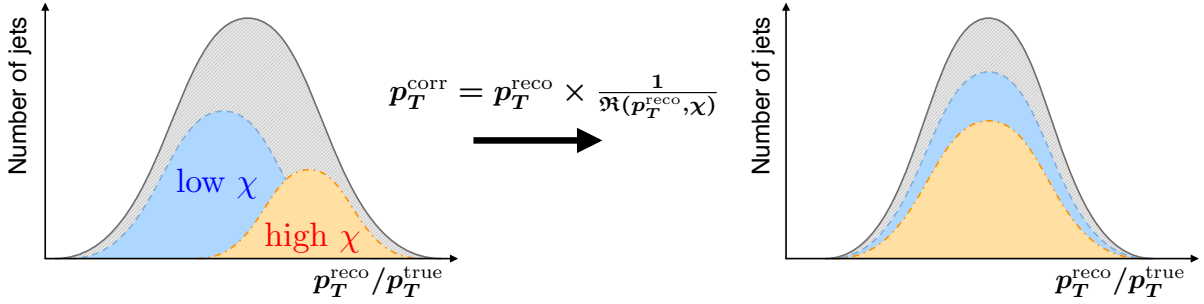


Figure 4.29.: Illustration of the technique adopted by the Global Sequential Calibration. The response is Gaussian distributed, if the truth jet p_T and the jet property χ is fixed. If the average jet response $\mathfrak{R}(p_T^{\text{reco}}, \chi)$ depends on χ , a correction p_T^{corr} as a function of χ is derived to shift¹² the average response for a fixed χ to unity, and as a result the width of the energy response distribution is reduced with the same mean.

more jets have a response closer to unity and therefore leads to an improved relative jet energy resolution. In this procedure, the mean jet energy is left unchanged.

The choice of global jet properties used in the GSC is made to exploit characteristic topologies of the energy deposits, using both track and calorimeter observables, which are utilized sequentially:

1. fraction of the jet energy deposited in the first layer of the hadronic Tile calorimeter,
2. fraction of the jet energy deposited in the third layer of the EM LAr calorimeter,
3. number of tracks with $p_T^{\text{trk}} > 500$ MeV associated to the jet,
4. track width of the jet, defined as

$$\text{track width} = \frac{\sum_{\text{trk}} p_T^{\text{trk}} \times \Delta R(\text{jet}, \text{trk})}{\sum_{\text{trk}} p_T^{\text{trk}}}, \quad (4.18)$$

5. number of segments behind the jet in the muon chambers.

The calorimeter based observables, (1) and (2), characterize in particular the longitudinal structure of the jet and improve the resolution of EM+JES jets. The track based observables, (3) and (4), reduce the jet flavour dependence. Finally, (5) accounts for energy losses for "punch-through" jets, reaching beyond the hadronic calorimeter.

¹²Before the correction, there may be a "low χ " average response distribution, e.g. with a mean below unity, and for the same property, a "high χ " average response distribution, e.g. with a mean above unity. After corrected jets contributing to the two distributions, both should have a mean at unity.

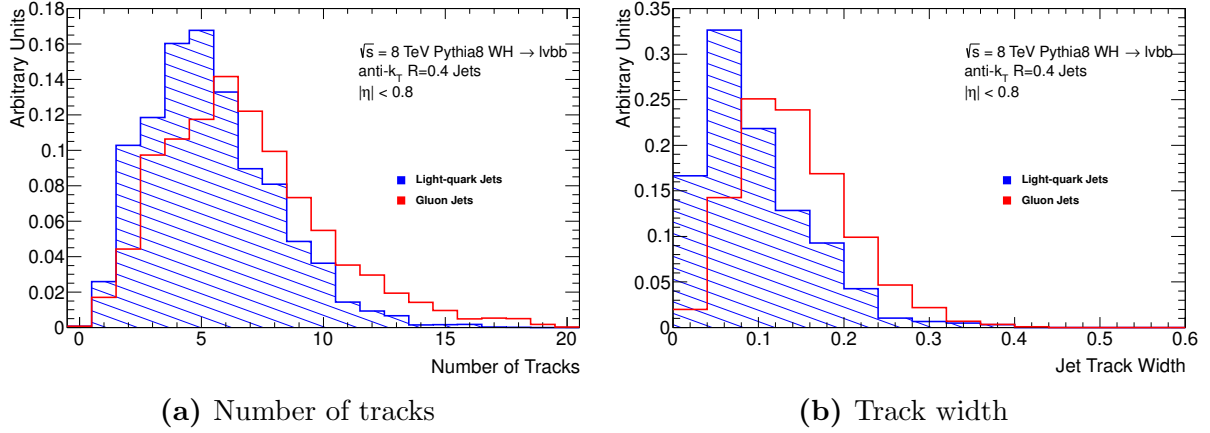


Figure 4.30.: Inclusive number of associated tracks (a) and track width (b) of light-quark and gluon-induced jets with $|\eta| < 0.8$ in 8 TeV simulated $WH \rightarrow \ell\nu b\bar{b}$ events.

The jet flavour discriminating power in the GSC arises only from (3) and (4), and has been only implemented for light-quark and gluon-induced jets. As previously discussed and shown in Figure 4.30, gluon jets have more associated tracks and a broader track width. A nice separation between the two flavours can be seen in Figure 4.31, showing their corresponding average number of tracks $\langle n_{\text{trk}} \rangle$ and average track width as a function of the reconstructed jet p_T^{reco} . Additionally, b -quark induced jets are shown, which are not part of the GSC. In terms of $\langle n_{\text{trk}} \rangle$, a better flavour separation is found at higher p_T^{reco} ,

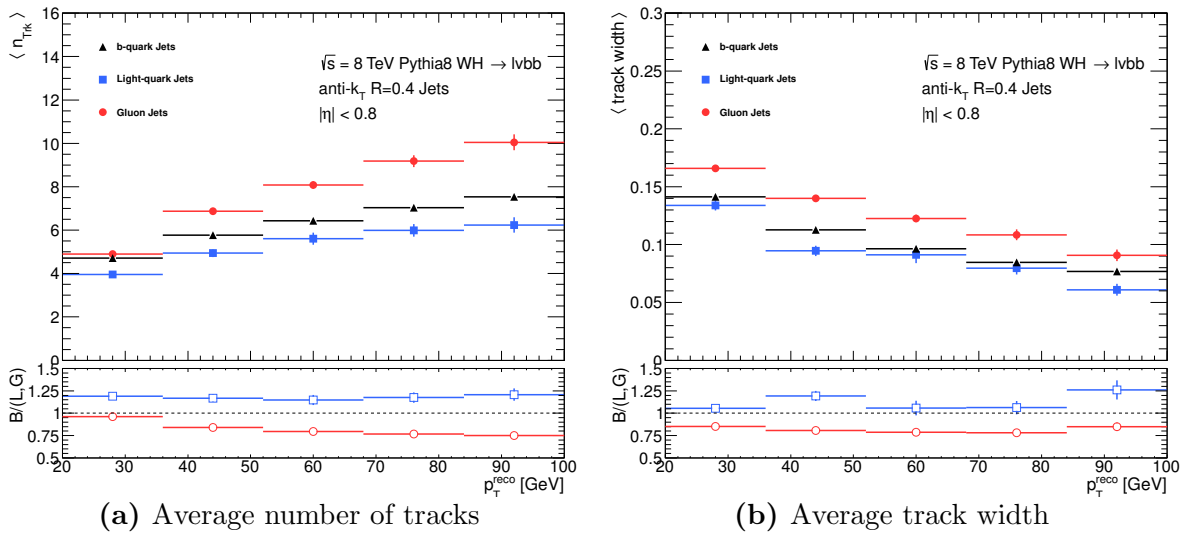


Figure 4.31.: Average number of associated tracks (a) and track width (b) of light-quark and gluon-induced jets as a function of the reconstructed jet p_T^{reco} for jets with $|\eta| < 0.8$ in 8 TeV simulated $WH \rightarrow \ell\nu b\bar{b}$ events. The ratio $B/(L,G)$ refers to b -quark jets (B) and light-quark (L) or gluon (G) jets.

and in this region, the ratio of b -quark induced jets to those induced by light-quarks or gluons indicates a separation of about 20-25%.

Residual in-situ calibration

Residual data-to-MC differences are assessed using in-situ calibration techniques, where the p_T balance between the to-be-calibrated jets and well-measured reference objects (photons, Z bosons or other jets) is measured:

$$\frac{\langle p_T^{\text{jet}}/p_T^{\text{ref}} \rangle_{\text{data}}}{\langle p_T^{\text{jet}}/p_T^{\text{ref}} \rangle_{\text{MC}}}. \quad (4.19)$$

This ratio is measured in dijet, Z +jet, γ +jet or multijet events and is applied to jets reconstructed in data [143].

In the 8 TeV dataset, an overall good agreement between data and MC simulation was found. The total jet energy scale uncertainty, derived by the in-situ calibration, is about 4% at low p_T^{jet} and decreases to about 1% at $p_T^{\text{jet}} > 100$ GeV.

Further energy corrections

A number of VH analysis specific jet energy corrections are derived after the event selections, as defined in Section 5.3. These corrections aim at improve the reconstructed dijet invariant mass resolution of $H \rightarrow b\bar{b}$ candidates. This includes a *semileptonic correction* (Section 5.4.3) accounting for muons reconstructed inside jets, a jet p_T^{reco} *resolution correction* (Section 5.4.4) to account for biases in the jet response due to resolution and scale effects obtained from VH signal MC events, and finally an *event-level kinematic likelihood fit* (Chapter 6) to improve the measurement of the jet kinematics in the $ZH \rightarrow \ell\ell b\bar{b}$ channel.

4.3.4. Identification of b -quark induced jets

The identification of jets originating from b -quark fragmentation, also denoted by b -tagging, is performed through an algorithm that exploits several unique properties of the hadronization process of b -quarks and aims to distinguish them from jets originating from light-quarks (u, d, s), gluons and c -quarks with a high efficiency. In the Standard

Model, b -quarks, once produced, form b -flavoured hadrons (given the flavour-blindness of the strong interaction) before undergoing a weak decay. The heaviest of all quarks, the t -quark, which decays only weakly, and according to $|V_{tb}| \approx 1$ in the CKM-matrix [30, 31], decays almost 100% to a b -quark and a W boson.

The b -quark fragments either directly into a ground state b -hadron ($\approx 13\%$) or into an excited b -hadron ($\approx 87\%$), such as a B^* or B^{**} , which instantly interacts strongly or electromagnetically and decays to a ground state b -hadron along with other particles. Since the displacement of the B^* or B^{**} decay vertices is experimentally not distinguishable from the primary decay vertex, only the final transition from the ground state b -hadrons is of interest. In this process, primarily B -mesons are produced. At $\sqrt{s} = 7$ TeV, the LHCb experiment measured $0.134 \pm 0.004^{+0.011}_{-0.010}$ for the ratio of \bar{B}_s to B^- and \bar{B}^0 meson production fractions and ~ 0.404 (p_T -dependent) for the ratio of Λ_b^0 baryon to B^- and \bar{B}^0 meson production fractions [147]. As part of this transition, most of the quark's energy is passed onto the final b -hadron, e.g. $\approx 70\%$ on average for b -quarks with a $p_T \approx 45$ GeV [148]. Generally, one finds that the fragmentation functions for b -quarks are harder, i.e. with a larger energy transfer, than those for light-quarks or c -quarks. This is particularly useful for b -tagging purposes.

The produced b -hadrons have a relatively large mass ($m_B \approx 5.28$ GeV), decay weakly with an average lifetime of (1.568 ± 0.009) ps and, with a relativistic boost, travel a distance at the level of millimetres [12], which is sufficient to be reconstructed by the ATLAS detector. This decay length (L_{xy}) would be for a momentum of 50 GeV about 3 mm. As illustrated in Figure 4.32, this results in a significantly displaced vertex, a secondary vertex (SV), with respect to the primary vertex (PV), and a significantly large decay angle of the b -hadron decay products with respect to the flight direction of the b -hadron (large impact parameter d_0).

Since $|V_{cb}|^2$ is significantly larger than $|V_{ub}|^2$ [30, 31], b -hadrons prefer to decay into c -hadrons along with other particles ($b \rightarrow c + X$). The c -hadrons, produced in the final states of e.g. $B \rightarrow (D^\pm, D^0, \bar{D}^0, D_s^\pm) + X$ decay modes, have a lifetime not much lower than b -hadrons, e.g. D^\pm -mesons have $\tau = (1.040 \pm 0.007)$ ps [12]. Thus a third vertex, a tertiary vertex (TV), which is displaced from both PV and SV, can be used for b -tagging purposes.

Furthermore, the presence of leptons in semileptonic b -hadron ($b \rightarrow \ell$) and subsequent c -hadron ($b \rightarrow c \rightarrow \ell$) decays can be exploited in b -tagging algorithms. The corresponding branching fractions are about 11% and 10% for $b \rightarrow \ell$ and $c \rightarrow \ell$ decays respectively,

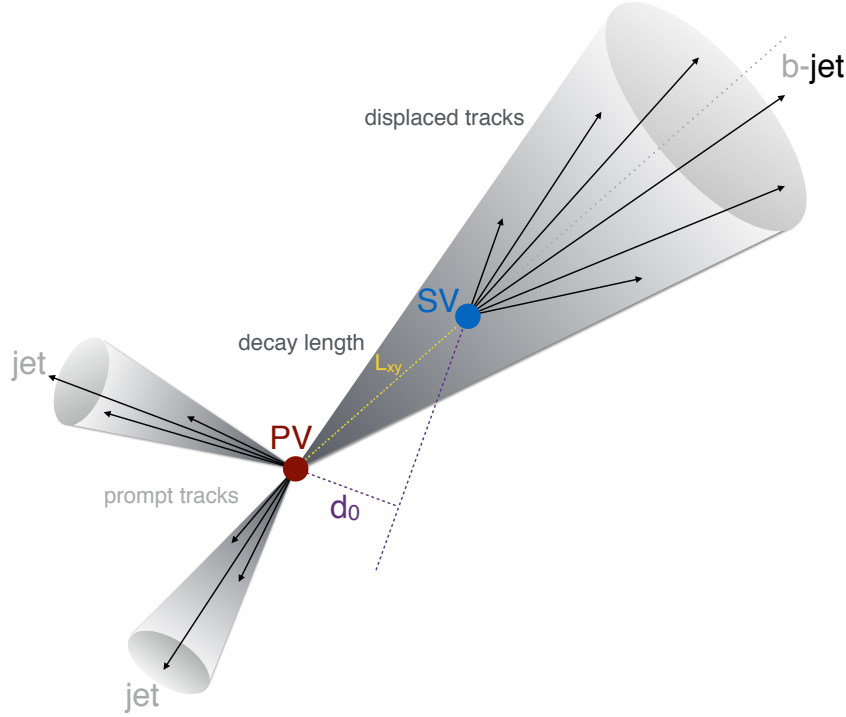


Figure 4.32.: Simplified illustration of the b -quark fragmentation, showing a displaced secondary vertex after a characteristic travelled distance L_{xy} , resulting in a large impact parameter d_0 .

where ℓ may either an electron or a muon (thus about 42% in total) [12]. The produced lepton will then have a $\langle p_T \rangle$ comparable to the mass of its parent b - or c -hadron. This means, one can search for a muon or an electron matched to a jet, require a significantly large p_T with respect to the axis of the jet, and combine other characteristics mentioned above, to tag a jet as a b -jet. This way, one can achieve a good rejection against light-quark jets faking b -jets, since in their case, leptons are mainly expected from in-flight charged pion and kaon decays, from Dalitz decays of neutral pions as well as from photon conversions and misidentified leptons.

ATLAS employs a series of algorithms to identify b -jets [149]. They are mainly based on the B -hadron properties mentioned above. In summary, these are:

- displaced secondary vertex with a significant decay length L_{xy} ,
- large B -hadron mass,
- large impact parameter d_0 ,
- semileptonic e/μ decay of the B -hadron.

Operating point	w value	b -jet eff. (%)	c -jet RF	τ -jet RF	l -jet RF
80 Loose (L)	0.4050	79.85	3.04	6.40	29.12
70 Medium (M)	0.7028	70.00	5.34	14.90	135.76
60 -	0.8353	59.99	10.45	33.92	453.53
50 Tight (T)	0.9237	49.99	26.22	120.33	1388.28

Table 4.3.: MV1c b -tagging operating points with their discriminating weight (w), b -jet efficiency and c -jet, τ -jet and light-quark (l) jet rejection factors (RF) [152].

The ATLAS MV1 b -tagging algorithm [149–151] combines¹³ in a neural network the information from an algorithm based on the track impact-parameter significance, an inclusive secondary vertex finder, and a $b \rightarrow c$ decay chain fit into a single discriminant w , ranging from 0 to 1. Jets with a large value of w are more likely to be a b -jet. In the

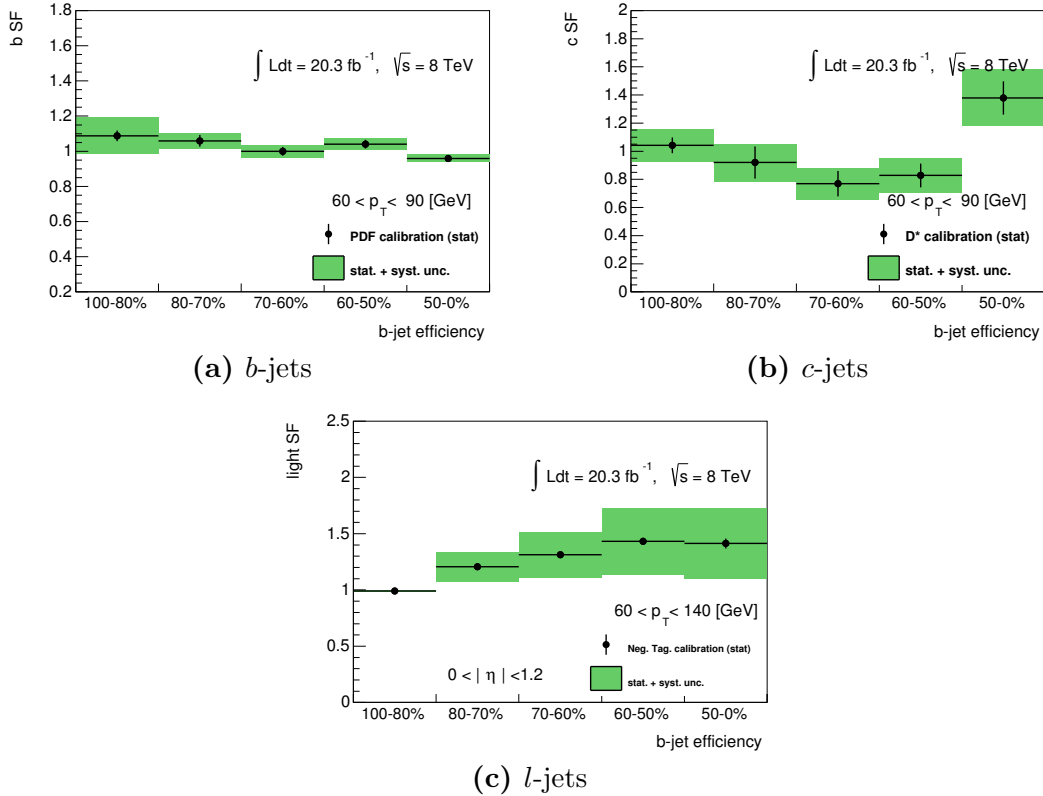


Figure 4.33.: MC-to-data calibration scale factors for b -jet (a), c -jet (b) and light-quark (l) jet (c) MV1c efficiencies in a representative jet p_T bin, $60 < p_T < 90$ GeV. The error bars are statistical uncertainties and the green error bands include systematic uncertainties as well [153].

VH analysis presented in this thesis, the *MV1c algorithm* is used, which is an improved version of MV1 with a higher c -jet rejection.

A continuous or pseudo-continuous b -tagging calibration scheme [153] is adopted, in which one can apply a lower and upper cut on w . This allows to derive different b -tagging quality criteria or *operating points*. As summarized in Table 4.3, the VH analysis uses four operating points with different average b -tagging efficiencies, 80%, 70%, 60% and 50%, and with different rejection factors for c -jets, τ -jets and light-quark jets. The 80%, 70% and 50% operating points are denoted *loose*, *medium* and *tight*, respectively. These operating points are inclusive, meaning a jet satisfying the tight criteria also satisfies the loose criteria. However, they can also be used exclusively, for instance, one can select jets, which satisfy the loose but not tight criteria. This allows to define in the analysis different regions of sensitivity. In order for the b -tagging efficiency obtained in MC simulation to match data, the distribution of w must be calibrated as a function of jet p_T , and in the case of light-quark jets, also $|\eta|$. A combinatorial likelihood method, described in [154], is used to calibrate the b -jet, c -jet and light-quark jet efficiencies in dedicated event samples such as $t\bar{t}$ [155, 156], D^* [157] and dijet [158] events, respectively. The corresponding efficiency scale factors in representative jet p_T bins are shown in Figure 4.33. Since these scale factors are dependent on the particular MC generator used for their derivation, additional MC-to-MC scale factors are used to account for any differences in e.g. the production of heavy-flavour hadrons and their decays.

4.4. Missing Transverse Momentum

The *missing transverse momentum* in a given collision event is defined as the momentum imbalance in the transverse plane (x, y), in which the conservation of momentum is expected [159, 160]. This imbalance indicates the presence of particles that are not visible to the detector and particularly in the context of the $ZH \rightarrow \nu\nu b\bar{b}$ and $WH \rightarrow \ell\nu b\bar{b}$ analyses refers to *neutrinos*¹⁴. In general, missing energy can only be measured in the transverse plane, given that the incoming protons' longitudinal momenta contain an unknown fraction, which escapes the detector after the hard scattering through proton remnants bypassing the acceptance.

¹³The output weight of different algorithms is used, namely the IP3D, SV1 and JETFITTER [149].

¹⁴The missing transverse momentum is a key signature for searches beyond the Standard Model, and e.g. may indicate the presence of stable, weakly-interacting supersymmetric particles.

4.4.1. Reconstruction principle

The missing transverse momentum vector $\mathbf{E}_T^{\text{miss}}$ (its magnitude is denoted by E_T^{miss}) is measured as the negative vector sum of the transverse momenta associated with topological energy clusters in the calorimeters with $|\eta| < 4.9$. The energy of these clusters is calibrated according to the associated reconstructed object in the event, such as jets, electrons, τ leptons, and photons. This also includes muons, for which the energy deposits in the calorimeters are removed to avoid double counting. The reconstruction and calibration of $\mathbf{E}_T^{\text{miss}}$ is rather complex, since an excellent knowledge of all detector effects is required in order to minimize the impact of the limited acceptance, the finite detector resolution, the presence of dead material and various sources of noise, which can mimic E_T^{miss} .

The $\mathbf{E}_T^{\text{miss}}$ reconstruction relies on measurements in both the calorimeters and the muon chambers. Thus, there are two components contributing to its derivation:

$$E_T^{\text{miss}} = \sqrt{(E_x^{\text{miss}})^2 + (E_y^{\text{miss}})^2}, \quad (4.20)$$

$$E_{(x,y)}^{\text{miss}} = E_{(x,y)}^{\text{miss, calo}} + E_{(x,y)}^{\text{miss, } \mu}, \quad (4.21)$$

where $E_{(x,y)}^{\text{miss}}$ are the negative sum of the momentum components p_x and p_y projected onto the x and y direction, respectively. Additionally, further information from the Inner Detector is used to include low p_T particles, which did not reach the calorimeters. Furthermore, in regions poorly covered by the muon spectrometer (e.g. $|\eta| \sim 0$, $|\eta| \sim 1.2$), muons are reconstructed from the Inner Detector (e.g. ST muons).

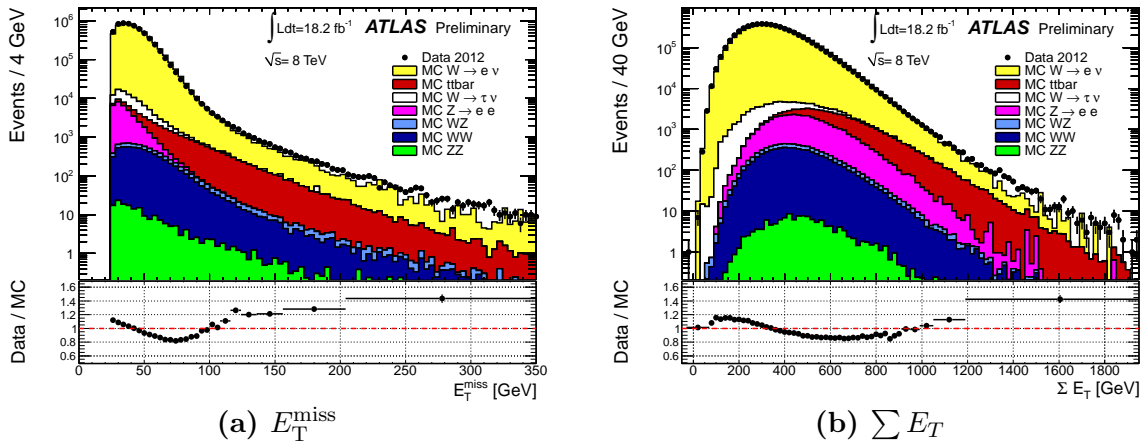


Figure 4.34.: Distribution of E_T^{miss} (a) and $\sum E_T$ (b) in a data sample of $W \rightarrow e\nu$ events [160].

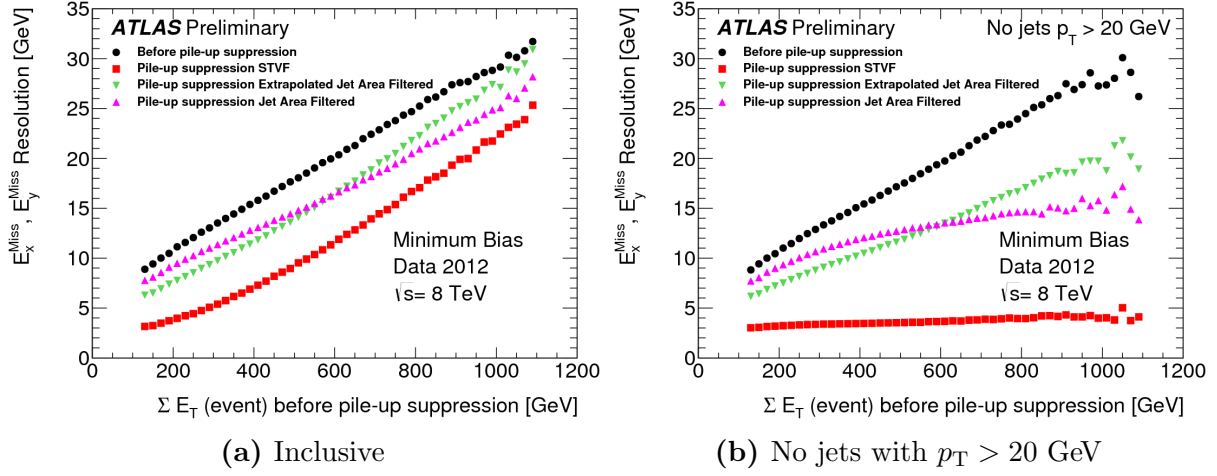


Figure 4.35.: E_x^{miss} and E_y^{miss} resolution inclusively (a) and with without jets with $p_T > 20$ GeV (b) as a function of the total transverse momentum in the event measured in data [160].

Another quantity used in the VH analysis is the track-based missing transverse momentum $\mathbf{p}_T^{\text{miss}}$, which is calculated as the negative vector sum of the transverse momenta of tracks with $|\eta| < 2.4$ associated with the primary vertex. This quantity is useful to suppress any non-collision background (i.e. halo energy deposit, no ID tracks) and to estimate any multijet background.

For the actual reconstruction of $\mathbf{E}_T^{\text{miss}}$ and $\mathbf{p}_T^{\text{miss}}$, the REFFINAL algorithm [62, 159–163] is used. Each object contributing to the $\mathbf{E}_T^{\text{miss}}$ calculation is calibrated, while no corrections are applied for the derivation of $\mathbf{p}_T^{\text{miss}}$.

A measurement of the genuine E_T^{miss} in $W \rightarrow e\nu$ events has been made in 8 TeV data and compared to different expectations from MC simulations, as shown in Figure 4.34a. The corresponding transverse energy of all reconstructed objects in the events is shown in Figure 4.34b. Generally, a good modelling of the data is achieved, although no pileup suppression techniques are applied. Different methods of pileup suppression have been developed [164], and are used in the VH analysis.

4.4.2. Resolution

The E_T^{miss} resolution can be, to a good approximation, described by the simple relation: $\sigma = k \times \sqrt{\sum E_T}$. The parameter k was determined to be about $0.55 \text{ GeV}^{1/2}$ [159]. The E_x^{miss} and E_y^{miss} resolution as a function of the total transverse momentum in the event measured in data is shown in Figure 4.35a inclusively, and in Figure 4.35b excluding jets

with a $p_T > 20$ GeV. The resolution after pileup suppression improves significantly in the latter case.

4.5. Final object selection

In the sections above, all physics objects used in the VH analysis have been introduced and defined: electron, muons, (b -)jets, and $\mathbf{E}_T^{\text{miss}}$. This section briefly defines the final selection of physics objects to be used in the analysis presented in Chapter 5.

Only physics objects and their quality criteria, as specified in Sections 4.2 to 4.4, are used, if additionally the following two requirements are satisfied:

1. **Jet Vertex Fraction (JVF):** The contamination by jets from pileup interactions is suppressed by limiting the JVF, defined as

$$\text{JVF}(\text{jet}_j, \text{vtx}_k) = \frac{\sum_i p_T^{\text{trk}_{ijk}}}{\sum_k \sum_i p_T^{\text{trk}_{ijk}}}, \quad (4.22)$$

where trk_{ijk} is the i^{th} track matched to the j^{th} jet associated to the k^{th} vertex. Jets with a $p_T > 50$ GeV and $|\eta| < 2.4$ must have $|\text{JVF}| > 0.5$. In case a jet has no matched tracks, it is retained.

2. **Overlap Removal:** Double-counting of physics objects is avoided by sequentially removing any ambiguities between loose leptons and jets:

- 2.1. if $\Delta R(\text{jet}, e) < 0.4$, the jet is discarded;
- 2.2. if $\Delta R(\text{jet}, \mu) < 0.4$, the jet is discarded if it has $N_{\text{trk}} \leq 4$ matched tracks¹⁵, otherwise the muon is discarded;
- 2.3. if $\Delta R(e, \mu) < 0.2$, the muon is discarded if it is a CaloTag muon, otherwise the electron is discarded.

¹⁵In this case, the jet is likely to originate from a muon, which produced a shower in the calorimeter.

4.6. Summary

In this chapter, the reconstruction of each final-state physics object considered for the analysis of the $ZH \rightarrow \nu\bar{\nu}b\bar{b}$, $WH \rightarrow \ell\nu b\bar{b}$ and $ZH \rightarrow \ell^+\ell^-b\bar{b}$ decay channels has been presented. These are (1) isolated electrons identified with a likelihood-based discriminant, (2) isolated MuID muons identified as CB/ST, CaloTag or SA, (3) jets reconstructed with the anti- k_T algorithm with a radius parameter $R = 0.4$, (4) b -tagged jets identified with the MV1c algorithm, and (5) missing transverse momentum reconstructed with the REFFINAL algorithm. The final definition of objects (1)-(5), as stated in Section 4.5, serves the $H \rightarrow b\bar{b}$ search strategy presented in Chapter 5. Furthermore, Section 4.3.3 laid out the foundation for the development of an event-level kinematic likelihood fit, which will be discussed in Chapter 6.

Chapter 5.

The $(W/Z)H \rightarrow b\bar{b}$ Analysis Strategy

In this chapter, the strategy to search for a $H \rightarrow b\bar{b}$ resonance in association with a W or Z boson is presented [8]¹. The search uses the full integrated luminosity accumulated by the ATLAS experiment during the Run-1 of the LHC and corresponds to 4.7 and 20.3 fb⁻¹ from proton-proton collisions at $\sqrt{s} = 7$ TeV and $\sqrt{s} = 8$ TeV in 2011 and 2012, respectively.

A general overview of the analysis structure and the employed techniques is discussed in Section 5.1, followed by a consecutive construction of the analysis in Sections 5.2 to 5.7. This includes a description of data and simulated samples, kinematic and topological event selections, energy calibrations of $H \rightarrow b\bar{b}$ dijet candidates, background compositions in each decay channel, contribution of systematic uncertainties, and finally the statistical procedure to combine all channels and to extract the signal yield.

5.1. Analysis Overview

As motivated in Section 2.3.1, the production of $H \rightarrow b\bar{b}$ via the Higgs-strahlung process provides additional final-state signatures from leptonically decaying vector bosons ($V \equiv W, Z$). Thus, different final states can be exploited, events can be categorized and the search in each category can be optimized based on "unique" kinematic and topological features.

¹The interested reader is referred to this reference for a detailed review of the analysis. The focus of this chapter is only on the main analysis aspects, which are relevant in the context of this thesis.

The analysis classifies events according to the number of charged leptons. Events containing zero, one, or two charged leptons are targeting the $Z \rightarrow \nu\bar{\nu}$, $W \rightarrow \ell\nu$, or $Z \rightarrow \ell\ell$ decay modes of the vector boson, respectively. The considered leptons, denoted by ℓ , are either electrons or muons. Thus, the analysis is performed in three distinct channels: the *0-lepton channel* is optimized for the $ZH \rightarrow \nu\bar{\nu}b\bar{b}$ process, the *1-lepton channel* is optimized for the $WH \rightarrow \ell\nu b\bar{b}$ process, and the *2-lepton channel* is optimized for the $ZH \rightarrow \ell^+\ell^-b\bar{b}$ process. However, the channels are not completely exclusive. For instance, in cases when the lepton from $W \rightarrow \ell\nu$ is produced outside of the ATLAS acceptance or is not identified, there is a non-negligible contribution from the 1-lepton channel in the 0-lepton channel. In addition, some background contributions are common between the different channels.

Each of the three analysis channels is further divided into different categories or phase space regions. These categories are defined based on the transverse momentum of the vector bosons (p_T^V), the number of reconstructed jets (either two or three), and the number of b -tagged jets. Kinematic and topological selection criteria are defined for each category in each channel, and are optimized to achieve a maximal sensitivity (i.e. $\text{signal}/\sqrt{\text{background}} = \text{max.}$) in the search for the $H \rightarrow b\bar{b}$ resonance.

The main source of background to this search originates from vector boson production in association with (heavy-flavour) jets and from $t\bar{t}$ production. Other backgrounds arise from the production of dibosons (VZ and WW), single-top quarks and QCD multijets. All of these are briefly reviewed here.

V + jet production If the vector boson is produced along with exactly two b -jets in the final state, this background becomes nearly irreducible. The corresponding tree-level production diagrams for the $q\bar{q}' \rightarrow W + b\bar{b}$, $q\bar{q} \rightarrow Z + b\bar{b}$ and $g\bar{g} \rightarrow Z + b\bar{b}$ processes are shown in Figures 5.1a and 5.1b. Different jet flavour combinations can also constitute a background: $V + bc$, $V + bl$, $V + c\bar{c}$, $V + cl$, and $V + ll$, where l denotes light jets (i.e. u , d , or s -quark, or gluon). In all of these case, their contribution to the overall background in this search relies strongly on the efficiency of the b -tagging algorithm, i.e. the misidentification of c -jets and l -jets as b -jets.

$t\bar{t}$ production. The other major background source is the t -quark pair production, which has a significantly larger cross-section (see Figure 3.3). Its tree-level production diagram is shown in Figure 5.1c. In case both W bosons from $t\bar{t}$ decay leptonically, the final state contains two b -jets, two leptons of opposite charge and significant E_T^{miss} . In case one W boson decays leptonically and the other hadronically, the final state contains

four jets (two always b -jets), one charged lepton and E_T^{miss} . Both of these cases are main backgrounds in the VH analysis (the all-hadronic case with six final-state jets contributes less). Different techniques can be employed to significantly suppress the $t\bar{t}$ background. For instance, besides two b -tagged jets, one can veto the presence of any additional jets in the event. Particularly at high p_T^W , one finds the b -jets from VH production more collimated than those recoiling b -jets from $t\bar{t}$ production. Therefore, the background from $t\bar{t}$ production can be suppressed by limiting the angular separation between the b -jet pair.

Diboson production. The diboson decays, WZ and ZZ , produce the same final-state signature as the VH production, but with a ~ 5 times larger cross-section. Since the invariant dijet mass from $Z \rightarrow b\bar{b}$ is considerably lower than the expected dijet mass from $H \rightarrow b\bar{b}$, one could efficiently suppress the background contribution from dibosons, if the reconstructed dijet mass resolution would be "good enough". This means that the signal contamination depends strongly on the jet reconstruction performance, i.e. how much the tails of both dijet mass distributions overlap. The corresponding tree-level production diagrams are shown in Figures 5.1d to 5.1f. The WW production, in case of its decay into $\ell\nu qq$, can also constitute a background, but has a minor contribution. This comes mainly from the hadronic $W \rightarrow cs$ decay and the misidentification of its jets as b -jets. Therefore, this background source depends strongly on the b -tagging efficiency.

Single-top production. Based on the weak interaction, single top-quarks are produced via three separate sub-processes, as shown at tree-level in Figures 5.1g to 5.1j. In the t -channel, a top quark is produced via the exchange of a virtual, space-like W boson in association with a bottom and light quark. In the s -channel, a top quark and a bottom quark are produced via the exchange of a virtual, time-like W boson. In the Wt -channel, a top quark in association with a real W boson is produced via a t - or s -channel. Each sub-process involves at least one b -jet in the final state. Similar to the $t\bar{t}$ production mentioned above, one can restrict the angular separation between the selected b -jets to suppress the background contributions from single-top production.

QCD multijet production. Multijet (MJ) events are produced via the strong interaction with an enormously large cross section at the LHC, and thus potentially give rise to large backgrounds. There are two classes of MJ background sources. The first class arises from light-quark jets or photon conversions misidentified as electrons and from semileptonic decays in heavy-flavour jets. Therefore, lepton isolation criteria, as discussed in Section 4.2.3, are crucial to discriminate between vector boson decay products and QCD multijets. The 1-lepton and 2-lepton channels are very sensitive to

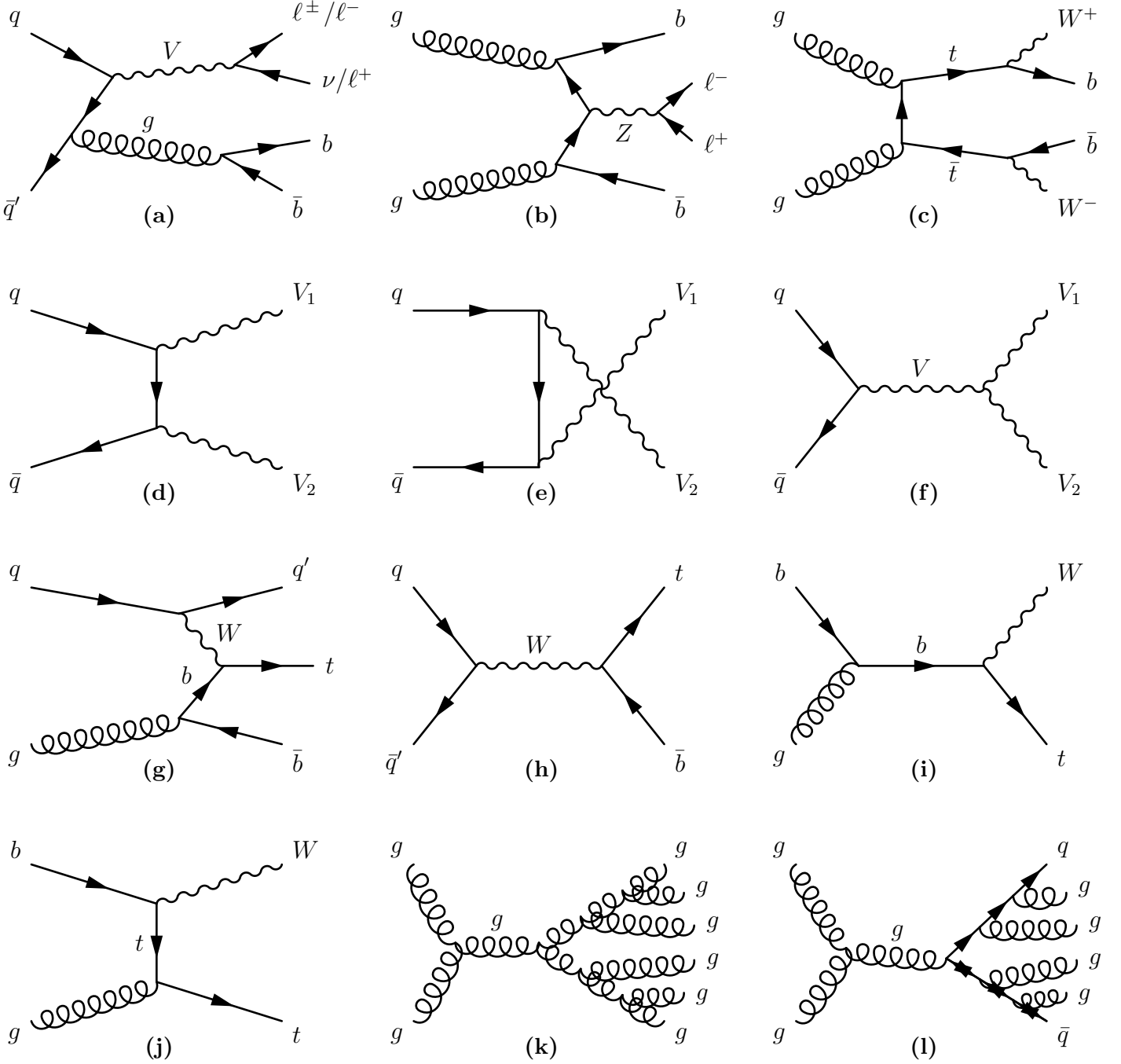


Figure 5.1.: Feynman diagrams of the main background production modes: (a) $q\bar{q}$ -initiated $V + b\bar{b}$; (b) gg -initiated $Z + b\bar{b}$; (c) $t\bar{t}$; (d) diboson t -chn., (e) u -chn., (f) s -chn.; (g) single-top t -chn., (h) s -chn., (i) Wt s -chn., (j) Wt t -chn.; (k,l) multijet examples.

this MJ class. The second class arises from fluctuations in calorimeter measurements of jet energies, which produce "fake" E_T^{miss} . This mainly affects the 0-lepton channel. Since these fluctuations cannot be accurately determined by MC simulations, the MJ background is estimated from data in each analysis channel. Figures 5.1k and 5.1l illustrate the production of QCD multijets.

There are *two approaches* or versions of the VH analysis:

1. a **dijet-mass analysis**, (cut-)based on the reconstructed invariant dijet mass of the $b\bar{b}$ system as the final discriminating variable,
2. a **multivariate analysis (MVA)**, based on different kinematic variables in addition to the dijet mass and b -tagging information, serving as the combined final discriminating variable.

Since the b -tagging information in the 8 TeV dataset is not available at the same level of detail in the statistically-limited 7 TeV dataset, the MVA is only used for the 8 TeV dataset. The MVA was chosen as the nominal analysis of the 8 TeV dataset, due to its expected higher sensitivity of the $H \rightarrow b\bar{b}$ search. Nevertheless, both MVA and dijet-mass analysis are presented in this thesis.

For the final statistical analysis, a binned maximum likelihood fit (also denoted by “global fit”) is used to not only extract the signal yield, but also to evaluate from data the normalisations and shapes of the backgrounds. The fit utilizes the different phase space regions in each channel and implements systematic uncertainties on the modelling of the signal and backgrounds in the form of “nuisance” parameters, which are varied in the fit. Another dedicated fit is used to validate the analysis procedure, where the yield of the $(W/Z)Z \rightarrow b\bar{b}$ production is measured in the same final states and with the same event selection as for the $H \rightarrow b\bar{b}$ search.

5.2. Data and MC samples

The analysis uses proton-proton collision data recorded by the ATLAS detector in 2011 and 2012, corresponding to 4.7 and 20.3 fb⁻¹ at $\sqrt{s} = 7$ TeV and $\sqrt{s} = 8$ TeV, respectively. Only collision data, collected during stable LHC beam conditions (see Section 3.1), with all relevant subdetectors producing data of very high quality, is considered.

The Higgs signal and all background processes in the ATLAS detector, as described above, are simulated using dedicated MC samples, based on the ATLFast-II simulation using the GEANT4 program (see Section 4.1). The different event generators, used for both signal and background simulations, are summarized in Table 5.1.

Process	Generator
Signal^(*)	
$q\bar{q} \rightarrow ZH \rightarrow \nu\nu b\bar{b}/\ell\ell b\bar{b}$	PYTHIA8
$gg \rightarrow ZH \rightarrow \nu\nu b\bar{b}/\ell\ell b\bar{b}$	POWHEG+PYTHIA8
$q\bar{q} \rightarrow WH \rightarrow \ell\nu b\bar{b}$	PYTHIA8
Vector boson + jets	
$W \rightarrow \ell\nu$	SHERPA 1.4.1
$Z/\gamma^* \rightarrow \ell\ell$	SHERPA 1.4.1
$Z \rightarrow \nu\nu$	SHERPA 1.4.1
Top-quark	
$t\bar{t}$	POWHEG+PYTHIA
t -channel	ACERMC+PYTHIA
s -channel	POWHEG+PYTHIA
Wt	POWHEG+PYTHIA
Diboson^(*)	
WW	POWHEG+PYTHIA8
WZ	POWHEG+PYTHIA8
ZZ	POWHEG+PYTHIA8

Table 5.1.: The generators used for the simulation of the signal and background processes.

(*) For 7 TeV data: PYTHIA8 is used for the $gg \rightarrow ZH$ process, and HERWIG for diboson processes [8].

The $q\bar{q}$ -initiated Higgs signal processes, $q\bar{q} \rightarrow VH$ (see Figure 4.1), are modelled using PYTHIA8 with the CTEQ6L1 [165] parton distribution functions (PDFs) and the AU2 tune [166, 167] for the parton showering, hadronization, and multiple parton interactions. This setup is further interfaced with the PHOTOS program [168] to simulate QED final-state radiation. While VH production is dominated by the $q\bar{q}$ -initiated process in the Standard Model, there is, in case of ZH production, also a significant contribution from the gluon-gluon (gg) initiated process (see Figure 5.2). Therefore, gg -initiated ZH events are generated at leading order (LO) in QCD with POWHEG using CT10 PDFs [169] (based on the MiNLO approach [170]) and showered with PYTHIA8 using the AU2 tune. One finds that the Higgs boson p_T spectrum is fundamentally different between the gg - and $q\bar{q}$ -initiated ZH productions. This effect arises from the threshold behaviour of the t -loop in $gg \rightarrow ZH$ [171]. The generated $q\bar{q} \rightarrow ZH$ samples and the $gg \rightarrow ZH$ samples are combined by deriving their individual event weights from their corresponding cross-sections. In case of $q\bar{q}$ -initiated VH production, the total cross-sections and

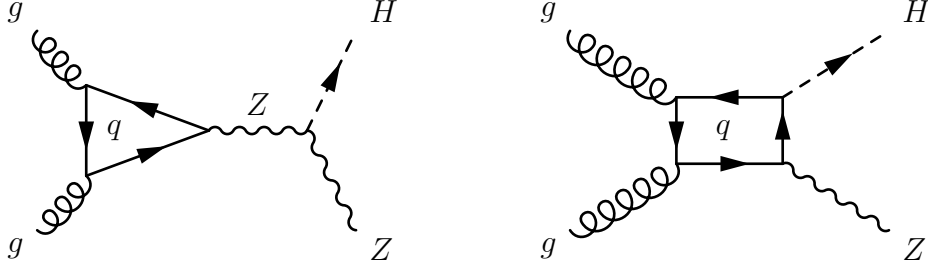


Figure 5.2.: Leading order Feynman diagrams for gg -initiated ZH production.

uncertainties (taken from [34]) are calculated at next-to-next-to-leading order (NNLO) in QCD [172–174], with next-to-leading order (NLO) electroweak corrections [175] applied as a function of p_T^V [176]. NLO corrections, derived in [177], are applied to the gg -initiated ZH production, and yields an increase of the total ZH production cross-section by $\sim 5\%$.

The branching ratios of the Higgs boson decay (taken from [34]) are computed with hdecay [178]. Signal samples are produced for eleven Higgs mass hypothesis, ranging from 100 to 150 GeV, in intervals of 5 GeV. Additionally to electrons and muons, τ leptons are considered in the simulation of the W and Z decays, since they can be also selected in the analysis².

Different event generators are used for the background processes. The simulation of the V +jets background is performed at LO in QCD with the SHERPA generator using CT10 PDFs. Their cross-sections are calculated at NNLO [179]. The production of $t\bar{t}$ is simulated with the POWHEG generator using also CT10 PDFs, and is interfaced with PYTHIA6 using CTEQ6L1 PDFs and the Perugia2011C tune [166, 167]. The $t\bar{t}$ cross-section is calculated at NNLO, including soft gluon terms via next-to-next-to-leading logarithmic resummation [180]. Both, diboson [181] and single-top productions [182–184] are simulated with POWHEG+PYTHIA6, as for $t\bar{t}$, except the single-top t -channel, which is simulated with the ACERMC generator instead of POWHEG.

5.3. Physics object and event selection

The analysis of the datasets begins with the identification of potentially *interesting events*. The selection of these is based on different event triggering criteria for each analysis channel. In the 0-lepton channel, events are selected by triggers based on significant E_T^{miss} with a threshold of 80 GeV (70 GeV) for 8 TeV (7 TeV) data. Since the luminosity

²A fraction of signal events is selected in the analysis due to $V \rightarrow \tau\nu$ with $\tau \rightarrow \nu_\tau \ell \nu_\ell$.

increased during data recording in 2011 and 2012 (see Section 3.1), the E_T^{miss} trigger menu and efficiency were improved, resulting in a complex configuration to maximize the event acceptance. In the very beginning of data taking, E_T^{miss} triggers were not available for a short period, thus, the 7 TeV dataset corresponds to only 4.6 fb^{-1} in the 0-lepton channel. In the 1-lepton channel, events are mainly selected by two sets of single-lepton triggers. The first set includes basic track isolation criteria for 8 TeV data, and has an electron E_T threshold of 24 GeV (20-22 GeV) and a muon p_T threshold of 24 GeV (18 GeV) for 8 TeV (7 TeV) data. The second set includes no isolation criteria and is only used for 8 TeV data with higher thresholds: 60 GeV for electrons and 36 GeV for muons. Due to the reduced muon trigger-chamber coverage in different regions of the detector (see Sections 3.2.5 and 4.2), E_T^{miss} triggers, as described above, complement the selection in the 1-lepton (μ) channel. In the 2-lepton channel, events are selected by single-lepton triggers, as in the 1-lepton channel, as well as dielectron and dimuon triggers with an electron E_T threshold of 12 GeV and a muon p_T threshold of 13 GeV for both 7 TeV and 8 TeV data.

All of the trigger-selected events are then processed and their final-state particle composition is evaluated. The signal physics objects of this analysis are isolated electrons and muons, jets originating from b -quark fragmentation, and significant E_T^{miss} . These objects are reconstructed, as discussed in Chapter 4, in each trigger-selected event, and must all satisfy the stringent object quality criteria, which have been defined in Section 4.5. Subsequently, their multiplicity, kinematics and topological formation in each event is evaluated and used to categorize them.

Any event is first classified based on its number of leptons. It is assigned to the

- **0-lepton channel**, if the event contains no loose leptons,
- **1-lepton channel**, if the event contains one tight lepton and no other loose leptons,
- **2-lepton channel**, if the event contains one medium lepton, one loose lepton and no other loose leptons.

If the event contains at least one jet with $p_T > 30 \text{ GeV}$ and $|\eta| > 2.5$, it is discarded. This requirement aims to reduce the $t\bar{t}$ background. To be considered for further processing, the *event must contain exactly two or three jets* with $p_T > 20 \text{ GeV}$ and $|\eta| < 2.5$. Only these jets are passed through the b -tagging algorithm. The highest- p_T (leading) b -jet must have $p_T > 45 \text{ GeV}$. The event is then further classified by the number of b -tagged jets, which are labelled according to the operating points defined in Table 4.3 (see Section 4.3.4

for definitions). If the event contains three loose b -jets, or contains three jets with the lowest- p_T jet being a loose b -jet, the event is rejected. The event is then assigned to the

1. **0-tag category**, if the event contains no loose b -jets,
2. **1-tag category**, if the event contains exactly one loose b -jet,
3. **2-tag category**, if the event contains exactly two b -jets, forming a dijet system under the
 - 3.1. **Tight (TT) category**, if both jets are tight b -jets,
 - 3.2. **Medium (MM) category**, if both jets are not TT-classified, but are medium b -jets,
 - 3.3. **Loose (LL) category**, if both jets are not TT/MM-classified, but are loose b -jets.

If the event contains three jets, the dijet system can be built from jets in the 2-tag category, or from a jet in the 1-tag category and the highest- p_T (leading) non- b -tagged jet in the event, or from the two leading jets in the 0-tag category.

After the above basic event selection and classification, a series of kinematic and topological restrictions are enforced to suppress background contributions and to maximize the sensitivity of the $H \rightarrow b\bar{b}$ search. These selection criteria are summarized in Table 5.2 and are further discussed here. Besides optimizing the event selection as a function of leptons, jets, b -tagged jets and their purity, one can also address different background contributions in terms of the boost of the (leptons + jets) system by constraining its topology as a function of the reconstructed p_T^V . In case of the 0-lepton channel, the magnitude p_T^Z refers to the reconstructed E_T^{miss} . In case of the 1-lepton channel, the magnitude p_T^W refers to the vector sum of the lepton p_T^ℓ and the $\mathbf{E}_T^{\text{miss}}$. In case of the 2-lepton channel, the magnitude p_T^Z refers to the vector sum of both leptons' p_T^ℓ . Generally, a better signal-to-background ratio can be achieved at higher p_T^V . The angular separation between the two selected jets, i.e. the $H \rightarrow b\bar{b}$ candidate, is correlated with p_T^V : as p_T^V increases, the collimation of the dijet system increases. Therefore, the requirement on $\Delta R(\text{jet}_1, \text{jet}_2)$ can be tightened as the p_T^V increases to emulate the expected signal (before the jets merge and jet substructure techniques must be employed). For instance, the background from $t\bar{t}$ production can be suppressed by limiting the dijet separation with a maximum value, while the background from $V + \text{jets}$ production can be reduced by requiring a minimum value for the dijet separation. This method, with five p_T^V bins, is

Variable	Dijet-mass analysis					Multivariate analysis	
Common selection							
p_{T}^{V} [GeV]	0–90	90 ^(*) –120	120–160	160–200	> 200	0–120	> 120
$\Delta R(\text{jet}_1, \text{jet}_2)$	0.7–3.4	0.7–3.0	0.7–2.3	0.7–1.8	< 1.4	> 0.7 ($p_{\text{T}}^{\text{V}} < 200$ GeV)	
0-lepton selection							
$p_{\text{T}}^{\text{miss}}$ [GeV]	NU	> 30	> 30			NU	> 30
$\Delta\phi(\mathbf{E}_{\text{T}}^{\text{miss}}, \mathbf{p}_{\text{T}}^{\text{miss}})$		< $\pi/2$	< $\pi/2$				< $\pi/2$
$\min[\Delta\phi(\mathbf{E}_{\text{T}}^{\text{miss}}, \text{jet})]$		–	> 1.5				> 1.5
$\Delta\phi(\mathbf{E}_{\text{T}}^{\text{miss}}, \text{dijet})$		> 2.2	> 2.8				> 2.8
$\sum_{i=1}^{N_{\text{jet}=2(3)}} p_{\text{T}}^{\text{jet}_i}$ [GeV]		> 120 (NU)	> 120 (150)				> 120 (150)
1-lepton selection							
m_{T}^{W} [GeV]	< 120					–	
H_{T} [GeV]	> 180		–			> 180	–
$E_{\text{T}}^{\text{miss}}$ [GeV]	–		> 20		> 50	–	> 20
2-lepton selection							
$m_{\ell\ell}$ [GeV]	83–99					71–121	
$E_{\text{T}}^{\text{miss}}$ [GeV]	< 60					–	

Table 5.2.: Kinematic and topological event selections for the dijet-mass analysis and the MVA. NU stands for "Not Used". (*) In the 0-lepton channel, the lower edge of the p_T^V bin is 100 GeV [8].

used in the dijet-mass analysis for exactly these reasons. The MVA, on the other hand, has only two p_T^V bins, but incorporates both p_T^V and $\Delta R(\text{jet}_1, \text{jet}_2)$ as input variables (see Table 5.4), which contribute to the final discriminant.

The QCD multijet background in the 0-lepton channel is significantly reduced by constraining the event topology based on the angular separation between $\mathbf{E}_T^{\text{miss}}$ and the track-based $\mathbf{p}_T^{\text{miss}}$, the nearest jet and the $H \rightarrow b\bar{b}$ dijet candidate. The $t\bar{t}$ background in the 1-lepton channel is reduced by imposing an upper limit on the transverse mass $m_T^W \equiv \sqrt{2p_T^\ell E_T^{\text{miss}}(1 - \cos(\phi^\ell - \phi^{\text{miss}}))}$, where ϕ^ℓ and ϕ^{miss} are the azimuthal angles of the lepton and E_T^{miss} , respectively. The MJ contamination is also suppressed by setting a lower bound on the scalar sum of E_T^{miss} , the p_T of the two leading jets, and p_T^ℓ (denoted by the variable H_T). In the 2-lepton channel, the reconstructed dilepton mass $m_{\ell\ell}$ is bound to be consistent with the Z boson mass.

The *signal regions* of the analysis contain events from the 2-tag category and are defined in terms of the corresponding lepton channel (0, 1 or 2), the p_T^V interval, the

$m_H = 125 \text{ GeV}$ at $\sqrt{s} = 8 \text{ TeV}$				
Process	Cross section \times BR [fb]	Acceptance [%]		
		0-lepton	1-lepton	2-lepton
$q\bar{q} \rightarrow (Z \rightarrow \ell\ell)(H \rightarrow b\bar{b})$	14.9	–	1.3 (1.1)	13.4 (10.9)
$gg \rightarrow (Z \rightarrow \ell\ell)(H \rightarrow b\bar{b})$	1.3	–	0.9 (0.7)	10.5 (8.1)
$q\bar{q} \rightarrow (W \rightarrow \ell\nu)(H \rightarrow b\bar{b})$	131.7	0.3 (0.3)	4.2 (3.7)	–
$q\bar{q} \rightarrow (Z \rightarrow \nu\nu)(H \rightarrow b\bar{b})$	44.2	4.0 (3.8)	–	–
$gg \rightarrow (Z \rightarrow \nu\nu)(H \rightarrow b\bar{b})$	3.8	5.5 (5.0)	–	–

Table 5.3.: Standard Model values for cross section times branching ratio (BR) and acceptance for the three channels at 8 TeV. The acceptance is shown for the MVA (dijet-mass analysis) [8].

jet multiplicity (2 or 3), and in case of the dijet-mass analysis, the TT, MM and LL categories. The latter distinction is incorporated in the MVA via directly including the raw $MV1c$ b -tagging weights (see Table 5.4).

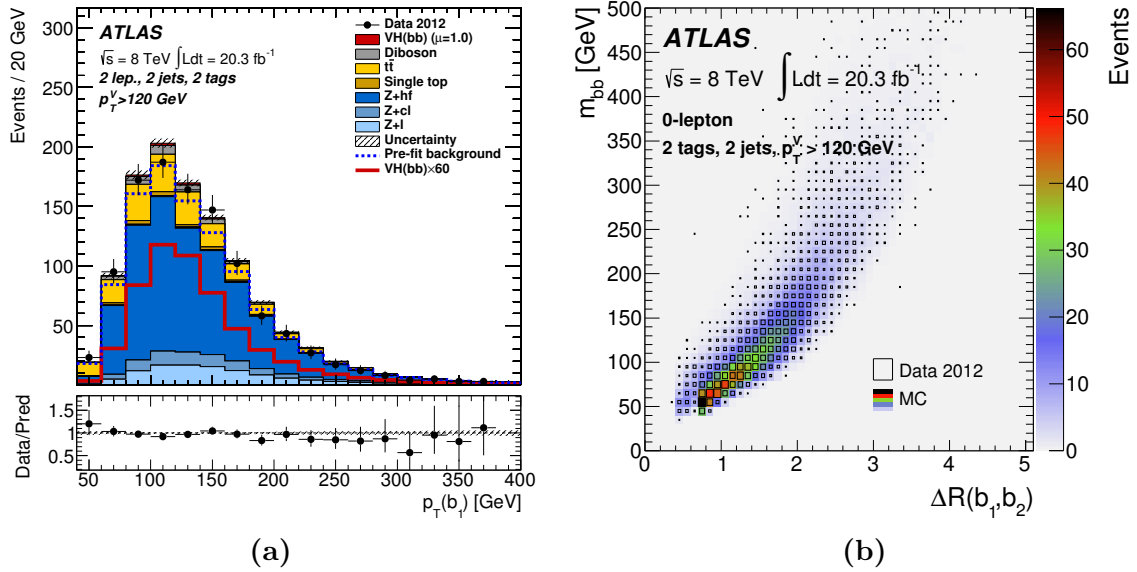
This concludes the discussion of the event selection for the dijet-mass analysis. In case of the MVA, events are further processed to further improve the discrimination between signal and backgrounds (see below). Before events are passed to the final global fit (see Section 5.7), the energy calibration of the selected b -tagged jets is improved, as described in Section 5.4 and Chapter 6.

The signal acceptance, and corresponding cross section times branching ratio, is shown in Table 5.3 for each $q\bar{q}$ - and gg -initiated process considered. The acceptance is computed as the fraction of remaining events in the combined 2-tag signal regions after performing the full event selection. The 0-lepton channel, with respect to the 1-lepton channel, adds about 7% in acceptance to the $W(\ell\nu)H$ process, and the 1-lepton channel, with respect to the 2-lepton channel, adds about 9% in acceptance to the $Z(\ell\ell)H$ process.

MVA processing. After the full event selection and jet energy calibrations, events are passed on as inputs to the MVA processing. Unlike in the cut-based dijet mass analysis, the MVA aims to further improve the signal-to-background discrimination by utilizing distinct variables, in addition to the dijet mass m_{bb} , providing kinematic, topological and b -tagging information. The combination of this information is based on the concept of machine learning. Boosted Decision Trees (BDTs) [185, 186] are trained and evaluated in the 2-tag signal regions, as defined above. The training of the BDTs is performed with the Toolkit for Multivariate Analysis (TMVA) [187] and utilizes different MC samples for the evaluation of characteristic variables. The complete set of input

Variable	0-Lepton	1-Lepton	2-Lepton
p_T^V		×	×
E_T^{miss}	×	×	×
$p_T^{b_1}$	×	×	×
$p_T^{b_2}$	×	×	×
m_{bb}	×	×	×
$\Delta R(b_1, b_2)$	×	×	×
$ \Delta\eta(b_1, b_2) $	×		×
$\Delta\phi(V, bb)$	×	×	×
$ \Delta\eta(V, bb) $			×
H_T	×		
$\min[\Delta\phi(\ell, b)]$		×	
m_T^W		×	
$m_{\ell\ell}$			×
$MV1c(b_1)$	×	×	×
$MV1c(b_2)$	×	×	×
Only in 3-jet events			
$p_T^{\text{jet}_3}$	×	×	×
m_{bbj}	×	×	×

Table 5.4.: MVA input variables for the 0-, 1- and 2-lepton channels [8].

Figure 5.3.: Example input variables to the MVA in the (LL, MM, TT)-combined 2-jet 2-tag category: (a) leading jet p_T after the kinematic likelihood fit in the 2-lepton channel; (b) $H \rightarrow b\bar{b}$ candidate mass as a function of $\Delta R(b_1, b_2)$ [8].

variables used by the BDTs is shown in Table 5.4. A good agreement between data and MC is found for the input variables and their correlations, as Figures 5.3a and 5.3b show. Figure 5.3a corresponds to the direct output of the kinematic likelihood fit (see Chapter 6) in the 2-lepton channel. Finally, the MVA provides a single output, a discriminating variable, denoted by BDT_{VH} . The distributions of this variable for each analysis channel are shown in Figure 5.12.

5.4. Energy calibration of Higgs candidates

All jets are reconstructed from topoclusters using the anti- k_T algorithm, as discussed in Section 4.3.2. Subsequently, their energy is calibrated using the EM+JES or the GSC, whereas the latter includes the EM+JES calibration. The entire calibration chain for jets, in order to be considered as physics objects in the VH analysis, has been already presented in Section 4.3.3. In this section, the impact of these calibrations on selected $H \rightarrow b\bar{b}$ dijet candidates is evaluated. This evaluation is carried out after the full event selection in terms of the reconstructed $b\bar{b}$ invariant mass in the (LL+MM+TT)-combined³ 2-tag signal region of the analysis (Section 5.4.2). Furthermore, two additional corrections are presented to improve the energy calibration of the selected b -jets. This includes a semileptonic correction (Section 5.4.3) and a resolution correction (Section 5.4.4). These are applied in all three channels of the analysis and improve the mass resolution significantly. In case of the 2-lepton channel, a kinematic likelihood fit replaces the resolution correction, and is presented in Chapter 6. The dijet mass resolution is evaluated and compared between the different jet energy calibrations, using the fit model introduced in Section 5.4.1.

5.4.1. Mass resolution fit model

Different methods to evaluate resolution effects to dijet resonances have been employed in the past, e.g. the standard deviation over the mean or Gaussian distributions to fit the core of the dijet mass distribution. The former does not provide a good description of the core resolution, given a significant contribution from the tails of the distribution. The latter tries to provide a good description of the core, but is strongly dependent on the fit range, particularly, if the tails of the distribution are asymmetric. Even

³Thereafter, (LL+MM+TT)-combined may be denoted by *combined* only.

the convolution of multiple Gaussians cannot solve this problem completely, since each Gaussian is symmetric. A reasonable solution of this problem is achieved by using a logarithmic Gaussian distribution, the *Novosibirsk function* [188]. However, as recent performance studies have shown [189], the quality of fits with this function varied between 8-10% around the peak position, i.e. the error associated to the peak evaluation varied significantly. Since this analysis requires to evaluate resolution effects with a higher precision, the basic Novosibirsk function cannot be used. Instead a variation of the Novosibirsk function is considered: the *Bukin function* [190]. It is defined as

$$\mathcal{P}(x; x_p, \sigma_p, \xi, \rho_i) = A_p \exp \left[\frac{\xi \sqrt{\xi^2 + 1} (x - x_{\text{low}}) \sqrt{2 \ln 2}}{\sigma_p (\sqrt{\xi^2 + 1} - \xi)^2 \ln(\sqrt{\xi^2 + 1} + \xi)} + \rho_i \left(\frac{x - x_i}{x_p - x_i} \right)^2 - \ln 2 \right], \quad (5.1)$$

where x corresponds to the x -value of the distribution (e.g. jet response, dijet mass), A_p is an overall normalization factor, x_p is the peak position, σ_p is the Gaussian width of the core (FWHM, "full width at half maximum", divided by 2.335), ξ is an asymmetry parameter, and $i \in \{\text{low}, \text{high}\}$ corresponds to the lower (left) or higher (right) tail of the distribution, beginning at

$$x_i = x_p + \sigma_p \sqrt{2 \ln 2} \left(\frac{\xi}{\sqrt{\xi^2 + 1}} \mp 1 \right). \quad (5.2)$$

If $x < x_{\text{low}}$, then $\rho_i = \rho_{\text{low}}$ is the size of the lower tail, and if $x \geq x_{\text{high}}$, then $\rho_i = \rho_{\text{high}}$ is the size of the higher tail. Unless otherwise noted, Equation 5.1 will be used for all fits presented in this section and Chapter 6. When resolutions and mean values are quoted in this context, these correspond to the σ_p and x_p Bukin fit results.

5.4.2. Evaluation of EM+JES and GS calibrations

On top of the basic EM+JES calibration, the GSC is applied to all jets in the analysis (Section 4.3.3). It applies sequential corrections to the reconstructed jet p_T as a function of the jet response dependence on different jet properties, and aims to reduce the jet energy resolution, while keeping the jet energy scale unchanged. The impact of using GS-calibrated b -tagged jets ("GSC b -jets") for the reconstruction of $H \rightarrow b\bar{b}$ candidates is evaluated in signal events with respect to the EM+JES calibration of b -tagged jets ("EM+JES b -jets").

Figure 5.4a shows the reconstructed dijet invariant mass, p_T^W -inclusively, in the combined 2-tag signal region of the 1-lepton channel using $WH \rightarrow \ell \nu b\bar{b}$ signal MC

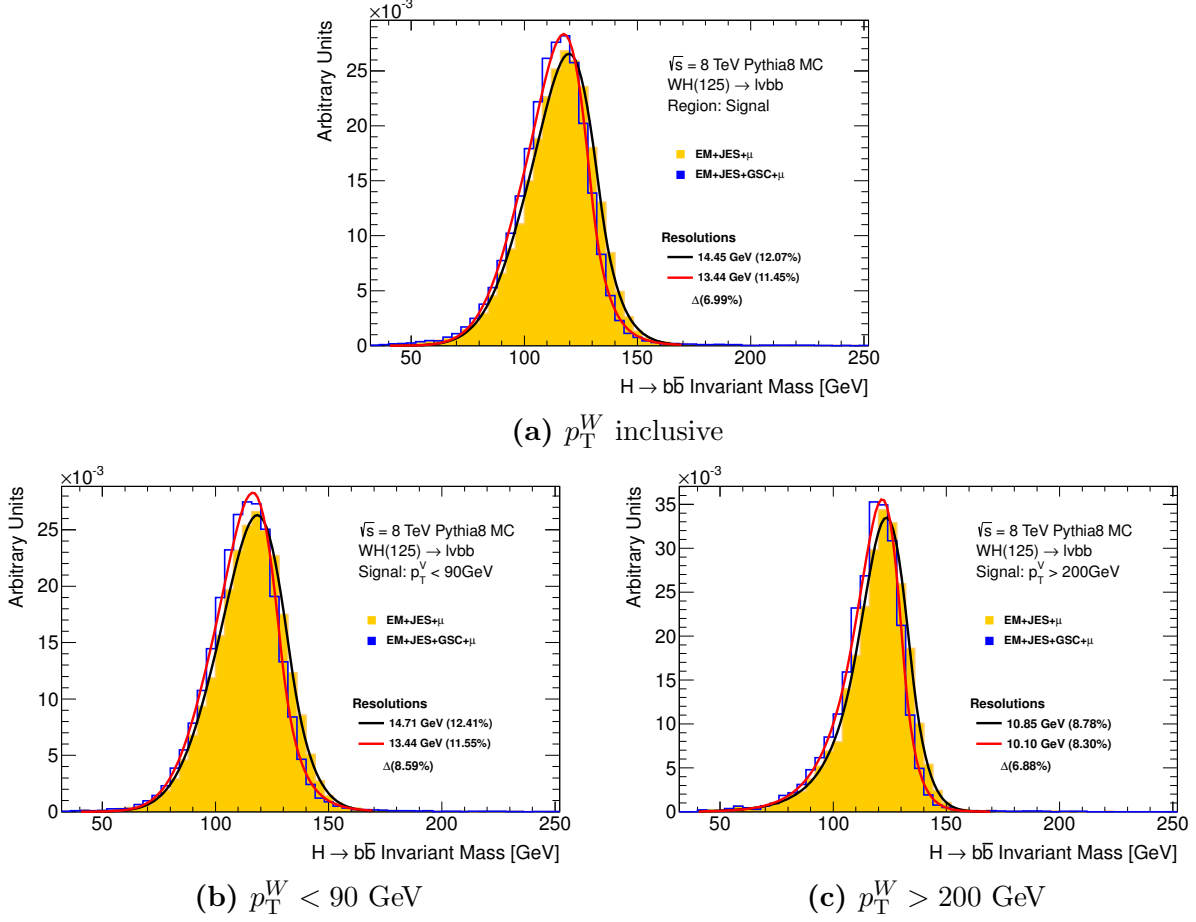


Figure 5.4.: Dijet-invariant-mass distributions for GSC and EM+JES calibrated b -jets from a Higgs boson with $m_H = 125$ GeV in the combined 2-tag signal region of the 1-lepton channel (dijet-mass analysis selection). The distributions are p_T^W inclusive in (a), with $p_T^W < 90$ GeV in (b), with $p_T^W > 200$ GeV in (c), and are each fitted to the Bukin function: the obtained mass resolution and in parentheses σ_p/x_p is shown, respectively.

(Table 5.1). Two mass distributions are shown: one with the mass formed by GSC b -jets, and another, superimposed, with the mass formed by EM+JES b -jets. Fits to both distributions reveal that the GSC improves the mass resolution by about 7% with respect to the EM+JES calibration. This is expected, as mentioned above. For each fit, the ratio σ_p/x_p in percentage is shown in parentheses in the figure. One finds the mean of the GSC distribution shifted to a $\sim 1\%$ lower mass. This relates to a scale shift between EM+JES and GSC at higher jet p_T , i.e. a difference in jet response, as further discussed and corrected for in Section 5.4.4.

The different jet energy resolution effects at lower and higher jet p_T translate directly into the invariant dijet mass reconstruction. Figures 5.4b and 5.4c show the dijet mass in two different phase space regions of the analysis: the former with $p_T^W < 90$ GeV and

the latter with $p_T^W > 200$ GeV. In general, the dijet mass resolution improves as the p_T^V increases. Comparing the low p_T^W bin with the high p_T^W bin, the resolutions of both EM+JES and GSC distributions improve by about 25-26%. The GSC improves the resolution with respect to the EM+JES calibration from $\sim 8.6\%$ at low p_T^W to about 1.7% less at high p_T^W . The mean of the GSC distribution shifts, similarly to the inclusive case, by about 1.8% at low p_T^W to about 1.5% at high p_T^W .

5.4.3. Muon-in-jet correction

As discussed in Section 4.3.4, about 42% of jets originating from b -quark fragmentation decay semileptonically. Thus, a non-negligible amount of their energy is carried by muons

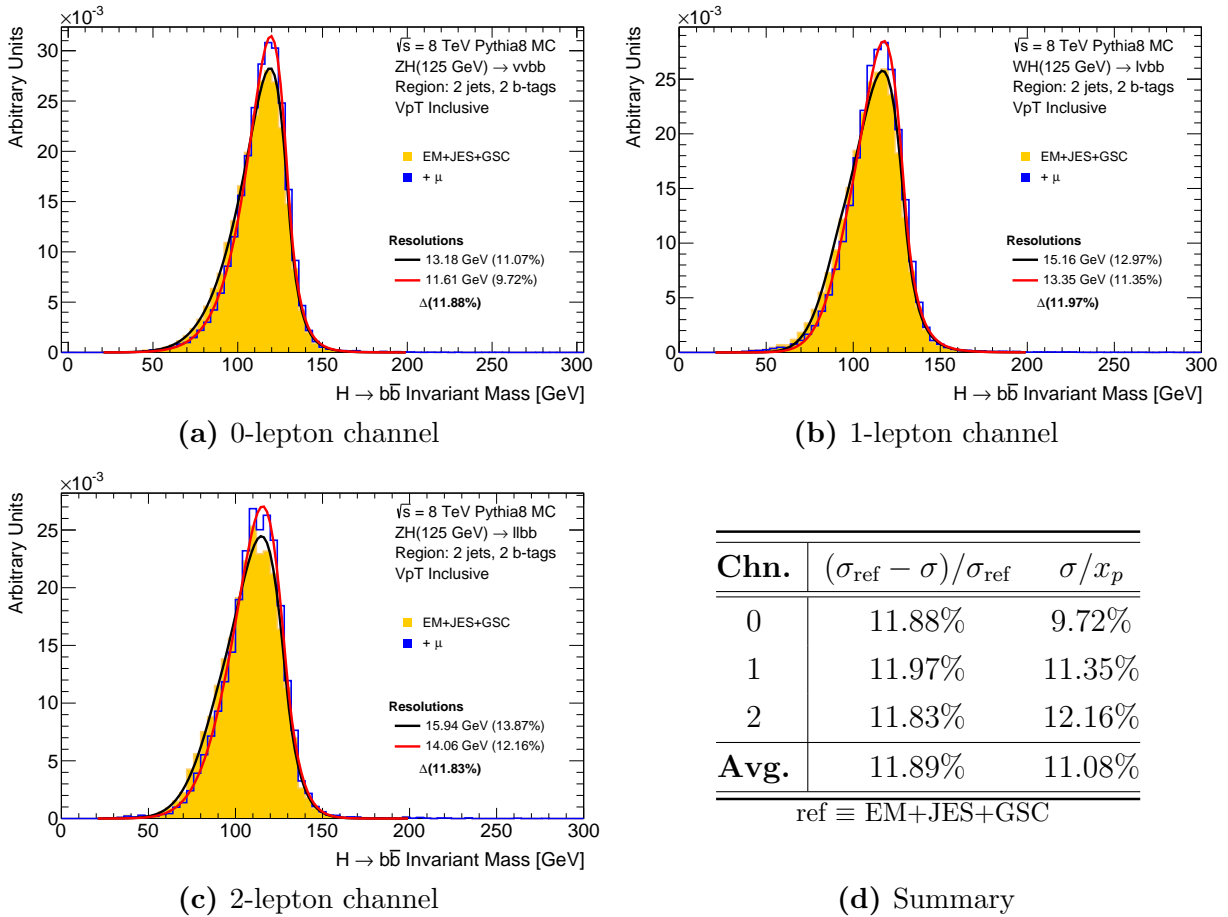


Figure 5.5.: Dijet-invariant-mass distributions of GS-calibrated $H \rightarrow b\bar{b}$ candidates before and after the muon-in-jet correction in the combined 2-tag signal regions of the 0-lepton channel (a), 1-lepton channel (b), and the 2-lepton channel (c). The dijet mass resolution improvements are summarized in (d).

and neutrinos, which escapes from the calorimeters. The correction described in the section focuses on muons, which are detected by the muon spectrometer and have a trajectory passing through a b -tagged jet cone. If the muon has a $p_T > 4$ GeV and a $\Delta R(\mu, b\text{-jet}) < 0.4$, the four-vector of the muon is added to the four-vector of the matched b -tagged signal jet after removing the energy deposited by the muon in the calorimeter. If two such muons are found within a jet, the one with the smaller ΔR is used.

This correction, denoted by *muon-in-jet correction*, is applied to all selected GSC b -jets in all three channels of the analysis and results in an improvement of the dijet mass resolution. Figure 5.5 shows the mass distributions, inclusive in p_T^V , before and after the muon-in-jet correction in the combined 2-tag signal region of each analysis channel in simulated VH events. The dijet mass resolution for the signal is in average improved by $\sim 12\%$ after this correction and is $\sim 11\%$.

5.4.4. Jet momentum resolution correction

Besides muons from semileptonic b -jet decays, as addressed in the previous section, accompanying neutrinos may carry a significant fraction of the jet energy. This results in a substantial difference between the average *all-particle response*,

$$\mathfrak{R}^{\text{all}} = \left\langle \frac{p_T^{\text{reco}}}{p_T^{\text{truth}}} \right\rangle \quad \text{with} \quad p_T^{\text{truth}} \ni \mu/\nu, \quad (5.3)$$

and the average *calorimeter response*, p_T^{reco} ,

$$\mathfrak{R}^{\text{calo}} = \left\langle \frac{p_T^{\text{reco}}}{p_T^{\text{truth}}} \right\rangle \quad \text{with} \quad p_T^{\text{truth}} \not\ni \mu/\nu, \quad (5.4)$$

as a function of the reconstructed jet p_T^{reco} . $\mathfrak{R}^{\text{all}}$ corresponds to the energy scale calculated with respect to jets formed using all stable particles, i.e. including μ/ν from semileptonic decays. $\mathfrak{R}^{\text{calo}}$, on the other hand, excludes μ/ν in the p_T^{truth} calculation, and is typically used for basic JES calibrations.

A multiplicative p_T^{reco} -dependent correction, $\langle p_T^{\text{truth}}/p_T^{\text{reco}} \rangle = 1/\mathfrak{R}^{\text{all}}$, is derived to account for biases in the jet response due to resolution effects, such as those mentioned above. This correction, denoted by *resolution correction*, is determined for the p_T^{reco} spectrum of b -tagged jets from the decay of a Higgs boson with $m_H = 125$ GeV in simulated

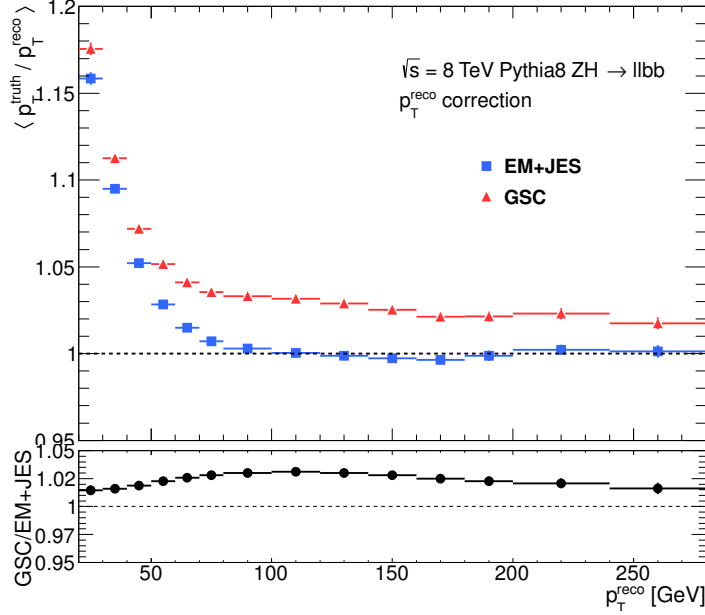


Figure 5.6.: Resolution correction for EM+JES and GS-calibrated b -jets as a function of the reconstructed jet p_T^{reco} , derived from the p_T spectrum of jets from the $b\bar{b}$ decay of a Higgs boson with $m_H = 125$ GeV in simulated VH events.

VH events. It incorporates information about the interplay of the jet resolution and the underlying signal p_T spectrum, i.e. how the spectrum is affected by various resolution effects.

The resolution correction is shown in Figure 5.6 for both EM+JES and GS-calibrated b -tagged jets. Besides different resolution effects at low p_T^{reco} , the correction addresses also scale effects mostly at higher p_T^{reco} . The scale shift, observed between EM+JES and GSC b -jets, can be understood as the product of two separate scaling contributions. Let these be denoted by e.g. $\alpha \times \beta$. Given a falling-off jet p_T spectrum, it is more likely for jets to migrate to higher than to lower p_T . Thus the correction must contain a term with $\alpha < 1$. The all-particle scale is expected to be less than 1, since p_T^{reco} misses a fraction of the energy carried by neutrinos. The calorimeter response, which misses muons and neutrinos in p_T^{truth} , is for EM+JES calibrated jets expected to be larger than 1, while, by construction of the GSC (see Section 4.3.3), it is about 1 for GS-calibrated jets. This is the main source of the scale differences between the two calibrations. Since both calibrations are based on the calorimeter response, the correction must contain a term with $\beta > 1$ to map to the all-particle scale. In case of the EM+JES response, the scale contributions to the resolution correction, $\alpha \times \beta$, balance out to unity, while for the GSC response a scale difference (magnitude of β) with respect to the EM+JES response remains. This scale shift turns out to be about 2-3% at higher p_T^{reco} .

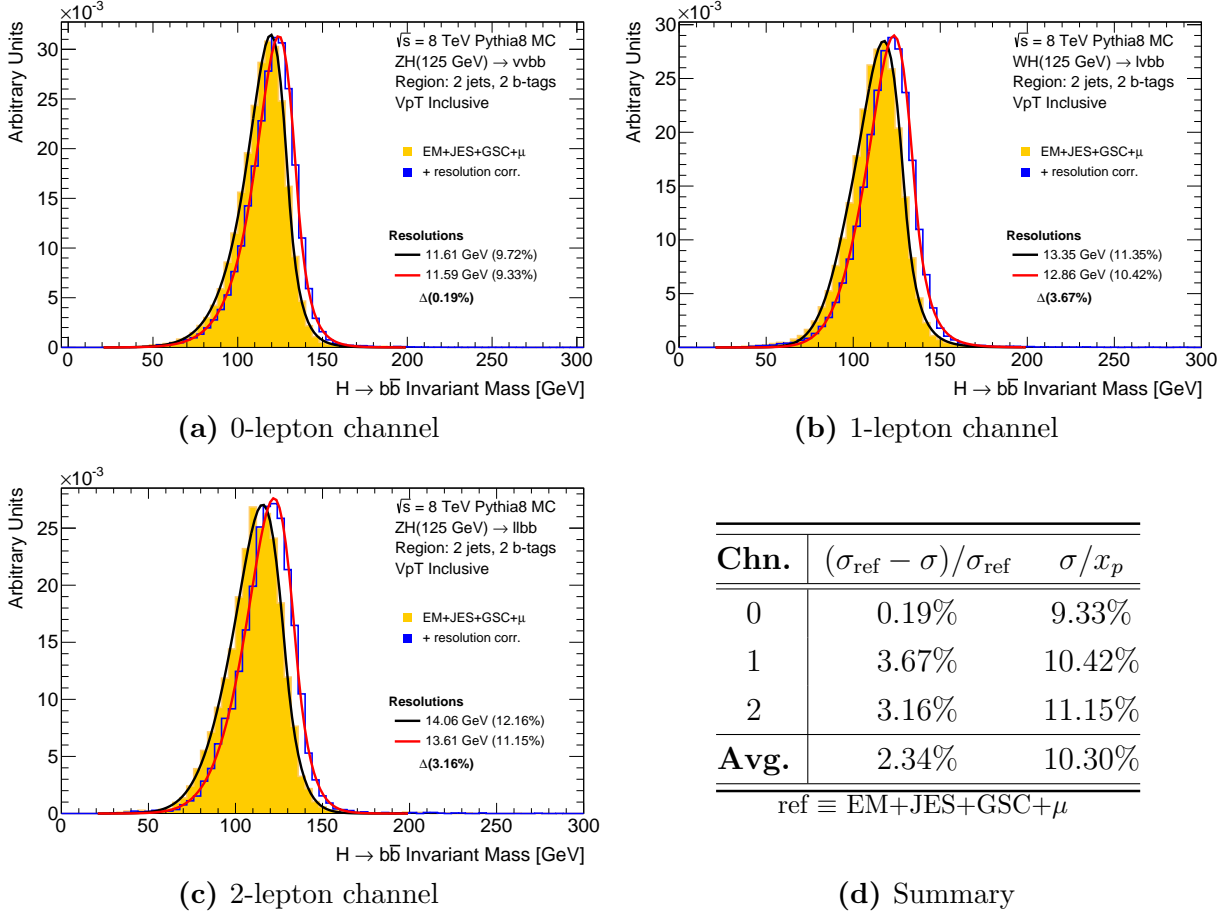


Figure 5.7.: Dijet-invariant-mass distributions of GS-calibrated, muon-in-jet-corrected $H \rightarrow b\bar{b}$ candidates before and after the resolution correction in the combined 2-tag signal regions of the 0-lepton channel (a), 1-lepton channel (b), and the 2-lepton channel (c). The dijet mass resolution improvements are summarized in (d).

This correction is applied only after the muon-in-jet correction. Figure 5.7 shows the dijet mass distributions, inclusive in p_T^V , before and after the resolution correction in the combined 2-tag signal region of each analysis channel in simulated VH events. The dijet mass resolution for the signal is in average improved by $\sim 2\%$ after this correction and is $\sim 10\%$.

5.4.5. Energy calibration summary

The total dijet mass resolution improvements after applying the muon-in-jet correction and the resolution correction are shown for each channel of the dijet-mass analysis in

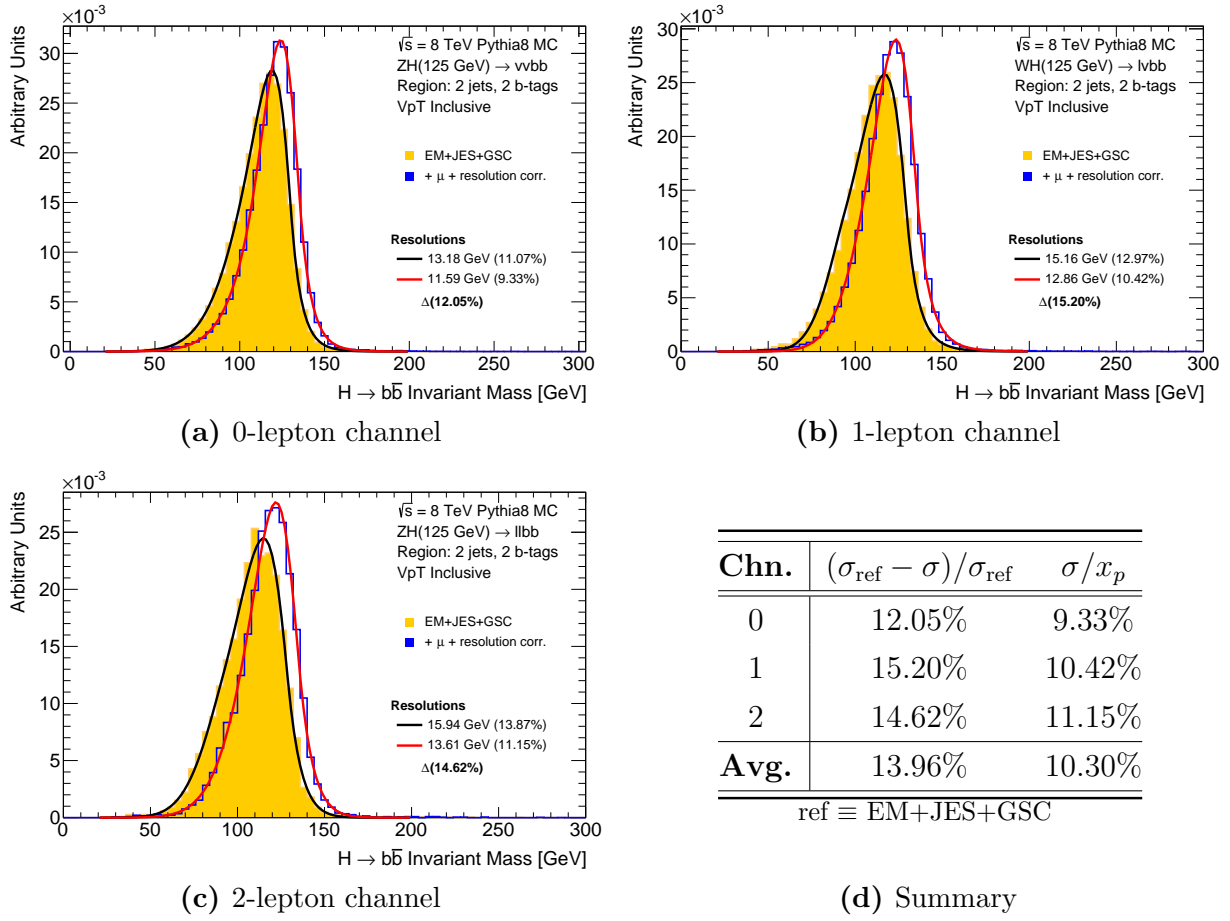


Figure 5.8.: Dijet-invariant-mass distributions of GS-calibrated $H \rightarrow b\bar{b}$ candidates before and after the muon-in-jet correction with subsequent resolution correction in the combined 2-tag signal regions of the 0-lepton channel (a), 1-lepton channel (b), and the 2-lepton channel (c). The dijet mass resolution improvements are summarized in (d).

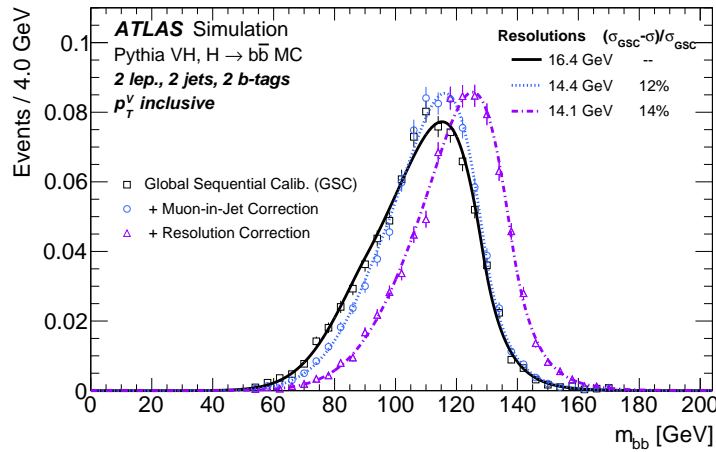


Figure 5.9.: Dijet-invariant-mass distributions as in Figure 5.8c, but for the 2-lepton MVA selection, using jets after the GSC (solid), after adding muons inside jets (dotted), and after correcting resolution effects (dash-dotted).

Figure 5.8. For comparison, the results are also shown for the 2-lepton MVA event selection in Figure 5.9.

In both cases, the mass resolution for the signal is improved by about 14% after both corrections and is about 10%.

5.5. Background composition

In this section, the composition and modelling of backgrounds in each channel of both the dijet-mass analysis and the MVA are reviewed. The likelihood fit, described in Section 5.7, is used to extract the normalisations of the various backgrounds and to adjust their shapes within the constraints from systematic uncertainties discussed in Section 5.6. The inputs to this fit are estimated from data for the MJ background and are taken from simulation for the other backgrounds. In case of the V +jets⁴ and $t\bar{t}$ backgrounds, dedicated corrections are applied before the fit, as explained below, and their normalisations are left free to float in the fit. All distributions presented in this section, are based on the background normalisations and shapes extracted from the fit.

Corrections. As mentioned before, the categorization of the analysis in bins of p_T^V plays a crucial role in the search for $H \rightarrow b\bar{b}$, since the sensitivity increases as a function of p_T^V (i.e. the higher bins provide most sensitivity). Therefore, an accurate modelling of its distribution is vital. Studies of the V +jets backgrounds in the 0-tag regions have revealed a significant mismodelling of the p_T^V distribution, which was found to be strongly correlated with the mismodelling of the $\Delta\phi(\text{jet}_1, \text{jet}_2)$ distribution [191]. A reweighting of the latter distribution, derived via fitting a parameterised function to the data-MC ratio (see Figure 5.10a), considerably improves the modelling of the p_T^V distribution (see Figures 5.10c and 5.10d), but also of other distributions, such as the dijet mass. The $\Delta\phi(\text{jet}_1, \text{jet}_2)$ reweighting is derived independently for both W +jets and Z +jets backgrounds, and is applied in all regions of all analysis channels, based on the different flavour compositions⁵. In $t\bar{t}$ -dominated regions, a mismodelling of the p_T^V variable has also been observed. As mentioned in Section 5.2, $t\bar{t}$ production is simulated with the POWHEG generator interfaced to PYTHIA. Since it was found that the top quark p_T

⁴In the following, Z +hf denotes $V + b\bar{b}$, $V + bc$, $V + bl$, and $V + cc$.

⁵In case of W +jets, the reweighting is only applied to $W + l$ and $W + cl$. In case of Z +jets, the reweighting is only applied to $Z + l$, but a dedicated p_T^Z reweighting is used for $Z + c$ and $Z + b$.

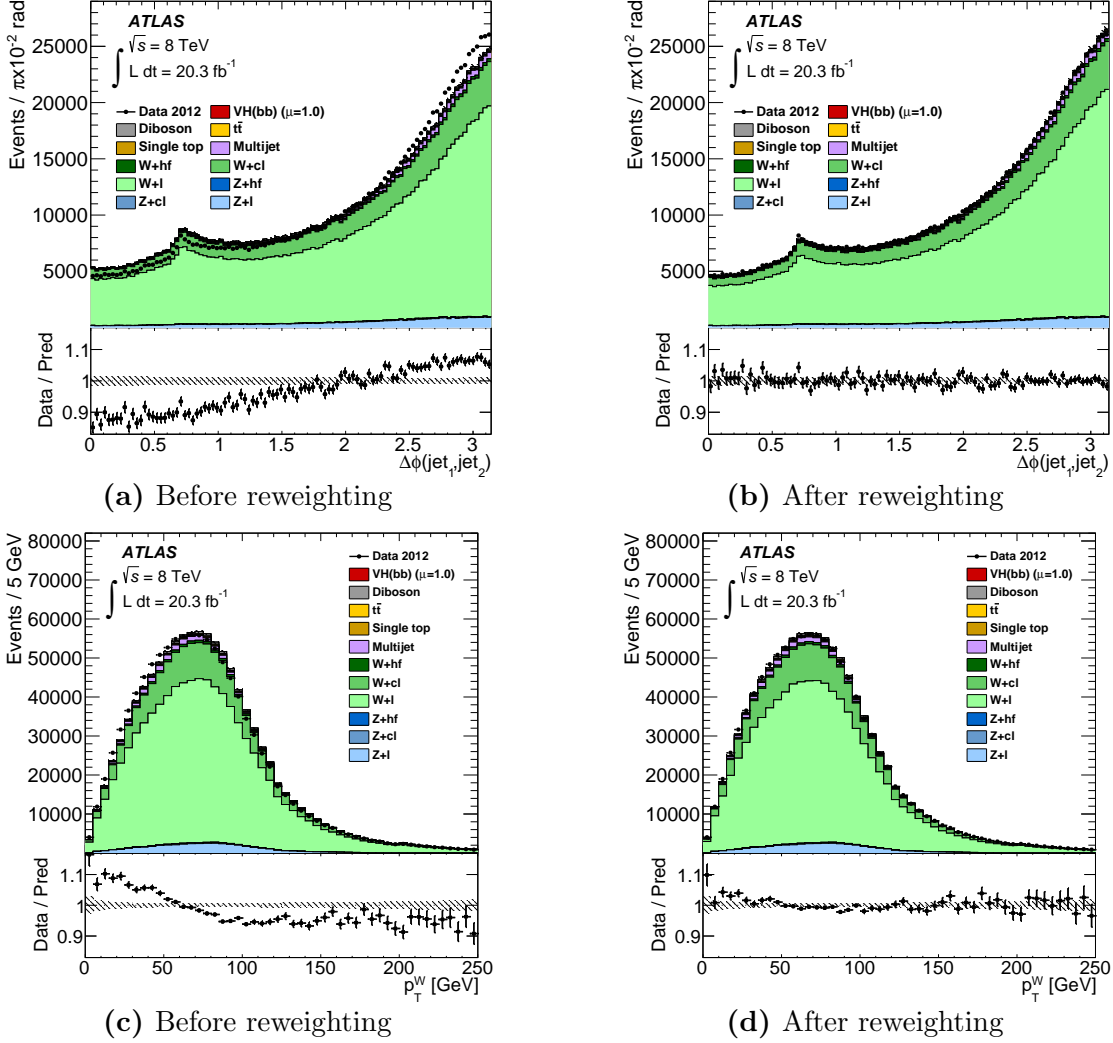
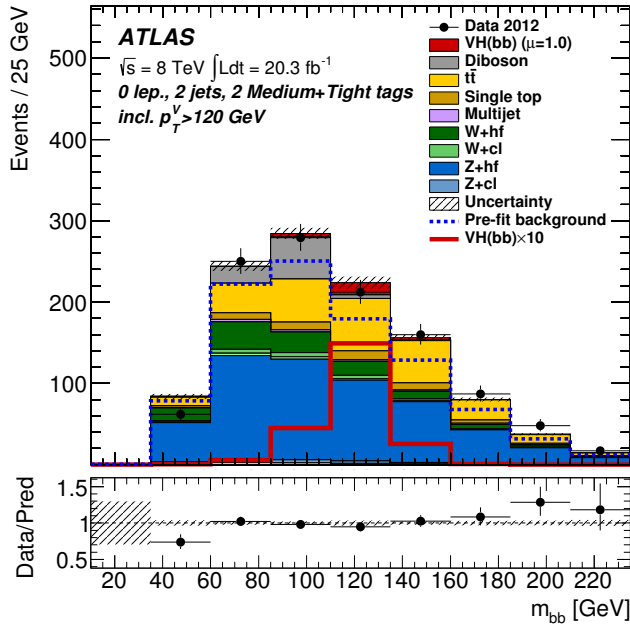


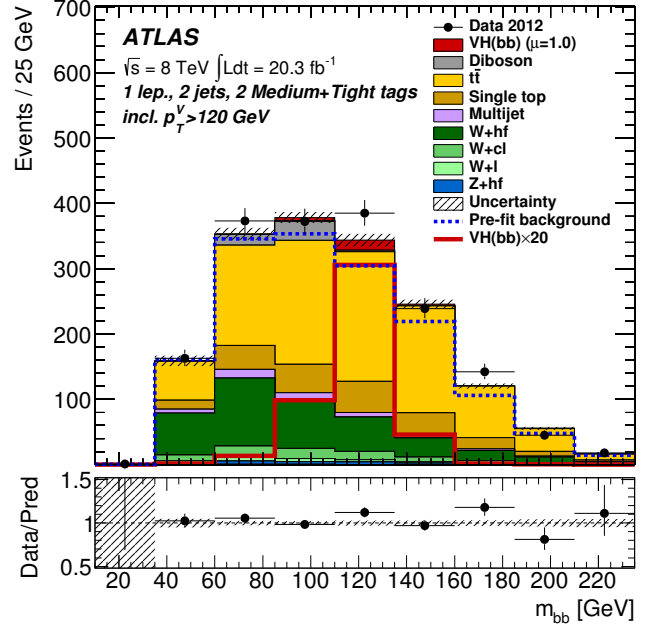
Figure 5.10.: The $\Delta\phi(\text{jet}_1, \text{jet}_2)$ and p_T^W distributions in the 2-jet 2-tag control region of the 1-muon sub-channel using the MVA selection (a/c) before and (b/d) after $\Delta\phi(\text{jet}_1, \text{jet}_2)$ reweighting, which is derived from the data-MC ratio in (a) [8].

spectrum in $t\bar{t}$ events predicted by POWHEG [192] is too hard compared to the data, a corresponding generator-level correction is applied to all $t\bar{t}$ samples used in the analysis.

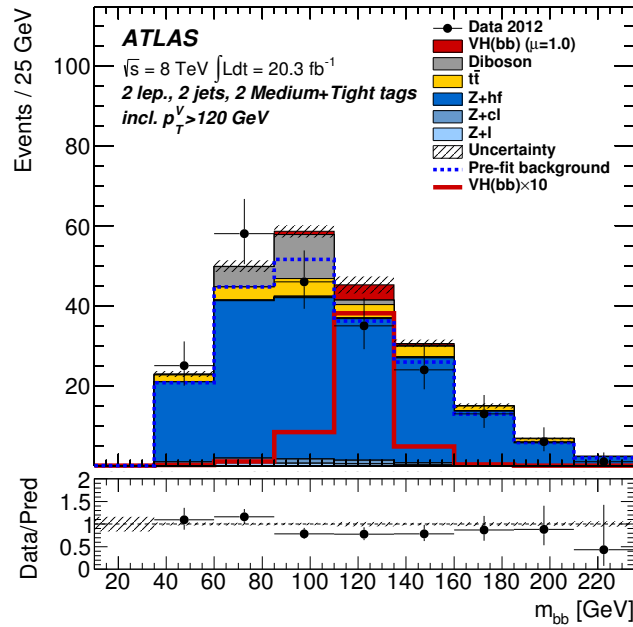
Dijet-mass analysis. Significant variations of the background compositions between the different categories (p_T^V intervals, jet multiplicity, b -tagging) of the three analysis channels are observed. In general, the ratio of signal events (S) over background events (B) is enhanced in 2-jet events with medium and tight b -tagging (MM, TT) and is strongly reduced in 3-jet events with loose b -tagging (LL). Figures 5.11a to 5.11c shows representative dijet mass distributions for each analysis channel in the 2-jet MM+TT categories with $p_T^V > 120$ GeV. In case of the 0-lepton channel, the main backgrounds arise from V +hf (mainly $b\bar{b}$ dijets) and $t\bar{t}$ production. In case of the 1-lepton channel, $t\bar{t}$ production is the largest source of background and is supplemented with significant



(a) 0-lepton channel

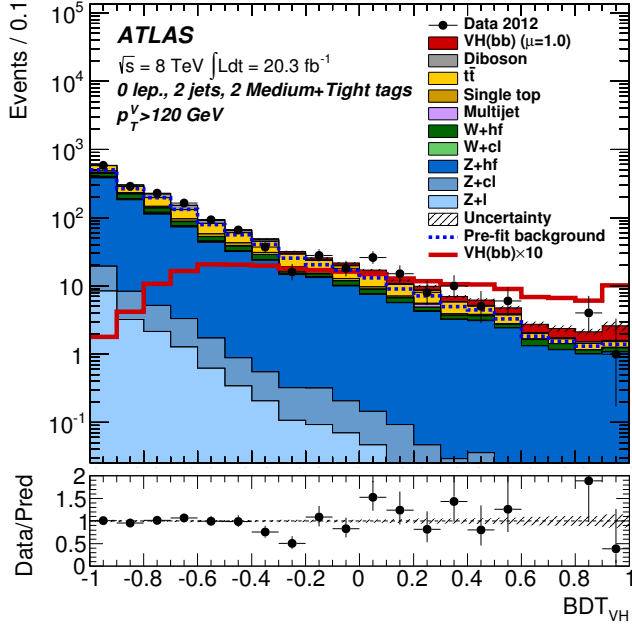


(b) 1-lepton channel

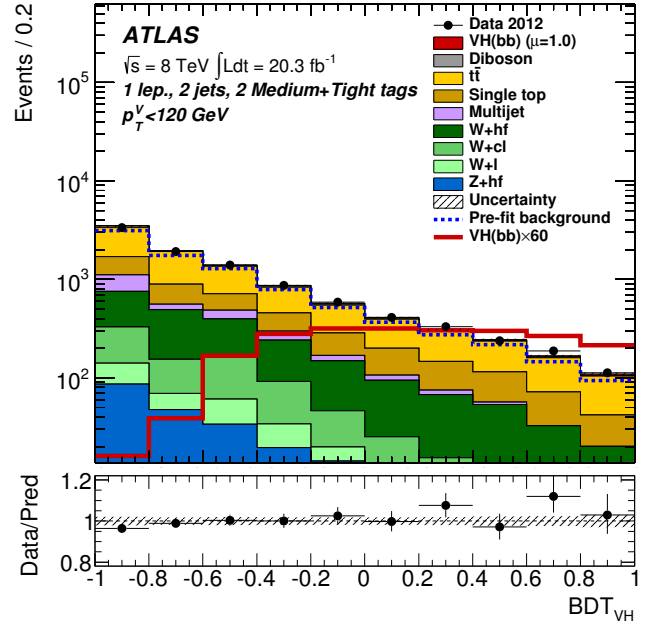


(c) 2-lepton channel

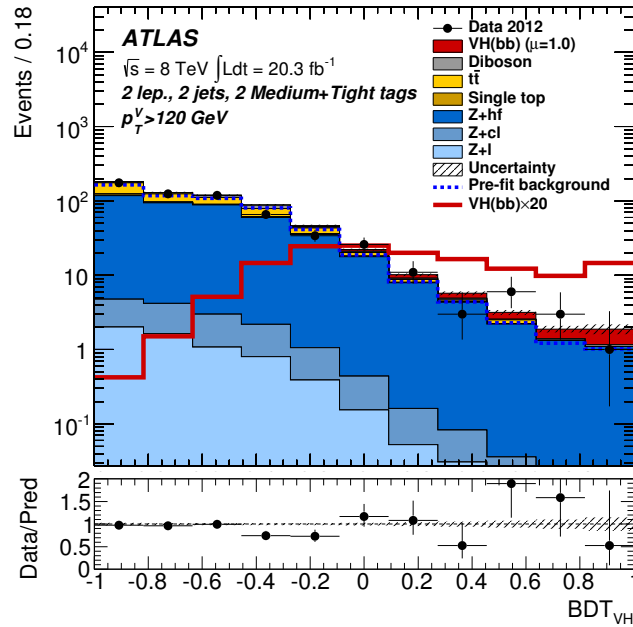
Figure 5.11.: The dijet-mass distributions with MM and TT b -tagging and $p_T^V > 120 \text{ GeV}$ for the 2-jet signal regions of each analysis channel [8].



(a) 0-lepton channel

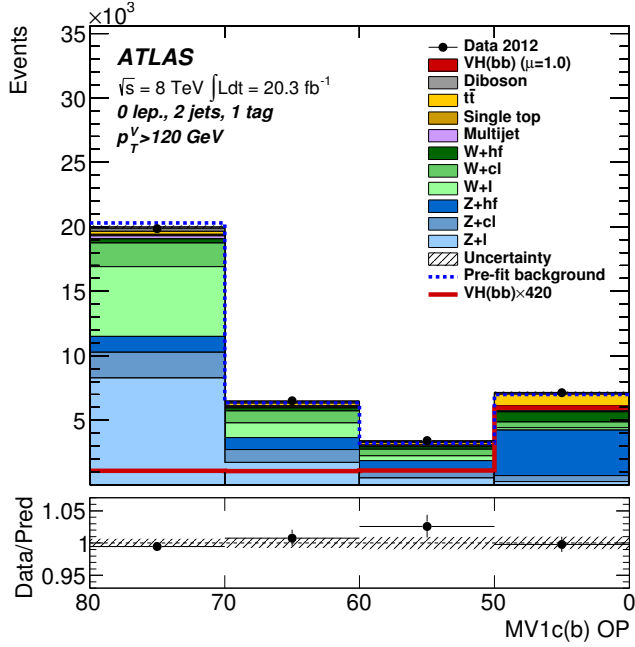


(b) 1-lepton channel

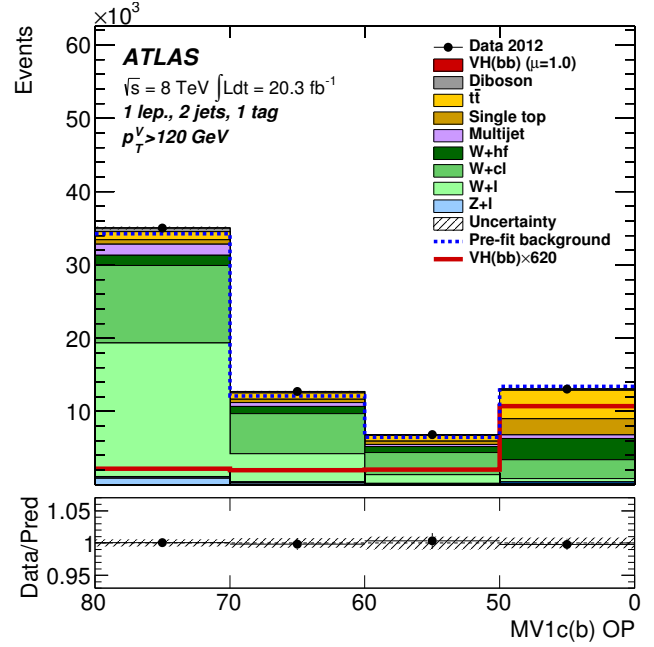


(c) 2-lepton channel

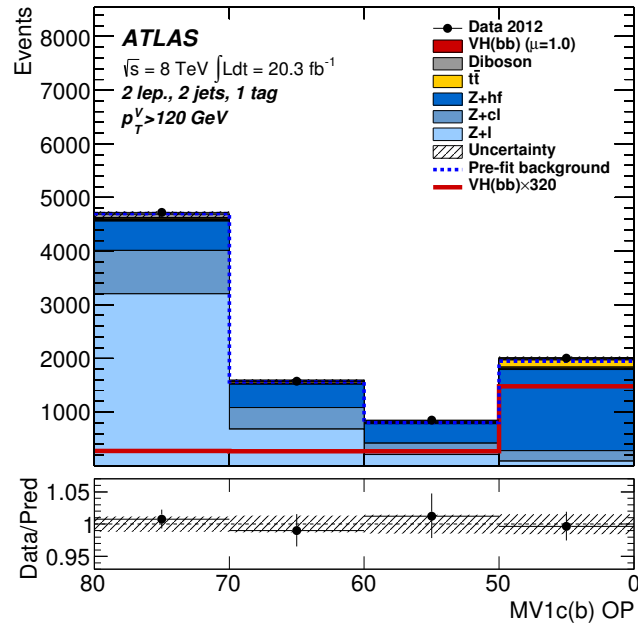
Figure 5.12.: The BDT_{VH} distributions with MM and TT b -tagging and $p_T^V > 120 \text{ GeV}$ for the 2-jet signal regions of each analysis channel [8].



(a) 0-lepton channel



(b) 1-lepton channel



(c) 2-lepton channel

Figure 5.13.: The MV1c output distributions for the 1-tag control regions in the 2-jet category [8].

contributions from single top, multijet and W +hf (mainly $b\bar{b}$ dijets) productions. In case of the 2-lepton channel, Z +hf (mainly $b\bar{b}$ dijets) is clearly the dominant background and receives significant contributions from $t\bar{t}$ and diboson productions.

MVA. The final discriminants of the MVA are the BDT_{VH} output values, which for the signal are expected to be larger than for the backgrounds. These values range from -1 to $+1$. Figures 5.12a to 5.12c shows representative BDT_{VH} distributions for each analysis channel in the 2-jet MM+TT categories with $p_T^V > 120$ GeV. At high values, the background composition is similar to the observations in the dijet-mass analysis discussed above. The dominant contributions arise from V +hf (mainly $b\bar{b}$ dijets) and $t\bar{t}$ production. Since the MVA has a looser constraint on the $\Delta R(\text{jet}_1, \text{jet}_2)$ (see Table 5.2) than the dijet-mass analysis, the $t\bar{t}$ contamination is larger. At low values, one finds backgrounds accumulating, which contain mainly light-quark jets and to a lesser extent, c -quark jets. Besides these distributions, the likelihood fit (Section 5.7) uses also the output weight of the $MV1c$ algorithm (Section 4.3.4) in the 1-tag category (Section 5.3). The corresponding distributions, i.e. for the different b -tagging operating points (Table 4.3), in 2-jet events with $p_T^V > 120$ GeV are shown for each analysis channel in Figures 5.13a to 5.13c. One can see that especially the V +jets backgrounds with mainly light-quark and c -quark jets can be constrained with these distributions in the likelihood fit.

Further distributions can be found in the Appendix A.

5.6. Systematic uncertainties

This analysis is affected by a number of different systematic uncertainties, both experimental and theoretical. In this section, the different sources of these uncertainties, which are taken into account by the likelihood fit (Section 5.7), are summarized below. For a more detailed review, the reader is referred to [8, 143, 152].

Experimental uncertainties. These uncertainties affect the trigger selection, and the physics object reconstruction, identification, energy/momentum calibration and final resolution. Many of these have a small impact on the discriminants of the analysis. For instance, for electrons and muons, these are typically less than 1%. In terms of the jet energy scale (JES), relative uncertainties of about 3% to 1% are assigned to jets with $p_T \sim 20$ GeV to 1 TeV, respectively. The different b -jet energy calibrations and corrections to improve the dijet mass resolution are accounted for with uncertainties of the order

Signal	
Cross section (scale)	1% ($q\bar{q}$), 50% (gg)
Cross section (PDF)	2.4% ($q\bar{q}$), 17% (gg)
Branching ratio	3.3 %
Acceptance (scale)	1.5%–3.3%
3-jet acceptance (scale)	3.3%–4.2%
p_T^V shape (scale)	S
Acceptance (PDF)	2%–5%
p_T^V shape (NLO EW correction)	S
Acceptance (parton shower)	8%–13%
Z+jets	
$Z + l$ normalisation, 3/2-jet ratio	5%
$Z + cl$ 3/2-jet ratio	26%
$Z+hf$ 3/2-jet ratio	20%
$Z+hf/Zbb$ ratio	12%
$\Delta\phi(\text{jet}_1, \text{jet}_2)$, p_T^V , $m_{b\bar{b}}$	S
W+jets	
$W + l$ normalisation, 3/2-jet ratio	10%
$W + cl$, $W+hf$ 3/2-jet ratio	10%
$W + bl$ / $W + bb$ ratio	35%
$W + bc$ / $W + bb$, $W + cc$ / $W + bb$ ratio	12%
$\Delta\phi(\text{jet}_1, \text{jet}_2)$, p_T^V , $m_{b\bar{b}}$	S
$t\bar{t}$	
3/2-jet ratio	20%
High/low- p_T^V ratio	7.5%
Top-quark p_T , $m_{b\bar{b}}$, E_T^{miss}	S
Single top	
Cross section	4% (s -, t -channel), 7% (Wt)
Acceptance (generator)	3%–52%
$m_{b\bar{b}}$, $p_T^{b_2}$	S
Diboson	
Cross section and acceptance (scale)	3%–29%
Cross section and acceptance (PDF)	2%–4%
$m_{b\bar{b}}$	S
Multijet	
0-, 2-lepton channels normalisation	100%
1-lepton channel normalisation	2%–60%
Template variations, reweighting	S

Table 5.5.: Theoretical uncertainties on the VH signal and background modelling. An “S” denotes when only a shape uncertainty is assessed [8].

1-2%. In terms of the jet energy resolution (JER), η -dependent relative uncertainties ranging from 10-20% to 5% are assigned to jets with $p_T \sim 20$ GeV to 1 TeV, respectively. All JES uncertainties are propagated to the E_T^{miss} calculation. The contributions from lepton-related uncertainties are rather small. The energy calibration and associated resolution of energy clusters in the calorimeter, which are not associated to any other physics object, are taken into account with an uncertainty of 8% and 2.5%, respectively. Further uncertainties are related to the flavour-tagging efficiency of jets (e.g. MC-to-data scale factor uncertainties ranging from 2-8%) and to the measurement of the integrated luminosity (2.8%) and the average number of interactions per bunch crossing (4%).

Theoretical uncertainties. There are mainly two categories of theoretical uncertainties, those affecting the VH signal modelling, and those affecting the background modelling. For instance, the former category includes an uncertainty on the cross-sections, which are used to normalize the $q\bar{q} \rightarrow WH$, $q\bar{q} \rightarrow ZH$, and $gg \rightarrow ZH$ MC signal samples. The latter category includes, for instance, uncertainties on the used normalisations, cross-sections, and ratios between 3-jet and 2-jet regions of the analysis. These are summarized in Table 5.5. Their ranking, i.e. their importance in the analysis, is shown in Figure 5.14.

5.7. Statistical procedure

In this section, the statistical procedure to extract the signal strength for $VH(b\bar{b})$ production from data is described. The corresponding results using the full LHC Run-1 dataset are presented in Chapter 7.

The procedure is based on a binned likelihood function, $\mathcal{L}(\mu, \boldsymbol{\theta})$, which is constructed as the product of Poisson-probability terms over the bins of input distributions, and is defined as:

$$\mathcal{L}(\mu, \boldsymbol{\theta}) = \text{Pois}(n | \mu S(\boldsymbol{\theta}) + B(\boldsymbol{\theta})) \left[\prod_{b \in \text{bins}} \frac{\mu Y(\boldsymbol{\theta})_b^{\text{sig}} + Y(\boldsymbol{\theta})_b^{\text{bkg}}}{\mu S(\boldsymbol{\theta}) + B(\boldsymbol{\theta})} \right] \text{Pois}(m | B_{\text{CR}}), \quad (5.5)$$

where $\text{Pois}(\cdot)$ are Poisson distributions with n, m for the number of events. It is a function of the signal strength parameter, μ , that multiplies the expected Standard Model Higgs boson production cross-section, i.e. the expected signal yield $Y(\boldsymbol{\theta})^{\text{sig}}$, in each input bin (b). Since the signal samples are normalized to this cross-section, any deviation from the measured μ value implies a deviation from the Standard Model. The

background content in each bin is denoted by $Y(\boldsymbol{\theta})^{\text{bkg}}$. The expected (total) signal (S) and background (B) yields are functions of nuisance parameters (NPs), $\boldsymbol{\theta}$, which represent their dependence on the systematic uncertainties described in Section 5.6 and are constrained by Gaussian or log-normal probability density functions. Furthermore, an additional “penalty term”, $\text{Pois}(m|B_{\text{CR}})$, is added and serves as a prior to a given NP θ . If θ shifts away from its nominal value of zero, it is decreased by its prior. This term is introduced to emphasise the fact that a NP has been measured in a different dataset (m), where CR refers to a control region (see below).

A test statistic q_μ is then built from the profile likelihood ratio Λ_μ , defined as

$$q_\mu = -2 \ln \Lambda_\mu = -2 \ln \frac{\mathcal{L}(\mu, \hat{\boldsymbol{\theta}}_\mu)}{\mathcal{L}(\hat{\mu}, \hat{\boldsymbol{\theta}})}, \quad (5.6)$$

where the $\hat{\mu}$ and $\hat{\boldsymbol{\theta}}$ parameters maximise the likelihood within $0 \leq \hat{\mu} \leq \mu$, and $\hat{\boldsymbol{\theta}}_\mu$ are NPs that maximise the likelihood for a given μ . The q_μ statistic can then be used to measure the background-only hypothesis with the observed data, $q_0 = -2 \ln \Lambda_0$, and to derive exclusion intervals based on the CL_s method [193, 194].

The input distributions to this test statistics have been already discussed in the previous sections and are summarized in Table 5.6 and discussed here. The inputs to the fit in the dijet-mass analysis comprise:

- 81 2-tag signal regions, i.e. $m_{b\bar{b}}$ distributions in 0/1/2 lepton channels, up to 5 p_{T}^V bins, 2/3-jet and LL/MM/TT categories;

	Dijet-mass analysis			MVA		
Channel	0-lepton	1-lepton	2-lepton	0-lepton	1-lepton	2-lepton
1-tag	$MV1c$			$MV1c$		
LL	$m_{b\bar{b}}$			BDT ^(*)	BDT	
MM 2-tag	$m_{b\bar{b}}$			BDT ^(*)	BDT	BDT
TT	$m_{b\bar{b}}$				BDT	

Table 5.6.: The different input distributions entering the likelihood fit in the dijet-mass analysis and the MVA. (*) In the low p_{T}^V interval of the 0-lepton channel, the MVA uses the $m_{b\bar{b}}$ distributions in the LL, MM and TT 2-tag categories as well as the $MV1c$ distribution in the 1-tag category [8].

- 11 1-tag control regions, i.e. $MV1c$ distributions combined in $p_T^V < 120$ GeV and $p_T^V > 120$ GeV.

The inputs to the fit in the MVA comprise:

- 24 2-tag signal regions, i.e. BDT_{VH} distributions in 0/1/2 lepton channels, up to p_T^V bins, 2/3-jet and LL/MM/TT categories. In the 0-lepton and 1-lepton channels, MM and TT categories are merged. In the 2-jet region with $p_T^V = 100 - 120$ GeV of the 0-lepton channel, the $m_{b\bar{b}}$ distributions are used in addition to the BDT_{VH} discriminants;
- 14 1-tag control regions, i.e. $MV1c$ distributions in both MVA p_T^V regions, and in the 2-jet region with $p_T^V = 100 - 120$ GeV of the 0-lepton channel.

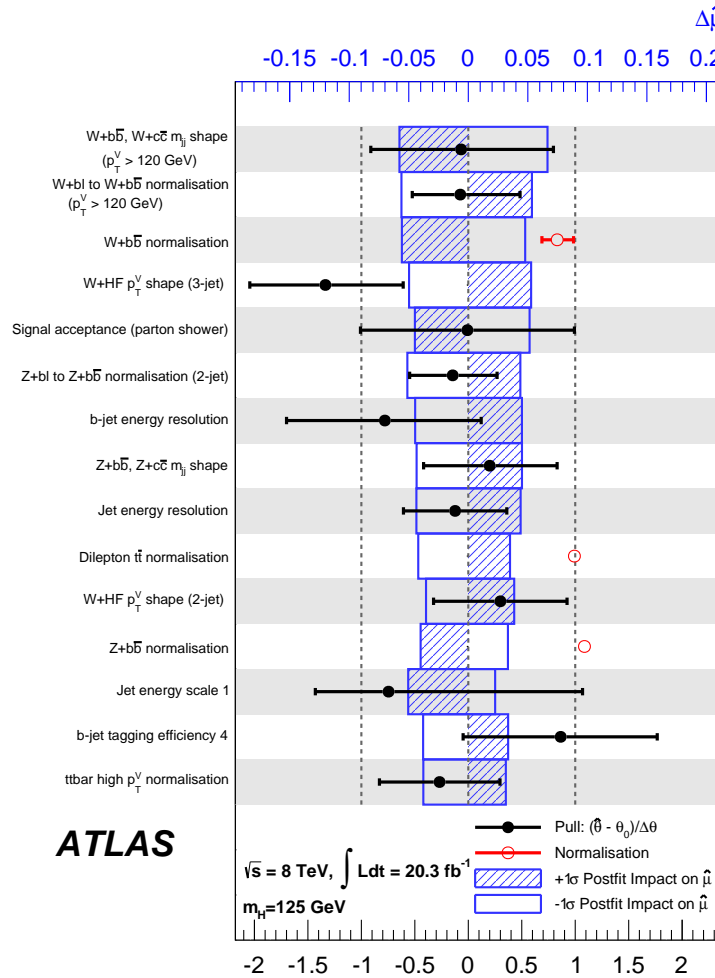


Figure 5.14.: The ranking of the systematic uncertainties in the MVA analysis, ordered by their decreasing impact on $\hat{\mu}$ [8].

In total, the dijet-mass analysis has 584 $m_{b\bar{b}} / MV1c$ input bins in 92 regions, and the MVA has 251 $\text{BDT}_{VH} / MV1c$ input bins in 38 regions.

The impact of the various systematic uncertainties on $\hat{\mu}$ in the 8 TeV MVA analysis is summarized in Figure 5.14. The NPs are ranked in decreasing order of their impact. Concerning the jet energy calibrations presented in this thesis, one should note that the jet energy resolution NP is among the top 10 of this ranking.

Besides the main fit to extract the signal strength for $VH(b\bar{b})$ production, the analysis procedure is validated using a very similar final-state signature: the diboson production VZ with $Z \rightarrow b\bar{b}$, which has a cross-section about five times larger than the production of a Standard Model Higgs boson with $m_H = 125$ GeV. The results of this fit are discussed in Chapter 7.

5.8. Summary

In this chapter, the ATLAS LHC Run-1 analysis strategy for the search of a Standard Model Higgs boson $H \rightarrow b\bar{b}$ resonance produced in association with a W or Z boson has been presented. This included a careful choice of MC samples to model the different signal and background processes and a high-quality physics object (based on Chapter 4) and event selections, which were optimized based on the number of leptons, in bins of p_T^V , the jet multiplicity, and different b -tagging categories. Furthermore, a set of different jet energy calibrations of $H \rightarrow b\bar{b}$ candidates have been derived and improved the dijet mass resolution in the signal significantly. The different background contributions in each channel and the systematic uncertainties affecting this analysis were reviewed. Finally, an overview of the statistical fitting procedure was discussed. The results of this strategy are presented in Chapter 7.

Chapter 6.

Event-level Kinematic Likelihood Fitting

Due to the imperfect nature of particle detectors, i.e. their finite segmentation, material impurities, and technological readout limitations, each and every recorded event contains a variation of reconstruction effects, meaning the relative contributions of these effects may vary on an event-by-event basis. Furthermore, significant contributions arise also from initial and final state radiation effects. As a result, these different reconstruction effects may decrease the $H \rightarrow b\bar{b}$ resonance resolution significantly, while comparably decreasing the probability of observing this signal decay over the background.

The reconstruction performance of ATLAS has been already discussed in Chapters 3 and 4, and several techniques to improve the dijet invariant mass resolution in the 2-tag signal region of the $VH(b\bar{b})$ analysis were presented in Section 5.4. One powerful and well-established technique to improve the resonance resolution and to possibly increase the sensitivity of this search is to utilize an event-level *Kinematic Likelihood Fit* (KF), which exploits the full kinematic potential of any given event topology within the detector uncertainty of its reconstructed signatures.

This chapter presents a kinematic likelihood fit targeting the event topology of the $ZH \rightarrow \ell\ell b\bar{b}$ process. It is applied after the full event selection (Section 5.3) and muon-in-jet corrections in the 2-lepton 2-tag signal regions of both the dijet-mass analysis and the MVA. In Section 6.1, the basic concept or methodology for a KF in this channel is discussed, followed by Section 6.2, with the introduction of the derived event-level likelihood model. The inputs to this model are physics object resolutions and are reviewed in Section 6.3. The corresponding KF software framework, implementing the likelihood

model and all inputs, is described in Section 6.4. Finally, the performance of the KF is evaluated in Section 6.5.

A kinematic likelihood fit may also provide improvements, albeit smaller, in the other decay channels, $WH \rightarrow \ell \nu b \bar{b}$ and $ZH \rightarrow \nu \bar{\nu} b \bar{b}$. However, these KF's are left for future versions of this analysis.

6.1. Methodology

The analysis of the $ZH \rightarrow \ell \ell b \bar{b}$ process has the beneficial feature that the expected or true signal event topology is fully reconstructed and balanced in the transverse plane. At the Monte Carlo truth level of this process, the E_T^{miss} should only arise from the inherent transverse momentum of the colliding partons and from semileptonic b -jet decays. The former determines the resolution to which the transverse energy of any given event can be balanced. Therefore, one can vary the energies of the reconstructed particles to constrain the event to a balanced configuration within the respective resolutions. Electrons and muons from the Z boson decay have a significantly better energy resolution than the b -jets from the Higgs boson, therefore, the jet energies are essentially balanced against nearly static lepton objects. This is illustrated in Figure 6.1. Therefore, one can improve the measurement of the jet kinematics by maximizing an event-level likelihood, built from the expected $VH(b\bar{b})$ signal topology, but without considering the expected mass of the dijet system, i.e. the Higgs boson mass.

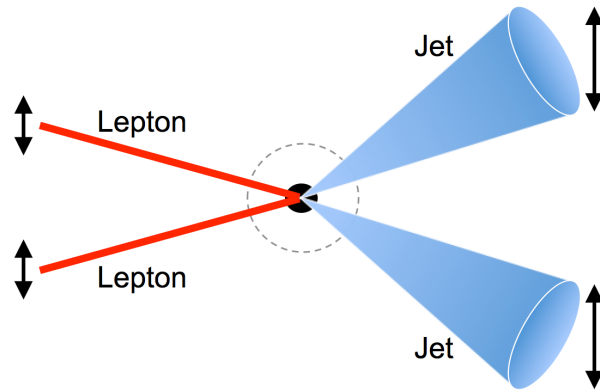


Figure 6.1.: Illustration of the event-level simultaneous parameter set $\{E, \eta, \phi, \dots\}$ variation (arrows) within each parameter's uncertainty (arrow magnitude) of the $Z(\ell\ell)H(b\bar{b})$ system.

The event-level likelihood estimation is based on the *method of maximum likelihood*. This means that the probability density of observing a measurement y_i^{obs} (e.g. the reconstructed b -jet momentum from a Higgs boson candidate) given a corresponding prediction y_i^{pred} of an underlying hypothesis or *likelihood model* is maximized within the constraints associated to y_i in a given event. This likelihood model (Section 6.2) is based on the expected $Z(\ell\ell)H(b\bar{b})$ kinematics and topology and is derived from Monte Carlo simulations. It comprises a set of characteristic probability density functions (PDFs), $f(y_i^{\text{obs}}|y_i^{\text{pred}})$, associated to the $\ell\ell b\bar{b}$ system and each object. These are then combined in a *likelihood function*,

$$\mathcal{L}(y_1^{\text{obs}}, \dots, y_N^{\text{obs}} | y_1^{\text{pred}}, \dots, y_N^{\text{pred}}) = \prod_i^N f(y_i^{\text{obs}} | y_i^{\text{pred}}), \quad (6.1)$$

from which a test statistic is built, using the corresponding log-likelihood $-2\ln \mathcal{L}^1$, which can then be minimized by simultaneous variation of the likelihood model parameters using numerical minimization techniques.

6.2. Likelihood model

A model has been constructed in which the reconstructed $\ell\ell b\bar{b}$ system is constrained to be balanced in the transverse plane. This model is optimized for the 2-jet 2-tag signal region² of the 2-lepton analysis, i.e. the event contains 2 jets, from which both are at least loosely b -tagged. Although most of the sensitivity in the 2-lepton channel arises from this region, the model considers also events with 3 jets, from which only two are at least loosely b -tagged. This region contains more contributions from hard final and initial state radiation.

The likelihood model uses *fundamental input parameters* (Section 6.2.1), which characterize the event kinematics and topology of the ZH final-state signatures, and employs *fundamental constraints* (Section 6.2.2) to bound the variation of the parameters. The term “fundamental” refers to the fact that only basic properties of the signatures’ four-vectors and their combination are considered. This choice is motivated to obtain a baseline of a KF, which can be easily integrated in the overall $VH(b\bar{b})$ analysis. As

¹The “minus” sign and the factor “2” are purely conventional and are used for numerical *minimization* purposes.

²See Section 5.3 for naming conventions.

studies have shown, variations of this likelihood model do not significantly improve the performance of the KF. Some of these studies will be discussed in the context of Section 6.5.

6.2.1. Fit parameters and constraints

The inputs of the likelihood model are comprised by 14 fit parameters:

- the energies of two electrons (E) or inverse transverse momenta of two muons ($1/p_T$) from the selected Z boson candidate, denoted respectively by the symbol $\Omega_\ell = \{E, 1/p_T\}$,
- the transverse momenta of two b -tagged jets from the selected $H \rightarrow b\bar{b}$ candidate,
- the pseudorapidities (η_i) and azimuthal angles (ϕ_i) of the two selected electrons or muons ($i = \{\ell_1, \ell_2\}$) and the two selected b -tagged jets ($i = \{j_1, j_2\}$),
- the transverse momentum of the $\ell\ell b\bar{b}$ system, evaluated with the sum of all lepton and jet momenta in the x - and y - direction, denoted by $\sum p_{x,y}^{\ell\ell b\bar{b}}$,
- the reconstructed dilepton mass $m_{\ell\ell}$,

$$m_{\ell\ell}^2 = (E_1 + E_2)^2 - \sum_{i=x,y,z} (p_{i,1} + p_{i,2})^2,$$

formed by the two selected electrons or muons from the Z boson candidate.

The variation of these parameters are bound by 4 fit constraints:

- the $m_{\ell\ell}$ is constrained to follow a Breit-Wigner (\mathcal{B}) distribution,

$$\mathcal{B}(m_{\ell\ell}|M_Z) = \frac{k}{(m_{\ell\ell}^2 - M_Z^2)^2 + M_Z^2 \Gamma_Z^2} \quad \text{with} \quad k = \text{const.},$$

around a pole mass ($M_Z = 91.1876$ GeV) and width ($\Gamma_Z = 2.4952$ GeV) of the Z boson,

- the $\sum p_{x,y}^{\ell\ell b\bar{b}}$ is constrained to be zero with a nominal width of ~ 9 GeV, as determined from ZH simulated events,

- the jet transverse momenta are constrained by dedicated asymmetric transfer functions (TF), relating the true jet transverse momenta to their reconstructed values (Section 6.3.2),
- all other jet and lepton parameters are assumed to follow Gaussian distributions (\mathcal{G}), i.e. the PDFs are defined as

$$\mathcal{G}(y_i^{\text{obs}}|y_i^{\text{pred}}) = \frac{1}{\sqrt{2\pi}\sigma_{y_i}} \exp\left(-\frac{(y_i^{\text{obs}} - y_i^{\text{pred}})^2}{2\sigma_{y_i}^2}\right),$$

with the corresponding object resolutions σ_{y_i} , as discussed in Section 6.3.

Furthermore, similar to the resolution correction in the 0-lepton and 1-lepton channels (Section 5.4.4), an in-situ correction is applied via introducing a prior built from the expected true jet p_T spectrum in ZH simulated events (Section 6.3.2).

6.2.2. Event-level Likelihood Function

Given the fit parameters and constraints defined above, the probability density function is defined as

$$\mathcal{L} = \prod_i f(y_i^{\text{obs}}|y_i^{\text{pred}}) \quad (6.2)$$

$$= \mathcal{G}(\Omega_\ell^n; \Omega_\ell^0, \sigma_\Omega^0) \quad (6.3)$$

$$\times \prod_{i=j} \mathcal{L}_{\text{TF}}^i(p_{T,i}^n; p_{T,i}^0, \eta_i^0, \mu_{\text{lep},i}^0) \mathcal{L}_{\text{truth}}^i(p_{T,i}^n; p_{T,i}^0, p_{T,i}^{\ell\ell,0}, \eta_i^0, \mu_{\text{lep},i}^0) \quad (6.4)$$

$$\times \prod_{i=\ell,j} \mathcal{G}(\eta_i^n; \eta_i^0, \sigma_\eta^0) \mathcal{G}(\phi_i^n; \phi_i^0, \sigma_\phi^0) \quad (6.5)$$

$$\times \prod_{i=x,y} \mathcal{G}\left(\sum p_i^n; \sum p_i, \sigma_{\sum p_i}^0\right) \quad (6.6)$$

$$\times \mathcal{B}(m_{\ell\ell}^n; M_Z, \Gamma_Z), \quad (6.7)$$

where (6.3) and (6.4) are the energy/momentum PDFs, (6.5) are the angular PDFs, (6.6) is the constraining $\sum p_{x,y}^{\ell\ell\bar{b}\bar{b}}$ PDF, and (6.7) is the Z boson Breit-Wigner PDF. The indices (i) refer to either $\ell = \{e_1, e_2\}$ (electrons) or $\ell = \{\mu_1, \mu_2\}$ (muons), $j = \{j_1, j_2\}$ (jets), and $\{x, y\}$ (x - and y -directions). The integrated \mathcal{L}_{TF} likelihood corresponds to the jet transfer functions, which are derived as a function of the reconstructed jet p_T and η for both semileptonic ($\mu_{\text{lep}} \equiv 1$) and non-semileptonic ($\mu_{\text{lep}} \equiv 0$) b -jet decays, i.e.

with or without reconstructed muon within the jet (see Section 5.4.3). The integrated $\mathcal{L}_{\text{truth}}$ likelihood corresponds to the in-situ resolution corrections, which are derived as a function of the reconstructed jet p_T , the dilepton $p_T^{\ell\ell}$ and the jet η for both semileptonic and non-semileptonic b -jet decays. Both \mathcal{L}_{TF} and $\mathcal{L}_{\text{truth}}$ are discussed in Section 6.3.2.

Finally, Equation 6.2 is used to build a test statistic,

$$\begin{aligned}
 -2 \ln \mathcal{L} = & \frac{(\Omega_\ell^n - \Omega_\ell^0)^2}{\sigma_\Omega^2} - 2 \sum_{i=j} (\ln L_{\text{TF}}^i + \ln L_{\text{truth}}^i) \\
 & + \sum_{i=\ell,j} \left(\frac{(\eta_i^n - \eta_i^0)^2}{\sigma_\eta^2} + \frac{(\phi_i^n - \phi_i^0)^2}{\sigma_\phi^2} \right) \\
 & + \sum_{i=x,y} \frac{(\sum p_i^n - \sum p_i)^2}{\sigma_{\sum p_i}^2} + 2 \ln ((m_{\ell\ell}^2 - M_Z^2)^2 + M_Z^2 \Gamma_Z^2)
 \end{aligned} \tag{6.8}$$

where all constant terms are discarded, since only the minimum is of interest. This statistic is then used to minimize and balance the reconstructed $\ell\ell b\bar{b}$ system on an event-by-event basis.

6.3. Fit resolutions

The parameter variation in the kinematic likelihood fit is performed within the boundaries of the associated physics object resolutions. These fit input distributions are summarized this section.

6.3.1. Electrons and muons

The electron/muon energy/momentum resolution and scale has already been discussed in Section 4.2.2. The electron energy resolution is obtained for a given reconstructed energy cluster and a particular η region from e.g. Figure 4.7 (similar for other η bins). Figure 6.2a shows the inclusive distribution of the electron energy resolution, with and without the effective constant term (Equation 4.4, Figure 4.6) applied, in the 2-tag signal region using simulated $Z(ee)H$ events. Similarly, the muon momentum resolution is obtained for a given muon p_T and a particular η region from e.g. Figure 4.8. Figure 6.2b shows the inclusive distribution of the muon momentum resolution (q/p), with and without the resolution scale factors from Figure 4.9 applied, in the 2-tag signal region

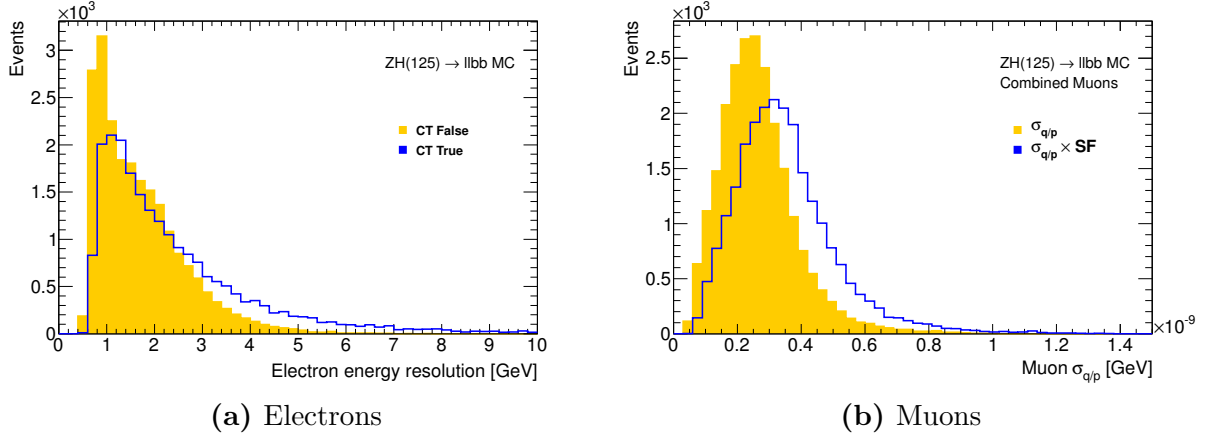


Figure 6.2.: Inclusive distributions of (a) the electron energy resolution, with and without the effective constant term (CT) applied, and of (b) muon momentum resolution, with and without resolution scale factors applied.

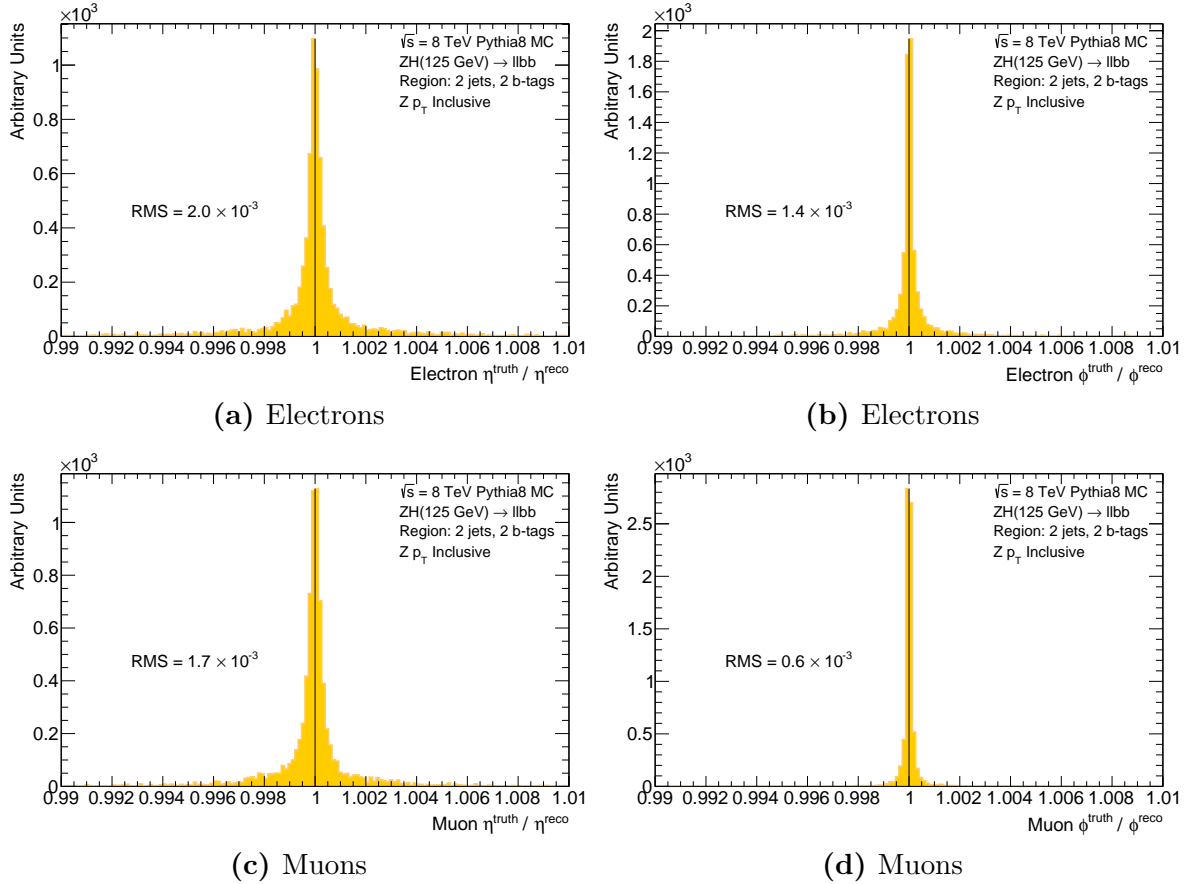


Figure 6.3.: Inclusive distributions of the $\eta^{\text{truth}} / \eta^{\text{reco}}$ and $\phi^{\text{truth}} / \phi^{\text{reco}}$ ratios for electrons (a,b) and muons (c,d).

using simulated $Z(\mu\mu)H$ events. Figure 6.3 compares the angular properties of the reconstructed electron or muon to the true electron or muon from the Z boson decay associated with the Higgs boson decay in ZH simulated events. The pseudorapidity ratio $\eta^{\text{truth}}/\eta^{\text{reco}}$ and azimuthal-angle ratio $\phi^{\text{truth}}/\phi^{\text{reco}}$ are shown for both electrons and muons, and exhibit a significantly smaller standard deviation when compared to the corresponding distributions for jets, as shown in Figure 6.4. This suggests that the lepton η and ϕ parameters in Equation 6.8 may be considered as nearly static parameters with respect to those from jets, i.e. very small improvements in the post-fit dijet invariant mass resolution may be gained from including the η or ϕ parameters of the leptons in the likelihood maximization. Dedicated KF studies, with and without these parameters, have confirmed this. Furthermore, when four degrees of freedom are removed from the likelihood with these parameters, the computation performance increases substantially.

6.3.2. Jets

Similarly, the angular properties of the reconstructed b -tagged jets are compared to the true b -jets from the $H \rightarrow b\bar{b}$ decay in ZH simulated events. Figure 6.4 shows the $\eta^{\text{truth}}/\eta^{\text{reco}}$ and $\phi^{\text{truth}}/\phi^{\text{reco}}$ ratios in the 2-tag regions. The former distribution has a larger standard deviation than the latter distribution, and, as already mentioned, both distributions are significantly wider than those of leptons. Further angular properties are discussed in the context of Section 6.5. In the remainder of this section, the corresponding PDFs of \mathcal{L}_{TF} and $\mathcal{L}_{\text{truth}}$ in Equation 6.2 are derived and discussed.

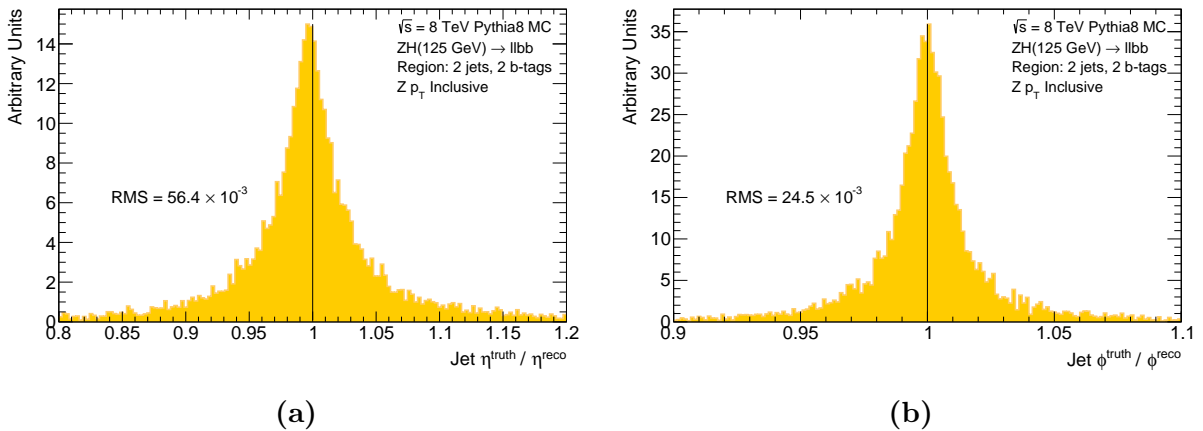


Figure 6.4.: Inclusive distributions of the $\eta^{\text{truth}}/\eta^{\text{reco}}$ (a) and $\phi^{\text{truth}}/\phi^{\text{reco}}$ (b) ratios for selected b -jets .

Transfer functions for b -tagged jets

Unlike for electrons and muons, the p_T resolution of jets cannot be assumed to be Gaussian-distributed, given the asymmetric tails observed in the jet response. Instead, dedicated *jet transfer functions* are derived, which relate the true jet p_T^{truth} , including muons and neutrinos from semileptonic decays, to their corresponding reconstructed jet p_T^{reco} . These are ratios of $p_T^{\text{reco}}/p_T^{\text{truth}}$ as a function of p_T^{reco} . This is shown in Figure 6.5a inclusively, after the muon-in-jet correction has been applied to both jets in the 2-jet 2-tag signal region. As expected, the core of the distribution is below one, given that a fraction of the energy is carried by neutrinos and is not accounted for in p_T^{reco} . Applicable transfer functions can then be derived by dividing this distribution into bins of p_T^{reco} and by fitting each individual distribution, which can then be used as a PDF in \mathcal{L}_{TF} . As Figure 6.5b shows, the functions become more and more narrow and with a mean closer to one as the p_T^{reco} rises. This can also be seen in Figure 6.6, which shows the σ of each Bukin fit as a function of the centre of the fitted p_T^{reco} bin.

In the kinematic likelihood fit, these transfer functions are then used as follows: a $p_T^{\text{reco}}/p_T^{\text{fit}}$ ratio is chosen such that at this value the $p_T^{\text{reco}}/p_T^{\text{truth}}$ ratio is maximal. Technically speaking, the corresponding maximal y -value represents a "likelihood value" and replaces \mathcal{L}_{TF} in Equation 6.8.

One can further compare the shape of the transfer functions for semileptonic and non-semileptonic b -jets. This is shown inclusively in Figure 6.7a. The semileptonic

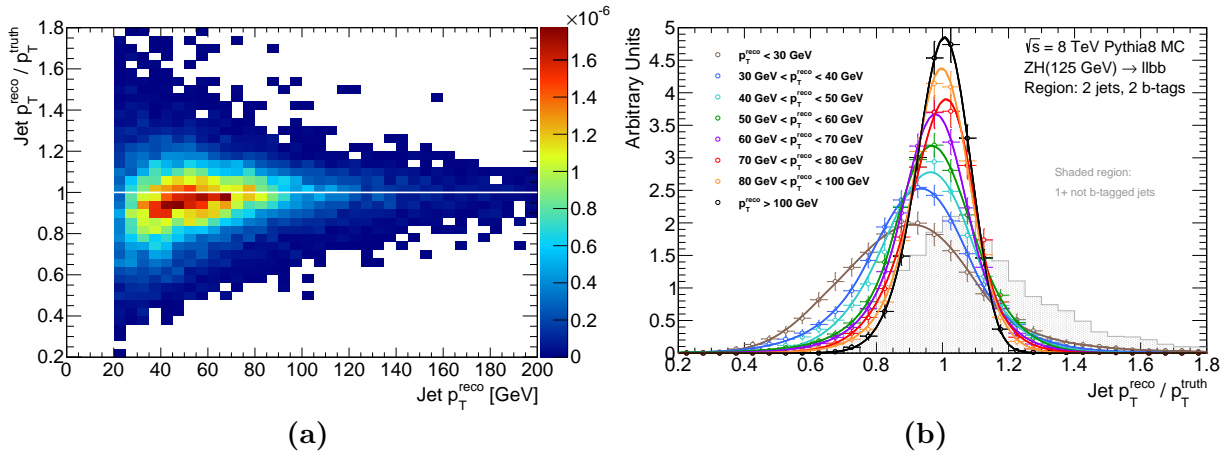


Figure 6.5.: Jet transfer functions, inclusive (a) and in bins of p_T^{reco} (b). The shaded distribution in (b) corresponds to non- b -tagged jets from Figure 6.8 and is only shown for comparison.

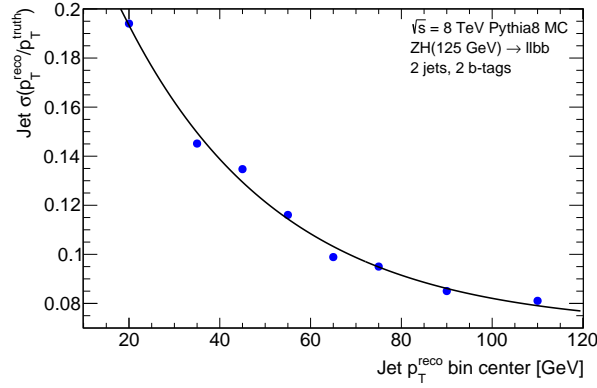


Figure 6.6.: The σ of the fitted transfer functions in Figure 6.5b as a function of the corresponding p_T^{reco} bin centre, fitted with an exponential function.

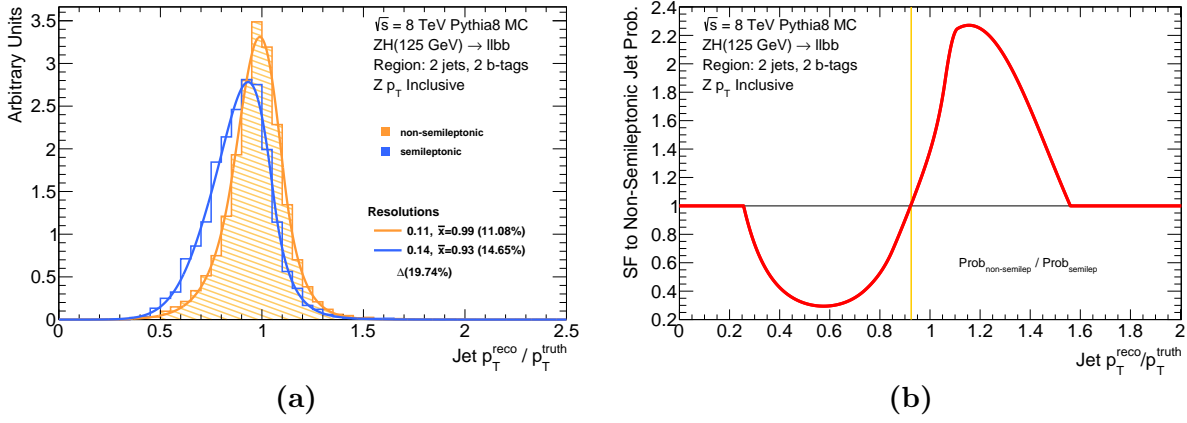


Figure 6.7.: Jet transfer functions, inclusive in p_T^{reco} , for both semileptonic and non-semileptonic b -jet decays in the 2-jet 2-tag signal region (a). The difference between the two functions is shown in (b) in terms of the scale factors from the semileptonic to the non-semileptonic probability value.

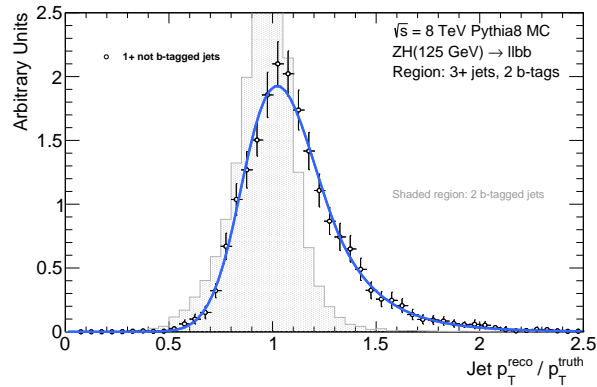


Figure 6.8.: Jet transfer function, inclusive in p_T^{reco} , for non- b -tagged jets in events with at least three jets, two of them b -tagged. For comparison, the shaded distribution corresponds to the two b -tagged jets.

distribution is found with a lower mean below one and a width of about 20% larger than the non-semileptonic distribution. These differences can also be expressed in terms of a scaling factor (SF), transforming a semileptonic jet probability into a non-semileptonic jet probability as a function of $p_T^{\text{reco}}/p_T^{\text{truth}}$. This is shown in Figure 6.7b.

The distribution in Figure 6.8, which is also shown for comparison in the shaded region of Figure 6.5b, corresponds to the transfer function for non- b -tagged jets in events with at least three jets, where exactly two of them are b -tagged. As one can see, it has a long high tail with a mean larger than one, i.e. the p_T^{reco} is mostly larger than the predicted p_T^{truth} . In comparison, the shaded distribution in this figure corresponds to the two b -tagged jets in the event and, as in the 2-jet 2-tag case, it has a more narrow shape with a mean below one.

In-situ resolution correction for b -tagged jets

Similar to the resolution correction discussed in Section 5.4.4, an in-situ correction is integrated in the kinematic likelihood as a prior built from the truth jet p_T^{truth} spectrum as a function of the reconstructed Z boson transverse momentum, $p_T^{\ell\ell}$. The resulting distributions are fitted and used as PDFs in $\mathcal{L}_{\text{truth}}$. As Figure 6.9 shows, the functions become broader at higher $p_T^{\ell\ell}$ with longer tails at higher p_T^{truth} . In the kinematic likelihood fit, these functions are used as follows: a p_T^{fit} value is chosen for a given $p_T^{\ell\ell}$, such that

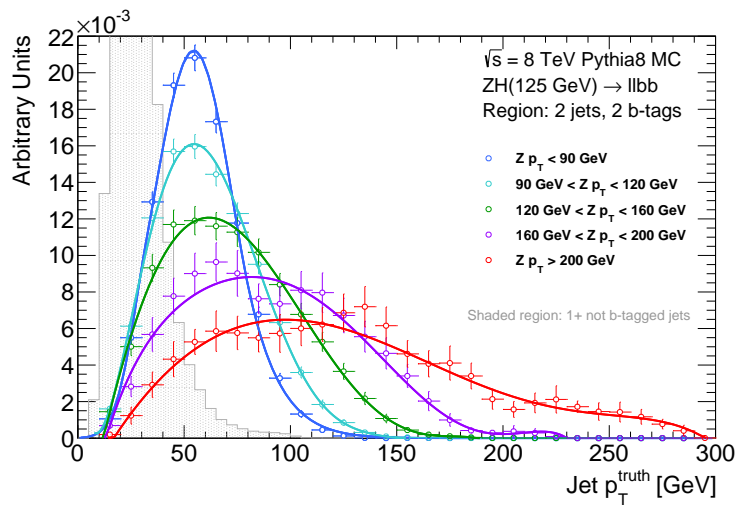


Figure 6.9.: In-situ resolution correction, in the form of a prior, built from the expected p_T^{truth} spectrum as a function of the reconstructed Z boson transverse momentum. The shaded distribution corresponds to non- b -tagged jets from Figure 6.11 and is only shown for comparison.

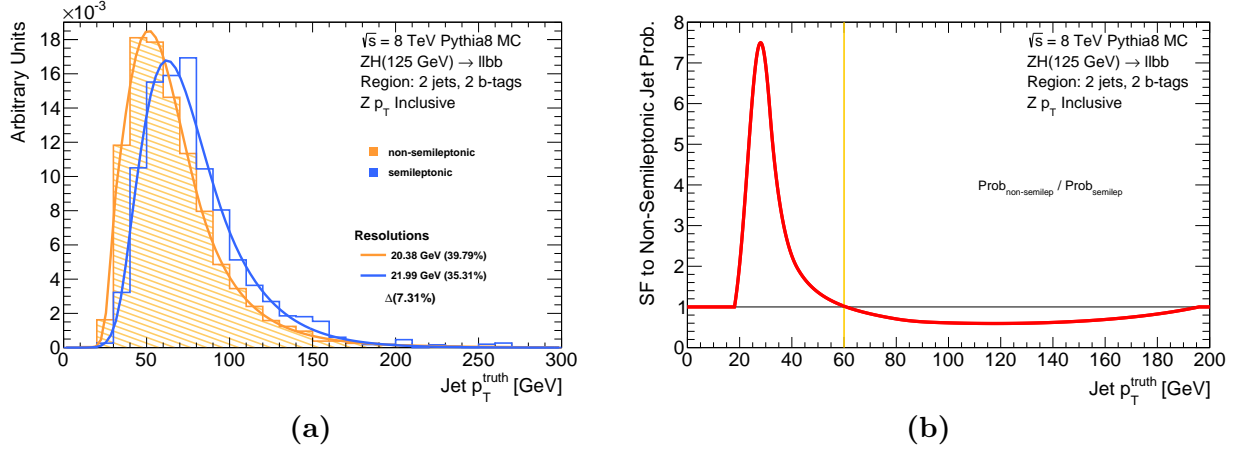


Figure 6.10.: In-situ resolution correction, inclusive in $p_T^{\ell\ell}$, for both semileptonic and non-semileptonic b -jet decays in the 2-jet 2-tag signal region (a). The difference between the two functions is shown in (b) in terms of the scale factors from the semileptonic to the non-semileptonic probability value.

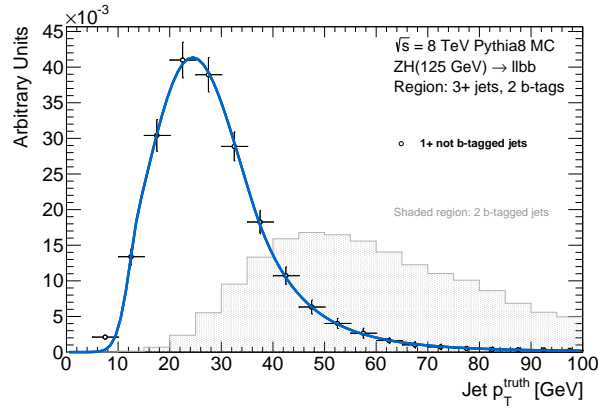


Figure 6.11.: In-situ resolution correction, inclusive in $p_T^{\ell\ell}$, for non- b -tagged jets in events with at least three jets, two of them b -tagged. For comparison, the shaded distribution corresponds to the two b -tagged jets.

at this value the p_T^{truth} is maximal. Technically speaking, as for the transfer functions discussed above, the corresponding maximal y -value represents a "likelihood value" and replaces $\mathcal{L}_{\text{truth}}$ in Equation 6.8. As for the transfer functions, the semileptonic and non-semileptonic differences are evaluated in Figure 6.10. The semileptonic distribution has a width of about 7% larger than the non-semileptonic distribution. For comparison, the inclusive p_T^{truth} distribution for non- b -tagged jets, in events with at least three jets, from which two are b -tagged, is shown in Figure 6.11 and in the shaded region of Figure 6.9. It peaks sharply at low p_T^{truth} .

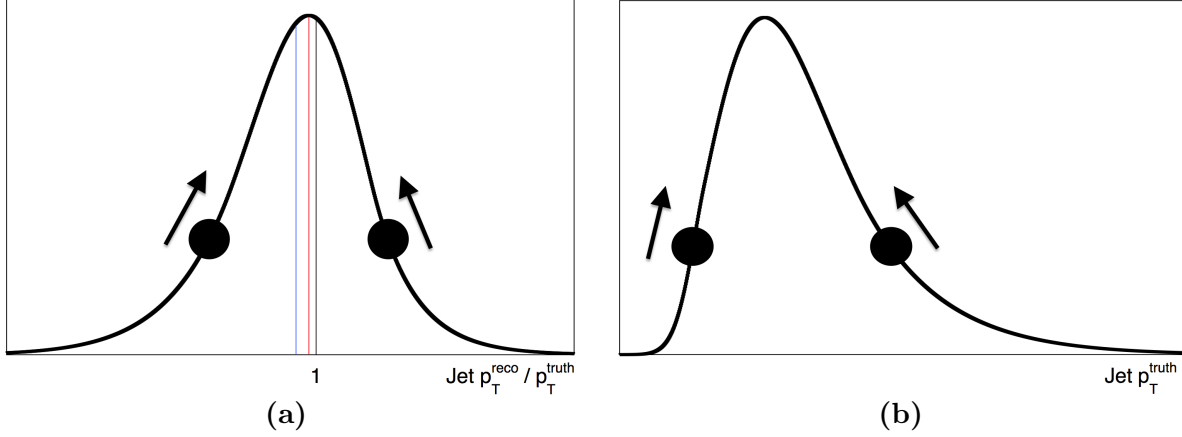


Figure 6.12.: Illustration of the interference of two different PDFs used in the kinematic likelihood fit as a result of jet resolution/scale effects. The PDFs are the jet transfer functions (a) and the in-situ resolution correction (b). The large black dots represent reconstructed jets at the indicated region of the spectrum. In (a), the black line refers to unity, the red line refers to the maximum of the distribution, and the blue line refers to the mean of the distribution (see text for details).

PDF interference: jet resolution and scale

In Section 5.4, jet resolution and scale effects were already discussed in the context of the global sequential calibration. Furthermore, a resolution correction was derived by taking the mean of $p_T^{\text{reco}}/p_T^{\text{truth}}$ in bins of p_T^{reco} . As we've seen in Figure 5.6, there is a scale shift, which can be corrected, on average, using this method. In the kinematic likelihood fit, this information is embedded slightly differently: the scale correction is in the mean of the jet transfer functions, i.e. the mean is not at one. This is illustrated in Figure 6.12a and can introduce an interference with the in-situ resolution correction, i.e. the p_T^{truth} PDF (Figure 6.12b). One can imagine two different scenarios:

1. A given jet is found on the left-hand side of the p_T^{truth} spectrum. Both PDFs tend to pull the jet p_T in the same direction, meaning the p_T^{truth} PDF increases the jet p_T as well as the $p_T^{\text{reco}}/p_T^{\text{truth}}$ PDF, given that $p_T^{\text{reco}}/p_T^{\text{truth}} = p_T^{\text{reco}}/p_T^{\text{fit}} < 1$.
2. A given jet is found on the right-hand side of the p_T^{truth} spectrum. The PDFs tend to pull the jet p_T in opposite directions, meaning the p_T^{truth} PDF pulls the jet p_T to lower values, while the $p_T^{\text{reco}}/p_T^{\text{truth}}$ PDF still tends to increase the jet p_T . This is due to the scale offset from one.

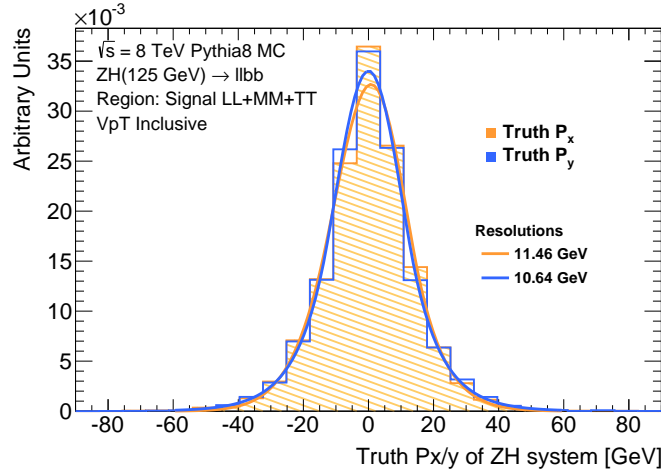


Figure 6.13.: The fitted distribution of the true $\sum p_{x,y}^{\ell b \bar{b}}$, obtained from Monte Carlo simulations.

Due to many other constraints in the model, the impact of such a PDF interference is rather small. Nevertheless, it can be completely eliminated by applying a scale correction before the KF, and by sampling the $p_T^{\text{reco}}/p_T^{\text{truth}}$ PDF with the corresponding offset. This means, the fit begins always with $p_T^{\text{reco}}/p_T^{\text{fit}}$ at one.

Measurement of the $\sum p_{x,y}^{\ell b \bar{b}}$ resolution

The likelihood model uses a fixed value for the resolution of the $\sum p_{x,y}^{\ell b \bar{b}}$ constraint. This resolution is derived from the true ZH system in simulated signal events. The result is shown in Figure 6.13 and yields a resolution of about 11 GeV. A previous estimate (at an earlier stage of the VH analysis) was obtained with a resolution of 9 GeV. At this point in time, the analysis has been frozen, i.e. no more changes were possible. Therefore, the 9 GeV has been used as the nominal value. In Section 6.5, the impact of this choice is quantified.

6.4. Kinematic fitting framework

A kinematic likelihood fitting software package has been developed (written in C++) for a flexible integration with any kind of data analysis framework. The basic concept is illustrated in Figure 6.14. The kinematic likelihood fitter is integrated within the event loop of a given analysis framework. After all object calibrations and event selections, the

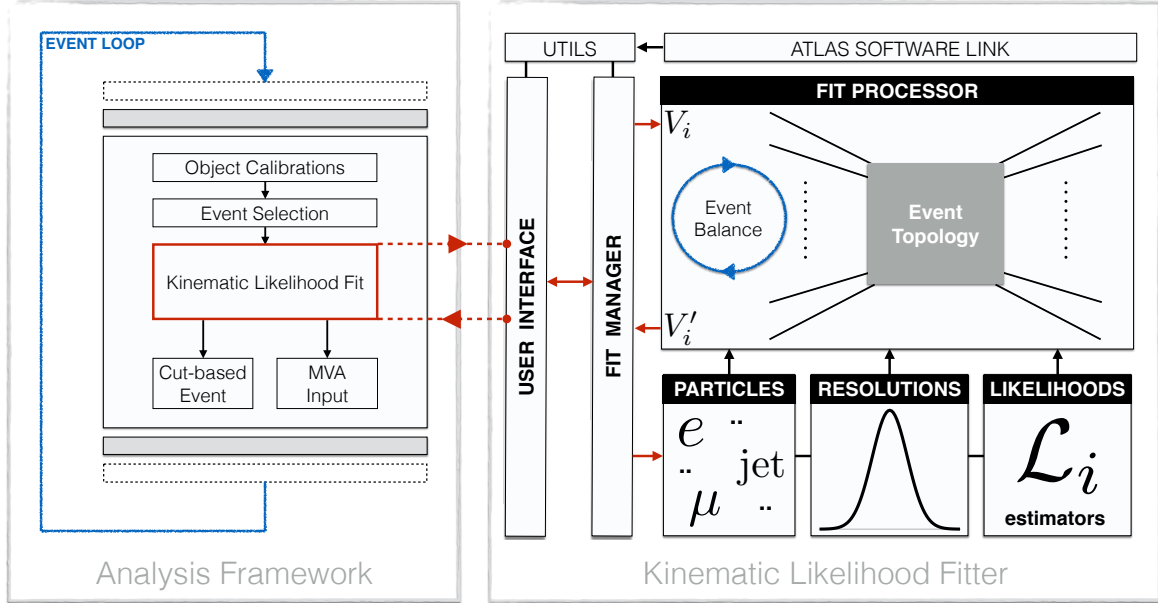


Figure 6.14.: Illustration of the kinematic likelihood fitting software package and its integration in an analysis framework.

reconstructed four-vectors of each considered physics object in the event are passed via an user interface to the kinematic likelihood fitter. All objects are received by the fit manager, which supervises all in- and output operations as well as all internal processes. The fit processor receives from the fit manager all reconstructed objects and performs the actual minimization of the test statistic using numerical methods implemented in MINUIT [195]. The post-fit four-vectors are then return to the analysis framework for further processing.

In the context of the VH analysis, this software package has been integrated in a number of Higgs boson analysis frameworks. In case of the dijet-mass analysis, the output of the kinematic likelihood fit serves as a direct input to the global profile likelihood fit (Section 5.7). In case of the MVA, the kinematic likelihood fit output is used as an input to the BDTs.

6.5. Results

The event-level kinematic likelihood fit, as introduced in the previous sections, has been used to balance the $ZH \rightarrow \ell\ell b\bar{b}$ system in ZH simulated events for a Higgs boson mass

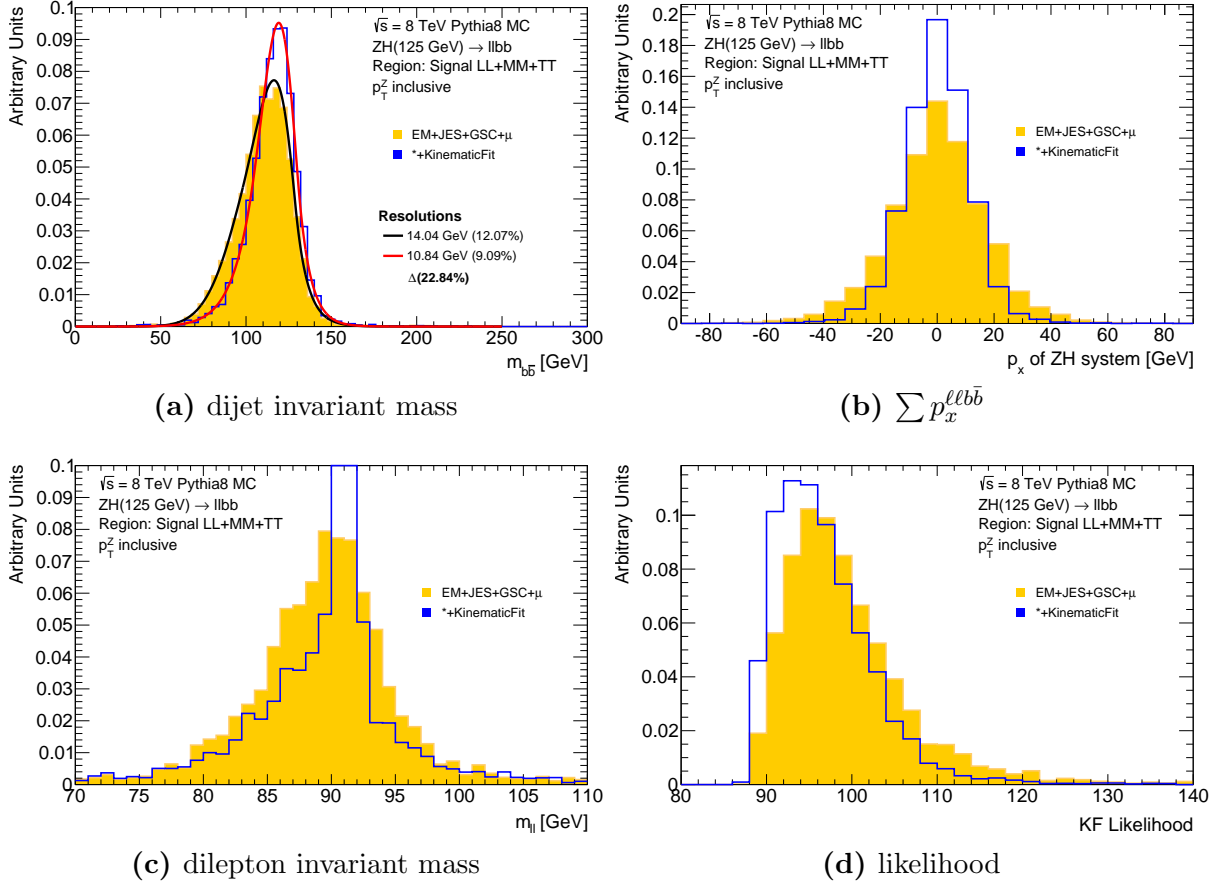


Figure 6.15.: Pre-fit and post-fit distributions of the dijet invariant mass (a), the $\sum p_x^{\ell b \bar{b}}$ constraint (b), the dilepton invariant mass (c), and the likelihood output (d).

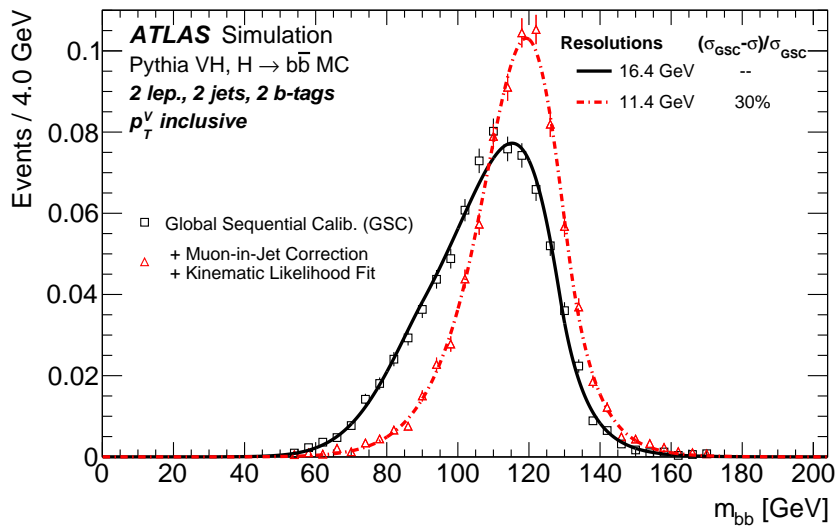


Figure 6.16.: Dijet-invariant-mass distributions for the 2-lepton MVA selection, showing the total resolution improvement from the kinematic likelihood fit together with the muon-in-jet correction with respect to the global sequential calibration.

hypothesis of $m_H = 125$ GeV. As shown in Figure 6.15a, the KF achieves an improvement of the dijet invariant mass resolution of about 23% with respect to the resolution after the muon-in-jet correction. The $\sum p_x^{\ell\ell b\bar{b}}$ distribution, before and after the KF, is shown in Figure 6.15b. As expected, the post-fit distribution is more narrow. The reconstructed dilepton system is constrained to follow a Breit-Wigner distribution and is shown in Figure 6.15c, with the peak near the expected Z boson pole mass. The raw value of the event-level test statistic (Equation 6.8) is shown in Figure 6.15d, which exhibits the overall minimization.

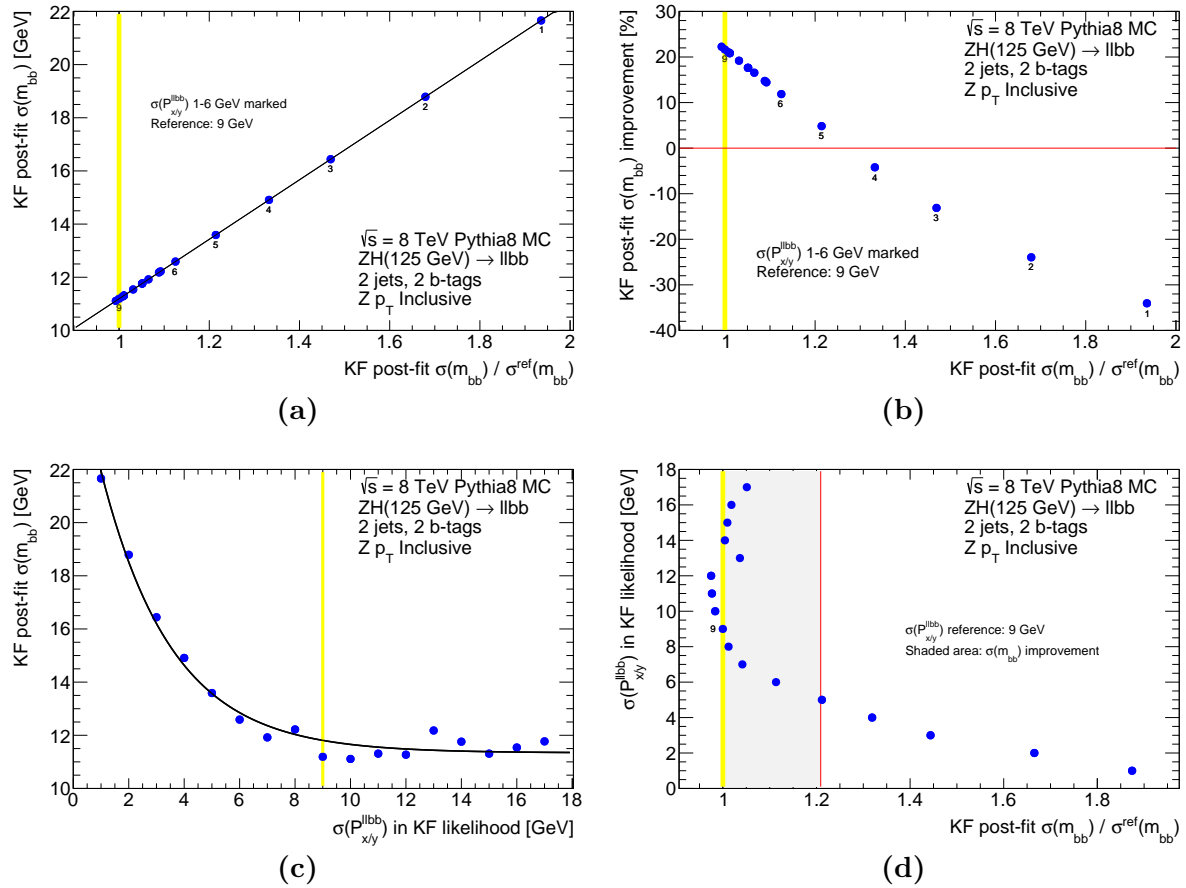


Figure 6.17.: The dependence of the post-fit dijet mass resolution $\sigma(m_{b\bar{b}})$ and its improvement for different values of $\sum p_{x,y}^{\ell\ell b\bar{b}}$, as used in Equation 6.8 by the kinematic likelihood fit. The $\sigma^{\text{ref}}(m_{b\bar{b}})$ represents the resolution for the nominal value of $\sum p_{x,y}^{\ell\ell b\bar{b}} = 9$ GeV and is highlighted with a yellow line. The (a) post-fit $\sigma(m_{b\bar{b}})$, (b) relative $\sigma(m_{b\bar{b}})$ improvement and (d) $\sum p_{x,y}^{\ell\ell b\bar{b}}$ variation are shown as a function of the post-fit $\sigma(m_{b\bar{b}})$ ratio with $\sigma^{\text{ref}}(m_{b\bar{b}})$. The post-fit $\sigma(m_{b\bar{b}})$ is also shown as a function of the $\sum p_{x,y}^{\ell\ell b\bar{b}}$ variation in (c). The red line in both (b) and (d) marks the minimal improvement of the $\sigma(m_{b\bar{b}})$.

Figure 6.16 summarizes the main achievement in the 2-lepton channel after the MVA selection: the kinematic likelihood fit together with the muon-in-jet correction improve the dijet mass resolution by 30% with respect to the global sequential calibration.

The main constraint employed by the likelihood model is $\sum p_{x,y}^{\ell\ell b\bar{b}} \rightarrow 0$. This constraint is bound by a fixed resolution. As discussed further below, the choice of this resolution has a direct impact on the performance of the kinematic fit, i.e. the final mass resolution improvement. As previously explained, a nominal or reference value of 9 GeV is used. This reference can be compared to a variation of different resolutions, $\sigma(p_{x,y}^{\ell\ell b\bar{b}})$ (e.g. between 1 and 20 GeV, and their relative impact on $\sigma(m_{b\bar{b}})$). Figure 6.17 shows that there is no improvement in the dijet mass resolution for $\sigma(p_{x,y}^{\ell\ell b\bar{b}}) \leq 4$ GeV. Above this value, the dijet mass resolution begins to improve and reaches a plateau at about 12 GeV. The dijet

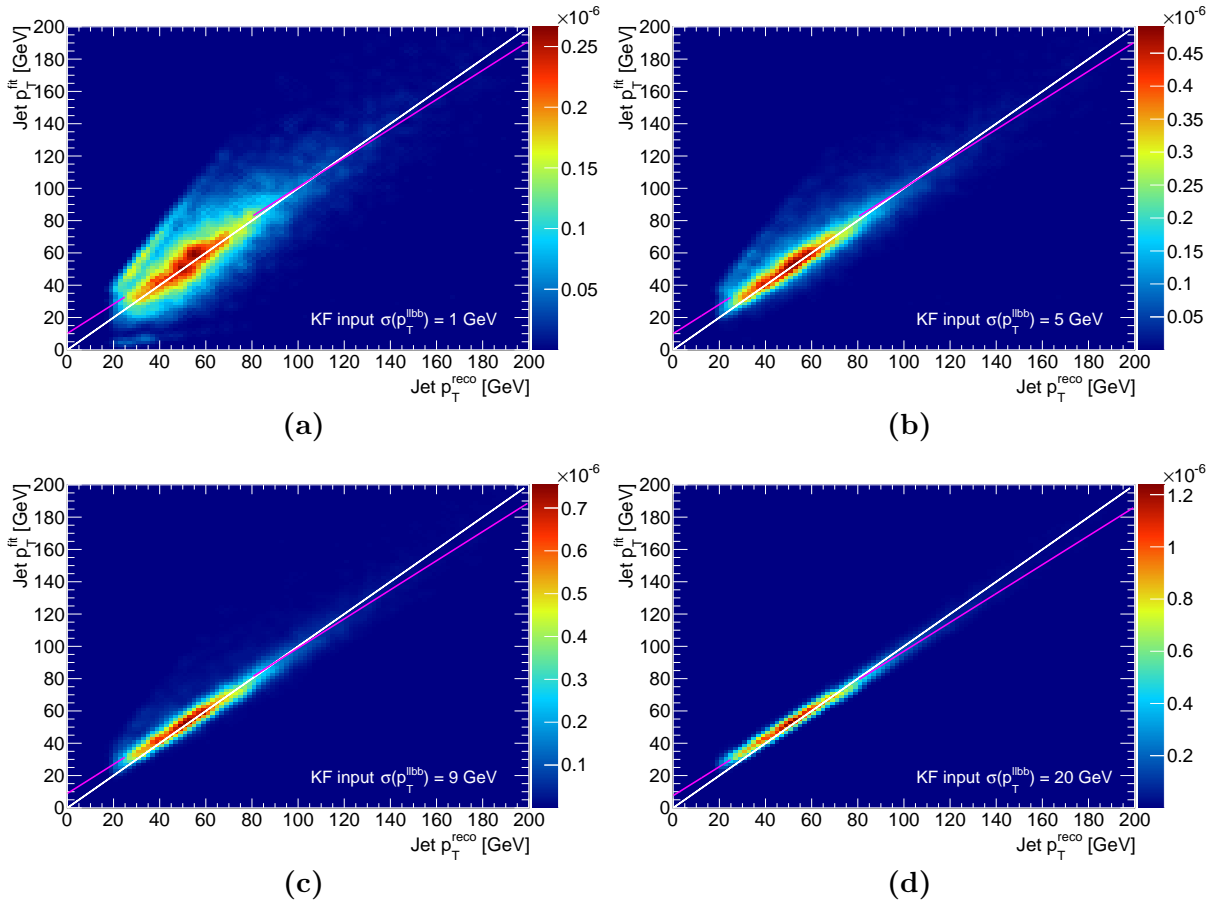


Figure 6.18.: The correlation between the pre-fit and post-fit p_T for different values of $\sigma(p_{x,y}^{\ell\ell b\bar{b}})$, as used in Equation 6.8 by the kinematic likelihood fit: (a) 1 GeV, (b) 5 GeV, (c) nominal 9 GeV, and (d) 20 GeV. A linear function, shown in purple, is fitted to the core of each distribution and is compared to a white reference line, which is identical in all Figures.

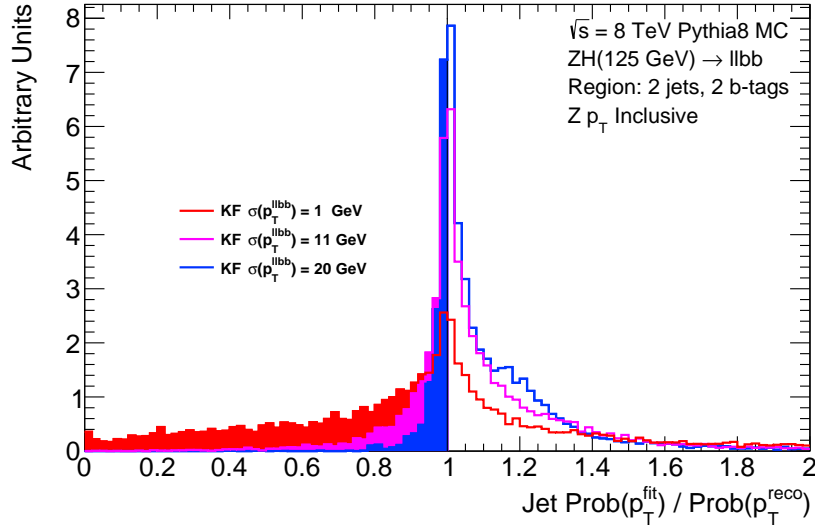


Figure 6.19.: Probability ratio of p_T^{fit} and p_T^{reco} for three different choices of $\sigma(p_{x,y}^{\ell\ell b\bar{b}})$. The coloured distributions below one highlight the relative difference of the area covered by each distribution.

mass resolution degrades, if the system is constrained too hard. This could be due to the fact that the imbalance of the ZH system can be caused by low p_T objects, which are not reconstructed and are not properly recovered by this method. In the following, further effects associated with the choice of $\sigma(p_{x,y}^{\ell\ell b\bar{b}})$ are discussed.

Figure 6.18 shows the post-fit jet p_T^{fit} as a function of the pre-fit jet p_T^{reco} as a function of different $\sigma(p_{x,y}^{\ell\ell b\bar{b}})$ choices, which have been used to derive p_T^{fit} . Generally, one can see that the spread of jet momenta increases as $\sigma(p_{x,y}^{\ell\ell b\bar{b}})$ decreases. In each case, the core of the distribution can be fitted with a linear function with nearly the same slope. Mostly, $p_T^{\text{fit}} > p_T^{\text{reco}}$ in all four causes. However, in case of very small $\sigma(p_{x,y}^{\ell\ell b\bar{b}})$, such as 1 GeV, jet momenta are even pulled to significantly lower values than their reconstructed ones.

Figure 6.19 shows the ratio of probabilities associated to the p_T^{fit} and p_T^{reco} . As discussed in Section 6.3.2 and shown in Figure 6.7, the p_T^{fit} is expected to have a higher probability value than p_T^{reco} . The probability ratio shows most contributions below one from the case when $\sigma(p_{x,y}^{\ell\ell b\bar{b}}) = 1$ GeV. At higher $\sigma(p_{x,y}^{\ell\ell b\bar{b}})$, the p_T^{fit} probabilities are mostly larger and above one. Further details can be found in Appendix B.

6.6. Summary

In this chapter, an event-level kinematic likelihood fit has been presented, targeting the signal hypothesis of the $ZH \rightarrow \ell\ell b\bar{b}$ production process. A likelihood model has been

constructed, based on a maximum likelihood technique, and optimized for the 2-jet 2-tag signal region of the 2-lepton channel. The corresponding fit parameters and constraints have been chosen accordingly. For b -tagged jets, dedicated transfer functions were derived and evaluated also for semileptonic b -jet decays. An extensive software package was developed, for which the basic integration and functionalities were described. The overall improvement of the dijet invariant mass resolution in ZH simulated events is 23% for the dijet-mass analysis and, including the muon-in-jet correction, in total 30% for the nominal 2-lepton MVA analysis. The final impact of using the kinematic likelihood fit in the $VH(b\bar{b})$ analysis is evaluated in Section 7.

Chapter 7.

LHC Run-1 $VH(b\bar{b})$ Analysis Results

In this chapter, the final results of the search for a Higgs boson decaying into a $b\bar{b}$ pair in association with a leptonically decaying W or Z boson using the full LHC Run-1 dataset recorded by the ATLAS detector are presented. The results are based on an optimized reconstruction of each physics object (Chapter 4), an optimized selection of events in terms of kinematic and topological features (Section 5.3), an optimized b -jet energy calibration of Higgs boson candidates (Section 5.4, Chapter 6), an optimized modelling of backgrounds (Section 5.5) and a careful evaluation of systematic uncertainties (Section 5.6), and an optimized fit model to extract the final signal strength (Section 5.7).

In Section 7.1, a significance test is shown to quantify the improvements from jet energy calibrations. In Section 7.2, a validation of the analysis procedure using diboson production is discussed, before in Section 7.3 the final Higgs boson results are presented.

7.1. Significance of jet energy calibrations

Dedicated jet energy calibrations are used in this analysis to improve the dijet mass resolution of $H \rightarrow b\bar{b}$ candidates. After the full event selection, a muon-in-jet correction is applied to all selected GS-calibrated b -jets in all three analysis channels. In addition, a momentum resolution correction is applied in the 0-lepton and 1-lepton channels, and an event-level kinematic likelihood fit is applied in the 2-lepton channel. Besides the dijet mass resolution improvement, these correction aim to also improve the sensitivity of this search. In this section, the statistical significance \mathcal{Z} , in terms of the dijet mass,

is evaluated for each jet energy correction to quantify the improvement with respect to the dijet mass before each jet energy correction. This evaluation is based on the log-likelihood derived in [194], and is defined as

$$\mathcal{Z} = \sqrt{2 \left((S + B) \ln \left(1 + \frac{S}{B} \right) - S \right)} = \frac{S}{\sqrt{B}} (1 + \mathcal{O}(S/B)), \quad (7.1)$$

with S for the signal hypothesis of a Higgs boson with $m_H = 125$ GeV and B for the corresponding backgrounds.

Table 7.1 summarizes the significance improvements from the different jet energy calibrations in the combined 2-tag signal region of each analysis channel. The results are presented in the signal-dominated region, where $100 < m_{b\bar{b}} < 160$ GeV, as well as inclusive in $m_{b\bar{b}}$ in parentheses. The muon-in-jet correction improves the significance in average by about 6.9% (4.3%), the resolution correction after the muon-in-jet correction improves the significance in average by about 3% (0.5%), and in the 2-lepton channel, the kinematic likelihood fit after the muon-in-jet correction improves the significance in average by about 11.1% (7.3%). The total significance improvement from all corrections

Calibration	\mathcal{Z}			$\langle \Delta \mathcal{Z} \rangle$
	0-lepton	1-lepton	2-lepton	
GSC	0.77 (0.81)	1.92 (2.06)	0.14 (0.16)	0.95 (1.01)
GSC+ μ	0.83 (0.85)	2.07 (2.16)	0.16 (0.16)	1.02 (1.06)
$\Delta \mathcal{Z}^{\text{GSC}} [\%]$	6.82 (4.17)	7.24 (4.78)	6.72 (4.08)	6.93 (4.34)
GSC+ μ +ResoCorr	0.84 (0.85)	2.14 (2.17)	0.16 (0.17)*	1.05 (1.06)
$\Delta \mathcal{Z}^{\text{GSC}+\mu} [\%]$	1.42 (0.20)	3.17 (0.46)	4.36 (0.90)*	2.98 (0.52)
GSC+ μ +KF	–	–	0.17 (0.18)	1.05 (1.07)**
$\Delta \mathcal{Z}^{\text{GSC}+\mu} [\%]$	–	–	11.08 (7.29)	5.22 (2.65)**
Improvement [%]	8.14 (4.36)	10.17 (5.22)	17.06 (11.07)	11.79 (6.88)

Table 7.1.: Significance improvements from jet energy calibrations in the (LL+MM+TT)-combined 2-tag signal region of each analysis channel using Monte Carlo simulations and a Higgs boson mass hypothesis of $m_H = 125$ GeV. The significance \mathcal{Z} is shown for the signal-dominated region $100 < m_{b\bar{b}} < 160$ and inclusively in parentheses. (*) The resolution correction, **ResoCorr**, is only shown for performance comparison in the 2-lepton channel. (**) The average is calculated using the 0-lepton and 1-lepton channel after **ResoCorr**, and the 2-lepton channel after the kinematic likelihood fit (KF).

with respect to the dijet mass using the bare GS-calibrated b -jets is observed to be about 8.1% (4.4%) in the 0-lepton channel, about 10.2% (5.2%) in the 1-lepton channel, and about 17.1% (11.1%) in the 2-lepton channel. In average, these corrections yield a significance improvement of 11.8% (6.9%).

7.2. Diboson observation

As mentioned in Section 5.7, the analysis procedure, i.e. the background estimate and the global fit configuration, is validated using a known signal with a similar signature to that of the $VH(b\bar{b})$ production: the diboson production in the channels $ZZ \rightarrow \nu\bar{\nu}b\bar{b}$, $WZ \rightarrow \ell\nu b\bar{b}$, and $ZZ \rightarrow \ell^+\ell^-b\bar{b}$. The p_T spectrum of their dijet system is softer and the $m_{b\bar{b}}$ distribution peaks at lower values (~ 90 GeV) than in the case of the Higgs boson production. Since it has a ~ 5 times larger cross section than VH production, the observation of diboson production requires less data. For the purpose of this validation, the event selection is kept the same. The VH processes are considered as backgrounds in the global fit and are included with their respective normalisations fixed to the Standard

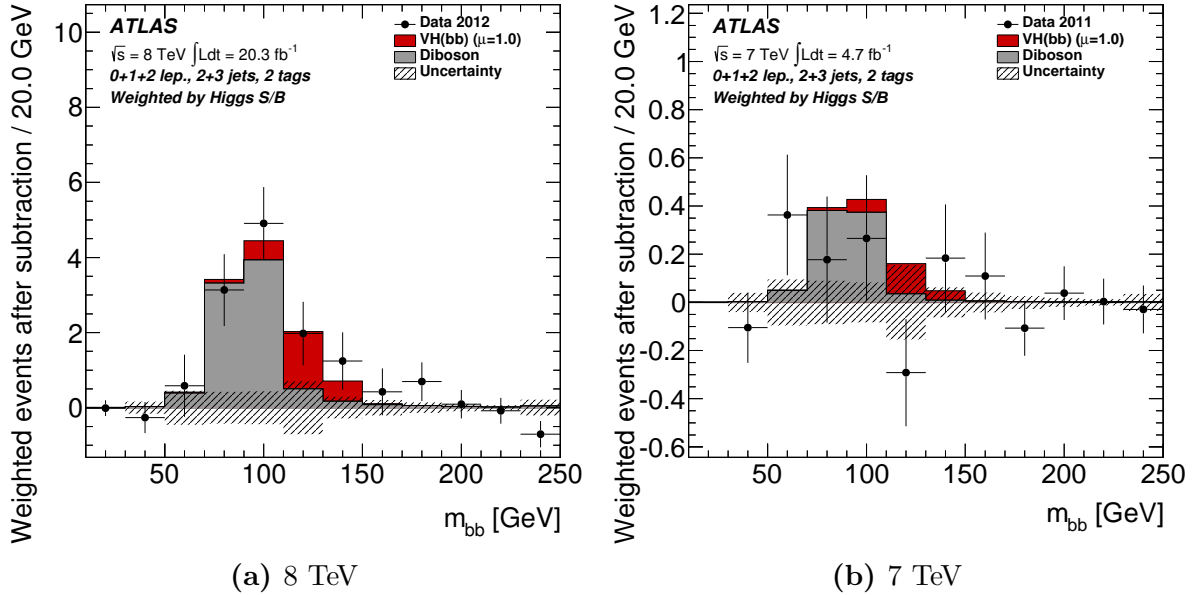


Figure 7.1.: The $m_{b\bar{b}}$ distribution observed in 8 TeV (a) and 7 TeV (b) data after subtracting all backgrounds except for diboson production, as obtained with the dijet-mass analysis. All contributions (lepton channels, p_T^V bins, jet multiplicity, combined 2-tag categories) are weighted by their corresponding ratios of the expected Higgs boson signal to the fitted background. The VH contribution is shown as expected for the Standard Model cross-section ($\mu = 1.0$) [8].

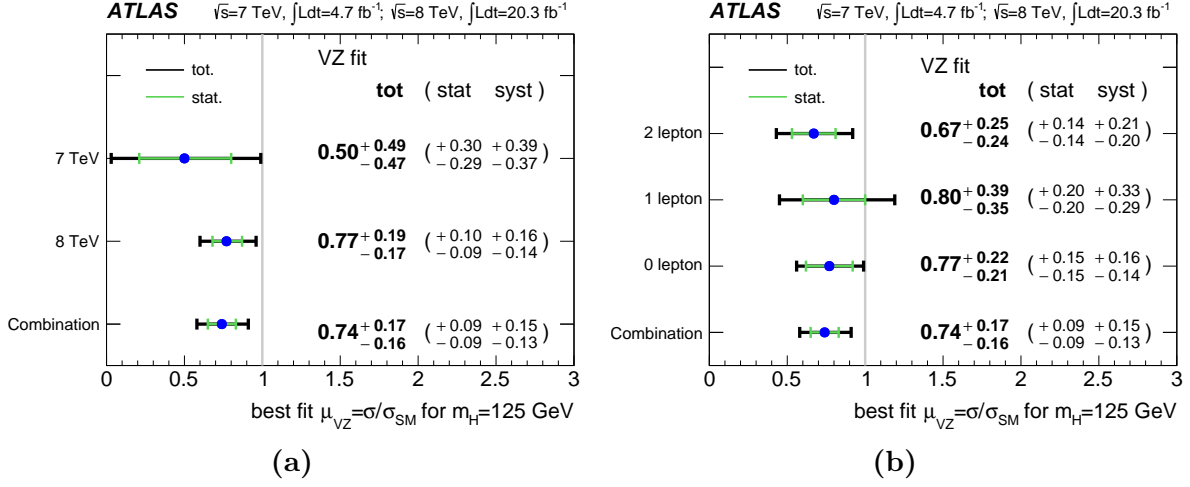


Figure 7.2.: The fitted diboson signal strength μ_{VZ} for the 7 and 8 TeV datasets and their combination. The results are shown lepton-channel inclusively (a) and dataset-inclusively (b). For the 8 TeV data, the MVA is used [8].

Model prediction for a Higgs boson with $m_H = 125$ GeV, but with an uncertainty of 50% [152]. The WW production is also treated as a background and constrained within its uncertainty.

Figure 7.1 shows the $m_{b\bar{b}}$ distribution measured in 7 and 8 TeV data after subtracting all background events except for the diboson processes mentioned above. The VZ production is clearly observed at the expected mass of the Z boson and the contribution from the VH signal is also shown as expected for the Standard Model cross-section. The diboson signal is found with an observed (expected) significance of 4.9σ (6.3σ). The measured diboson signal strength $\hat{\mu}_{VZ}$ values are compared to the Standard Model expectation of $\mu_{VZ} = 1$, and for both 7 and 8 TeV data (Figure 7.2a) are found to be

$$\begin{aligned}
 8 \text{ TeV (MVA)} : & \quad \hat{\mu}_{VZ} = 0.77 \pm 0.10(\text{stat.}) \pm 0.15(\text{syst.}) \\
 8 \text{ TeV (dijet-mass analysis)} : & \quad \hat{\mu}_{VZ} = 0.79 \pm 0.11(\text{stat.}) \pm 0.16(\text{syst.}) \\
 7 \text{ TeV (dijet-mass analysis)} : & \quad \hat{\mu}_{VZ} = 0.50 \pm 0.30(\text{stat.}) \pm 0.38(\text{syst.}) \\
 7+8 \text{ TeV (with MVA for 8 TeV)} : & \quad \hat{\mu}_{VZ} = 0.74 \pm 0.09(\text{stat.}) \pm 0.14(\text{syst.}),
 \end{aligned}$$

and for each lepton channel, as shown in Figure 7.2b, consistent at the 85% level. Furthermore, it should be noted that the diboson production has a relatively small contribution as a background to the VH production. This can be seen in the most significant bins of the BDT_{VH} discriminant in Table 7.2.

7.3. Final results

The profile likelihood fit, as described in Section 5.7, is performed to data with the Higgs boson signal strength $\hat{\mu}$ floating. For the 8 TeV data, the fit inputs from the MVA are used, since its expected sensitivity is higher than the dijet-mass analysis. For the 7 TeV data, the fit inputs from the dijet-mass analysis are used.

The bins of the fit input distributions in all signal regions can be combined into bins of $\log(S/B)$. The resulting event yields as a function of $\log(S/B)$ for data, fitted background (B) and expected Higgs boson signal (S) with $m_H = 125$ GeV are shown in Figure 7.3 for both 7 and 8 TeV data. The corresponding number of events in each bin of Figure 7.3a are shown in Table 7.2.

For seven different Higgs boson mass hypotheses ranging from $m_H = 110 - 140$ GeV, upper limits on the cross-section times branching ratio for $pp \rightarrow VH(b\bar{b})$ are derived at the 95% confidence level (CL). The results are shown for all lepton channels and 7/8 TeV data combined in Figure 7.4a. The observed (expected, in the absence of signal) limits

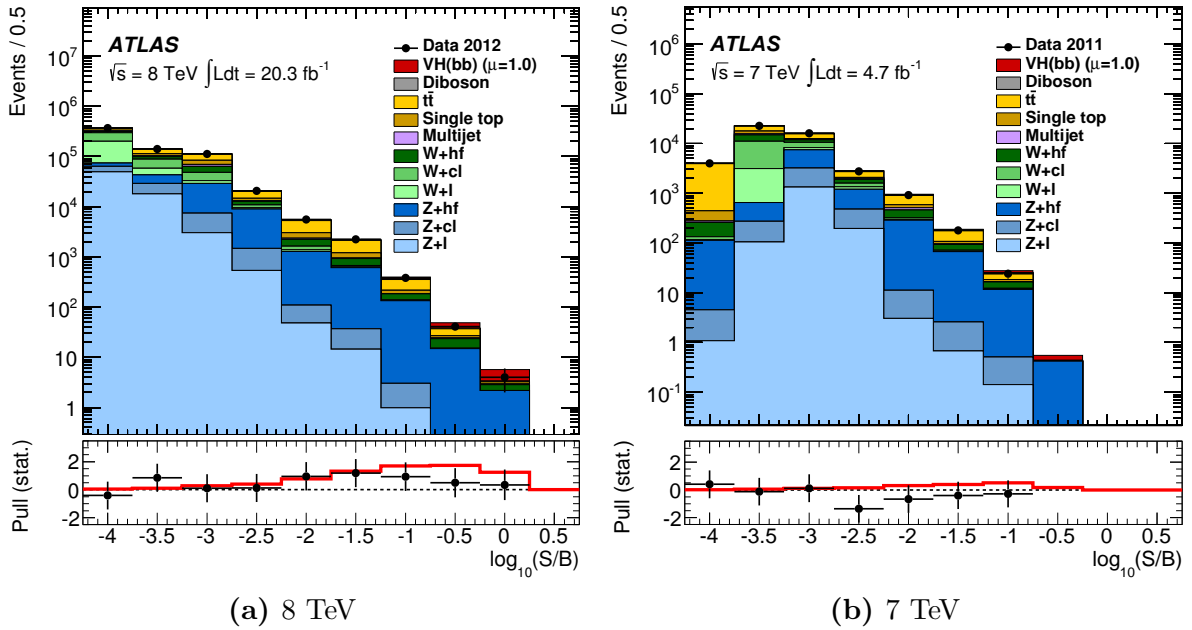


Figure 7.3.: Combined event yields as a function of $\log(S/B)$ for data, fitted background (B) and expected Standard Model Higgs boson signal (S) with $m_H = 125$ GeV (SM cross section; $\mu = 1.0$) in both 8 TeV data (a) and 7 TeV data (b). The yield in each bin is obtained from combining all signal regions of all lepton channels. The pull of the data with respect to the background-only prediction is shown with statistical errors only. The pull of the signal and background prediction with respect to the background-only prediction is shown (red full line) [8].

Process	Bin 1	Bin 2	Bin 3	Bin 4	Bin 5	Bin 6	Bin 7	Bin 8	Bin 9
Data	368550	141166	111865	20740	5538	2245	382	41	4
Signal	29	43	96	57	58	62	32	10.7	2.3
Background	368802	140846	111831	20722	5467	2189	364	37.9	3.4
S/B	8×10^{-5}	0.0003	0.0009	0.003	0.01	0.03	0.09	0.3	0.7
$W+hf$	14584	10626	15297	1948	618	250	45	8.2	0.7
Wcl	96282	30184	15227	1286	239	47	4.2	0.2	0.005
Wl	125676	14961	3722	588	107	16	1.3	0.03	0.001
$Z+hf$	10758	14167	21684	7458	1178	577	130	14.8	2.2
Zcl	13876	11048	4419	941	61	22	2.1	0.1	0.008
Zl	49750	18061	3044	537	48	15	1	0.05	0.004
$t\bar{t}$	30539	24824	26729	5595	2238	922	137	10	0.3
Single top	10356	9492	14279	1494	688	252	31	2.7	0.1
Diboson	4378	1831	1247	474	186	62	9.7	1	0.2
Multijet	12603	5650	6184	400	103	26	3	0.9	0

Table 7.2.: The number of events in the bins of Figure 7.3a for 8 TeV data, fitted background, and expected Standard Model Higgs boson signal with $m_H = 125$ GeV [8].

on $\sigma/\sigma_{\text{SM}}$ are 1.4 (0.8), 2.3 (3.2), and 1.2 (0.8) times the Standard Model expectation at $m_H = 125$ GeV, derived at the 95% CL, for the 8 TeV, 7 TeV datasets and their combination, respectively.

The probability p_0 of obtaining a result at least as signal-like as the one observed from the background-only hypothesis is obtained using the test statistic q_0 (see Equation 5.6). For a Higgs boson mass of $m_H = 125$ GeV, the observed p_0 is 8% and corresponds to an excess with a significance of 1.4σ . This result has to be compared to the expected p_0 of 0.5%, corresponding to a 2.6σ significance, in the presence of a Standard Model Higgs boson with a mass of 125 GeV and its SM signal strength. These values are for the combined 7 and 8 TeV datasets. For 8 TeV data, the observed (expected) level of significance is 1.7σ (2.5σ), and for 7 TeV data, the expected significance is 0.7σ and a deficit in data (negative $\hat{\mu}$, see below) is observed. This deficit, i.e. the data undershoots the MC prediction, has been previously observed and found to be compatible with the background-only hypothesis within 2σ [196]. The observed and expected p_0 values are shown in Figure 7.4b as a function of m_H .

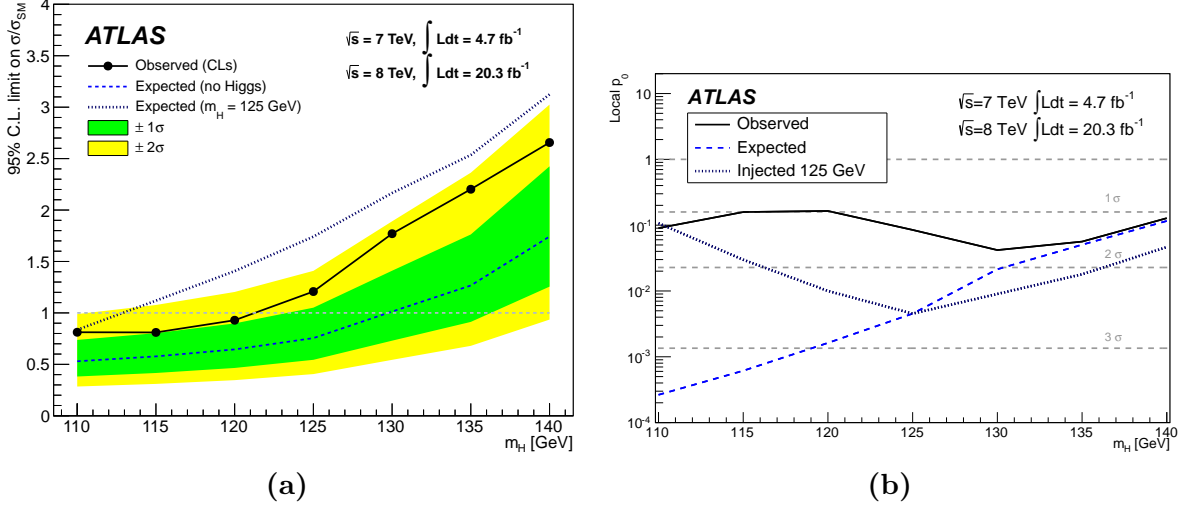


Figure 7.4.: Observed (solid) and expected (a) 95% CL cross-section upper limits on the normalised signal strength, and (b) p_0 values, as a function of m_H for all lepton channels and 7/8 TeV datasets combined. For the expected upper limit or p_0 values, the background-only hypothesis (dashed) and an injected SM Higgs boson with $m_H = 125$ GeV (dotted) are shown [8].

The fitted $\hat{\mu}$ values are compared to the Standard Model expectation of $\mu = 1$, and with all lepton channels combined (Figure 7.5a), are found for $m_H = 125$ GeV to be

$$\begin{aligned} 8 \text{ TeV} : \quad & \hat{\mu} = 0.65 \pm 0.32(\text{stat.}) \pm 0.26(\text{syst.}) \\ 7 \text{ TeV} : \quad & \hat{\mu} = -1.6 \pm 1.2(\text{stat.}) \pm 0.9(\text{syst.}) \\ 7+8 \text{ TeV} : \quad & \hat{\mu} = 0.51 \pm 0.31(\text{stat.}) \pm 0.24(\text{syst.}). \end{aligned}$$

As presented in Section 2.3.3, a Higgs boson mass of $m_H = 125.36 \pm 0.37(\text{stat.}) \pm 0.18(\text{syst.})$ GeV (Equation 2.32) was measured using the bosonic decay modes $H \rightarrow \gamma\gamma$ and $H \rightarrow ZZ^* \rightarrow 4\ell$. At this mass, the fitted $\hat{\mu}$ is found to be $0.52 \pm 0.32(\text{stat.}) \pm 0.24(\text{syst.})$.

The fits are also performed for the WH and ZH processes separately (Figure 7.5b) as well as for each of the lepton channels separately (Figure 7.5c). The $\hat{\mu}$ values for the $(W/Z)H$ processes are consistent at the level of 20%, and the $\hat{\mu}$ values for the lepton channels are consistent at the level of 8% (72%) for the 8 TeV (7 TeV) data. Low $\hat{\mu}$ values are found for the ZH process and in the 0-lepton channel. This is due to a data deficit, observed in the most sensitive (highest) BDT_{VH} bins, as shown in Figure 5.12a.

In comparison to the MVA result, a $\hat{\mu}$ value of $1.23 \pm 0.44(\text{stat.}) \pm 0.41(\text{syst.})$ is found for 8 TeV in the dijet-mass analysis. As for the MVA, the $\hat{\mu}$ values for the lepton channels are consistent at the 8% level. An observed (expected) significance of 2.2σ (1.9σ) is

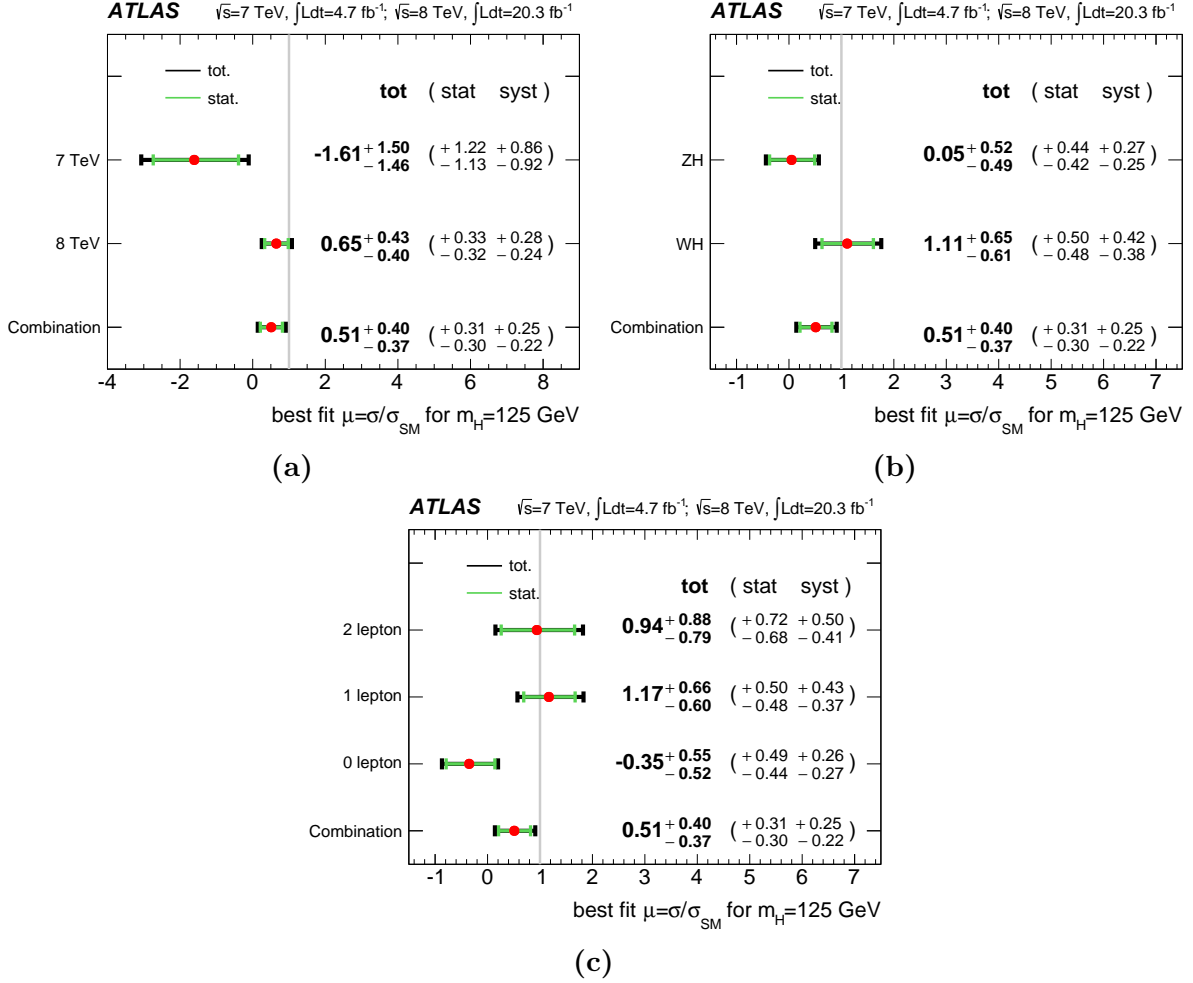


Figure 7.5.: The fitted $\hat{\mu}$ values for the hypothesis of a Standard Model Higgs boson with $m_H = 125$ GeV for (a) the 7 and 8 TeV datasets, (b) the ZH and WH processes, and (c) the three lepton channels, individually and combined [8].

found. Since the MVA has a higher expected significance (2.5σ), it is chosen for the nominal results.

7.4. Summary

The final LHC Run-1 results for the search of a Standard Model Higgs boson in the $VH(b\bar{b})$ channel by the ATLAS collaboration have been presented in this chapter. A series of jet energy calibrations have shown to not only improve the invariant dijet mass resolution in the signal regions of all lepton channels, but also to improve the expected statistical significance by about 12% in average. The analysis procedure has

been validated using the diboson production, $(W/Z)Z$ with $Z \rightarrow b\bar{b}$, with an observed (expected) significance of 4.9σ (6.3σ) and a fitted signal strength of $\hat{\mu}_{VZ} = 0.74^{+0.17}_{-0.16}$. For a Higgs boson mass of 125.36 GeV, the observed (expected) significance is found to be 1.4σ (2.6σ) and the fitted signal strength is $\hat{\mu} = 0.52 \pm 0.32(\text{stat.}) \pm 0.24(\text{syst.})$.

Chapter 8.

Conclusions

This thesis has presented a direct search for the Standard Model Higgs boson, decaying into a b -quark pair, and produced in association with a leptonically decaying W or Z boson. The considered production channels were: $ZH \rightarrow \nu\bar{\nu}b\bar{b}$, $WH \rightarrow \ell\nu b\bar{b}$, and $ZH \rightarrow \ell^+\ell^-b\bar{b}$ with ℓ denoting either a charged electron or muon. The search was performed with the ATLAS detector and was based on the full Run-1 LHC dataset, corresponding to integrated luminosities of 4.7 fb^{-1} and 20.3 fb^{-1} from proton-proton collisions at $\sqrt{s} = 7 \text{ TeV}$ in 2011 and $\sqrt{s} = 8 \text{ TeV}$ in 2012, respectively. This thesis has drawn particular attention to the evaluation and optimization of techniques to identify and to reconstruct the final state signatures of the $pp \rightarrow (W/Z)(H \rightarrow b\bar{b})$ production. The primary focus has been on the reconstruction of the dijet invariant mass formed by b -quark-induced jets from Higgs boson candidates. Several energy calibrations for b -tagged jets were derived and have shown to significantly improve the dijet mass resolution and subsequently, to also improve the sensitivity of this search. A concluding review of the material, in the order it was presented in this thesis, is given below.

THE *journey* began with the construction of the Standard Model of Particle Physics, combining QCD and EW theory in a unified framework. A central part of the theory was found to be associated to the Higgs boson: its field allows the generation of mass in the model and its existence is required for the theory to be physical. Although its couplings are highly constrained in the theory, its mass is not predicted and a priori unknown. The Higgs boson was the only Standard Model particle not observed before the turn-on of the LHC. It was discovered only through its bosonic decay modes with a mass of about 125 GeV. However, at this mass, the theory predicts the Higgs boson to predominantly couple to fermions by decaying into a $b\bar{b}$ -pair with a branching ratio of 58%. An inclusive search for $H \rightarrow b\bar{b}$ at the LHC is, however, nearly impossible, given the overwhelming QCD multijet background in the dominant gluon fusion process $gg \rightarrow H \rightarrow b\bar{b}$. Instead,

the associated $VH(b\bar{b})$ production offers a promising alternative, given that the final states of the vector bosons can be used more efficiently for triggering and background reduction purposes.

THE *journey* continued with the “coarse” identification and reconstruction of signatures expected in the final states of the associated $VH(b\bar{b})$ production in the ATLAS detector. The corresponding methods had to be applicable to the expected kinematics in proton-proton collisions at centre-of-mass energies of 7 and 8 TeV. The procedure began by mapping electronic signals fired in the different subsystems of the ATLAS detector to the actual particles produced in each collision and involved the combination of the information from each subsystem of the ATLAS detector, followed by dedicated offline reconstruction algorithms. Once a collection of all “bare” particles was built for each event, their four-vectors had to be calibrated and compared to Monte Carlo simulations.

THE *journey* entered then the analysis-specific reconstruction and selection of the so-called physics objects, i.e. particles to be used in the final $VH(b\bar{b})$ data analysis. These objects were required to be of very high purity, meaning with a relatively low fake rate associated to them. For prompt electrons and muons from vector boson decays, stringent track- and calorimeter isolation criteria were applied, in order to limit background contributions. The corresponding isolation efficiency was measured in both data and Monte Carlo simulations, and scaling factors between the two were derived using the tag-and-probe technique. For the reconstruction of jets, the anti- k_T algorithm was used. Their energy deposit associated to the reconstructed jet cone had to be calibrated, for which the global sequential calibration scheme was adopted. For the identification of jets originating from b -quark fragmentation, the $MV1c$ b -tagging algorithm was used. It combined, in a neural network, the information of different ATLAS algorithms based on the track impact-parameter significance and displaced b - and c -hadron decay vertices. For neutrinos, the presence of a significant amount of missing transverse momentum was used. Its reconstruction was based on the energy deposits in the calorimeters and the muon chambers, which are not associated to any reconstructed object in the event.

THE *journey* proceeded by selecting physics objects based on their kinematic and topological properties in each event. This selection involved the categorization of objects and events based on the reconstructed vector boson p_T , the (b) -jet multiplicity, and different levels of b -tagging purity. In each category, the selection was optimized to improve the signal-over-background ratio, considering the hypothesis of a Higgs boson mass resonance at 125 GeV, produced in association with a W/Z boson. This strategy was implemented in two independent analyses: a dijet-mass analysis and a multivariate

analysis (MVA). Their difference lies in the final discriminant: the former uses the $m_{b\bar{b}}$ distribution, and the latter uses the BDT_{VH} distribution that, besides the $m_{b\bar{b}}$, includes further background-discriminating variables. In order to improve the $m_{b\bar{b}}$ resolution, a series of b -jet energy corrections were derived and implemented in each analysis: one to add the energy of muons reconstructed within a jet to the calorimeter-based jet energy; one to correct for any biases in the jet response due to resolution/scale effects from the underlying signal p_T spectrum; and one to constrain the reconstructed $\ell\ell b\bar{b}$ system to be balanced in the transverse plane using an event-level kinematic likelihood fit. In total, these corrections improved the dijet mass resolution of the signal up to 30%, and improved the statistical significance by about 12%. Finally, a profile-likelihood fit has been derived, using the bins of the $m_{b\bar{b}}$ and $MV1c$ distributions in the 92 regions of the dijet-mass analysis, and the bins of the BDT_{VH} and $MV1c$ distributions in the 38 regions of the MVA. All systematic uncertainties affecting this search have been considered.

THE *journey* concluded by extracting the signal strength, i.e. the ratio of the measured signal yield to the prediction of the Standard Model, from the 7 and 8 TeV datasets. For the 7 TeV data, the dijet-mass analysis was used, while for the 8 TeV data, the MVA was used, given its higher expected sensitivity. The analysis procedure was validated using the $(W/Z)(Z \rightarrow b\bar{b})$ production, showing an excess compatible with the Z boson mass with an observed (expected) significance of 4.9σ (6.3σ) and a signal strength of $\hat{\mu}_{VZ} = 0.74 \pm 0.09(\text{stat.}) \pm 0.14(\text{syst.})$. Considering a Higgs boson with a mass of 125.36 GeV, the observed (expected) deviation from the background-only hypothesis was found with a significance of 1.4σ (2.6σ), and the signal strength was determined to be $\hat{\mu} = 0.52 \pm 0.32(\text{stat.}) \pm 0.24(\text{syst.})$.

THE *journey, however, is not even nearly finished*. Run-2 of the LHC, launching with $\sqrt{s} = 13$ TeV in 2015, will provide, as always when entering a new energy frontier, new opportunities. One key lesson learned from the $VH(b\bar{b})$ analysis in the Run-1 data is the significant sensitivity gain at higher transverse momenta of the vector boson. This means that the topology of the "boosted" $V + H$ system becomes more distinguishable from backgrounds using the techniques described in this thesis. As we enter a new energy regime, there will be sufficient statistics at higher transverse momenta, where the two b -jets are more and more collimated and eventually merge and form one large jet. A series of substructure techniques may then be employed to decompose the jet. Given such a peculiar signature, background suppression in a "boosted" $VH(b\bar{b})$ analysis is expected to be more efficient.

Appendix A.

Supplemental VH analysis plots

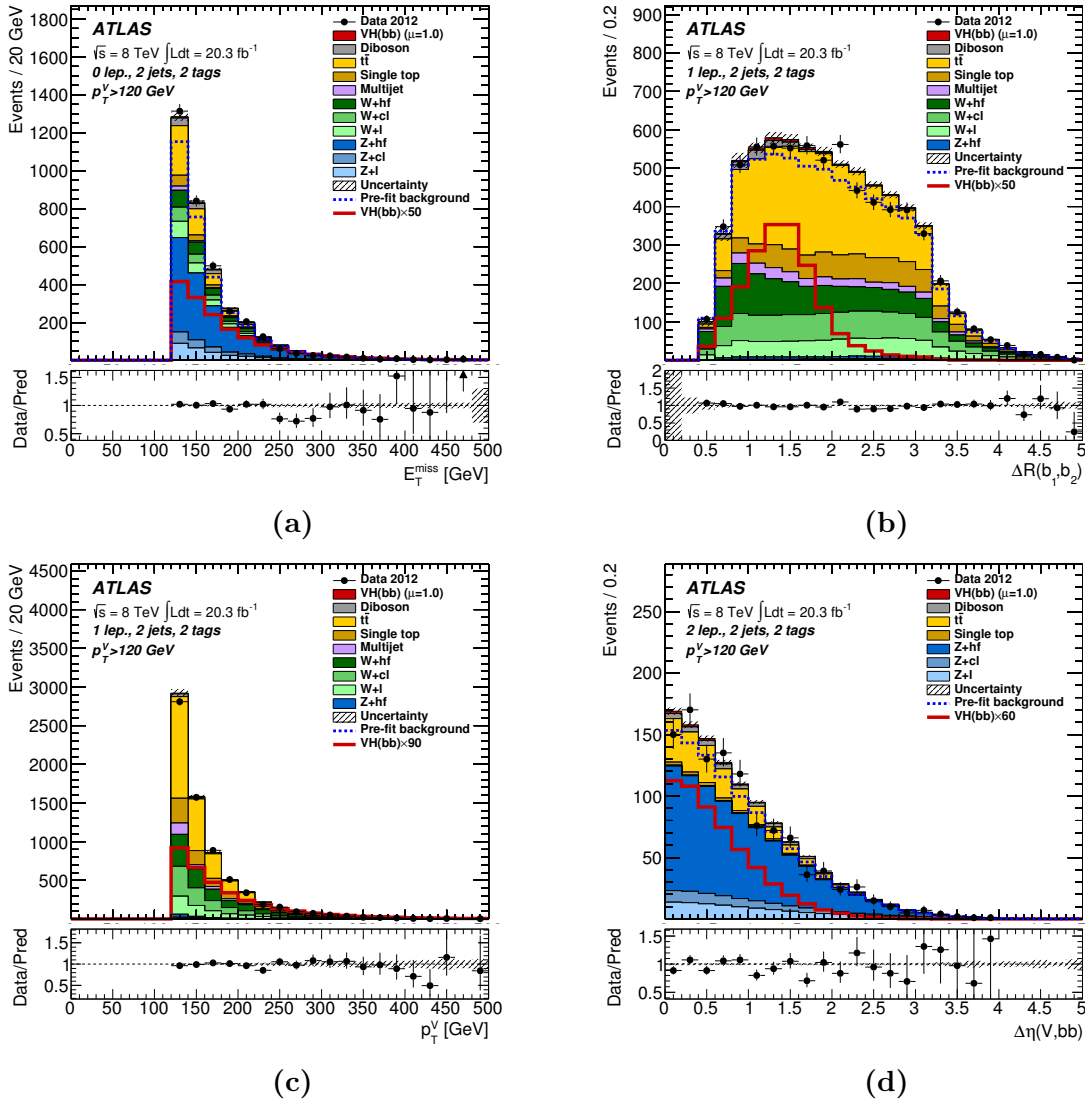


Figure A.1.: Example input variables to the MVA in the (LL, MM, TT)-combined 2-jet 2-tag category: (a) E_T^{miss} in the 0-lepton channel; (b) $\Delta R(b_1, b_2)$ in the 1-lepton channel; (c) p_T^V in the 1-lepton channel; (d) $\Delta\eta(V, b\bar{b})$ in the 2-lepton channel [8].

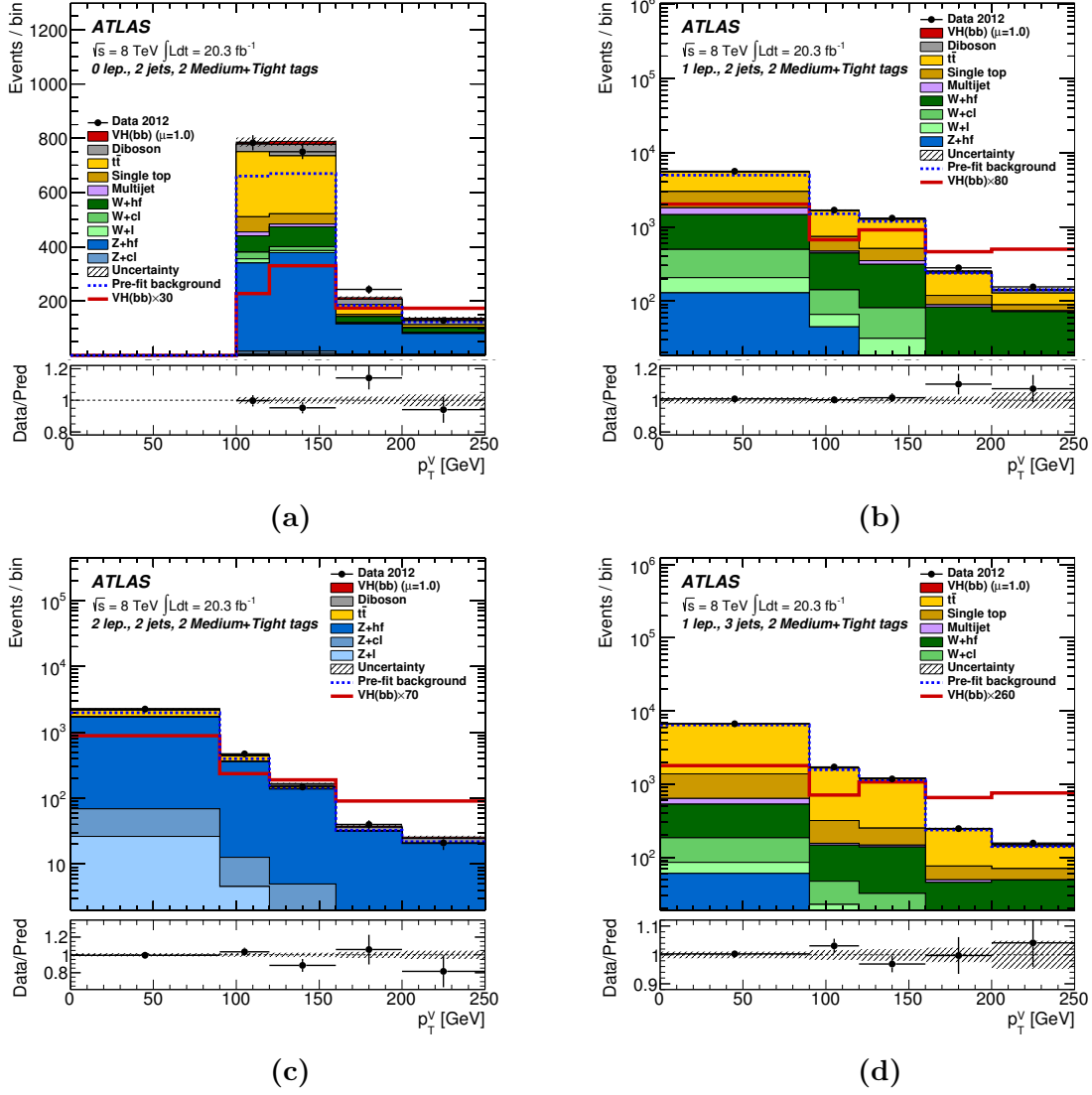


Figure A.2.: Distributions of the p_T^V with MM and TT b -tagging for the 2-jet signal regions of the 0-lepton channel (a), the 1-lepton channel (b), the 2-lepton channel (c), and for the 3-jet signal region of the 1-lepton channel (d) [8].

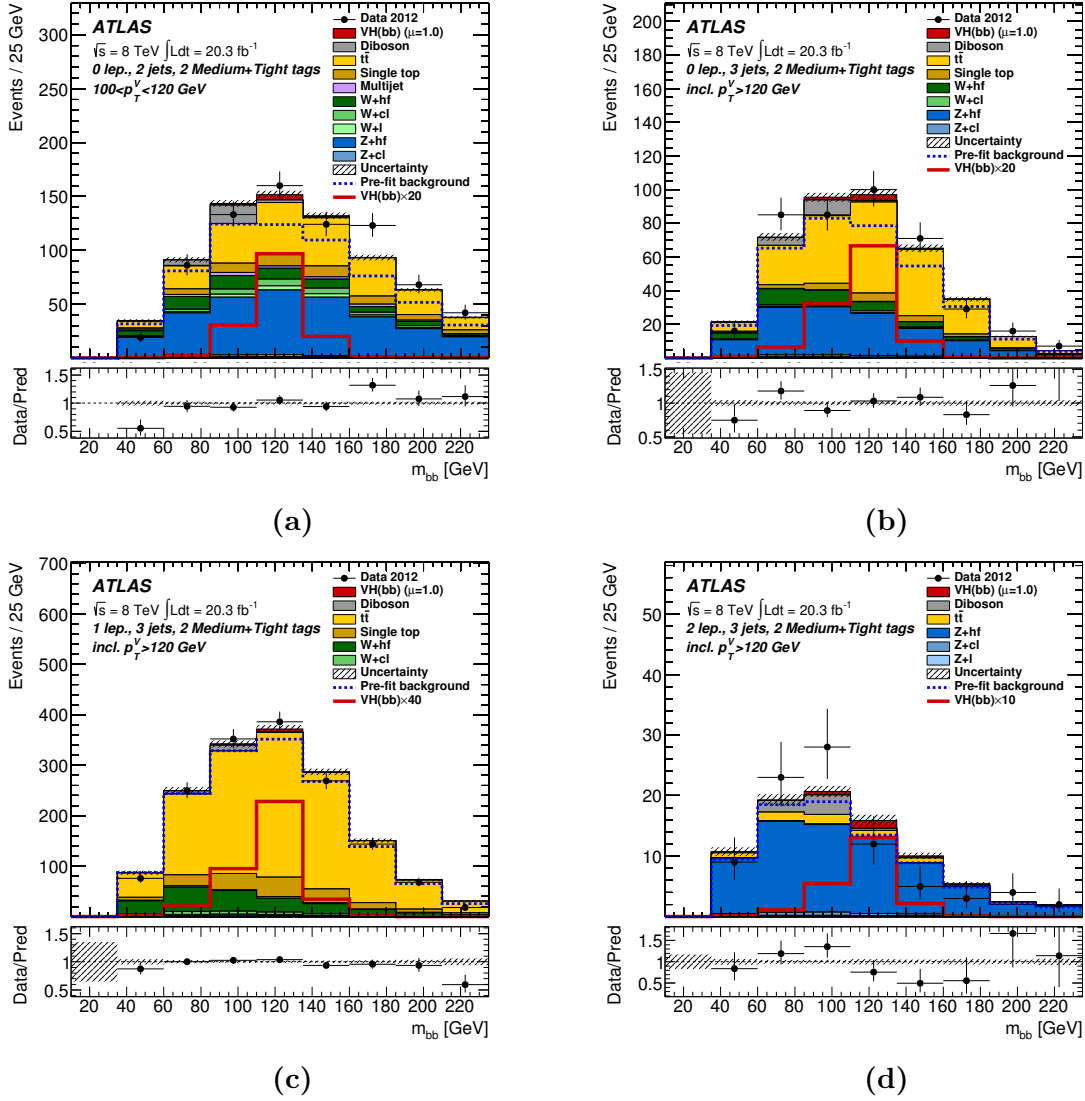


Figure A.3.: The dijet-mass distributions with MM and TT b -tagging for (a) the 2-jet signal region with $100 < p_T^V < 120$ GeV of the 0-lepton channel, and for the 3-jet signal regions with $p_T^V > 120$ GeV of the (b) 0-lepton channel, (c) 1-lepton channel, and (d) 2-lepton channel [8].

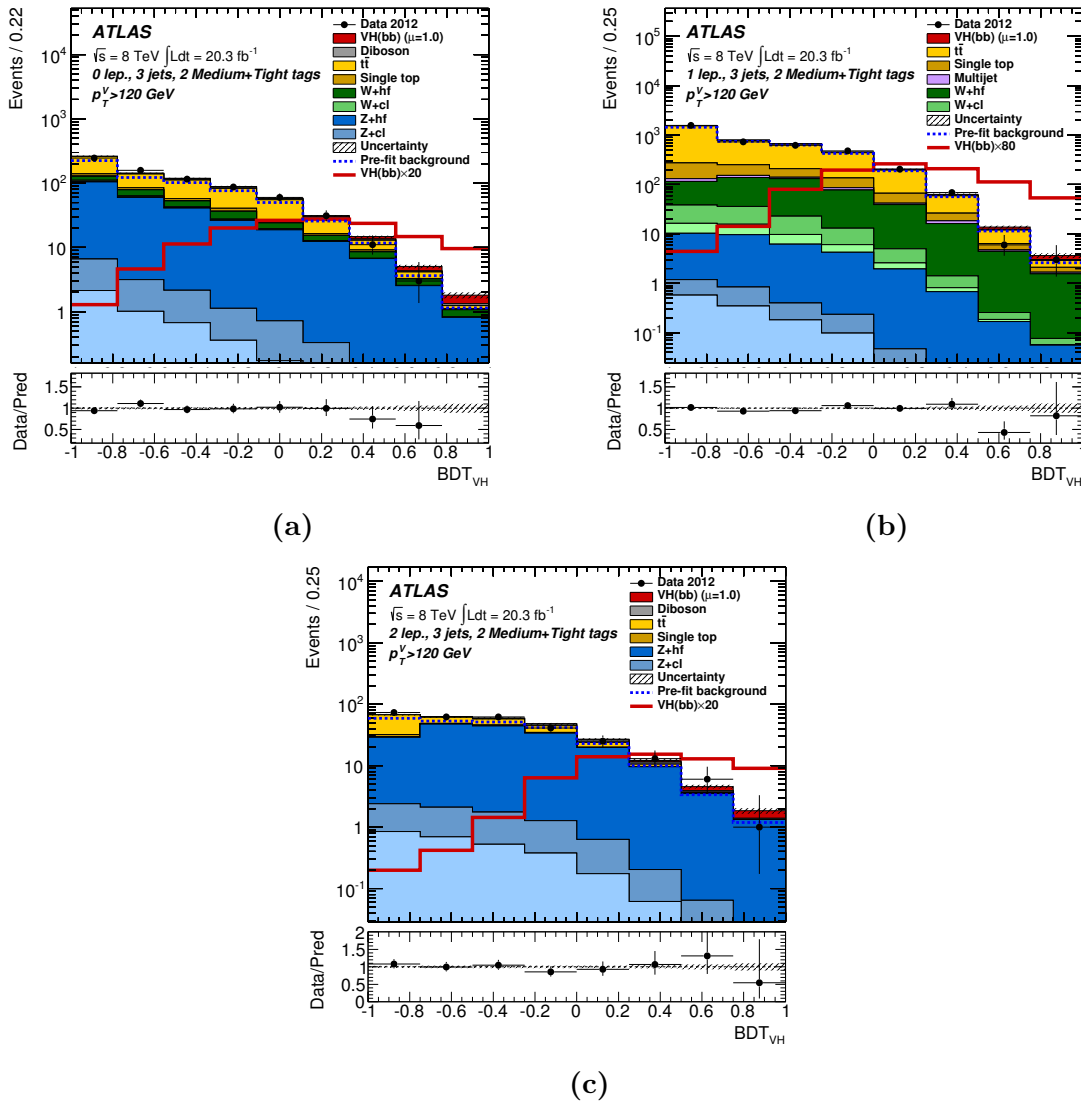


Figure A.4.: Distributions of the BDT_{VH} discriminant with MM and TT b -tagging for the 3-jet signal regions of the 0-lepton channel (a), the 1-lepton channel (b), and the 2-lepton channel (c) [8].

$0 < p_T^V < 90 \text{ GeV}$									
Type	0-lepton			1-lepton			2-lepton		
	LL	MM	TT	LL	MM	TT	LL	MM	TT
Tot. Bkg.	–	–	–	5534.04	2968.56	2007.38	1777.26	1121.79	862.42
Signal	–	–	–	7.36	11.60	13.07	3.57	5.79	6.58
S/B	–	–	–	1.33e-03	3.91e-03	6.51e-03	2.01e-03	5.16e-03	7.63e-03
Data	–	–	–	5891	3230	2364	2009	1284	980

Table A.1.: The pre-fit event yield for $0 < p_T^V < 90 \text{ GeV}$ in the dijet-mass analysis. The yield is shown for each b -tagging category and lepton channel.

$90 < p_T^V < 120 \text{ GeV}$									
Type	0-lepton			1-lepton			2-lepton		
	LL	MM	TT	LL	MM	TT	LL	MM	TT
Tot. Bkg.	806.20	384.34	275.95	1545.21	880.40	620.03	347.61	222.12	177.65
Signal	2.19	3.53	3.98	2.56	3.86	4.37	0.99	1.57	1.77
S/B	2.71e-03	9.19e-03	1.44e-02	1.66e-03	4.39e-03	7.05e-03	2.86e-03	7.07e-03	9.94e-03
Data	887	477	306	1570	984	700	378	264	209

Table A.2.: The pre-fit event yield for $90 < p_T^V < 120 \text{ GeV}$ in the dijet-mass analysis. The yield is shown for each b -tagging category and lepton channel.

$120 < p_T^V < 160 \text{ GeV}$									
Type	0-lepton			1-lepton			2-lepton		
	LL	MM	TT	LL	MM	TT	LL	MM	TT
Tot. Bkg.	766.95	390.32	279.07	1174.86	701.88	480.91	133.69	81.16	64.85
Signal	3.08	5.00	5.84	3.37	5.25	6.02	0.74	1.23	1.45
S/B	4.01e-03	1.28e-02	2.09e-02	2.87e-03	7.48e-03	1.25e-02	5.52e-03	1.51e-02	2.24e-02
Data	856	438	312	1208	776	535	153	83	65

Table A.3.: The pre-fit event yield for $120 < p_T^V < 160 \text{ GeV}$ in the dijet-mass analysis. The yield is shown for each b -tagging category and lepton channel.

$160 < p_T^V < 200 \text{ GeV}$									
Type	0-lepton			1-lepton			2-lepton		
	LL	MM	TT	LL	MM	TT	LL	MM	TT
Tot. Bkg.	236.63	109.53	75.57	310.21	152.92	84.92	34.31	18.41	14.34
Signal	1.63	2.64	3.11	1.55	2.55	3.17	0.34	0.57	0.72
S/B	6.88e-03	2.41e-02	4.12e-02	5.00e-03	1.66e-02	3.73e-02	9.93e-03	3.09e-02	5.02e-02
Data	239	146	97	323	180	100	33	23	17

Table A.4.: The pre-fit event yield for $160 < p_T^V < 200 \text{ GeV}$ in the dijet-mass analysis. The yield is shown for each b -tagging category and lepton channel.

$p_T^V > 200 \text{ GeV}$									
Type	0-lepton			1-lepton			2-lepton		
	LL	MM	TT	LL	MM	TT	LL	MM	TT
Tot. Bkg.	178.81	74.33	49.76	220.25	94.55	46.65	28.13	12.50	9.44
Signal	1.80	2.66	3.08	1.83	2.90	3.21	0.36	0.59	0.69
S/B	1.01e-02	3.58e-02	6.18e-02	8.30e-03	3.07e-02	6.89e-02	1.30e-02	4.69e-02	7.34e-02
Data	185	86	43	198	101	54	42	9	12

Table A.5.: The pre-fit event yield for $p_T^V > 200 \text{ GeV}$ in the dijet-mass analysis. The yield is shown for each b -tagging category and lepton channel.

Type	$0 < p_T^V < 120 \text{ GeV}$					
	0-lepton		1-lepton		2-lepton	
	LL	MM + TT	LL	MM + TT	LL	MM + TT
Tot. Bkg.	–	–	9523.58	8590.21	3991.88	5989.35
Signal	–	–	10.77	35.54	5.48	18.62
S/B	–	–	1.13e-03	0.00868	1.37e-03	3.11e-03
Data	–	–	9941	9422	4313	6501

Table A.6.: The pre-fit event yield for $0 < p_T^V < 120 \text{ GeV}$ in the MVA. The yield is shown for each b -tagging category and lepton channel.

$p_T^V > 120 \text{ GeV}$						
Type	0-lepton		1-lepton		2-lepton	
	LL	MM + TT	LL	MM + TT	LL	MM + TT
Tot. Bkg.	1735.70	1381.66	3933.53	3312.4	484.12	547.22
Signal	6.92	23.39	9.31	30.72	2.03	6.99
S/B	3.99e-03	1.69e-02	2.37e-03	0.01965	4.19e-03	1.28e-02
Data	1860	1592	4072	3604	517	570

Table A.7.: The pre-fit event yield for $p_T^V > 120 \text{ GeV}$ in the MVA. The yield is shown for each b -tagging category and lepton channel.

Appendix B.

Supplemental kinematic fit plots

The following plots provide further evaluations of different $\sigma(p_{x,y}^{\ell\ell b\bar{b}})$ choices in the kinematic likelihood fit. Comparisons are shown in terms of the pre-fit and post-fit p_T and their corresponding probabilities, as discussed in Chapter 6.

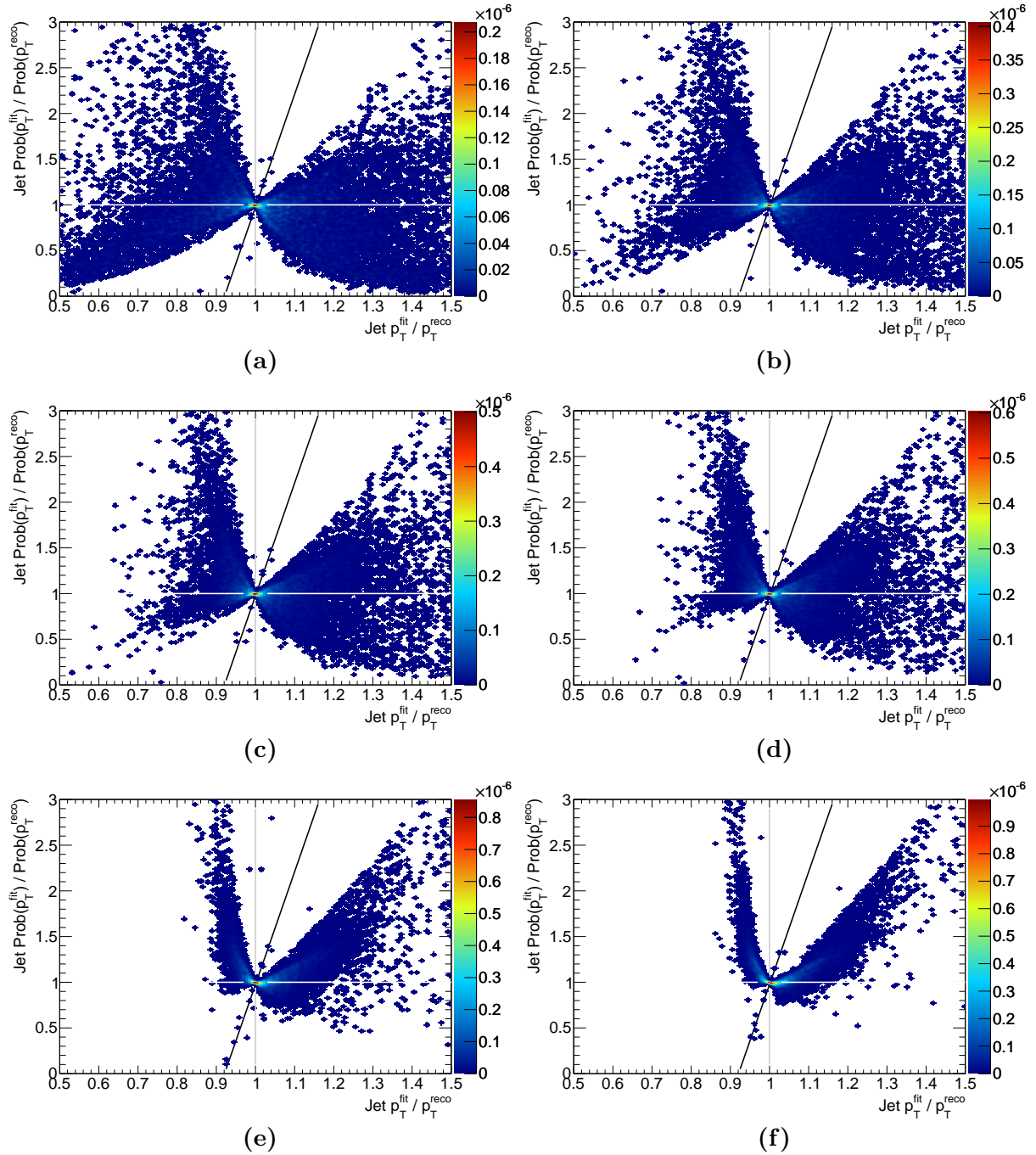


Figure B.1.: The probability ratio of the post-fit and post-fit jet p_T as a function of the ratio of their corresponding momenta, shown for different $\sigma(p_{x,y}^{\ell b \bar{b}})$: (a) 1 GeV, (b) 5 GeV, (c) 7 GeV, (d) 9 GeV, (e) 15 GeV, and (f) 20 GeV.

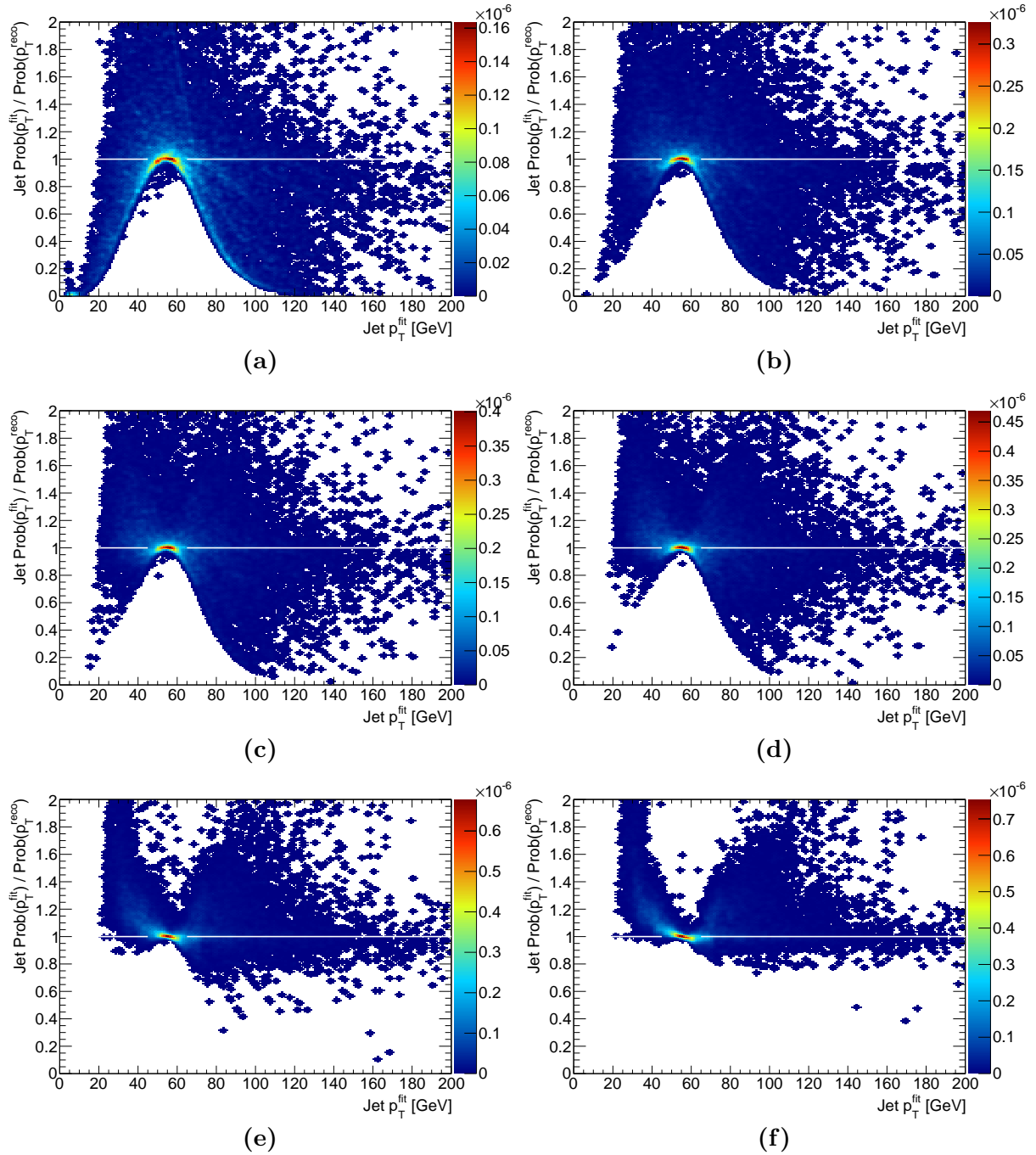


Figure B.2.: The probability ratio of the post-fit and post-fit jet p_T as a function of the post-fit jet p_T , shown for different $\sigma(p_{\ell\ell b\bar{b}})$: (a) 1 GeV, (b) 5 GeV, (c) 7 GeV, (d) 9 GeV, (e) 15 GeV, and (f) 20 GeV.

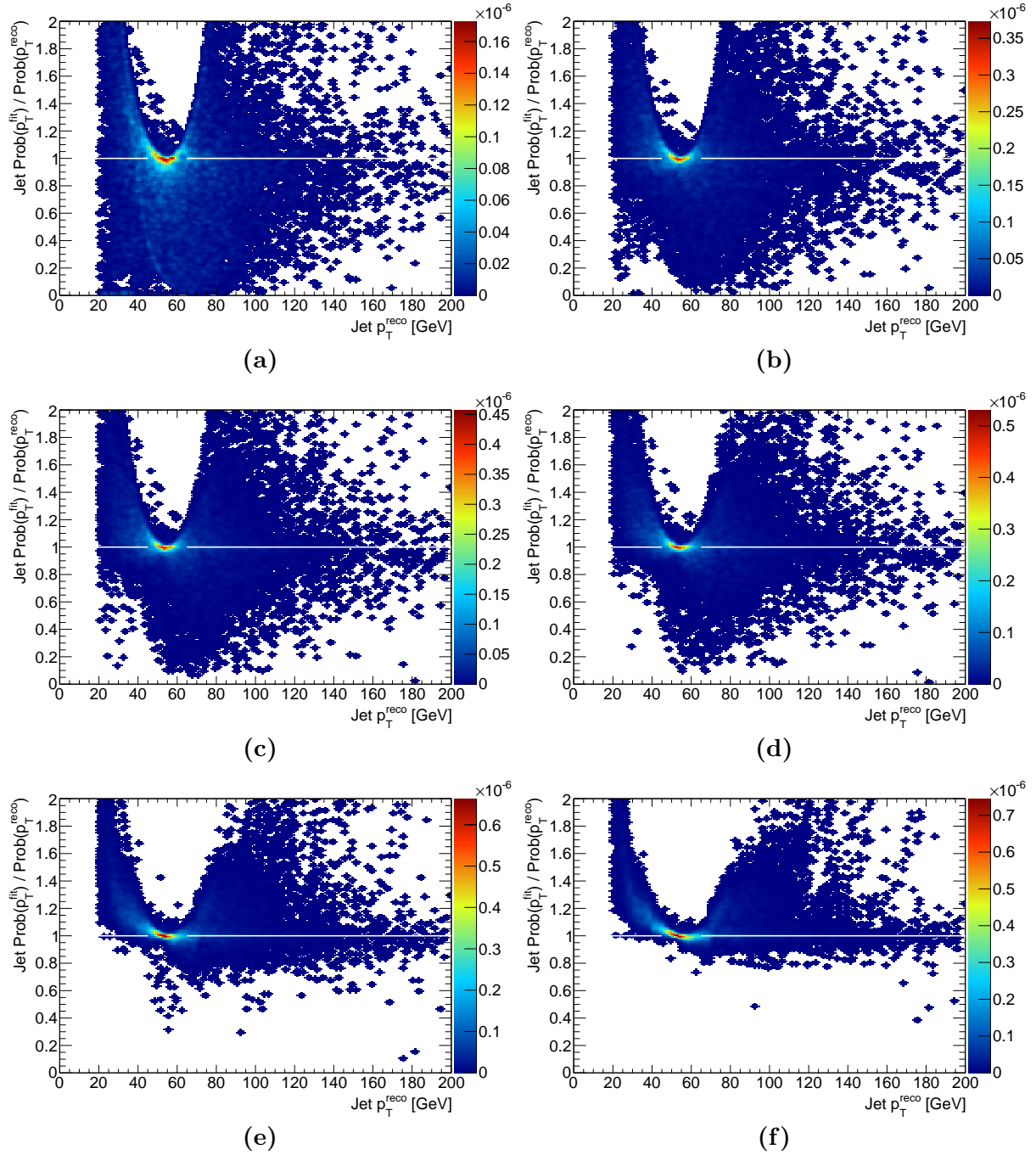


Figure B.3.: The probability ratio of the post-fit and post-fit jet p_T as a function of the pre-fit jet p_T , shown for different $\sigma(p_{x,y}^{\ell\bar{\ell}b\bar{b}})$: (a) 1 GeV, (b) 5 GeV, (c) 7 GeV, (d) 9 GeV, (e) 15 GeV, and (f) 20 GeV.

Bibliography

- [1] P. W. Higgs, *Broken Symmetries, Massless Particles and Gauge Fields*, **Phys. Lett.** **12** (1964) 132–133.
- [2] P. W. Higgs, *Broken Symmetries and the Masses of Gauge Bosons*, **Phys. Rev. Lett.** **13** (1964) 508–509.
- [3] F. Englert and R. Brout, *Broken Symmetry and the Mass of Gauge Vector Mesons*, **Phys. Rev. Lett.** **13** (1964) 321–323.
- [4] G. Guralnik, C. Hagen, and T. Kibble, *Global Conservation Laws and Massless Particles*, **Phys. Rev. Lett.** **13** (1964) 585–587.
- [5] ATLAS Collaboration, *Observation of a new particle in the search for the Standard Model Higgs boson with the ATLAS detector at the LHC*, **Phys. Lett. B** **716** (2012) 1–29, [arXiv:1207.7214 \[hep-ex\]](#).
- [6] CMS Collaboration, *Observation of a new boson at a mass of 125 GeV with the CMS experiment at the LHC*, **Phys. Lett. B** **716** (2012) 30–61, [arXiv:1207.7235 \[hep-ex\]](#).
- [7] ATLAS Collaboration, *Evidence for Higgs boson Yukawa couplings in the $H \rightarrow \tau\tau$ decay mode with the ATLAS detector*, Tech. Rep. ATLAS-CONF-2014-061, CERN, Geneva, Oct, 2014.
- [8] ATLAS Collaboration, *Search for the $b\bar{b}$ decay of the Standard Model Higgs boson in associated $(W/Z)H$ production with the ATLAS detector*, **JHEP** **1501** (2015) 069, [arXiv:1409.6212 \[hep-ex\]](#).
- [9] M. E. Peskin and D. V. Schroeder, *An introduction to quantum field theory*. Reading, Mass., Wokingham: Addison-Wesley, 1996.
- [10] A. Djouadi, *The Anatomy of electro-weak symmetry breaking. I: The Higgs boson in the standard model*, **Phys.Rept.** **457** (2008) 1–216, [arXiv:hep-ph/0503172](#)

- [hep-ph].
- [11] P. Langacker, *Introduction to the Standard Model and Electroweak Physics*, [arXiv:0901.0241](#) [hep-ph].
- [12] K.A. Olive and Particle Data Group, *Review of Particle Physics*, [Chinese Physics C](#) **38** (2014) no. 9, 090001.
- [13] G. 't Hooft, *The birth of asymptotic freedom*, [Nuclear Physics B](#) **254** (1985) no. 0, 11 – 18.
- [14] G. Costa and G. Fogli, *Symmetries and group theory in particle physics. An introduction to space-time and internal symmetries*, [Lect.Notes Phys.](#) **823** (2012) 1–288.
- [15] E. Noether, *Invariante Variationsprobleme*, Nachr. D. Knig. Gesellsch. D. Wiss. Zu Gttingen, Math-phys. Klasse (1918) 235257.
- [16] S. L. Glashow, *Partial-symmetries of weak interactions*, [Nuclear Physics](#) **22** (1961) no. 4, 579 – 588.
- [17] S. Weinberg, *A Model of Leptons*, [Phys. Rev. Lett.](#) **19** (1967) 1264–1266.
- [18] A. Salam, *Weak and Electromagnetic Interactions*, Proc. of the 8th Nobel Symposium (1969) 367–377.
- [19] C. N. Yang and R. L. Mills, *Conservation of Isotopic Spin and Isotopic Gauge Invariance*, [Phys. Rev.](#) **96** (1954) 191–195.
- [20] M. Gell-Mann, *A Schematic Model of Baryons and Mesons*, [Phys.Lett.](#) **8** (1964) 214–215.
- [21] G. Zweig, *An SU_3 model for strong interaction symmetry and its breaking I*. CERN, Geneva, 1964. CERN-Report 8182/TH401.
- [22] H. Fritzsch, M. Gell-Mann, and H. Leutwyler, *Advantages of the Color Octet Gluon Picture*, [Phys.Lett.](#) **B47** (1973) 365–368.
- [23] D. J. Gross and F. Wilczek, *Ultraviolet Behavior of Nonabelian Gauge Theories*, [Phys.Rev.Lett.](#) **30** (1973) 1343–1346.
- [24] H. D. Politzer, *Reliable Perturbative Results for Strong Interactions?*, [Phys.Rev.Lett.](#) **30** (1973) 1346–1349.

- [25] G. 't Hooft and M. Veltman, *Example of a gauge field theory*, in *Proceedings of the Colloquium on Renormalization of Yang-Mills Fields*, pp. 1–38. 1972.
- [26] P. B. Pal, *Dirac, Majorana and Weyl fermions*, *Am. J. Phys.* **79** (2011) 485–498, [arXiv:1006.1718 \[hep-ph\]](#).
- [27] H. Georgi, *LIE ALGEBRAS IN PARTICLE PHYSICS. FROM ISOSPIN TO UNIFIED THEORIES*, *Front.Phys.* **54** (1982) 1–255.
- [28] L. Faddeev and V. Popov, *Feynman Diagrams for the Yang-Mills Field*, *Phys.Lett.* **B25** (1967) 29–30.
- [29] G. Prosperi, M. Raciti, and C. Simolo, *On the running coupling constant in QCD*, *Prog.Part.Nucl.Phys.* **58** (2007) 387–438, [arXiv:hep-ph/0607209 \[hep-ph\]](#).
- [30] N. Cabibbo, *Unitary Symmetry and Leptonic Decays*, *Phys. Rev. Lett.* **10** (1963) 531–533.
- [31] M. Kobayashi and T. Maskawa, *CP-Violation in the Renormalizable Theory of Weak Interaction*, *Progress of Theoretical Physics* **49** (1973) no. 2, 652–657, <http://ptp.oxfordjournals.org/content/49/2/652.full.pdf+html>.
- [32] R. Turra, *Energy calibration and observation of the Higgs boson in the diphoton decay with the ATLAS experiment*, .
- [33] S. Weinberg, *General Theory of Broken Local Symmetries*, *Phys. Rev. D* **7** (1973) 1068–1082.
- [34] LHC Higgs Cross Section Working Group, S. Dittmaier, C. Mariotti, G. Passarino, and R. Tanaka (Eds.), *Handbook of LHC Higgs Cross Sections: 1. Inclusive Observables*, CERN-2011-002 (CERN, Geneva, 2011) , [arXiv:1101.0593 \[hep-ph\]](#).
- [35] LHC Higgs Cross Section Working Group, S. Dittmaier, C. Mariotti, G. Passarino, and R. Tanaka (Eds.), *Handbook of LHC Higgs Cross Sections: 2. Differential Distributions*, CERN-2012-002 (CERN, Geneva, 2012) , [arXiv:1201.3084 \[hep-ph\]](#).
- [36] LHC Higgs Cross Section Working Group, S. Heinemeyer, C. Mariotti, G. Passarino, and R. Tanaka (Eds.), *Handbook of LHC Higgs Cross Sections: 3. Higgs Properties*, CERN-2013-004 (CERN, Geneva, 2013) , [arXiv:1307.1347 \[hep-ph\]](#).

- [37] A. Djouadi, J. Kalinowski, and M. Spira, *HDECAY: A program for Higgs boson decays in the Standard Model and its supersymmetric extension*, *Comput. Phys. Commun.* **108** (1998) 56–74, [arXiv:hep-ph/9704448 \[hep-ph\]](#).
- [38] R. Lafaye et al., *Measuring the Higgs Sector*, *JHEP* **08** (2009) 009, [arXiv:0904.3866 \[hep-ph\]](#).
- [39] S. L. Glashow, D. V. Nanopoulos, and A. Yildiz, *Associated production of Higgs bosons and Z particles*, *Phys. Rev. D* **18** (1978) 1724–1727. <http://link.aps.org/doi/10.1103/PhysRevD.18.1724>.
- [40] A. Stange, W. J. Marciano, and S. Willenbrock, *Higgs bosons at the Fermilab Tevatron*, *Phys. Rev. D* **49** (1994) 1354–1362, [arXiv:hep-ph/9309294 \[hep-ph\]](#).
- [41] A. Stange, W. J. Marciano, and S. Willenbrock, *Associated production of Higgs and weak bosons, with $H \rightarrow b\bar{b}$, at hadron colliders*, *Phys. Rev. D* **50** (1994) 4491–4498, [arXiv:hep-ph/9404247 \[hep-ph\]](#).
- [42] ATLAS Collaboration, *Measurement of the Higgs boson mass from the $H \rightarrow \gamma\gamma$ and $H \rightarrow ZZ^* \rightarrow 4\ell$ channels in pp collisions at center-of-mass energies of 7 and 8 TeV with the ATLAS detector*, *Phys. Rev. D* **90** (2014) 052004.
- [43] ATLAS Collaboration, *Measurements of Higgs boson production and couplings in diboson final states with the ATLAS detector at the LHC*, *Phys. Lett. B* **726** (2013) no. 13, 88 – 119. <http://www.sciencedirect.com/science/article/pii/S0370269313006369>.
- [44] ATLAS Collaboration, *Evidence for the spin-0 nature of the Higgs boson using ATLAS data*, *Phys.Lett. B* **726** (2013) 120–144, [arXiv:1307.1432 \[hep-ex\]](#).
- [45] ATLAS Collaboration, *Study of the spin of the Higgs-like boson in the two photon decay channel using 20.7 fb⁻¹ of pp collisions collected at $\sqrt{s} = 8$ TeV with the ATLAS detector*, Tech. Rep. ATLAS-CONF-2013-029, CERN, Geneva, Mar, 2013.
- [46] ATLAS Collaboration, *Study of the spin properties of the Higgs-like particle in the $H \rightarrow WW^{(*)} \rightarrow e\nu\mu\nu$ channel with 21 fb⁻¹ of $\sqrt{s} = 8$ TeV data collected with the ATLAS detector.*, Tech. Rep. ATLAS-CONF-2013-031, CERN, Geneva, Mar, 2013.
- [47] Y. Gao, A. V. Gritsan, Z. Guo, K. Melnikov, M. Schulze, et al., *Spin determination of single-produced resonances at hadron colliders*, *Phys.Rev.* **D81** (2010) 075022, [arXiv:1001.3396 \[hep-ph\]](#).

- [48] L. Landau, *On the angular momentum of a two-photon system*, Dokl.Akad.Nauk Ser.Fiz. **60** (1948) 207–209.
- [49] C.-N. Yang, *Selection Rules for the Dematerialization of a Particle Into Two Photons*, [Phys.Rev. **77** \(1950\) 242–245](#).
- [50] Super-Kamiokande Collaboration, *Evidence for an oscillatory signature in atmospheric neutrino oscillation*, [Phys.Rev.Lett. **93** \(2004\) 101801](#), [arXiv:hep-ex/0404034 \[hep-ex\]](#).
- [51] SNO Collaboration, *Measurement of the rate of $\nu_e + d \rightarrow p + p + e^-$ interactions produced by 8B solar neutrinos at the Sudbury Neutrino Observatory*, [Phys.Rev.Lett. **87** \(2001\) 071301](#), [arXiv:nucl-ex/0106015 \[nucl-ex\]](#).
- [52] OPERA Collaboration, *Observation of a first ν_τ candidate in the OPERA experiment in the CNGS beam*, [Phys.Lett. **B691** \(2010\) 138–145](#), [arXiv:1006.1623 \[hep-ex\]](#).
- [53] A. Einstein, *The Formal Foundation of the General Theory of Relativity*, Sitzungsber.Preuss.Akad.Wiss.Berlin (Math.Phys.) **1914** (1914) 1030–1085.
- [54] A. Einstein and N. Rosen, *The Particle Problem in the General Theory of Relativity*, [Phys.Rev. **48** \(1935\) 73–77](#).
- [55] T. Appelquist, A. Chodos, and P. Freund, *MODERN KALUZA-KLEIN THEORIES*, .
- [56] H. P. Nilles, *Supersymmetry, Supergravity and Particle Physics*, [Phys.Rept. **110** \(1984\) 1–162](#).
- [57] J. Wess and J. Bagger, *Supersymmetry and supergravity*, .
- [58] J. Terning, *Modern supersymmetry: Dynamics and duality*, .
- [59] Planck Collaboration, *Planck 2013 results. I. Overview of products and scientific results*, [arXiv:1303.5062 \[astro-ph.CO\]](#).
- [60] Planck Collaboration, *Planck 2013 results. I. Overview of products and scientific results*, [arXiv:1303.5062 \[astro-ph.CO\]](#).
- [61] L. Evans and P. Bryant, *LHC Machine*, [JINST **3** \(2008\) S08001](#).
- [62] ATLAS Collaboration, *The ATLAS experiment at the CERN Large Hadron*

- Collider*, **JINST 3** (2008) S08003.
- [63] CMS Collaboration, *The CMS experiment at the CERN Large Hadron Collider*, **JINST 3** (2008) S08004.
- [64] *LEP design report: vol. 2. The LEP main ring*, Tech. Rep. CERN-LEP-84-01, Geneva, 1984. <https://cdsweb.cern.ch/record/102083>.
- [65] F. Marcastel, *CERN's Accelerator Complex. La chane des acclrateurs du CERN*, . Adapted from OPEN-PHO-CHART-2013-001.
- [66] W. Stirling, *private communication*, 2012.
- [67] J. Jowett, *private communication*, May, 2014.
- [68] M. Lamont, *LHC, HL-LHC and Beyond*, PoS **EPS-HEP2013** (2014) 149.
- [69] *Luminosity public results*. ATLAS Collaboration, 2010-2012. <https://twiki.cern.ch/twiki/bin/view/AtlasPublic/LuminosityPublicResults>.
- [70] ALICE Collaboration, *The ALICE experiment at the CERN Large Hadron Collider*, **JINST 3** (2008) S08002.
- [71] LHCb Collaboration, *The LHCb detector at the Large Hadron Collider*, **JINST 3** (2008) S08005.
- [72] TOTEM Collaboration, *The TOTEM experiment at the CERN Large Hadron Collider*, **JINST 3** (2008) S08007.
- [73] LHCf Collaboration, *The LHCf detector at the CERN Large Hadron Collider*, **JINST 3** (2008) S08006.
- [74] J. Pinfold et al., *Technical Design Report of the MoEDAL Experiment*, Tech. Rep. CERN-LHCC-2009-006. MoEDAL-TDR-001, CERN, Geneva, Jun, 2009.
- [75] L. Evans, *The Large Hadron Collider*, **New J. Phys.** **9** (2007) 335.
- [76] J. Pequenaio, *Computer generated image of the whole ATLAS detector*, Mar, 2008.
- [77] ATLAS Collaboration, *Expected performance of the ATLAS experiment: detector, trigger and physics*. CERN, Geneva, 2009.
- [78] R. Gluckstern, *Uncertainties in track momentum and direction, due to multiple scattering and measurement errors*, **Nuclear Instruments and Methods** **24** (1963)

- no. 0, 381 – 389.
- [79] W. B. L. Rolandi, W. Riegler, *Particle Detection with Drift Chambers*. Springer Berlin Heidelberg, 2008.
- [80] *Event Displays*. ATLAS Collaboration, 2010-2012. <https://twiki.cern.ch/twiki/bin/view/AtlasPublic/EventDisplayStandAlone>.
- [81] ATLAS Collaboration, *ATLAS pixel detector electronics and sensors*, *J. Instrum.* **3** (2008) P07007.
- [82] ATLAS Collaboration, *ATLAS Insertable B-Layer Technical Design Report*, Tech. Rep. CERN-LHCC-2010-013. ATLAS-TDR-19, CERN, Geneva, Sep, 2010.
- [83] ATLAS Collaboration, *The silicon microstrip sensors of the ATLAS semiconductor tracker*, *Nuclear Instruments and Methods in Physics Research Section A: Accelerators, Spectrometers, Detectors and Associated Equipment* **578** (2007) no. 1, 98 – 118.
- [84] ATLAS TRT Collaboration, *The ATLAS Transition Radiation Tracker (TRT) proportional drift tube: Design and performance*, *JINST* **3** (2008) P02013.
- [85] A. Vogel, *ATLAS Transition Radiation Tracker (TRT): Straw Tube Gaseous Detectors at High Rates*, Tech. Rep. ATL-INDET-PROC-2013-005, CERN, Geneva, Apr, 2013.
- [86] R. Wigmans, *Calorimetry - Energy Measurement in Particle Physics*. Oxford University Press, 2000.
- [87] C. W. Fabjan and F. Gianotti, *Calorimetry for particle physics*, *Rev. Mod. Phys.* **75** (2003) 1243–1286.
- [88] D. Froidevaux and P. Sphicas, *General-Purpose Detectors for the Large Hadron Collider*, *Annual Review of Nuclear and Particle Science* **56** (2006) no. 1, 375–440.
- [89] T. Gabriel, D. Groom, P. Job, N. Mokhov, and G. Stevenson, *Energy dependence of hadronic activity*, *Nuclear Instruments and Methods in Physics Research Section A: Accelerators, Spectrometers, Detectors and Associated Equipment* **338** (1994) no. 23, 336 – 347.
- [90] ATLAS Collaboration, *Readiness of the ATLAS Tile Calorimeter for LHC collisions*, *The European Physical Journal C* **70** (2010) no. 4, 1193–1236.

- [91] D. Gingrich, *Construction, assembly and testing of the ATLAS hadronic end-cap calorimeter*, *Journal of Instrumentation* **2** (2007) no. 05, P05005.
- [92] A. Artamonov et al., *The ATLAS Forward Calorimeter*, *Journal of Instrumentation* **3** (2008) no. 02, P02010.
- [93] ATLAS Collaboration, *Standalone vertex finding in the ATLAS muon spectrometer*, *Journal of Instrumentation* **9** (2014) no. 02, P02001.
- [94] A. Krasznahorkay, *The evolution of the Trigger and Data Acquisition System in the ATLAS experiment*, Tech. Rep. ATL-DAQ-PROC-2013-018, CERN, Geneva, Sep, 2013.
- [95] O. Igonkina, *ATLAS trigger menu and performance in Run 1 and prospects for Run 2*, *Nuclear Science Symposium and Medical Imaging Conference (NSS/MIC), 2013 IEEE* (2013) 1–4.
- [96] J. G. Panduro Vazquez, *Atlas Data Acquisition: from Run I to Run II*, Tech. Rep. ATL-DAQ-SLIDE-2014-387, CERN, Geneva, Jul, 2014.
<https://cds.cern.ch/record/1727972/>.
- [97] ATLAS Collaboration, *ATLAS Computing : technical design report*, Tech. Rep. CERN-LHCC-2005-022, CERN, Geneva, June, 2005.
<https://cdsweb.cern.ch/record/837738/>.
- [98] I. Bird, *Computing for the Large Hadron Collider*, *Annual Review of Nuclear and Particle Science* **61** (2011) no. 1, 99–118.
- [99] ATLAS Collaboration, *Search for the Standard Model Higgs boson in produced in association with a vector boson and decaying to bottom quarks with the ATLAS detector*, Tech. Rep. ATLAS-CONF-2012-161, CERN, Geneva, Nov, 2012.
- [100] F. Krauss, *private communication (Durham University/SHERPA)*, 2014.
- [101] T. Sjöstrand, S. Mrenna, and P. Z. Skands, *A brief introduction to PYTHIA 8.1*, *Comput. Phys. Commun.* **178** (2008) 852–867, [arXiv:0710.3820 \[hep-ph\]](https://arxiv.org/abs/0710.3820).
- [102] T. Sjöstrand, S. Mrenna, and P. Z. Skands, *PYTHIA 6.4 Physics and Manual*, *JHEP* **05** (2006) 026, [arXiv:hep-ph/0603175](https://arxiv.org/abs/hep-ph/0603175).
- [103] T. Gleisberg, S. Höche, F. Krauss, M. Schönherr, S. Schumann, et al., *Event generation with SHERPA 1.1*, *JHEP* **0902** (2009) 007, [arXiv:0811.4622](https://arxiv.org/abs/0811.4622)

- [hep-ph].
- [104] G. Corcella, I. Knowles, G. Marchesini, S. Moretti, K. Odagiri, et al., *HERWIG6: An event generator for hadron emission reactions with interfering gluons (including supersymmetric processes)*, *JHEP* **0101** (2001) 010, [arXiv:hep-ph/0011363](#) [hep-ph].
- [105] P. Nason, *A New method for combining NLO QCD with shower Monte Carlo algorithms*, *JHEP* **11** (2004) 040, [arXiv:hep-ph/0409146](#) [hep-ph].
- [106] S. Frixione, P. Nason, and C. Oleari, *Matching NLO QCD computations with Parton Shower simulations: the POWHEG method*, *JHEP* **11** (2007) 070, [arXiv:0709.2092](#) [hep-ph].
- [107] S. Alioli, P. Nason, C. Oleari, and E. Re, *A general framework for implementing NLO calculations in shower Monte Carlo programs: the POWHEG BOX*, *JHEP* **06** (2010) 043, [arXiv:1002.2581](#) [hep-ph].
- [108] B. P. Kersevan and E. Richter-Was, *The Monte Carlo event generator AcerMC version 2.0 with interfaces to PYTHIA 6.2 and HERWIG 6.5*, [arXiv:hep-ph/0405247](#) [hep-ph].
- [109] GEANT4 Collaboration, *GEANT4: A Simulation toolkit*, *Nucl. Instrum. Meth. A* **506** (2003) 250–303.
- [110] ATLAS Collaboration, *The ATLAS Simulation Infrastructure*, *Eur. Phys. J C* **70** (2010) 823, [arXiv:1005.4568](#) [physics.ins-det].
- [111] J. Chapman, K. Assamagan, P. Calafiura, D. Chakraborty, D. Costanzo, et al., *The ATLAS detector digitization project for 2009 data taking*, *J.Phys.Conf.Ser.* **219** (2010) 032031.
- [112] ATLAS Collaboration, *Electron efficiency measurements with the ATLAS detector using the 2012 LHC proton-proton collision data*, Tech. Rep. ATLAS-CONF-2014-032, CERN, Geneva, Jun, 2014.
- [113] ATLAS Collaboration, *Electron reconstruction and identification efficiency measurements with the ATLAS detector using the 2011 LHC proton-proton collision data*, *Eur.Phys.J. C* **74** (2014) 2941, [arXiv:1404.2240](#) [hep-ex].
- [114] W. Lampl, S. Laplace, D. Lelas, P. Loch, H. Ma, S. Menke, S. Rajagopalan, D. Rousseau, S. Snyder, and G. Unal, *Calorimeter Clustering Algorithms:*

- Description and Performance*, Tech. Rep. ATL-LARG-PUB-2008-002.
ATL-COM-LARG-2008-003, CERN, Geneva, Apr, 2008.
- [115] ATLAS Collaboration, *Improved electron reconstruction in ATLAS using the Gaussian Sum Filter-based model for bremsstrahlung*, Tech. Rep. ATL-COM-CONF-2012-047, CERN, Geneva, May, 2012.
- [116] ATLAS Collaboration, *Electron and photon energy calibration with the ATLAS detector using LHC Run 1 data*, *Eur.Phys.J.* **C74** (2014) no. 10, 3071, [arXiv:1407.5063 \[hep-ex\]](#).
- [117] J. Alison, K. Brendlinger, S. Heim, J. Kroll, and C. M. Lester, *Description and Performance of the Electron Likelihood Tool at ATLAS using 2012 LHC Data*, Tech. Rep. ATL-COM-PHYS-2013-378, CERN, Geneva, Apr, 2013.
- [118] ATLAS Collaboration, *Measurement of the muon reconstruction performance of the ATLAS detector using 2011 and 2012 LHC proton-proton collision data*, [arXiv:1407.3935 \[hep-ex\]](#).
- [119] T. Lagouri, D. Adams, K. Assamagan, M. Biglietti, G. Carlino, et al., *A Muon Identification and Combined Reconstruction Procedure for the ATLAS Detector at the LHC at CERN*, *IEEE Trans.Nucl.Sci.* **51** (2004) 3030–3033.
- [120] ATLAS Collaboration, *Measurement of the inclusive isolated prompt photon cross section in pp collisions at $\sqrt{s} = 7$ TeV with the ATLAS detector*, *Phys.Rev.* **D83** (2011) 052005, [arXiv:1012.4389 \[hep-ex\]](#).
- [121] K. Ecker, M. Goblirsch-Kolb, and O. Kortner, *Muon Response Modelling for the Measurement of the Mass of the Higgs Boson Candidate in 4l Final State*, Tech. Rep. ATL-COM-PHYS-2012-1736, CERN, Geneva, Nov, 2012.
- [122] ATLAS Collaboration, *Preliminary results on the muon reconstruction efficiency, momentum resolution, and momentum scale in ATLAS 2012 pp collision data*, Tech. Rep. ATLAS-CONF-2013-088, CERN, Geneva, Aug, 2013.
- [123] ATLAS Collaboration, *Electron performance measurements with the ATLAS detector using the 2010 LHC proton-proton collision data*, *Eur.Phys.J.* **C72** (2012) 1909, [arXiv:1110.3174 \[hep-ex\]](#).
- [124] J. Alison et al., *Supporting document on electron performance measurements using the 2011 LHC proton-proton collisions*, Tech. Rep. ATL-PHYS-INT-2014-016,

- CERN, Geneva, Jun, 2014.
- [125] G. P. Salam, *Towards Jetography*, *Eur.Phys.J.* **C67** (2010) 637–686, [arXiv:0906.1833 \[hep-ph\]](#).
- [126] G. F. Sterman and S. Weinberg, *Jets from Quantum Chromodynamics*, *Phys.Rev.Lett.* **39** (1977) 1436.
- [127] G. P. Salam and G. Soyez, *A Practical Seedless Infrared-Safe Cone jet algorithm*, *JHEP* **0705** (2007) 086, [arXiv:0704.0292 \[hep-ph\]](#).
- [128] J. Dorfan, *A Cluster Algorithm for the Study of Jets in High-energy Physics*, *Z.Phys.* **C7** (1981) 349.
- [129] H. Daum, H. Meyer, and J. Burger, *A Cluster Algorithm for Jet Studies*, *Z.Phys.* **C8** (1981) 167.
- [130] K. Lanius, H. Roloff, and H. Schiller, *SELECTION OF JETS IN MULTI - HADRON FINAL STATES PRODUCED BY $e^+ e^-$ ANNIHILATION*, *Z.Phys.* **C8** (1981) 251.
- [131] A. Backer, *NORMICITY, A GENERAL JET MEASURE*, *Z.Phys.* **C12** (1982) 161–166.
- [132] T. Sjostrand, *The Lund Monte Carlo for $e^+ e^-$ Jet Physics*, *Comput.Phys.Commun.* **28** (1983) 229.
- [133] M. Cacciari and G. P. Salam, *Dispelling the N^3 myth for the k_t jet-finder*, *Phys.Lett.* **B641** (2006) 57–61, [arXiv:hep-ph/0512210 \[hep-ph\]](#).
- [134] Y. L. Dokshitzer, G. Leder, S. Moretti, and B. Webber, *Better jet clustering algorithms*, *JHEP* **9708** (1997) 001, [arXiv:hep-ph/9707323 \[hep-ph\]](#).
- [135] M. Wobisch and T. Wengler, *Hadronization corrections to jet cross-sections in deep inelastic scattering*, [arXiv:hep-ph/9907280 \[hep-ph\]](#).
- [136] M. Wobisch, *Measurement and QCD analysis of jet cross-sections in deep inelastic positron proton collisions at $s^{*}(1/2) = 300\text{-GeV}$* , .
- [137] S. D. Ellis and D. E. Soper, *Successive combination jet algorithm for hadron collisions*, *Phys.Rev.* **D48** (1993) 3160–3166, [arXiv:hep-ph/9305266 \[hep-ph\]](#).
- [138] M. Cacciari, G. P. Salam, and G. Soyez, *The Anti- $k(t)$ jet clustering algorithm*,

- JHEP **0804** (2008) 063, [arXiv:0802.1189 \[hep-ph\]](#).
- [139] ATLAS Collaboration, *Jet energy measurement with the ATLAS detector in proton-proton collisions at $\sqrt{s} = 7$ TeV*, [Eur.Phys.J. **C73** \(2013\) 2304](#), [arXiv:1112.6426 \[hep-ex\]](#).
- [140] M. Cacciari and G. P. Salam, *Pileup subtraction using jet areas*, [Phys.Lett. **B659** \(2008\) 119–126](#), [arXiv:0707.1378 \[hep-ph\]](#).
- [141] ATLAS Collaboration, *Pile-up subtraction and suppression for jets in ATLAS*, Tech. Rep. ATLAS-CONF-2013-083, CERN, Geneva, Aug, 2013.
- [142] ATLAS Collaboration, *Pile-up corrections for jets from proton-proton collisions at $\sqrt{s} = 7$ TeV in ATLAS in 2011*, Tech. Rep. ATLAS-CONF-2012-064, CERN, Geneva, Jul, 2012.
- [143] ATLAS Collaboration, *Jet energy measurement and its systematic uncertainty in proton-proton collisions at $\sqrt{s} = 7$ TeV with the ATLAS detector*, [arXiv:1406.0076 \[hep-ex\]](#).
- [144] OPAL Collaboration, G. Abbiendi et al., *Experimental properties of gluon and quark jets from a point source*, [Eur.Phys.J. **C11** \(1999\) 217–238](#), [arXiv:hep-ex/9903027 \[hep-ex\]](#).
- [145] ATLAS Collaboration, *Light-quark and Gluon Jets in ATLAS*, Tech. Rep. ATLAS-CONF-2011-053, CERN, Geneva, Apr, 2011.
- [146] ATLAS Collaboration, *Light-quark and Gluon Jets: Calorimeter Response, Jet Energy Scale Systematics and Properties*, Tech. Rep. ATLAS-CONF-2012-138, CERN, Geneva, Sep, 2012.
- [147] LHCb Collaboration, *Measurement of b -hadron production fractions in 7 TeVpp collisions*, [Phys.Rev. **D85** \(2012\) 032008](#), [arXiv:1111.2357 \[hep-ex\]](#).
- [148] DELPHI Collaboration, *A study of the b -quark fragmentation function with the DELPHI detector at LEP I and an averaged distribution obtained at the Z Pole*, [Eur.Phys.J. **C71** \(2011\) 1557](#), [arXiv:1102.4748 \[hep-ex\]](#).
- [149] ATLAS Collaboration, *Commissioning of the ATLAS high-performance b -tagging algorithms in the 7 TeV collision data*, Tech. Rep. ATLAS-CONF-2011-102, CERN, Geneva, Jul, 2011.

- [150] ATLAS Collaboration, *Calibration of b -tagging using dileptonic top pair events in a combinatorial likelihood approach with the ATLAS experiment*, Tech. Rep. ATLAS-CONF-2014-004, CERN, Geneva, Feb, 2014.
- [151] ATLAS Collaboration, *Calibration of the performance of b -tagging for c and light-flavour jets in the 2012 ATLAS data*, Tech. Rep. ATLAS-CONF-2014-046, CERN, Geneva, Jul, 2014.
- [152] F. Ahmadov, A. Da Palma, L. Alio, B. Allbrooke, T. Bristow, D. Buescher, A. Buzatu, Y. Coadou, P. Conde Muio, C. Debenedetti, Y. Enari, G. Facini, W. Fisher, P. Francavilla, G. Gaycken, J. Gentil, R. Goncalo, G. Gonzalez Parra, H. Gray, J. Grivaz, C. Gwilliam, S. Hageboeck, G. Halladjian, M. Jackson, D. Jamin, R. Jansky, K. Kiuchi, V. Kostyukhin, K. Lohwasser, D. Lopez Mateos, U. Mallik, J. Maneira, G. Marchiori, M. Martinez Perez, A. Mehta, K. Mercurio, K. Mochizuki, N. Morange, Y. Ming, P. Mullen, Y. Nagai, J. Nielsen, I. Ochoa, A. Palma, C. Pandini, R. Pedro, G. Piacquadio, M. Proissl, T. Ravenscroft, P. Rose, T. Scanlon, E. Schopf, S. Shaw, B. Smart, V. Sorin, M. Sousa, F. Sforza, J. Therhaag, P. Thompson, L. Vacavant, J. Wang, C. Wang, S. Wang, C. Weiser, R. Zaidan, and L. Zhang, *Supporting Document for the Search for the $b\bar{b}$ decay of the Standard Model Higgs boson in associated $(W/Z)H$ production with the ATLAS detector*, Tech. Rep. ATL-COM-PHYS-2014-051, CERN, Geneva, Jan, 2014.
- [153] P. Berta, F. Filthaut, V. Dao, E. Le Menedeu, F. Parodi, G. Piacquadio, T. Scanlon, M. Ughetto, and L. Zhang, *Continuous b -tagging for the ATLAS experiment*, Tech. Rep. ATL-COM-PHYS-2014-035, CERN, Geneva, Jan, 2014.
- [154] G. Piacquadio, *Calibration of b -tagging using di-leptonic top pair events and a combinatorial likelihood approach*, Tech. Rep. ATL-COM-PHYS-2013-395, CERN, Geneva, Apr, 2013.
- [155] G. Piacquadio, *Calibration of b -tagging using di-leptonic top pair events applying the combinatorial likelihood approach to 2011 data*, Tech. Rep. ATL-COM-PHYS-2013-1083, CERN, Geneva, Aug, 2013.
- [156] ATLAS Collaboration, *Calibration of b -tagging using dileptonic top pair events in a combinatorial likelihood approach with the ATLAS experiment*, Tech. Rep. ATLAS-CONF-2014-004, CERN, Geneva, Feb, 2014.
- [157] G. Aad, H. Arnold, and C. Weiser, *b -jet tagging calibration on c -jets produced in association with W^\pm bosons*, Tech. Rep. ATL-COM-PHYS-2013-1365, CERN,

- Geneva, Sep, 2013.
- [158] I. Burmeister, I. Connelly, A. Ferretto, F. Filthaut, R. Goncalo, R. Hawkings, H. Esch, F. Parodi, D. Sidorov, C. Schiavi, J. Thomas-Wilsker, J. Yu, and M. Zur Nedden, *Measurement of the b-tagging performance in the 2012 ATLAS data*, Tech. Rep. ATL-COM-PHYS-2013-456, CERN, Geneva, Apr, 2013.
 - [159] ATLAS Collaboration, *Performance of Missing Transverse Momentum Reconstruction in Proton-Proton Collisions at 7 TeV with ATLAS*, [Eur.Phys.J. C72 \(2012\) 1844](#), [arXiv:1108.5602 \[hep-ex\]](#).
 - [160] ATLAS Collaboration, *Performance of Missing Transverse Momentum Reconstruction in ATLAS studied in Proton-Proton Collisions recorded in 2012 at 8 TeV*, Tech. Rep. ATLAS-CONF-2013-082, CERN, Geneva, Aug, 2013.
 - [161] ATLAS Collaboration, *Performance of the missing transverse energy reconstruction in proton-proton collisions at center-of-mass energy of $\sqrt{s} = 7$ TeV with the ATLAS detector*, Tech. Rep. ATLAS-CONF-2010-039, CERN, Geneva, Jul, 2010.
 - [162] ATLAS Collaboration, *Performance of the missing transverse energy reconstruction in minimum bias events at \sqrt{s} of 900 GeV and 2.36 TeV with the ATLAS detector*, Tech. Rep. ATLAS-CONF-2010-008, CERN, Geneva, Jun, 2010.
 - [163] ATLAS Collaboration, *Performance of the Missing Transverse Energy Reconstruction and Calibration in Proton-Proton Collisions at a Center-of-Mass Energy of 7 TeV with the ATLAS Detector*, Tech. Rep. ATLAS-CONF-2010-057, CERN, Geneva, Jul, 2010.
 - [164] ATLAS Collaboration, *Pile-up Suppression in Missing Transverse Momentum Reconstruction in the ATLAS Experiment in Proton-Proton Collisions at $\sqrt{s} = 8$ TeV*, Tech. Rep. ATLAS-CONF-2014-019, CERN, Geneva, May, 2014.
 - [165] J. Pumplin, D. Stump, J. Huston, H. Lai, P. M. Nadolsky, et al., *New generation of parton distributions with uncertainties from global QCD analysis*, [JHEP 0207 \(2002\) 012](#), [arXiv:hep-ph/0201195 \[hep-ph\]](#).
 - [166] ATLAS Collaboration, *ATLAS tunes of PYTHIA 6 and Pythia 8 for MC11*, .
 - [167] ATLAS Collaboration, *New ATLAS event generator tunes to 2010 data*, .
 - [168] P. Golonka and Z. Was, *PHOTOS Monte Carlo: A Precision tool for QED*

- corrections in Z and W decays*, *Eur.Phys.J.* **C45** (2006) 97–107, [arXiv:hep-ph/0506026 \[hep-ph\]](#).
- [169] H.-L. Lai, M. Guzzi, J. Huston, Z. Li, P. M. Nadolsky, et al., *New parton distributions for collider physics*, *Phys.Rev.* **D82** (2010) 074024, [arXiv:1007.2241 \[hep-ph\]](#).
- [170] G. Luisoni, P. Nason, C. Oleari, and F. Tramontano, *$HW^\pm/HZ + 0$ and 1 jet at NLO with the POWHEG BOX interfaced to GoSam and their merging within MiNLO*, *JHEP* **1310** (2013) 083, [arXiv:1306.2542 \[hep-ph\]](#).
- [171] C. Englert, M. McCullough, and M. Spannowsky, *Gluon-initiated associated production boosts Higgs physics*, *Phys.Rev.* **D89** (2014) no. 1, 013013, [arXiv:1310.4828 \[hep-ph\]](#).
- [172] J. Ohnemus and W. J. Stirling, *Order α_s corrections to the differential cross-section for the WH intermediate mass Higgs signal*, *Phys.Rev.* **D47** (1993) 2722–2729.
- [173] H. Baer, B. Bailey, and J. Owens, *$O(\alpha_s)$ Monte Carlo approach to $W + \text{Higgs}$ associated production at hadron supercolliders*, *Phys.Rev.* **D47** (1993) 2730–2734.
- [174] O. Brein, A. Djouadi, and R. Harlander, *NNLO QCD corrections to the Higgs-strahlung processes at hadron colliders*, *Phys.Lett.* **B579** (2004) 149–156, [arXiv:hep-ph/0307206 \[hep-ph\]](#).
- [175] M. Ciccolini, S. Dittmaier, and M. Kramer, *Electroweak radiative corrections to associated WH and ZH production at hadron colliders*, *Phys.Rev.* **D68** (2003) 073003, [arXiv:hep-ph/0306234 \[hep-ph\]](#).
- [176] A. Denner, S. Dittmaier, S. Kallweit, and A. Muck, *EW corrections to Higgs strahlung at the Tevatron and the LHC with HAWK*, *PoS EPS-HEP2011* (2011) 235, [arXiv:1112.5258 \[hep-ph\]](#).
- [177] L. Altenkamp, S. Dittmaier, R. V. Harlander, H. Rzehak, and T. J. Zirke, *Gluon-induced Higgs-strahlung at next-to-leading order QCD*, *JHEP* **1302** (2013) 078, [arXiv:1211.5015 \[hep-ph\]](#).
- [178] A. Djouadi, J. Kalinowski, and M. Spira, *HDECAY: A Program for Higgs boson decays in the standard model and its supersymmetric extension*, *Comput.Phys.Commun.* **108** (1998) 56–74, [arXiv:hep-ph/9704448 \[hep-ph\]](#).

- [179] K. Melnikov and F. Petriello, *Electroweak gauge boson production at hadron colliders through $O(\alpha(s)^{**2})$* , *Phys.Rev.* **D74** (2006) 114017, [arXiv:hep-ph/0609070](#) [[hep-ph](#)].
- [180] M. Czakon, P. Fiedler, and A. Mitov, *Total Top-Quark Pair-Production Cross Section at Hadron Colliders Through $O(\frac{4}{S})$* , *Phys.Rev.Lett.* **110** (2013) 252004, [arXiv:1303.6254](#) [[hep-ph](#)].
- [181] P. Nason and G. Zanderighi, *W^+W^- , WZ and ZZ production in the POWHEG-BOX-V2*, *Eur.Phys.J.* **C74** (2014) 2702, [arXiv:1311.1365](#) [[hep-ph](#)].
- [182] N. Kidonakis, *Next-to-next-to-leading-order collinear and soft gluon corrections for t -channel single top quark production*, *Phys.Rev.* **D83** (2011) 091503, [arXiv:1103.2792](#) [[hep-ph](#)].
- [183] N. Kidonakis, *NNLL resummation for s -channel single top quark production*, *Phys.Rev.* **D81** (2010) 054028, [arXiv:1001.5034](#) [[hep-ph](#)].
- [184] N. Kidonakis, *Two-loop soft anomalous dimensions for single top quark associated production with a W^- or H^-* , *Phys.Rev.* **D82** (2010) 054018, [arXiv:1005.4451](#) [[hep-ph](#)].
- [185] L. Breiman, J. Friedman, R. Olshen, and C. Stone, *Classification and Regression Trees*. Wadsworth and Brooks, Monterey, CA, 1984.
- [186] Y. Freund and R. Schapire, *Experiments with a new boosting algorithm*, in *Machine Learning, Proceedings of the Thirteenth International Conference (ICML)*. Morgan Kaufmann, 1996.
- [187] A. Hocker, J. Stelzer, F. Tegenfeldt, H. Voss, K. Voss, et al., *TMVA - Toolkit for Multivariate Data Analysis*, PoS **ACAT** (2007) 040, [arXiv:physics/0703039](#) [[PHYSICS](#)].
- [188] Belle Collaboration, *A detailed test of the $CsI(Tl)$ calorimeter for BELLE with photon beams of energy between 20-MeV and 5.4-GeV*, *Nucl.Instrum.Meth.* **A441** (2000) 401–426.
- [189] ATLAS JetETmiss Group, *Invariant Mass Studies for the $H \rightarrow b\bar{b}$ Measurements for LHCP (internal)*, 2013.
- [190] A. Bukin, *Fitting function for asymmetric peaks*, [arXiv:0711.4449](#) [[physics.data-an](#)].

-
- [191] S. Hoeche, F. Krauss, M. Schonherr, and F. Siegert, *QCD matrix elements + parton showers: The NLO case*, *JHEP* **1304** (2013) 027, [arXiv:1207.5030 \[hep-ph\]](#).
- [192] ATLAS Collaboration, *Measurements of normalized differential cross-sections for $t\bar{t}$ production in pp collisions at $\sqrt{s}=7$ TeV using the ATLAS detector*, *Phys.Rev.* **D90** (2014) 072004, [arXiv:1407.0371 \[hep-ex\]](#).
- [193] A. L. Read, *Presentation of search results: The $CL(s)$ technique*, *J.Phys.* **G28** (2002) 2693–2704.
- [194] G. Cowan, K. Cranmer, E. Gross, and O. Vitells, *Asymptotic formulae for likelihood-based tests of new physics*, *Eur.Phys.J.* **C71** (2011) 1554, [arXiv:1007.1727 \[physics.data-an\]](#).
- [195] F. James and M. Roos, *Minuit: A System for Function Minimization and Analysis of the Parameter Errors and Correlations*, *Comput.Phys.Commun.* **10** (1975) 343–367.
- [196] ATLAS Collaboration, *Search for the $b\bar{b}$ decay of the Standard Model Higgs boson in associated W/ZH production with the ATLAS detector*, Tech. Rep. ATLAS-CONF-2013-079, CERN, Geneva, Jul, 2013.

List of Figures

2.1. Standard Model of Particle Physics	9
2.2. Measurements of the running coupling $\alpha_s(Q)$	11
2.3. Illustration of the Higgs potential	16
2.4. Feynman diagrams of Higgs production modes at LHC	19
2.5. Standard Model Higgs boson production cross-sections	20
2.6. Standard Model Higgs boson branching ratios	21
2.7. Invariant Higgs mass distributions for $H \rightarrow \gamma\gamma$ and $H \rightarrow WW^*$	22
2.8. The observed local significance as a function of the Higgs boson mass	23
2.9. Higgs mass measurement using the $H \rightarrow \gamma\gamma$ and $H \rightarrow ZZ^* \rightarrow 4\ell$ decay channels	24
2.10. Likelihood contours for diboson final states	25
2.11. The $H \rightarrow \tau^+\tau^-$ signal strength μ	26
2.12. One-loop radiative corrections to the Higgs boson mass	28
3.1. The CERN accelerator complex	32
3.2. Cross-section of a LHC dipole magnet	33
3.3. Standard Model proton - (anti)proton cross-sections	34
3.4. ATLAS Beam Envelopes	35

3.5. The mean number of interactions per bunch crossing (a) and the total integrated (b) and peak instantaneous (c) luminosity delivered by the LHC to, and recorded by ATLAS during stable beams at $\sqrt{s} = 7$ TeV and $\sqrt{s} = 8$ TeV[69].	37
3.6. LHC layout	38
3.7. ATLAS layout	39
3.8. Particles interacting with ATLAS detector volumes	40
3.9. ATLAS magnet system	43
3.10. ATLAS Inner Detector	44
3.11. ATLAS Barrel Inner Detector	45
3.12. ATLAS End-Cap Inner Detector	45
3.13. ATLAS Inner Detector Material	46
3.14. Charged Particle Tracking	47
3.15. Vertex display of ATLAS events	48
3.16. Layout of the ATLAS calorimetry system	51
3.17. Layout of a barrel module of the ATLAS electromagnetic calorimeter	53
3.18. Simplified schematic illustration of an hadronic cascade	54
3.19. Logic flow diagram of an hadronic shower	55
3.20. Material distribution up to the first muon spectrometer layer	57
3.21. Cross-sectional views of the ATLAS Muon Spectrometer	58
3.22. ATLAS Forward Detectors	60
3.23. ATLAS Trigger and Data Acquisition system	62
4.1. Leading-order Feynman diagram for quark-initiated VH production.	64
4.2. ATLAS event displays of Higgs to $b\bar{b}$ candidates in associated with a W or Z boson	66

4.3. Sketch of a LHC proton-proton collision event	68
4.4. Measured electron identification efficiency for different likelihood-based identification criteria	70
4.5. Measured muon reconstruction efficiency for different muon reconstruction types	73
4.6. Electron energy scale and effective constant term corrections	76
4.7. Electron energy resolution and contributions to its uncertainty	76
4.8. Relative dimuon mass resolution as a function of the average p_T	78
4.9. Muon momentum and resolution scale factors	79
4.10. Dimuon invariant mass resolution and data/MC ratio	80
4.11. Statistics in different tag-and-probe quality variation bins measured in data	83
4.12. Electron and muon isolation efficiencies in data/MC and derived scale factors	84
4.13. Muon isolation efficiency and scale factors as a function of $\Delta R(\mu, \text{nearest jet})$	85
4.14. Distribution of the ΔR between a probing electron and the nearest jet . .	86
4.15. Electron isolation scale factors as a function of η in three $\Delta R(e, \text{close-by jet})$ bins, using Z +jets and ZH MC	87
4.16. Ratio of electron isolation efficiency scale factors in different $\Delta R(e, \text{close-by jet})$ regions, using Z +jets and ZH simulations	87
4.17. Muon isolation scale factors as a function of η and p_T in three $\Delta R(\mu, \text{close-by jet})$ bins, using Z +jets MC	88
4.18. Jet multiplicity in the vicinity of probing leptons and their isolation efficiency dependence	88
4.19. Muon isolation efficiency and scale factors as a function of the number of reconstructed vertices	90
4.20. Muon isolation efficiency, with the track- and calorimeter isolation criteria separated, as a function of the number of reconstructed vertices	90

4.21. Illustration of topological energy cluster building	92
4.22. Simulation of a parton-level event, generated with HERWIG, showing the particle clustering of different jet algorithms	93
4.23. Overview of jet collections used in the VH analysis	94
4.24. Overview of jet calibrations used in the VH analysis	95
4.25. Performance of pileup suppression techniques and their effect on the sensitivity to in-time and out-of-time pileup effects	96
4.26. Average jet response at the EM scale as a function of jet η	97
4.27. Eta correction as a function of the reconstructed jet η	98
4.28. Jet response difference of light-quark and gluon-induced jets for the EM+JES calibration and GSC	99
4.29. Illustration of the technique adopted by the Global Sequential Calibration	100
4.30. Inclusive number of associated tracks (a) and track width (b) of light-quark and gluon-induced jets	101
4.31. Average number of associated tracks (a) and track width (b) of light-quark and gluon-induced jets as a function of the reconstructed jet p_T^{reco}	101
4.32. Illustration of the b -quark fragmentation with its key quantities used for b -tagging	104
4.33. MC-to-data calibration scale factors for b -jet, c -jet and light-quark jet MV1c efficiencies	105
4.34. Distribution of E_T^{miss} and $\sum E_T$ in a data sample of $W \rightarrow e\nu$ events . . .	107
4.35. E_x^{miss} and E_y^{miss} resolution as a function of the total transverse momentum in the event measured in data	108
5.1. Leading order Feynman diagrams of the main background production modes	114
5.2. Leading order Feynman diagrams for gg -initiated ZH production	117
5.3. Example input variables to the MVA in the (LL, MM, TT) combined 2-jet 2-tag category	122

5.4. Dijet-invariant-mass distribution of $H \rightarrow b\bar{b}$ candidates in the combined 2-tag signal region of the 1-lepton channel, for both GSC and EM+JES calibrated b -jets	125
5.5. Dijet-invariant-mass distributions of GS-calibrated $H \rightarrow b\bar{b}$ candidates before and after the muon-in-jet correction in the combined 2-tag signal regions of all three channels	126
5.6. Resolution correction for EM+JES and GS-calibrated b -jets, obtained from VH signal events	128
5.7. Dijet-invariant-mass distributions of GS-calibrated, muon-in-jet-corrected $H \rightarrow b\bar{b}$ candidates before and after the resolution correction in the combined 2-tag signal regions of all three channels	129
5.8. Dijet-invariant-mass distributions of GS-calibrated $H \rightarrow b\bar{b}$ candidates before and after the muon-in-jet correction with subsequent resolution correction in the combined 2-tag signal regions of all three channels . . .	130
5.9. Dijet-invariant-mass distribution for the decay products of a Higgs boson with $m_H = 125$ GeV in the 2-lepton MVA selection	130
5.10. The $\Delta\phi(\text{jet}_1, \text{jet}_2)$ and p_T^W distributions before and after reweighting . . .	132
5.11. Distributions of the dijet-mass in each analysis channel	133
5.12. Distributions of the BDT discriminants in each analysis channel	134
5.13. Distributions of the MV1c output in each analysis channel	135
5.14. The ranking of the systematic uncertainties in the MVA analysis, ordered by their decreasing impact on $\hat{\mu}$	140
6.1. Illustration of the event-level simultaneous parameter set $\{E, \eta, \phi, ..\}$ variation within each parameter's uncertainty of the $Z(\ell\ell)H(b\bar{b})$ system . . .	143
6.2. Inclusive distributions of the electron energy and muon momentum resolutions used in the kinematic likelihood fit	148
6.3. Inclusive distributions of the $\eta^{\text{truth}}/\eta^{\text{reco}}$ and $\phi^{\text{truth}}/\phi^{\text{reco}}$ ratios for electrons and muons	148
6.4. Inclusive distributions of the $\eta^{\text{truth}}/\eta^{\text{reco}}$ and $\phi^{\text{truth}}/\phi^{\text{reco}}$ ratios for jets . .	149

6.5. Jet transfer functions, inclusive and in bins of p_T^{reco}	150
6.6. The $\sigma(p_T^{\text{reco}}/p_T^{\text{truth}})$ of fitted jet TFs as a function of the corresponding p_T^{reco} bin centres	151
6.7. Jet transfer functions, inclusive in p_T^{reco} , for both semileptonic and non-semileptonic b -jet decays in the 2-jet 2-tag signal region, and the difference between the two functions in terms of the scale factors from the semileptonic to the non-semileptonic probability value.	151
6.8. Jet transfer function, inclusive in p_T^{reco} , for non- b -tagged jets in events with at least three jets, two of them b -tagged	151
6.9. In-situ resolution correction in the form of a prior built from the expected p_T^{truth} spectrum	152
6.10. In-situ resolution correction, inclusive in $p_T^{\ell\ell}$, for both semileptonic and non-semileptonic b -jet decays in the 2-jet 2-tag signal region, and the difference between the two functions is shown in terms of the scale factors from the semileptonic to the non-semileptonic probability value	153
6.11. Jet transfer function, inclusive in p_T^{reco} , for non- b -tagged jets in events with at least three jets, two of them b -tagged	153
6.12. Illustration of the interference of two different PDFs used in the kinematic likelihood fit as a result of jet resolution/scale effects	154
6.13. The fitted distribution of the true $\sum p_{x,y}^{\ell\ell b\bar{b}}$, obtained from Monte Carlo simulations	155
6.14. Illustration of the kinematic likelihood fitting software package and its integration in an analysis framework	156
6.15. Distributions of different variables, before and after applying an event-level kinematic likelihood fit	157
6.16. Dijet-invariant-mass distributions for the 2-lepton MVA selection, showing the total resolution improvement from the kinematic likelihood fit together with the muon-in-jet correction with respect to the global sequential calibration.	157

6.17. The dependence of the dijet mass resolution and its improvement for different values of the resolution for balancing the $\ell\ell b\bar{b}$ system in the transverse plane	158
6.18. The correlation between the pre-fit and post-fit p_T for different $\sigma(p_{x,y}^{\ell\ell b\bar{b}})$.	159
6.19. Probability ratio of p_T^{fit} and p_T^{reco} for different choices of $\sigma(p_{x,y}^{\ell\ell b\bar{b}})$	160
7.1. The $m_{b\bar{b}}$ distribution observed in data after subtracting all backgrounds except for diboson production	164
7.2. The fitted diboson signal strength μ_{VZ} for the 7 and 8 TeV datasets and their combination	165
7.3. Event yields as a function of $\log(S/B)$ for data, background and expected Higgs boson signal for 7 and 8 TeV data	166
7.4. Observed and expected 95% CL cross-section upper limits and p_0 values as a function of m_H for the 7 and 8 TeV datasets combined	168
7.5. The fitted values of the Higgs boson signal strength for $m_H = 125$ GeV .	169
A.1. Example input variables to the MVA in the (LL, MM, TT) combined 2-jet 2-tag category	174
A.2. Distributions of the p_T^V with MM and TT b -tagging in each lepton channel	175
A.3. The dijet-mass distributions with MM and TT b -tagging in each lepton channel	176
A.4. Distributions of the BDT_{VH} with MM and TT b -tagging in each lepton channel	177
B.1. The probability ratio of the post-fit jet p_T and the pre-fit jet p_T as a function of the ratio of their corresponding momenta	186
B.2. The probability ratio of the post-fit jet p_T and the pre-fit jet p_T as a function of the post-fit jet p_T	187
B.3. The probability ratio of the post-fit jet p_T and the pre-fit jet p_T as a function of the pre-fit jet p_T	188

List of Tables

2.1. The Standard Model fermions and their quantum numbers	7
3.1. LHC beam parameters	36
3.2. ATLAS performance goals	41
3.3. ATLAS Muon Spectrometer subdetector parameters	59
4.1. Electron identification efficiencies for different likelihood-based identification criteria	71
4.2. Inclusive loose, medium and tight lepton object definitions in the VH analysis.	75
4.3. MV1c b -tagging operating points with their b -jet efficiency and c -jet, τ -jet and light-quark jet rejection factors	105
5.1. The MC generators used for the simulation of the signal and background processes	116
5.2. Kinematic and topological event selections for the dijet-mass analysis and the MVA	120
5.3. Standard Model values for cross section times branching ratio (BR) and acceptance for the three channels at 8 TeV. The acceptance is shown for the MVA (dijet-mass analysis)[8].	121
5.4. MVA input variables for the 0-, 1- and 2-lepton channels	122
5.5. Theoretical uncertainties on the VH signal and background modelling. .	137
5.6. The different distributions in each region entering the likelihood fit . . .	139

7.1. Significance improvements from jet energy calibrations	163
7.2. The number of events in the bins of Figure 7.3a for data, fitted background, and expected Higgs boson signal	167
A.1. The pre-fit event yield for $0 < p_T^V < 90$ GeV in the dijet-mass analysis. . .	178
A.2. The pre-fit event yield for $90 < p_T^V < 120$ GeV in the dijet-mass analysis. .	179
A.3. The pre-fit event yield for $120 < p_T^V < 160$ GeV in the dijet-mass analysis. .	180
A.4. The pre-fit event yield for $160 < p_T^V < 200$ GeV in the dijet-mass analysis. .	181
A.5. The pre-fit event yield for $p_T^V > 200$ GeV in the dijet-mass analysis. . . .	182
A.6. The pre-fit event yield for $0 < p_T^V < 120$ GeV in the MVA.	183
A.7. The pre-fit event yield for $p_T^V > 120$ GeV in the MVA.	184